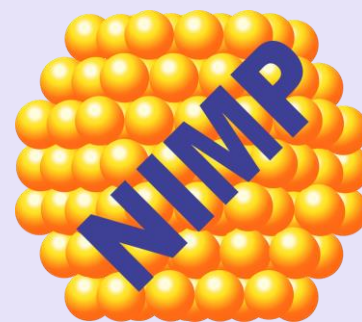


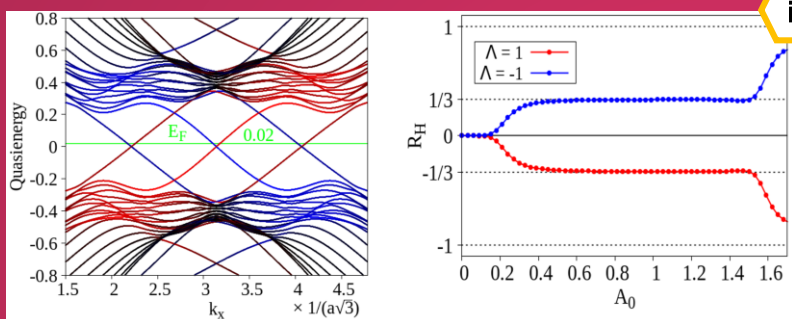
**i**



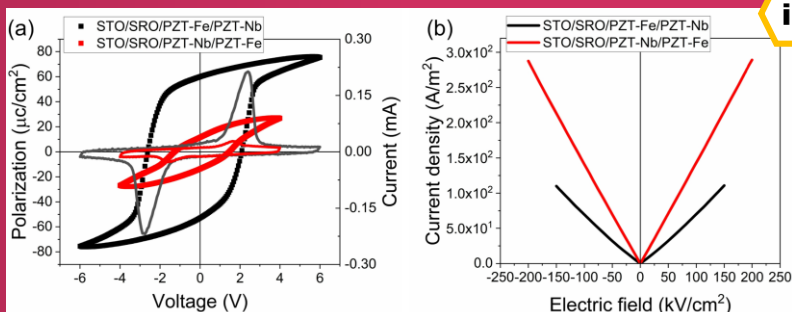
**National Institute of  
Materials Physics**

**ANNUAL  
REPORT  
2023**

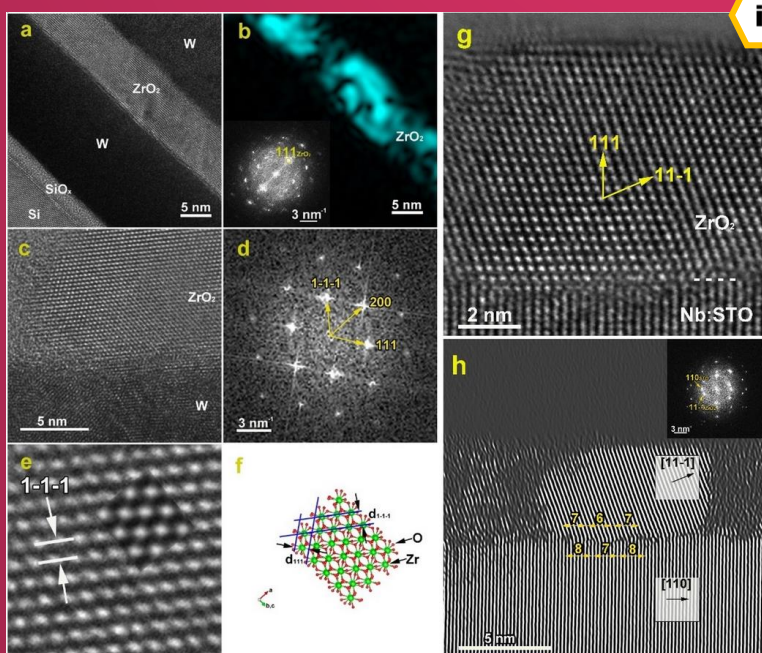
**Ministry of Research,  
Innovation and  
Digitalization**



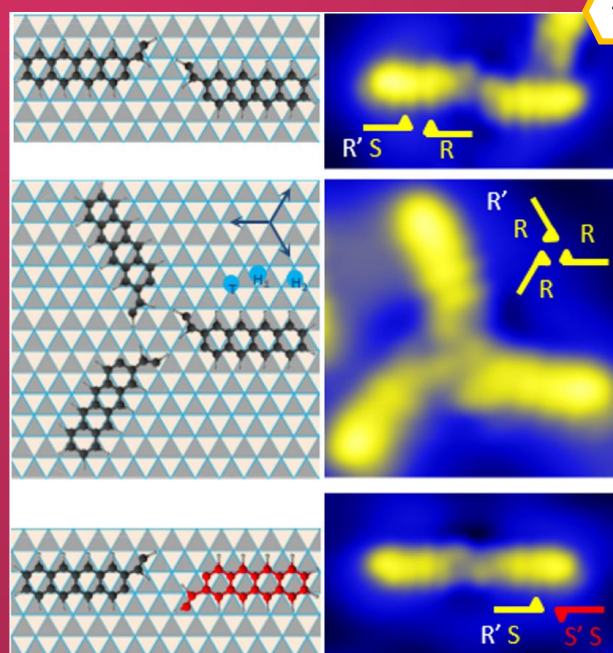
**ii**



**iii**



**iv**



**v**

# National Institute of Materials Physics

## ANNUAL REPORT 2023

### Cover page – Figures reproduced/adapted from:

- i) **C.G. Sanz, A. Aldea, D. Oprea, M. Onea, A.T. Enache, M.M. Barsan**, “Novel Cells Integrated Biosensor based on Superoxide Dismutase on Electrospun Fiber Scaffolds for the Electrochemical Screening of Cellular Stress”, *Biosensors & Bioelectronics* 220, 114858 (2023).
- ii) **A. Pena**, “Control of Spectral, Topological and Charge Transport Properties of Graphene via Circularly Polarized Light and Magnetic Field”, *Results in Physics* 46, 106257 (2023).
- iii) **G.A. Boni, C. Chirila, L. Trupina, L.D. Filip, V. Moldoveanu, I. Pintilie, L. Pintilie**, “Resistive-like Behaviour in Ferroelectric p-n Homojunction based on Epitaxial  $\text{Pb}(\text{Zr}_{0.2}\text{Ti}_{0.8})\text{O}_3$  Thin Films”, *ACS Applied Electronic Materials* 5, 957–967 (2023).
- iv) **A.P.S. Crema, M.C. Istrate, A. Silva, V. Lenzi, L. Domingues, M.O. Hill, V.S. Teodorescu, C. Ghica, M.J.M. Gomes, M. Pereira, L. Marques, J.L. MacManus-Driscoll, J.P. B. Silva**, “Ferroelectric Orthorhombic  $\text{ZrO}_2$  Thin Films Achieved Through Nanosecond Laser Annealing”, *Advanced Science* 10, 2207390 (2023). & **J.P.B. Silva, M.C. Istrate, M. Hellenbrand, A. Jan, M.T. Becker, J. Symonowicz, F.G. Figueiras, V. Lenzi, M.O. Hill, C. Ghica, K.N. Romanyuk, M.J.M. Gomes, G. Di Martino, L. Marques, J.L. MacManus-Driscoll**, “Negative Piezoelectric Coefficient in Ferroelectric Orthorhombic Phase Pure  $\text{ZrO}_2$  Thin Films”, *Applied Materials Today* 30, 101708 (2023).
- v) **B. Borca, T. Michnowicz, F. Aguilar-Galindo, R. Pétuya, M. Pristl, V. Schendel, I. Pentegov, U. Kraft, H. Klauk, P. Wahl, A. Arnau, U. Schlickum**, “Chiral and Catalytic Effects of Site-Specific Molecular Adsorption”, *The Journal of Physical Chemistry Letters* 14, 2072 (2023).

# **Research Laboratories**

# LABORATORY 10

## “Functional Nanostructures”

**Head of laboratory:** Dr. Silviu POLOȘAN, Senior Researcher rank 1 ([silv@infim.ro](mailto:silv@infim.ro))

**Personnel:** 36 members – 11 × SR1, 9 × SR3, 3 × SR, 10 × RA, and 3 × technician (\*SR stands for Senior Researcher; RA stands for Research Assistant).

### Main research directions:

The group deals with nanostructures and nanostructured materials preparation and development of applications. Both chemical/electrochemical (chemical bath deposition, electrochemical deposition with and without a template, chemical vapor deposition) and physical (sputtering, thermal evaporation in vacuum, electrospinning and forcespinning) methods are employed for nanostructures and nanostructured materials preparation. Different types of materials are used, including here metals, metal oxides, organometallic compounds and polymers. The nanostructures developed by this approach are used as building blocks for different types of functional devices (*e.g.*, transistors or diodes, biosensors, actuators). Several specific examples follow:

- Nanostructures and devices based on nanostructures – physical and chemical methods are employed for preparing nanostructures. Electrochemical or chemical deposition is used for preparing nanowires of zinc oxide with diameters down to 10 nm. Thermal oxidation of metal foils is used for obtaining metal oxide nanowires with diameters down to 20 nm. Further, the nanowires can be employed as building blocks for electronic devices such as diodes and transistors using microlithographic (photolithography and electron beam lithography). Devices complexity can be employed (*e.g.*, core shell devices can be fabricated) by covering the nanowires with thin-films employing methods such as magnetron sputtering or thermal evaporation. Chemical vapor deposition is employed for preparing thin nanostructured films such as metal oxides or graphene.
- Materials for applications in optics, optoelectronics and photonics for devices which include diodes and transistors for light emitting applications, glasses or modular composition fibers for photonic applications.
- Biosensors and biomedical devices based on nanostructures or on devices containing nanostructures as building blocks.

Nanostructures and nanostructured materials can be exploited successfully in biosensors, mainly due to the high specific surface but also due to other specific functionalities induced by the low dimensionality. Electrochemical sensors are developed based on nanostructured materials and are functionalized with different types of biomolecules in such a way in which both the desired sensitivity and selectivity are obtained. In this context, different types of substrates and configurations of functionalization are investigated with the goal of optimizing device performances. Novel applications are considered, including wearable sensors for physiologic parameters monitoring. Several specific examples follow:

- Submicrometer fibers; biomimetic devices based on microfiber web electrodes. In our group, methods of fabricating polymer submicrometric fibers were developed namely: electrospinning and forcespinning. By further functionalization, transparent and flexible electrodes based on metal covered polymer fiber webs are obtained. These electrodes can be applied on a wide range of substrates including here materials such as textiles and paper and can become the functional element of devices such as biosensors or for applications such as artificial muscles. Functionality can be increased by covering with electroactive polymers, leading to devices with highly superior performances when compared to classic architectures.
- Biocompatible materials represent another research direction of the group, several approaches being developed, including both biopolymeric fibers (collagen or cellulose), natural membranes (eggshell membrane) or nanostructured materials such as hydroxyapatite. Further

functionalization includes covering with different compounds or nanostructures or doping and leads to multiple fields of applications, the main one being that of medical devices.

The research directions of Lab. 10 are mostly interconnected for developing devices with direct applications. Equipment for fabricating fibers by means of electrospinning and forcespinning were designed and developed in the laboratory with the support of the engineers from the application department.

### **Relevant infrastructure:**

The activity of Lab. 10 relies on several fully-equipped chemistry and electrochemistry laboratories (dedicated to different types of applications) as well as clean room infrastructure, essential for devices fabrication:

- Electron-beam nanolithography equipment with Raith Elphy systems with laser interferometers and Hitachi S3400 and Zeiss Merlin compact electron microscopes;
- Lithography/Mask Alignment EVG®620 NT system with nanoimprint capabilities;
- CVD equipment for preparation of carbon-based nanostructures;
- CVD equipment for deposition of semiconducting materials;
- Laboratory for optical characterization including UV – Vis absorption spectrometers (Cary 5 and Perkin Elmer 35), photoluminescence spectrometers (Edinburgh and Perkin Elmer LS55), near field photoluminescence microscope, plasmonic resonance spectrometer with potentiostat;
- Liquid chromatography equipment with mass spectroscopy;
- Laboratory for cytocompatibility testing, including cell culture facilities and multi-parametric analysis methods (flow cytometry, spectrophotometry, fluorescence microscopy).

### **Available services:**

- Scanning electron microscopy characterization of materials (micromorphology, composition);
- Optical characterization by means of optical spectroscopy;
- Development of equipment for producing micrometric and submicrometric fibers by means of electrospinning and forcespinning.

### **Main results:**

- 9 research projects (2 × PED, 4 × PCE, 1 × POC, 1 × Marie Skłodowska-Curie Actions (MSCA), and 1 × PD);
- More than 50 articles published in Web of Science®-indexed journals with impact factor (of which 27 with main author from Lab. 10);
- 2 OSIM awarded patents;
- 10 OSIM patent applications.

### **Highlights:**

- Nanostructured surfaces based on silver nanoparticles decorated ZnO-CuO core-shell nanowire arrays & Carbon inks-based screen-printed electrodes for qualitative analysis of amino acids [see *Scientific Reports* 13, 10698 (2023); *International Journal of Molecular Sciences* 24, 1129 (2023)];
- Various types of electrodes such as transparent conductive electrodes (TCE) obtained by the electrospinning method and integrated architectures of electrodes and flexible porous substrates for point-of-care testing [see *Micromachines* 14, 543 (2023); *Current Opinion in Electrochemistry* 42, 101418 (2023)];
- New selective AB3 aptamer for the hematologic tumor cells' detection; Proteasome inhibitor anticancer drug bortezomib and electrochemical protein-based bioanalytical devices for drug

- analysis [see *Sensors and Actuators B-Chemical* 394, 134389 (2023); *Molecules* 28, 3277 (2023); *Current Topics in Medicinal Chemistry* 23, 1448 (2023)];
- Metallic thin films with various applications [see *Coatings* 13, 984 (2023)].

# LABORATORY 20

## “Complex Heterostructures and Multifunctional Materials”

**Head of laboratory:** Dr. George STAN, Senior Researcher rank 1 ([george\\_stan@infim.ro](mailto:george_stan@infim.ro))

**Personnel:** 33 members – 8 × SR1, 4 × SR2, 7 × SR3, 2 × SR, 8 × RA, 3 × sub-engineer/engineer, and 1 × technician.

23 team members hold PhD titles in physics, chemistry, or materials engineering, including 1 PhD supervisor. Additionally, there are 2 PhD students and 3 MSc students on the team.

### Main research directions:

- Ferroelectric materials and related structures for electronic, optoelectronic and sensing applications (including non-volatile memories, UV and IR detectors, piezoelectric devices);
- Materials and devices with application in microelectronics, photovoltaic conversion and light/particle detection (including field-effect transistors, hybrid perovskite and kesterite solar cells, and silicon-based particle detectors);
- Superconducting and magnetic materials, strongly correlated electron systems;
- Dielectric and ferroelectric materials for microwave devices (*e.g.*, dielectric resonators, ferroelectric varactors, filters, antennas).
- Materials for healthcare applications.

### Relevant infrastructure:

Laboratory 20 possesses a noteworthy infrastructure, covering the entire technological chain from the preparation of materials in the form of powders, bulk and thin layers and their complex physico-chemical characterization, to the integration of the optimized materials into functional devices. Amongst the most important systems and equipment one can mention:

- SURFACE SCIENCE pulsed laser deposition (PLD) work station (**Fig. 20–1a**) equipped with: 2 deposition chambers, each with 4-target carousels; a KrF excimer laser with 248 nm wavelength, repetition rate of 1 – 10 Hz, and maximum energy of 700 mJ; control of laser fluence; substrate heating up to 1000 °C; control of working gases pressure; *in-situ* reflection high-energy electron diffraction (RHEED) capabilities. One reaction chamber is used to deposit ferroelectric layers based on perovskites and other metal oxides (*e.g.*, doped ZnO, HfO<sub>2</sub>), whilst the other chamber is used to prepare superconductor thin-films.
- SURFACE SCIENCE hybrid system for thin-films synthesis from temperature-sensitive materials by (i) matrix assisted pulsed laser evaporation (MAPLE) and (ii) PLD, constituted of: a deposition chamber with *in-situ* freezing facilities for targets (*e.g.*, frozen suspensions of organic materials or inorganic nanoparticles in a support matrix); a KrF excimer laser with 248 nm wavelength, 1 – 10 Hz repetition rate, and 700 mJ maximum power; maximum heating temperature of the substrate: 500 °C – MAPLE & 700 °C – PLD.
- Multi-cathode radio-frequency (RF), direct current (DC) and pulsed direct current (p-DC) magnetron sputtering (MS) systems with various facilities: bias, etching and heating (up to 800 °C) of substrates; vacuum load-lock for sample transfer; vacuum systems (down to ~10<sup>-6</sup> Pa); computerized control and process automation. The latest MS equipment, AJA PHASE II J, purchased in 2016, is shown in **Fig. 20–1b**. Each MS system in Laboratory 20 is dedicated to a distinct class of materials: metallic contacts; semiconductor and dielectric materials; biocompatible materials.
- Chemistry laboratory for the preparation of powders, bulk materials and thin-films by chemical (wet) methods, equipped with high-temperature annealing furnaces; spin-coating systems; fume hoods, aggregate mills; weighting scales; in-house made glove-boxes; glassware; *etc.*

- Doctor blade/Slot-die MTI system for large area deposition equipped with 100 mm width adjustable micrometer applicator, a slot-die head and an adjustable speed syringe pump. Additionally, two in-house built Doctor blade/Slot-die systems are also available.
- Professional Glove-box MBraun with two chambers (3 and 4 gloves), with integrated spin-coater and closed cycle gas purification system capable of maintaining an atmosphere with  $\text{H}_2\text{O}$  and  $\text{O}_2$  under 0.1 ppm and with a solvent filter.
- Laboratory for the preparation of piezoelectric and superconducting materials, polycrystals and single crystals.
- Ceramic materials 3D printing laboratory, equipped with a NORDSON EFD, EV series, robocasting (direct ink writing) printing system, with Ultimius V dispenser (**Fig. 20–2a**); an ANTON PARR MCR302e modular rheometer (**Fig. 20–2b**); and a THINKY ARE-250 ceramic mixing & degassing machine.

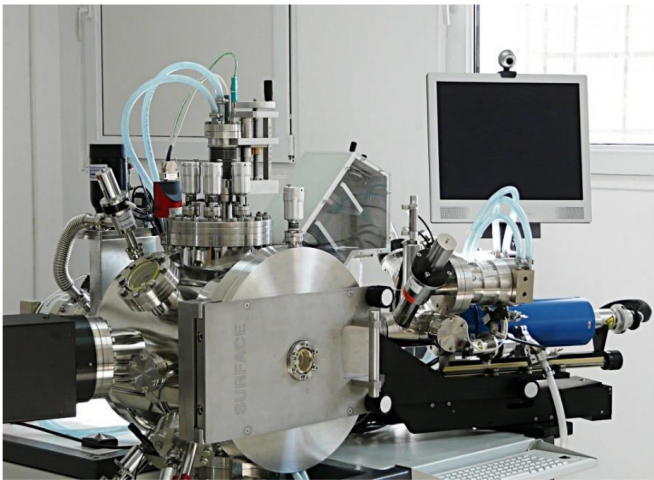


**Fig. 20–1a** PLD workstation assembly, SURFACE SCIENCE, for the deposition of ferroelectric thin-films.



**Fig. 20–1b** RF, DC and p-DC magnetron sputtering system, AJA PHASE II, for the deposition of semiconductor thin-films.



**Fig. 20–2a** 3D printing system by robocasting (direct ink writing) technology, NORDSON EFD, EV series, with Ultimius V dispenser.



**Fig. 20–2b** ANTON PARR MCR302e modular rheometer.

- X-ray diffraction systems for structure analysis of thin-films (a RIGAKU SmartLab 3 kW/2017 from room-temperature to 1100 °C – **Fig. 20–3a** and a BRUKER D8 Advance/2006)

and powders (ANTON PAAR XRDynamic500 – from 600 °C to –180°C and a BRUKER D8 Advance/2007).

- Optical and structural characterization systems, including a (i) variable angle spectroscopic ellipsometer (WOOLLAM) with wavelength range 200 – 1700 nm (6.2 – 0.73 eV), angle of incidence (35 – 90°), automated sample translation stage (for mapping) 150 mm × 150 mm, and an Instec temperature control stage (-160 – 600 °C) and (ii) a near infrared (NIR), infrared (midIR) and far infrared (farIR) Fourier transform infrared (FTIR) JASCO spectrometry platform, encompassing the 12000 – 50 cm<sup>-1</sup> spectral range (**Fig. 20–3b**). VASE Woollam can be used in the following modes: (i) reflection ellipsometry on semiconductor/dielectric thin-films or multilayers (inferred sample parameters: thicknesses, refractive index, extinction coefficient, absorption coefficient, dielectric function, band gap, critical point energies, electrical parameters for degenerate semiconductors – resistivity/conductivity, carrier density, scattering time, carrier mobility, phase transition in the temperature range -160 – 600 °C); and (ii) transmission ellipsometry on uniaxial/biaxial crystals, glasses and glass ceramics (derived sample parameters: linear birefringence and linear dichroism, Verdet constant/ Faraday rotation).
- Surface investigation by scanning probe microscopy (SPM) in contact or non-contact mode with piezoelectric (PFM), magnetic (MFM) or conductive (C-AFM) response.



**Fig. 20–3a** RIGAKU SmartLab 3 kW high-resolution XRD system for thin-films analysis.

Spectrometru FTIR cu vid, model JASCO 6800 FV-BB (MID & FAR IR)



Spectrometru FTIR, model JASCO (NEAR & MID IR)



**Fig. 20–3b** FTIR spectroscopic platform with extended NIR – MID – farIR spectral range, 12000 – 50 cm<sup>-1</sup>.

- Electrical measurements laboratory (see **Fig. 20–4**), including: 2 LAKE SHORE cryo-probers for electrical measurements in the temperature range of 10 – 400 K; one with vertical magnetic field up to 2.5 T, and one with horizontal magnetic field up to 1.5 T, each with at least 3 micro-manipulated arms with contact needles allowing electrical measurements from liquid helium to 400 K under various electric/magnetic fields and illumination conditions; 4 cryostats, covering a temperature range between 10 – 800 K; DLTS (deep-level transient spectroscopy) and TSC (thermally stimulated current) systems for the investigation of electrically active defects (charge carrier traps) in materials and MOS-like structures; set-up for pyroelectric measurements; ferritesters; various instruments for measuring currents, resistances and voltages (electrometers, nanovoltmeters, Lock-In amplifiers); voltage and current sources; RLC bridges; and impedance analyzers. These facilities are used to perform complex characterization of electrical (hysteresis loops; CV and I-V characteristics; impedance spectroscopy; defect spectroscopies; *etc.*) and superconductive properties (electron transport, thermodynamics, magnetic-field penetration depth measurements); determination of the d<sub>33</sub> piezoelectric coefficient.
- Solar cells testing laboratory (**Fig. 20–5**), with two Newport LED solar simulators (aperture 50 mm × 50 mm), VeraSol-2 AAA Class and a MiniSol ABA Class), with AM 1.5G solar spectrum and adjustable power coupled with a Keithley source 2601. A system for measuring

the Quantum Efficiency (EQE and IPCE) with accessories, working in the 250 – 2500 nm spectral range, is available.

- Microwave dielectric materials and devices testing laboratory, including:
  - Vector Network Analyzer PNA 8361A from Agilent (0.01 – 67 GHz) for two-ports complex S parameters. It uses electronic calibrator Agilent N4694-60001 in the range of 0.01 – 67 GHz. For access, 1.9 mm, 2.9 mm, 2.4mm, 3.5 mm, SMA or N connectors or adaptors are used.
  - Vector Network Analyzer PNA-X N5245A from Agilent (0.1 – 50 GHz standalone) with 4 ports and dual sources. It allows measurements of the S and X non-linear parameters. By using the millimeter wave extensions, the system covers a wide frequency band up to 500 GHz. Each extension pair allows the measurement of the two-ports parameter of waveguide devices. The millimeter wave extensions are from Agilent/OML (N5260A V10 VNA2, WR-10, 75-110 GHz; N5260A V06 VNA2, WR-06, 110-170 GHz; N5260A V05 VNA2, WR-05, 140-220 GHz; N5260A V03 VNA2, WR-03, 220-325 GHz; N5260A V02.2 VNA2, WR-02.2, 325-500 GHz).
  - Anechoic chamber with internal dimensions 3040 mm × 4100 mm × 2800 mm, for antenna characterizations (*e.g.*, directivity parameter) in the range of 0.9 – 40 GHz.
  - Microprobe station for direct *on-wafer* measurements of two-ports in the frequency range 0.1 – 67 GHz by using GSG probes with 150 μm and 100 μm pitches.
  - THz-TDS spectrometer from AISPEC Pulse IRS 2000 Pro, operating in the range of 200 GHz – 5 THz.
- In the framework of collaborative research activities, Laboratory 20 can access other NIMP infrastructures, such as: TEM and SEM equipment; XPS characterization (including at Elettra Synchrotron Trieste); magnetic measurements (SQUID, PPMS); other optical spectroscopy techniques (Raman, UV-Vis-NIR, luminescence); clean-room (photolithography, dry etching); and *in-vitro* preliminary biological testing of materials.



**Fig. 20–4** Laboratory for electrical characterization of dielectric, ferroelectric and semiconductor materials.

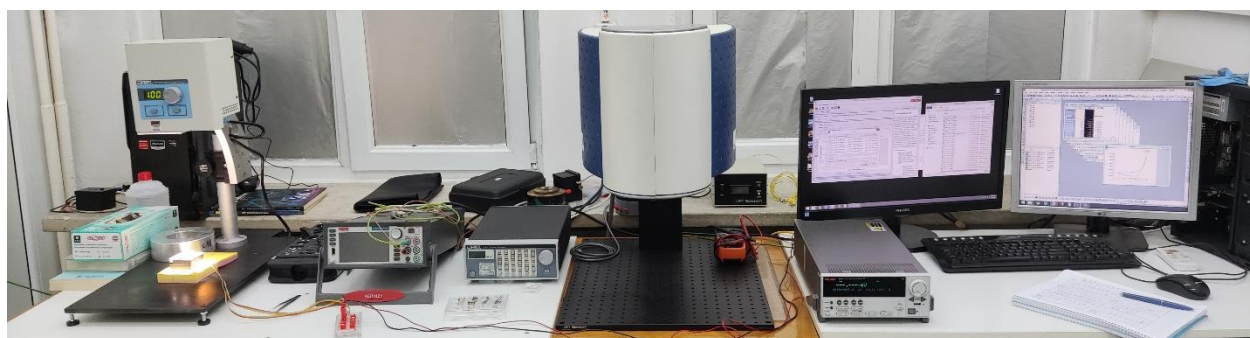


**Fig. 20–5** Solar cells testing laboratory.

**Available services:**

- Preparation of materials (nano-powders; bulk ceramics; fabrication of thin-films by various techniques, including chemical methods, CVD and PVD techniques);
- Investigation of charge carrier traps by DLTS and TSC;
- Electric characterization of materials in a wide temperature range, under electric and magnetic fields;
- Investigation of pyroelectric properties;
- Fabrication and characterization of materials by electrochemistry;
- Fabrication and characterization of perovskite solar cells;
- Fabrication and characterization of microelectronic devices (*e.g.*, FET, MOS);
- Characterization of microwave, millimeter waves and terahertz materials and devices;
- Antenna characterization (antenna directivity) in anechoic chamber in the frequency band from 900 MHz to 40 GHz;
- Electromagnetic design for microwaves devices/structures by using high accuracy software packages such as CST Studio Suite, Ansoft HFSS, and Ansoft Designer;
- Deposition of biocompatible (ceramic and glass) coatings on metallic implants;
- Characterizations by (*a*) reflection ellipsometry on semiconductor/dielectric thin-films or multilayers (thicknesses, refractive index, extinction coefficient, absorption coefficient, dielectric function, band gap, critical point energies, electrical parameters for degenerate semiconductors – resistivity/conductivity, carrier density, scattering time, carrier mobility, phase transition in the temperature range -160 – 600 °C); and (*b*) transmission ellipsometry on uniaxial/biaxial crystals, glasses and glass ceramics (optical constants, linear birefringence and linear dichroism, Verdet constant/ Faraday rotation).
- XRD characterizations for crystalline phase identification and their quantitative analysis; determination of the lattice parameters, average size of crystallites, macro- and micro-strains, preferred orientation, *etc*; analysis of homo- and hetero-epitaxial structures; X-ray reflectometry analyzes for inferring the thickness, density and roughness of the surface and interfaces of amorphous and crystalline layers and multi-layers; *etc*.
- FTIR spectroscopy analyses in transmission, specular reflectance (including at grazing incidence), attenuated total reflectance – ATR (RT – 180 °C), diffuse reflectance – DRIFT (RT – 500 °C) and integrating sphere modes.
- Morpho-compositional analyses by HR-SEM – EDXS;
- Surface characterization of materials by AFM, PFM, MFM, and C-AFM.

**Main results:**

- 9 research projects (1 × SEE, 2 × CERN, 1 × PED, 1 × PTE, 1 × PCE, 1 × PD, 1 × Sectorial, and 1 × RoNaQCI);
- 35 articles published in Web of Science®-indexed journals with impact factor (of which 12 with main author from Lab. 20);
- 1 OSIM awarded patent;
- 1 EPO patent application;
- 5 OSIM patent applications.

**Highlights:**

- Successful implementation of the economical contract with the Swarm European Services, tackling researches in the field of memristors for cryptographic key applications (the collaboration continues in 2024);
- EEA-Norway funded project, targeting the fabrication of large-area perovskite solar cells and their assembly into mini-solar panels;

- The analysis of the p-n ferroelectric homojunctions using Nb- and Fe-doped PZT layers has revealed unexpected quasi-linear current-voltage characteristics and resistance exhibiting exponential temperature dependence. These findings suggest the coexistence of electrons and holes in the junction, along with intricate charge compensation processes at the interfaces. [see *ACS Applied Electronic Materials* 5, 957–967 (2023)];
- Sn-doped  $V_2O_3$  thin films deposited on graphene/Al by pulsed laser ablation for lithium ion battery cathodes with improved electrochemical capacity and stability [see *Journal of Electroanalytical Chemistry* 933, 117290, (2023).];
- Nanostructuring in dense BST ceramics derived from fine-grained powder emerged as the solution for diminishing permittivity while preserving tunability, enhancing energy storage capacity, and promoting the formation of thermally stable polar nanoclusters. This supports the viability of nanostructured electroceramics in the context of tunable and microwave devices. [see *Journal of the European Ceramic Society* 43, 3250–3265 (2023)].

# LABORATORY 30

## “Magnetism and Superconductivity”

**Head of laboratory:** Dr. Victor KUNCSEK, Senior Researcher rank 1, Habil. ([kuncser@infim.ro](mailto:kuncser@infim.ro))

**Personnel:** 33 members – 5 × SR1, 8 × SR2, 7 × SR3, 3 × SR, 3 × RA, 2 × technological development engineer (\*1 × TDE2 and 1 × TDE3), 1 engineer, and 4 × technician.

In addition to scientific activities, the group is also involved in educational and training initiatives.

There are two PhD advisers coordinating PhD students annually, as well as undergraduate students performing their scientific training.

### **Main research directions:**

- Fundamental and applied research in the field of magnetic and magneto-functional materials for actuator and sensoristic applications as well as in the field of superconductivity, mainly targeting materials with superconducting properties with potential for practical applications. The research process covers all stages, from preparation (bulk materials, thin-films or nanostructures) to structural and electronic characterization, completed with a deep analysis of the magnetic and superconducting properties, respectively.
- Related to the magnetic behavior, mainly the functionalities mediated by magnetic reconfiguration controlled by temperature, magnetic and electric fields, applied or from interface interactions, are envisaged. The research is focused especially on the study of 0D, 1D and 2D nanostructures. In the case of magneto-functional structures, magnetic systems of nanoparticles, thin-films and multilayers, materials for colossal magnetoresistance (CMR), giant magnetoresistance (GMR) and tunneling magnetoresistance (TMR), soft and hard magnetic materials, Heusler compounds with spin polarization, heterogeneous multiferroic systems, magneto-caloric materials, diluted magnetic oxides/semiconductors, thermo-electric systems, *etc* are envisaged. In addition, bulk materials, advanced hybrid systems and composites / nanocomposites destined to operate in extreme conditions such as the ones in fusion and fission reactors, particle accelerators and in space, are investigated. Interactions at the interface and functionalities induced by them in nanostructured hybrid systems such as soft magnet / hard magnet (exchange-spring), ferromagnet/antiferromagnet (exchange-bias), ferromagnet-ferroelectric (magneto-electric coupling) represent other fields of interest related to fundamental and applicative aspects of smart multi-functional systems. In specific cases, the experimental studies are completed by theoretical studies approaching electronic configurations based on Density Functional Theory (DFT) and magnetic configurations based on finite-element simulation programs.
- Related to the superconducting behavior, studies of vortex matter, dynamics and pinning and nano-engineering of artificial pinning centers for high-magnetic field applications are envisaged. Exploration of fields of applicability of these materials and related ones considering, beyond superconductivity, other that may be important for applications, such as mechanical, biological, optical are also considered. The studied materials are mainly cuprate high temperature superconductors Y (rare earth)  $\text{Ba}_2\text{Cu}_3\text{O}_7$  (RE123) with nano-engineered pinning centers, Bi- and La- based superconducting cuprates,  $\text{MgB}_2$  (with various additions for increasing pinning properties), iron-based pnictide and chalcogenide multicomponent superconductors and low temperature (classic) metallic and intermetallic superconductors. Other materials of interest are  $\text{CeO}_2$ ,  $\text{SrTiO}_3$ ,  $\text{LiPdPtB}$ ,  $\text{PdO}$ , boron/carbide composites, selected steels, and archaeological ceramic materials. Most of the materials are obtained in the laboratory in various forms: powders, polycrystalline bulk samples, single crystals, wires/tapes, nanostructures, heterostructures and nanocomposites. The group uses advanced techniques for obtaining or processing materials: conventional powder synthesis in controlled atmosphere, cryochemistry or energy milling, crystal growth in flux or by melting zone,

growth of thin-films by laser ablation, sintering by spark plasma, lamination, arc melting, *etc.* Advanced analysis of superconducting properties aims in particular to determine vortex phase diagrams vortex dynamics and vortex pinning. Temperature dependence of magnetization and resistivity, isothermal hysteresis magnetization and magnetic relaxation, current-voltage characteristics, bulk pinning force and pinning potential, *etc.* are analyzed within the existing theoretical models or using recognized practical and theoretical methodologies developed by some members of the group, for example pinning potential determined from frequency-dependent AC susceptibility response, or the use of normalized magnetic relaxation rate to determine the cross-over between elastic and plastic vortex creep, and various field- and temperature-dependent creep exponents.

### **Relevant infrastructure:**

Amongst important research equipment, considering preparation facilities as well as characterization ones, the following can be listed:

- Spark plasma sintering, hot pressing sintering, microwave sintering (**Fig. 30–1**);
- Melt-spinning and various ball mills;
- Nanoparticle preparation systems by hydrothermal / solvothermal synthesis in autoclave and centrifugation for separation by sizes);
- RF/DC sputtering deposition system for magnetic thin-films and multilayers with 4 sources and base pressure in the range of  $10^{-9}$  mbar;
- Facility for inducing thermal transfer in radiofrequency magnetic field to determine specific absorption rates in dispersed nanoparticle systems;
- Thermogravimetric and differential scanning calorimetry systems;
- Vibrating Sample Magnetometry system in magnetic fields up to 9 Tesla;
- Mossbauer spectrometers with different accessories to perform measurements at variable temperatures (4.5 K – 1000 K) and in applied fields, *via* the detection of gamma radiation / X- rays / conversion electrons (the only group in Romania active in Mossbauer Spectroscopy) (**Fig. 30–1**);
- Complex system for measurements of physical properties (PPMS) with magnetic fields up to 14, DynaCool System in up to 9 T and a SQUID type magnetometer (**Fig. 30–1**) working in 7 T down to 2 K from Quantum Device with the corresponding facility for liquid He production (18 L /24 h);
- Magnetic texturing of thin-films is investigated by vectorial MOKE magnetometry;
- For high temperature domain, the laboratory possesses a Laser Flash Analyzer system that allows the determination of thermal diffusivity, specific heat and thermal conductivity of the volume materials or multilayers (3 layers, including liquids) in the range 25 – 1100 °C, a dilatometer (Netzsch 402 C, 2015) to determine thermal expansion coefficients (25 – 1600 °C) and an equipment (Netzsch, Nemesis 2015) to determine electrical conductivity and Seebeck coefficient (25 – 800 °C);
- In order to determine the composition in bulk / powder systems, an X-ray fluorescence device is available, while for very low concentrations/quantities the group possesses an inductively coupled plasma mass spectrometer (ICP-MS) (**Fig. 30–1**), with an extension for thin film analysis by laser ablation (LA), the last one being acquired in 2019;
- Mechanical properties are determined in quasistatic regime up to 1700 °C, using a recently-acquired equipment (INSTRON).



**Fig. 30–1** ICP-MS with LA for thin-films (upper left), Mossbauer spectrometers with closed circuit He cryostats (lower left) and SQUID device – Quantum Design, of high sensitivity (middle). Spark plasma sintering plant (FCT Systeme GmbH) used to obtain high density bulk materials (right).

#### Available services:

- Preparation of metallic and intermetallic compounds in the geometry of thin-films, ribbons or bulk;
- Synthesis of materials that are important for applications using state-of-the-art powder metallurgy techniques;
- Lyophilization from frozen materials;
- Treatment of powders and thin-films at high pressures and temperatures in non-corrosive gas atmosphere (hydrogen, nitrogen, methane, carbon dioxide, helium) and measurement of the formation kinetics and thermodynamics of the materials obtained by gas-solid reaction;
- High sensitivity magnetometry to characterize the magnetic properties of the elements (bulk, powders and nano-powders, ribbons and nanocomposites, 0-, 1- and 2-dimensional nanostructures);
- Characterization of the thermodynamic and transport properties (thermal, electric) of the materials in a large temperature domain;
- Determination of the Debye temperature, specific heat and entropy variation of solid materials in the temperature range of 2 – 300 K and in a magnetic field between 0 and 14 T;
- Determination of thermal conductivity of solid materials in the temperature range of 2 – 300 K and in a magnetic field between 0 and 14 T;
- Complex characteristics and specific properties of materials with iron evidenced by powerful nuclear gamma resonance investigation methods (Mossbauer spectroscopy);
- Specific temperature-dependent properties evidenced by modern differential thermal analysis methods, differential calorimetry and mass spectrometry;
- Atomistic simulation within the DFT of the materials for advanced applications and finite element micromagnetic modelling;
- Preparation / processing by various techniques of powders, single-crystals, thin-films / heterostructures / nanostructures, bulks, composites;
- Magnetic and transport measurements on superconducting materials;
- Analysis of experimental data obtained on superconductors with the determination and modeling of critical parameters (critical temperature, critical current density, irreversibility field, pinning force and pinning mechanisms, trapped field, vortex pinning energies, Debye temperature, and others);
- Mechanical measurements in quasistatic regime up to 1700 °C (bending / compression of hard materials);

- Analysis of mechanical properties and correlation with fractography aspects;
- Targets fabrication for thin-layer deposition.

The group also develops materials and technologies for a number of applications: superconducting thin layers and coated conductors from high critical temperature cuprates containing nano-engineered pinning centers; superconducting MgB<sub>2</sub> wires/tapes in metallic sheath; MgB<sub>2</sub>-based magnetic storage devices, magnetic concentrators and magnetic shieldings; MgB<sub>2</sub>-based powders, coatings and bulks for biomedical applications; boron-based super-hard materials for tools and extreme high temperature applications, integrated multifunctional devices.

#### **Main results:**

- 17 research projects (1 × SOL, 1 × SEE, 4 × EURATOM, 4 × PED, 1 × PCE, 2 × TE, 2 × PD, 1 × SNFR and, 1 × INUMMAT);
- 37 articles published in Web of Science®-indexed journals with impact factor (of which 21 with main author from Lab. 30);
- 1 OSIM awarded patent;
- 5 OSIM patent applications.

#### **Highlights:**

- Design and investigation of boron-based composites for operation in extreme conditions [see *Scientific Reports* 13, 6915 (2023); *Metals* 13, 715 (2023)];
- Local investigations down to single molecule level by advanced techniques [see *Nature Communications* 14, 8335 (2023); *The Journal of Physical Chemistry Letters* 14, 2072 (2023)];
- Design and characterization of novel RE-free nanocomposite magnets with enhanced magnetic performances [see *Nanomaterials*, 13, 3014 (2023); *Nanomaterials*, 13, 912 (2023)];
- Assessment of thermoelectric performances through synthesis and doping strategies in Mg<sub>2</sub>(Si,Sn) solid solutions [see *Journal of Alloys and Compounds* 944, 169270 (2023); *Journal of Materials Research and Technology* 26, 8904 (2023)];
- Vortex dynamics and pinning in some representative iron-based superconductors [see *Condensed Matter* 8, 93 (2023); *International Journal of Molecular Sciences* 24, 7896 (2023)];
- Optimizing processing conditions and developing original approaches to elucidate various functionalities of doped zinc-oxide nanostructures [see *Results in Physics* 51, 106644 (2023); *Materials* 16, 6156 (2023)];
- Advances in processing and characterization of materials for DEMO thermonuclear reactors [see *Fusion Engineering and Design* 194, 113925 (2023); *Nuclear Instruments and Methods in Physics Research B* 539, 73 (2023); *Nanomaterials* 13, 1012 (2023)].

# LABORATORY 40

## “Surface and Interface Science”

**Head of laboratory:** Dr. Cristian Mihail TEODORESCU, Senior Researcher rank 1, Habil. ([teodorescu@infim.ro](mailto:teodorescu@infim.ro))

**Personnel:** 21 members – 2 × SR1, 4 × SR2, 6 × SR3, 1 × TDE3, 3 × SR, 3 × RA, and 2 × technician.

### Main research directions:

- Surface and interface analysis by photoelectron spectroscopies (XPS–ESCA, ARUPS, spin-resolved PES, PED) *in situ* electron diffraction (LEED, RHEED), AES, scanning tunneling microscopy and spectroscopy STM–STS, photoelectron spectromicroscopy, low energy and photoemission electron microscopy (LEEM–PEEM);
- Surfaces, thin-films and heterostructure preparation by molecular beam epitaxy (MBE);
- Theoretical aspects of ferroic systems.

### New subjects:

- Analysis of ferroelectric surfaces, band bending in heterostructures;
- Molecular reactions at ferroelectric surfaces;
- In plane conduction properties of 2D systems on ferroelectric surfaces;
- ‘2D nanoreactors’, molecular reactions with reactants stabilized between graphene layers and substrates;
- Spin asymmetry in band structure of 2D systems;
- Photocatalysts with internal junctions;
- Multiferroic structures with indirect exchange or coupling through charge accumulation;
- Theoretical developments in the area of ferroic thin-films (ferroelectric, ferromagnetic);
- Ferromagnetic and ferroelectric domains;
- Development of new devices operating in ultrahigh vacuum (effusion cells, evaporators, manipulators);
- Development of software packages for data analysis.

### Relevant infrastructure:

- A complex cluster for surface and interface science (Specs, **Fig. 40–1**), composed by: (i) a chamber for photoelectron spectroscopy (XPS, ESCA, UPS, AES); (ii) a molecular beam epitaxy (MBE) chamber with *in situ* follow-up by low energy electron diffraction (LEED) and reflection high energy electron diffraction (RHEED) and residual gas analysis; (iii) a chamber for scanning tunneling microscopy and spectroscopy (STM/STS) and non-contact atomic force microscopy (AFM) with atomic resolution; (iv) load-lock and storage of samples in ultrahigh vacuum;
- An installation for X-ray photoelectron spectroscopy with possibilities of restricted area analyses (lateral resolution 2 μm) and automated change of samples / measuring areas, coupled to a reaction cell at high pressures and temperatures (Kratos, **Fig. 40–2**);
- A complex cluster for surface and interface science (Specs, **Fig. 40–3**), delocalized actually on the SuperESCA beamline at the Elettra synchrotron radiation facility in Trieste (Combined Spectroscopy and Microscopy on a Synchrotron – CoSMoS), composed by: (i) a chamber for photoelectron spectroscopy (XPS, ESCA, UPS, AES) with angle and spin resolution (ARPES, XPD, ARUPS, SR-UPS); (ii) a molecular beam epitaxy (MBE) chamber with *in situ* follow-up by low energy electron diffraction (LEED) and reflection high energy electron diffraction (RHEED) and residual gas analysis; (iii) a chamber for scanning tunneling microscopy and spectroscopy (STM/STS); (iv) load-lock and storage of samples in ultrahigh vacuum. This installation has allocated each semester from Elettra 5 days of „in-house research” beamtime

and 6 days of beamtime allocated based on research projects, reserved only from projects from Romania. In addition to synchrotron radiation beamtime, photoelectron spectroscopy using laboratory sources, or other experiments STM/STS, LEED, RHEED, Auger, *etc* are possible at any time, provided the personnel is able to travel at Elettra;

- An installation for low energy and photoemission electron microscopy: LEEM – PEEM, micro LEED, micro ARUPS (Specs). The installation is able to perform simultaneous imaging (*i.e.*, without scanning) of surfaces by using low energy electrons or photoelectrons produced by UV radiation. In the LEEM mode, the lateral resolution is about 5 nm, and in the PEEM mode about 50 nm. The advantages of using this installation are: (i) the possibility to record immediate imaging, to realize movies, to follow-up in real-time surface modifications; (ii) the fact that one uses low energy electrons makes this method suitable for delicate surfaces, which otherwise would be damaged by high energy electrons such as the ones used in scanning electron microscopy (SEM); (iii) one may obtain structural or electronic structure (densities of states, dispersion laws) information on nanometer scale.

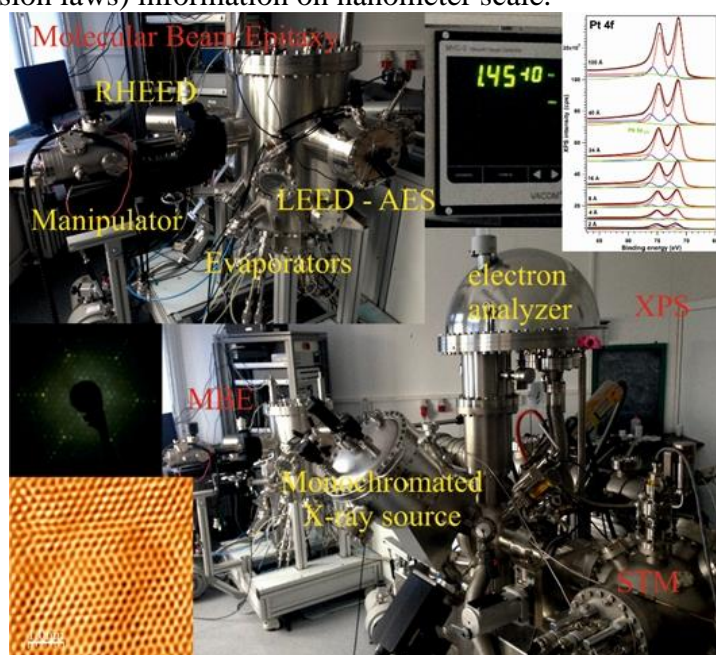


**Fig. 40–1** The first cluster of surfaces and interfaces (the “multi-method system” coupled to MBE), located at NIMP. With red, the principal components are denoted (XPS, STM, MBE). With yellow, the main devices. Other photographs from this panel plot the working pressures, the quality of XPS spectra, LEED and STM images. Produced by Specs, Berlin, Germany.

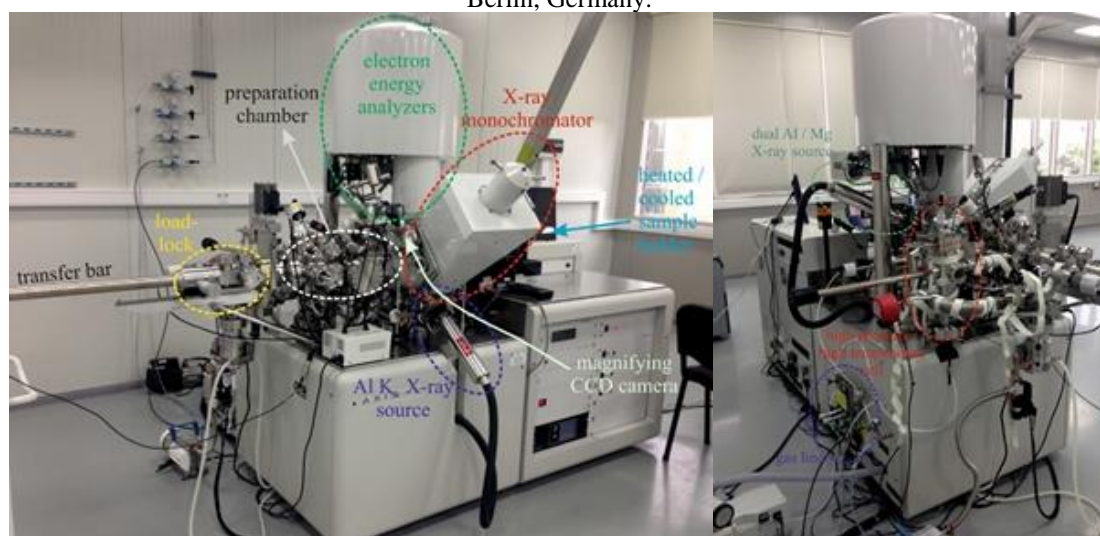


**Fig. 40–2** The installation for photoelectron spectroscopy with possibilities of analysis on micrometer areas and provided with a cell for sample treatment at elevated pressures and temperatures (4 bar / 1000 °C). Produced by Kratos, Manchester, United Kingdom.

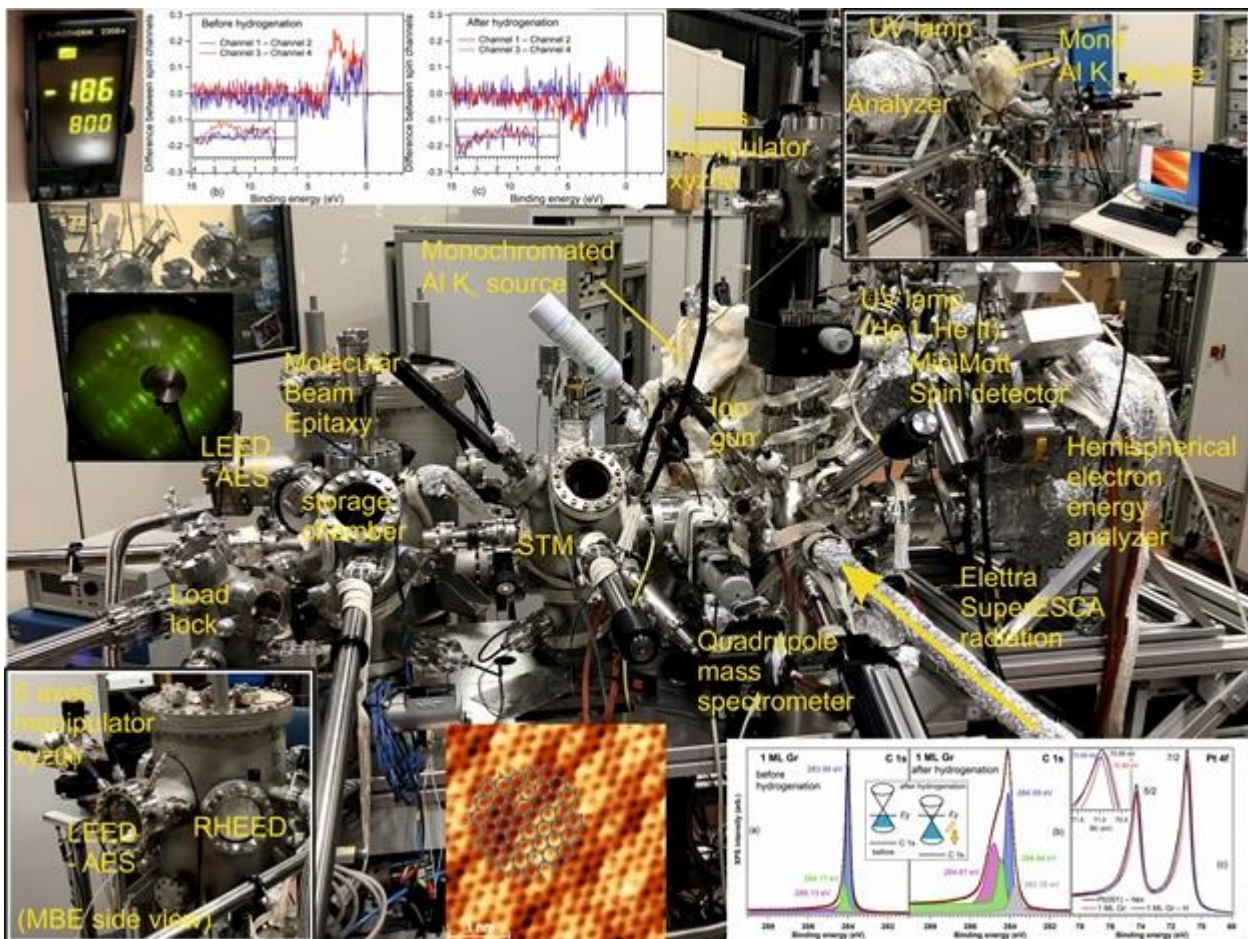


Fig. 40-3 The CoSMoS (combined spectroscopy and microscopy on a synchrotron) cluster coupled to the SuperESCA beamline at Elettra, Trieste. Produced by Specs, Berlin, Germany.

- Setup for extended X-ray absorption fine structure (EXAFS). Excitations: Mo  $K_{\alpha 1}$  (17479.34 eV), W  $L_{\alpha 1}$  (8397.6 eV), power 3 kW (40 kV, 75 mA); Ge(220), Ge(400), Ge(840) monochromators; detectors: proportional counters, scintillation detectors; measurement in transmission or fluorescence; simulation and analysis software. Produced by Rigaku, Tokyo, Japan.
- Magneto-optical Kerr effect microscope with possibilities of in-plane and out-of-plane magnetic fields up to 1 T, resolution 500 nm.

#### Available services:

- Photoelectron spectroscopy-based techniques: X-ray photoelectron spectroscopy (XPS) and diffraction (XPD), ultraviolet photoelectron spectroscopy (UPS), angle-resolved UPS (ARUPS), spin-resolved ARUPS;
- Auger electron spectroscopy (AES) and diffraction (AED);
- Low energy electron diffraction (LEED) and reflection high energy electron diffraction (RHEED) characterization of surfaces;
- Scanning tunneling microscopy (STM) and spectroscopy (STS) at variable temperature;
- Non-contact atomic force microscopy (AFM) with atomic resolution;
- Sample depth-profiling by ion sputtering assisted by XPS or AES;
- Surface cleaning and synthesis of epitaxial thin-films by molecular beam epitaxy (MBE);
- Thermally-programmed desorption of molecules from surfaces by residual gas analysis (RGA);
- Low energy electron microscopy (LEEM) and photoemission electron microscopy (PEEM), micro-LEED and micro-ARUPS;

- Extended X-ray absorption fine structure (EXAFS).

**Main results:**

- 4 research projects (1 × PCE, 1 × TE, 1 × ELI, and 1 × IOSIN);
- 25 articles published in Web of Science®-indexed journals with impact factor;
- 1 OSIM patent application.

**Highlights:**

- Revision of Kittel's theory for ferromagnetic domains, extension for thin films and for applied fields [see *Results in Physics* 46, 106287 (2023)]; extension of the theory for the case of two-dimensional domain structures for films with perpendicular and in-plane magnetic anisotropy [see *Results in Physics* 54, 107109 (2023)];
- Evidence by photoemission electron microscopy (PEEM) and low energy electron microscopy (LEEM) of surface charge dynamics upon exposure of ferroelectric thin films to soft X-ray radiation [see *Nanoscale* 15, 13062–13075 (2023)];
- Control of spectral, topological and charge transport properties of graphene *via* circularly polarized light and magnetic field [see *Results in Physics* 46, 106257 (2023)];
- Floquet topological insulators with spin-orbit coupling [see *Physical Review B* 109, 075121 (2024)].

# LABORATORY 50

## “Theoretical Physics and Computational Modeling”

**Head of laboratory:** Dr. Valeriu MOLDOVEANU, Senior Researcher rank 1 ([valim@infim.ro](mailto:valim@infim.ro))

**Personnel:** 7 members – 1 × SR1, 1 × SR2, 3 × SR3, 1 × SR, 1 × RA, and 1 × PhD student.

### Main research directions:

- Topological and transport properties of 2D materials and lattices;
- Hybrid quantum systems for nano-electronics and nano-optomechanics;
- Correlation effects in 2D lattices and artificial molecules.

### Main results:

- 7 articles published in Web of Science®-indexed journals with impact factor (of which 4 with main author from Lab. 50 and 3 in collaboration).

### Highlights:

- Investigation of the effects of interactions and their impact on the topology of bulk states within a multiparticle quantum walk framework. By comparing mean chiral displacements (MCDs) in both many-body and single-particle systems and analyzing Berry phase calculations, we uncover subtle variations in topological phases, with a particular focus on the SU(N) Su-Schrieffer-Heeger (SSH) model. Our findings offer valuable insights into the behavior of strongly correlated systems, highlighting the significant influence of electron-electron interactions on the emergence and characterization of topological phases. Moreover, this research opens new paths for innovative approaches to investigate and manipulate topology in interacting quantum systems while also contributing to our fundamental understanding of quantum phenomena. [see *Physical Review B* 108, 035126 (2023)];
- Theoretical calculations of the stationary and transient currents through a molecular nanomagnet of localized spin  $S$  coupled to spin-polarized leads and quantized vibrational modes. The role of the vibron-assisted transitions of the molecular spin on both sides of the anisotropy barrier is explained in two anti-parallel configurations of the source and drain probes. Such transitions are associated with vibron-dressed states and triggered under resonant conditions. In the first configuration, and far from a resonance point, a blockade is imposed on both the electronic and molecular spins via their exchange interaction. When sweeping the magnetic field through resonance, the spin-vibron interaction removes this blockade and allows the indirect reading of resonant transitions as the molecular spin climbs the left side of the anisotropy barrier. [see *Physical Review B* 108, 024416 (2023)];
- Theoretical analysis of the creation of logic gates in molecular systems submitted to external perturbations. Using a simple/non-interacting tight-binding model, we showcase several different scenarios that correspond to AND/OR/XOR logical functions for a given set of contacts. This setup is shown to be independent of the strength of the coupling to the leads and magnitude of the perturbation. We illustrate this approach in the case of bipartite and nonbipartite single carbon cycle molecules (fulvene and benzene) and double carbon cycle molecules (naphthalene and biphenyl). [see *Physical Review B* 108, 235307 (2023)].

# LABORATORY 60

## “Optical Processes in Nanostructured Materials”

**Head of Laboratory:** Dr. Mihaela BAIBARAC, Senior Researcher rank 1, Habil. ([barac@infim.ro](mailto:barac@infim.ro))

**Personnel:** 28 members – 6 × SR1, 3 × SR2, 4 × SR3, 5 × SR, 10 × RA, and 1 × technician.

From the 28 members, 18 possess PhD titles in physics. 1 PhD supervisor and 8 PhD students are involved in educational activities.

### Main research directions:

- Optical properties of composite materials based on macromolecular compounds and carbon nanoparticles (graphene, including graphene oxide and reduced graphene oxide, carbon nanotubes, fullerene) and phosphorene, respectively, for applications in the field of eco-nanotechnologies, health and energy storage (supercapacitors, rechargeable batteries);
- Photoluminescence of 2D inorganic materials (including dichalcogenides) and their applications in information technology, sensors and energy storage;
- Optical properties of plasmonic materials, quantum dots and their applications in the fields of eco-nano-technologies and the pharmaceutical field;
- Optical properties of the inorganic micro/nano-particles for applications in the fields of heritage and optoelectronics.

### Relevant infrastructure:

- An UV-VIS-NIR spectrophotometer, Lambda 950 model, from Perkin Elmer;
- A FTIR spectrophotometer, Vertex 80 model, from Bruker;
- A FT-Raman spectrophotometer, MultiRam model, from Bruker (**Fig. 60–1**);
- A Fluorolog FL-3.2.2.1 model with upgrade for the NIR range, from Horiba Jobin Yvon;
- A triple Raman spectrophotometer T64000 model, from Horiba Jobin Yvon, equipped with the lasers for the excitation in visible range;
- A FTIR imaging microscope SPOTLIGHT 400 from Perkin Elmer;
- A thermoluminescence reader Harshaw TLD 3500;
- A system for photoconductivity and I–V characteristics;
- A Scanning Near Field Optical Microscope (Multiview 4000 SNOM/SPM system from Nanonics) coupled with Atomic Force Microscope (AFM);
- A Fluoromax 4P with quantum efficiency and colorimetry options, for luminophores characterization, o system to measure surface/interfacial tension, contact angle and density;
- A Langmuir-Blodgett instruments, KSV 2000 system and KSV 5003 model;
- A potentiostat/galvanostat, Voltalab 80, from Radiometer Analytical;
- A multi-channel potentiostat/galvanostat, Origaflex model, from Origalys;
- An equipment for deposition by vacuum evaporation of organic materials;
- A broadband dielectric spectroscopy system from Novocontrol;
- An infrared spectro-microscope, Carry 600, from Agilent Scientific;
- A surface plasmons resonance (SPR) equipment from Reichert (**Fig. 60–2**);
- A hybrid Magnetron Sputtering – Pulsed Laser Deposition equipment for thin-films (**Fig. 60–3**);
- A physical Vapor Transport equipment for transition metal dichalcogenides (**Fig. 60–4**).

### Available services:

- Development of composite materials based on the conducting and insulating polymers and carbon nanoparticles of the type carbon nanotubes, graphene oxide, reduced graphene oxide, graphene quantum dots, fullerene and carbon nanohorns;

- Development of organic/inorganic hybrid materials based on conducting polymers and inorganic nanoparticles of the type ZnO, ZnS, CdS, TiO<sub>2</sub>;
- Chemical and electrochemical functionalization of 2D materials (reduced graphene oxide, phosphorene, *etc*) with the organic and macromolecular compounds;
- Synthesis of transition metal dichalcogenides (TDMs) of the type MoS<sub>2</sub>, WS<sub>2</sub>, *etc*;
- The preparation of the surface-enhanced Raman scattering (SERS) supports of the type of rough metallic (Ag, Au, Cu) films, the colloidal suspensions of the metallic nanoparticles and the graphene sheets decorated with metallic nanoparticles;
- Deposition of thin layers using magnetron sputtering and Langmuir Blodgett;
- Realization of organic/organic and organic/inorganic structures by vacuum evaporation and from solution;
- Controlled crystallization of thin-films in various atmospheres;
- Functionalization of metallic surfaces for development of optical sensors *via* surface plasmons resonance;
- Analyzes by the UV-VIS-NIR and IR absorption spectroscopy, Raman scattering, surface-enhanced Raman scattering (SERS), surface-enhanced infrared absorption (SEIRA) spectroscopy, photoluminescence, atomic force microscopy and broad-band dielectric spectroscopy;
- Structural characterization and phase identification in crystalline materials;
- Contact angle analysis for assessment of hydrophobic/hydrophile properties;
- Measurements of surface/interface tension and of the density of liquids;
- Colorimetry and quantum yield measurements for the characterization of phosphors;
- Calculated absorption coefficient of inorganic and macromolecular chain with density-functional theory (DFT);
- Electrochemical analysis by cyclic voltammetry, chronoamperometry, chronopotentiometry, electrochemical impedance spectroscopy, Tafel polarizations;
- Surface nano-patterning by UV Nano Imprint lithography (UV-NIL);
- Characterization of organic heterostructures for opto-electronic devices;
- Galvanostatic charge-discharge measurements for the testing nanomaterials as electrode active materials in supercapacitors and rechargeable batteries;
- The preparation of electrodes with the application in the field of the electrochemical sensors;
- Analysis concerning the stability of the drugs in the presence of UV light and various chemical agents by UV-VIS spectroscopy, photoluminescence, Raman scattering and FTIR spectroscopy.

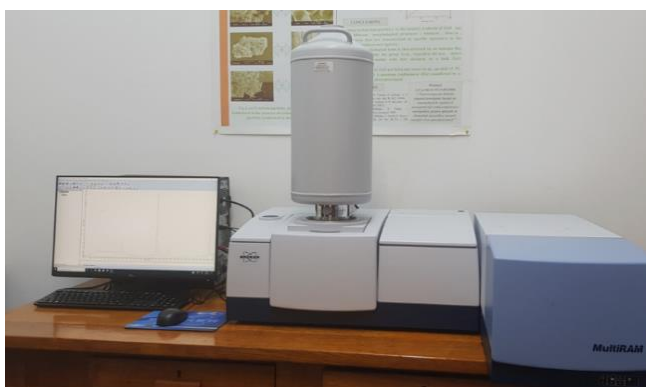


**Fig. 60–1** MultiRam FT-Raman spectrophotometer from Bruker.



**Fig. 60–2** Surface Plasmon Resonance equipment from Reichert.



**Fig. 60–3** Hybrid Magnetron Sputtering – Pulsed Laser Deposition equipment for thin-films.



**Fig. 60–4** Physical Vapor Transport equipment for transition metal dichalcogenides.

### Main results:

- 7 research projects projects (1 × SEE, 1 × M-ERA NET, 1 × POC-G, 1 × POC-TI, 2 × PED, and 1 × PCE); in addition, Lab. 60's team is involved in 2 COST actions.
- 33 articles published in Web of Science®-indexed journals with impact factor (of which 20 with main author from Lab. 60);
- 1 EPO patent application;
- 7 OSIM patent applications.

### Highlights:

- Functionalization of the graphene oxide sheets with organic compounds [see *Journal of Materials Science* 58, 7025 (2023)];
- Metasurfaces for metalens and thermal emitters applications [see *Scientific Reports* 13, 7499 (2023); *Nanomaterials* 13, 426 (2023)];
- Multi-analytical characterization of the white inlaid decoration on the prehistoric pottery from southern Romania [see *Solid State Sciences*, 140, 107193 (2023)].

# LABORATORY 70

## “Atomic Structures and Defects in Advanced Materials”

**Head of laboratory:** Dr. Corneliu GHICA, Senior Researcher rank 1 ([cghica@infim.ro](mailto:cghica@infim.ro))

**Personnel:** 31 members – 4 × SR1, 7 × SR2, 4 × SR3, 2 × SR, 10 × RA, 3 × engineers, and 1 × technician.

### Main research directions:

- Atomic scale structure-functionality correlations in advanced materials (nanostructures, thin-films, ceramics and special alloys);
- Paramagnetic point defects, either intrinsic or induced by impurities or radiations in insulators and wide-bandgap semiconductors;
- Investigation of the physical-chemical mechanisms underpinning the detection process in nanostructured materials for gas sensing applications;
- Dielectric and semiconductor thin-films for microelectronic applications of interest for environment, security, space, biomedicine, food safety;
- Cellular and non-cellular *in vitro* interactions and biomedical applications of inorganic nanomaterials and hybrid nanostructures.

### Main research infrastructure:

- Aberration-corrected analytical transmission electron microscope (HRTEM/HRSTEM) provided with EDS and EELS microanalytical facilities for sub-Ångström resolution imaging and atomic-resolution elemental mapping;
- High-resolution analytical electron microscope for electron tomography, *in situ* and *operando* experiments by specimen heating/cooling/electrical biasing;
- SEM-FIB dual analytical system used for morpho-structural and microanalytical investigations (SEM, EDS, EBSD) as well as for ion beam micro- and nano-processing;
- Continuous wave (cw) X-band (9.8 GHz) EPR spectrometer with variable temperature (VT) accessories in the 80 – 500 K range; cw Q-band (34 GHz) EPR spectrometer with ENDOR (Electron-Nuclear Double Resonance) and VT accessories (5 – 300 K);
- Pulse X-band (9.7 GHz) EPR spectrometer equipped with pulse ENDOR, pulse ELDOR (Electron-Electron Double Resonance) and VT accessories (5 – 300 K);
- Automatic liquid He plant completed with a helium recovery system; computer-controlled gas mixing station and associated electrical measurements chains for materials testing under controlled atmosphere;
- Chemical reactor and autoclave for hydrothermal and co-precipitation chemical synthesis;
- Magnetron sputtering installation for thin-films deposition, with *in situ* characterization/monitoring by Auger electron spectroscopy (AES), low-energy electron diffraction (LEED) and ellipsometry;
- Installation for rapid thermal annealing, oxidation and nitriding; horizontal furnace with 3 temperature zones for thermal treatments and physical vapor deposition (PVD);
- Measurement chains for electrical, ferroelectric and photoelectric characterization, Hall effect and magnetoresistance measurements.



**Fig. 70-1** (a) Bruker EPR spectrometer in X band (9.7 GHz) in pulsed regime with ENDOR accessories; (b) Bruker EPR spectrometer in CW Q-band with ENDOR accessory; (c) Setup for electrical measurements under controlled atmosphere gas mixing station; (d) JEM 2100 high-resolution analytical transmission electron microscope; (e) Tescan Lyra III analytical SEM-FIB dual system; (f) Magnetron sputtering installation for thin-films deposition, provided with in situ AES, LEED and ellipsometry; (g) Installation for rapid thermal processing (RTA, RTO, RTN), horizontal furnace with 3 temperature zones for thermal treatments and PVD; (h) Measurement chains for electrical, ferroelectric and photoelectric characterization, Hall effect and magnetoresistance measurements.

#### Available services:

- SEM morphological characterization of advanced materials;
- TEM characterization of nanostructured materials, thin-films, ceramics, alloys;
- Chemical elemental composition and elemental mapping by SEM-EDS and STEM-EDS;
- Multifrequency EPR characterization of bulk and nanostructured insulating and semiconductor materials: nature, concentration, localization, formation mechanism and stability of the paramagnetic centers in materials; chemical processes, structural or magnetic transitions;
- Controlled simulation of toxic and explosive gas environments (CO, CH<sub>4</sub>, NO<sub>2</sub>, H<sub>2</sub>S, NH<sub>3</sub>, SO<sub>2</sub>) for gas sensors testing and calibration; temperature-voltage calibration for the optimization of power consumption for substrates and gas sensors.
- Growth of thin-films and multilayers by magnetron sputtering;
- Rapid thermal annealing (RTA) and controlled oxidation (RTO) at temperatures within 200 – 1250 °C, heating rates up to 200 °C/s in gas flow (N<sub>2</sub>, O<sub>2</sub>, Ar, H<sub>2</sub>) and thermal treatments using the horizontal furnace with 3 temperature zones up to 1200 °C in vacuum or flow of Ar, N<sub>2</sub>;
- Electrical characterization under dark/illumination conditions, Hall effect measurements and modelling of experimental curves current-voltage (I–V) at varying temperature, in DC and AC, capacity-voltage (C–V), capacity-frequency (C–f), capacity-time (C–t), polarization-voltage (P–V), I–T and R–T; spectral characteristics of the photocurrent (I–λ) in modulated and continuous illumination; Hall measurements: V–I curves as a function of current, magnetic field and temperature.

LASDAM operates as Partner Facility within CERIC-ERIC (<https://www.ceric-eric.eu/>) on behalf of NIMP, the Romanian Representing Entity in the consortium along with research institutes and universities in Austria, Croatia, Czech Republic, Hungary, Italy, Poland, Slovenia.

**Main results:**

- 10 research projects (1 × PED, 3 × PCE, 1 × M-ERA.NET, 4 × TE, and 1 POC);
- 51 articles published in Web of Science®-indexed journals with impact factor (of which 5 with main author from Lab. 70);
- 1 OSIM awarded patent;
- 3 OSIM patent applications.

**Highlights:**

- Exploration of new materials for CO and CO<sub>2</sub> detection: the sensing mechanism in chemosensors based on NiO and Gd-doped SnO<sub>2</sub> as an interplay between ionosorption processes and the nanomorphology of the gas-sensitive material [see *Sensors and Actuators B: Chemical* 390, 134028 (2023); *Materials Chemistry and Physics* 296, 127354 (2023)];
- Nanoscale evidence of strain-induced ferroelectric phases in ZrO<sub>2</sub> thin films by atomic resolution analytical transmission electron microscopy [see *Advanced Science* 10, 2207390 (2023); *Applied Materials Today*, 30, 101708 (2023)];
- Role of extended crystal defects ((1-11) and (011) stacking faults, (1-11) twins, (10-1) nanotwins) in developing a high bending strength in TiB<sub>2</sub>-B<sub>4</sub>C ceramic composite evidenced by transmission electron microscopy observations [see *Scientific Reports*, 13, 6915 (2023)];
- EPR study regarding the atomic-scale insight into the decomposition of nanocrystalline zinc hydroxynitrate toward ZnO using Mn<sup>2+</sup> paramagnetic probes [see *Frontiers in Chemistry* 11, 1154219 (2023)].

## LABORATORY 80

### “Catalytic Materials and Catalysis”

**Head of laboratory:** Dr. Mihaela FLOREA, Senior Researcher rank 1, Habil. ([mihaela.florea@infim.ro](mailto:mihaela.florea@infim.ro))

**Personnel:** 6 members – 3 × SR1, 2 × SR3, and 1 × RA.

The MATCA group possesses expertise in the materials preparation with various properties, tailored to suit the applications for which they are designed.

#### **Main research directions:**

- Development of heterogeneous catalytic and photocatalytic materials (preparation and characterization);
- Catalytic reactions: selective oxidation reactions, hydrogenation reactions, synthesis of polymers from renewable/alternative resources, depolymerization of plastics, reduction of volatile organic compounds;
- Photocatalysis: water splitting, photocatalytic CO<sub>2</sub> transformation and artificial photosynthesis;
- Energy: synthesis of materials used as electrocatalysts in fuel cells.

#### **Relevant infrastructure:**

Lab. 80 has an infrastructure covering various methods of catalytic material preparation and physico-chemical characterization. Among the important infrastructures one can mention:

- Chemistry laboratory (**Fig. 80–1**) equipped with all necessary small equipment's for catalytic materials synthesis (ovens working in air or vacuum, rotavapors, magnetic stirrers, autoclaves for hydrothermal treatments, chemical niche, apparatus for milliQ water production, centrifuge, balances) and catalytic reactors (in house reactors for solid-gas phase and liquid-solid phase reactions);
- Thermo-programmed desorption and reduction equipment (TPD-TPR) – for determining the adsorption capacity and redox properties (**Fig. 80–2**);
- Spectroscopy analysis: UV-Vis and Raman portable (**Fig. 80–2**);
- Thermal analysis – to study the relationship between a sample property and its temperature as the sample is heated or cooled in a controlled manner (**Fig. 80–2**);
- Analysis of the reaction products – gas chromatograph with three detectors (TCD, FID, and BID) gas chromatograph coupled with mass spectrometer (**Fig. 80–2**);
- Adsorption analyzer with high performance capabilities - utilized to quantify the surface area, pore size, and pore volume of powders and particulate materials. The equipment is outfitted with a chemisorption feature that expands the scope of its application to encompass both physical and chemical adsorption. This enables the characterization of catalyst texture and active surface properties in catalyst supports, sensors, and several other materials. By including an automated injection loop, the TCD analytical range can be expanded through the utilization of pulse chemisorption;
- Catalytic flow reactor – is a highly advanced modular laboratory system for determining in real time the selectivity and activity of catalysts for different catalytic applications through different configurations and options.

The group has access to other infrastructures located at NIMP, through collaborative research activities, such as: SEM; TEM; XPS; optical spectroscopies (Raman, UV-Vis-NIR, FTIR); X-ray diffraction; ICP-MS; photoluminescence.

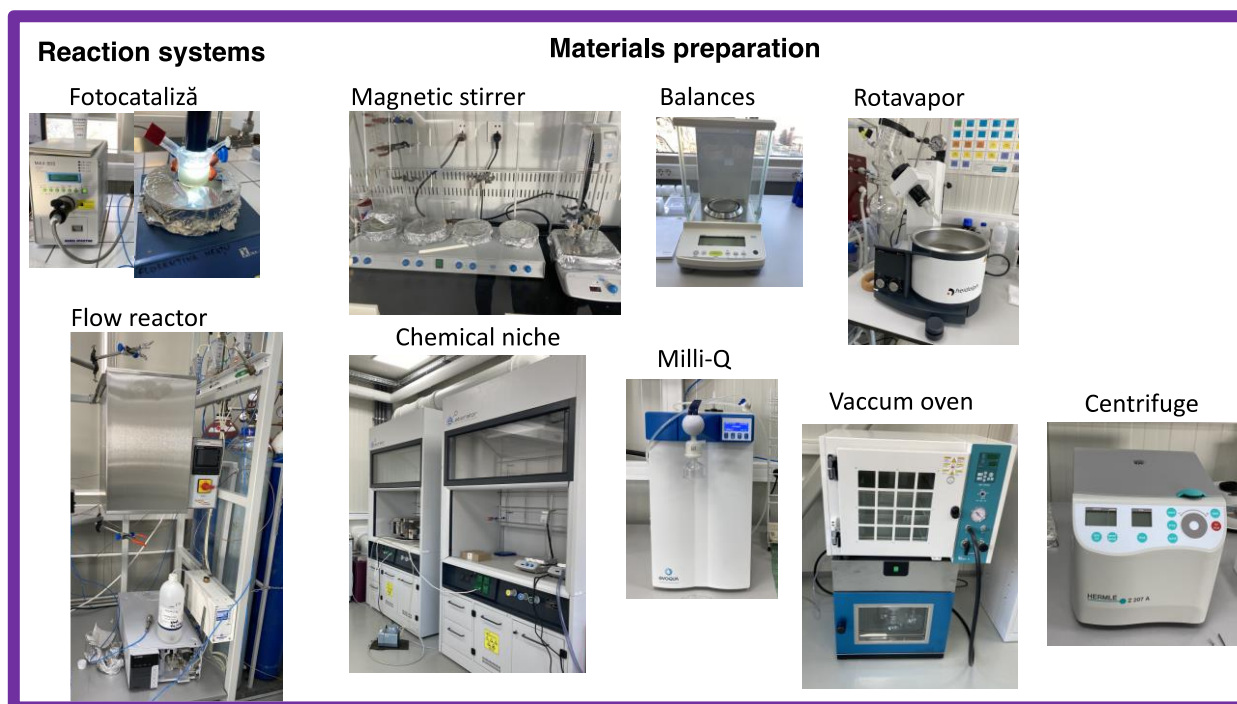


**Fig. 80–1** Chemistry laboratory.

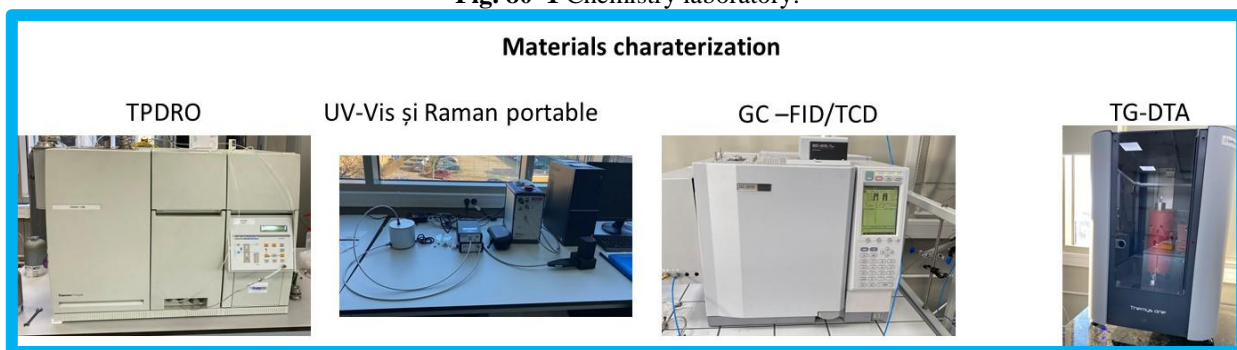


**Fig. 80–2** Equipment for materials characterization and analysis.

#### Available services:

- Catalytic materials preparation;
- Gas-solid and gas-liquid catalytic reaction;
- H<sub>2</sub> production through water splitting;
- Surface characterization;
- Structural and textural characterization of the catalytic materials;
- Investigation of acid-base and redox properties;
- Determination of acid and basic properties (qualitatively and quantitatively).

#### Main results:

- 3 research projects (1 × ERC-like, 1 × PTE, and 1 × PCE);
- 14 articles published in Web of Science®-indexed with high-impact factor (of which 6 with the main author from Lab. 80).

#### Highlights:

- Making 1D filaments of materials containing Ti, C, and O to split water under photocatalytic conditions and create H<sub>2</sub> gas is a straightforward, low-cost, and economically viable strategy thanks to a collaboration with a team of researchers at Drexel University headed by Prof. M. Barsoum (The partnership will continue into 2024 as well);
- The primary objective of the ERC-like project is to use surface-modified MAX-phase with various metal oxides to produce methanol *via* selective oxidation of methane;

- New photocatalytic systems based on *i*-MXene-semiconductor composites for hydrogen production *via* photocatalytic water splitting reaction are the main focus of the PCE-funded project;
- The development of the deposition method for hybrid perovskites to be used as an adsorber layer in solar cell devices. One of the employed methods is the slot die method, which operates under ambient conditions.

# **Materials modeling, preparation and characterization**

# Designing Nanostructured Surfaces based on ZnO-CuO Core-Shell Nanowires Decorated by Silver Nanoparticles with Low Water Adhesion and High Antibacterial Activity

N. Preda<sup>a</sup>, A. Costas<sup>a</sup>, I. Zgura<sup>a</sup>, N. Apostol<sup>a</sup>, A. Kuncser<sup>a</sup>, C. Curutiu<sup>b</sup>, I. Enculescu<sup>a</sup>,

<sup>a</sup>National Institute of Materials Physics, 077125 Magurele, Romania

<sup>b</sup>Microbiology Immunology Department, Faculty of Biology, University of Bucharest, 060101 Bucharest, Romania

Lately, the development of new solutions for micro/nanostructuring metallic surfaces has received increasing attention, specific properties and new functionalities, different from those presented by the raw metal bulk material, being achieved by the fabricated micro/nanostructured surfaces. Thus, in our study [1], nanostructured surfaces based on silver nanoparticles decorated ZnO-CuO core-shell nanowire arrays that can assure protection against various environmental factors such as water and bacteria were obtained by combining thermal oxidation in air, radio frequency (RF) magnetron sputtering and thermal vacuum evaporation.

The FESEM images of the prepared samples (Fig. 1) indicate the following aspects: (i) by thermal oxidation in air of Zn foil, ZnO nanowires featured by diameters down to 30 nm and lengths varying from several micrometers to tens of micrometers are obtained; (ii) by RF magnetron sputtering, on the surface of the ZnO nanowires is deposited a granular nanostructured uniform CuO layer leading to an increase of their diameters from ~30 nm to ~60 nm, the thickness of the CuO shell being estimated at ~15 nm; (iii) by thermal vacuum evaporation, the ZnO-CuO core-shell nanowires are decorated with Ag nanoparticles with irregular shape and sizes of ~40 nm, the thickness of the nanowire segments containing ZnO core - CuO shell - Ag nanoparticles increasing up to ~70 nm. The EDX elemental mapping of a single Ag nanoparticles decorated ZnO-CuO core-shell nanowire proves the formation of the core-shell morphology, the presence of Zn K in the inner part, Cu K in the outer part and Ag on the surface of the core-shell structure.

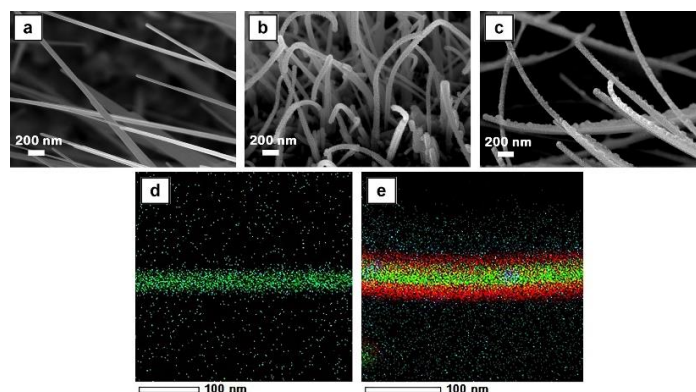


**Fig. 1** FESEM images of (a) ZnO nanowires, (b) ZnO-CuO core-shell nanowires, and (c) Ag nanoparticles-decorated ZnO-CuO core-shell nanowires. EDX elemental mappings in STEM mode including the spatial distribution of the Zn, Cu and Ag elements in (d) ZnO nanowire and (e) Ag nanoparticles-decorated ZnO-CuO core-shell nanowire.

The contact angle and roll-off measurements carried on the obtained samples (Fig. 2) reveal that all samples containing nanowires have contact angle value of ~134° while the contact angle of Zn foil is ~103°. Thus, the nanowire shape of the structures presented on the surface of the zinc foils plays the major role in their hydrophobicity. Further, the adhesion of the water droplets to the surface of the samples show: (i) the water droplet is highly adherent to the surface of the foils containing ZnO nanowires (similar to the water droplet behavior on the surface of Zn foil), resting stick, firmly pinned on the surface even when these were turned upside down; (ii) the water droplets rolled off very easily at slight tilt, the roll-off angle being evaluated at 55° for the foils having the surfaces covered with ZnO-CuO core-shell nanowires or 25° for the foils containing Ag nanoparticles decorated ZnO-CuO

core-shell nanowires. These surfaces with hydrophobic behavior and low water droplet adhesion can be effective for antibacterial uses.

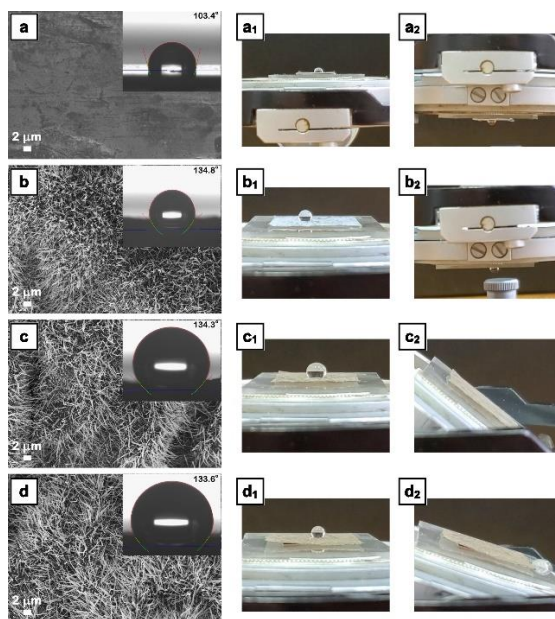


**Fig. 2** (a–d) FESEM images, (insets a–d) optical photographs of the water droplets shape and sequences of snapshots taken from a video camera showing the high or low adhesion of water droplets on the surface of (a, a<sub>1</sub>, a<sub>2</sub>)Zn foil, (b, b<sub>1</sub>, b<sub>2</sub>) ZnO nanowires, (c, c<sub>1</sub>, c<sub>2</sub>) ZnO-CuO core-shell nanowires, and (d, d<sub>1</sub>, d<sub>2</sub>)Ag nanoparticles-decorated ZnO-CuO core-shell nanowires. The contact angle is presented as the mean value.

In the FESEM image of a foil containing nanowires and *E. coli* bacteria on its surface (Fig. 3) can be seen that the nanowire shape plays also the significant role in achieving the excellent antibacterial response, the needle tip of the nanowire structures mechanically damaging the bacteria cells like a thorn that penetrates the membrane.

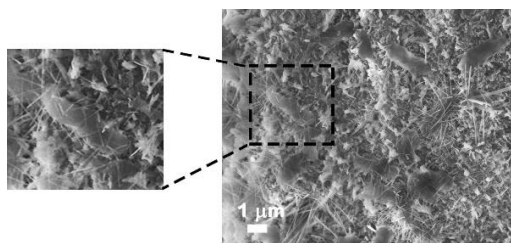


**Fig. 3** FESEM image of *E. coli* bacteria mechanically damaged by the nanowires.

This work emphasized that such functional surfaces can be viable candidates for water repellent surfaces with enhanced antibacterial activity.

#### References

1. A. Costas, N. Preda, I. Zgura, *et al.*, “Silver Nanoparticles Decorated ZnO–CuO Core–Shell Nanowire Arrays with Low Water Adhesion and High Antibacterial Activity”, *Scientific Reports* 13, 10698 (2023).

# Obtaining Photocatalytic Active TiO<sub>2</sub> Mixed Phase Nanoparticles

A. Stepanova<sup>a</sup>, T. Tite<sup>a</sup>, M. Enculescu<sup>a</sup>, C. Radu<sup>a</sup>, A.M. Rostas<sup>b</sup>, A.C. Galca<sup>a</sup>

<sup>a</sup>National Institute of Materials Physics, 077125 Magurele, Romania

<sup>b</sup>National Institute of Isotopic and Molecular Technologies, 400293 Cluj-Napoca, Romania

Titanium dioxide (TiO<sub>2</sub>) is a widely recognized photocatalyst material, known for its non-toxicity, easy activation by ultraviolet light, chemical stability, environmental friendliness, strong oxidizing ability of photogenerated holes, and chemical inertness, making it highly effective in decomposing various inorganic and organic pollutants.

While synthesizing titanium dioxide-based photocatalysts at a hydrothermal temperature of 160 °C and a short hydrothermal time of 6 h, it was observed that adjusting the pH of the solution during nanoparticle preparation by controlling the concentration of HCl significantly influences the composition, thereby impacting the results of the photocatalytic activity [1]. A lower pH value directly influenced the formation of rutile TiO<sub>2</sub>, while an increase in pH led to the formation of anatase and brookite phases. The hydrothermal technique, an affordable method, guarantees both high purity and size uniformity in the synthesis of one-dimensional TiO<sub>2</sub> nanostructures. In contrast to certain synthesis methods such as sol-gel, hydrothermal approaches offer a notable reduction in synthesis time. Despite the numerous studies employing hydrothermal methods, only a limited number have explored the impact of structural properties on the photodegradation process.

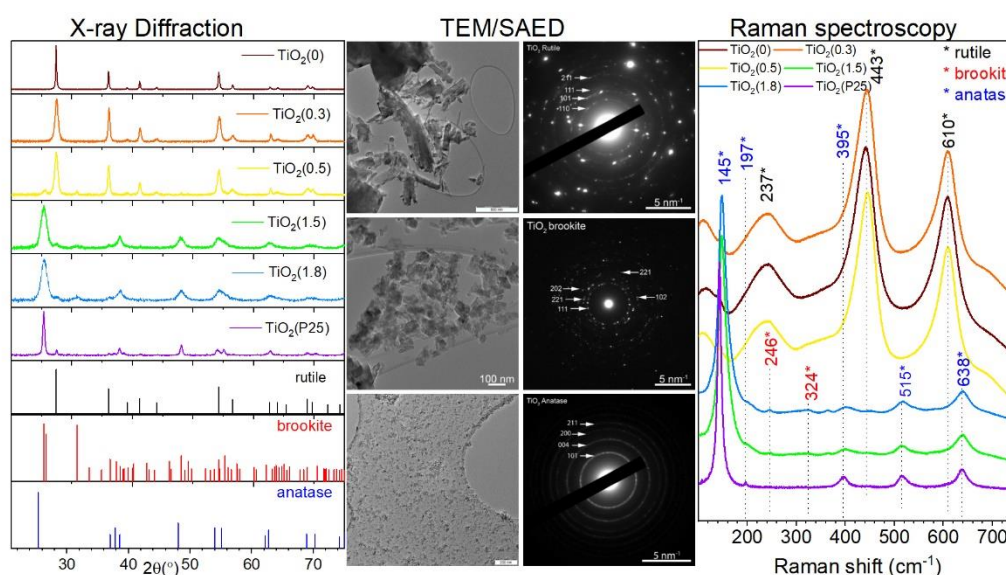


**Fig. 1** XRD patterns, High Resolution Transmission Electron micrographs and the corresponding Selected Area Electron Diffraction, and Raman spectra of TiO<sub>2</sub> nanoparticles obtained in different acidic media.

The X-ray diffraction (Fig. 1–left-hand side) revealed that the TiO<sub>2</sub>(0) and TiO<sub>2</sub>(0.3) samples, produced at the lowest pH of the initial solution, were mainly composed of rutile phase crystallites, as showed by the intense diffraction peaks corresponding to the *110*, *101*, *111*, *210*, *211*, *220*, *002*, *310*, *301*, and *112* reflections (ICDD # 01-086-4329). The average diameters of the rutile crystallites of the TiO<sub>2</sub>(0) and TiO<sub>2</sub>(0.3) samples were of ~64 nm and ~18 nm, respectively. TiO<sub>2</sub>(0.5) was a mixture of rutile/anatase (ICDD # 04-011-0664)/brookite (ICDD # 04-007-0758), with a weight fraction ratio of 76:6:18 and a rutile crystallite size of ~14 nm. The strong diffraction peaks of the TiO<sub>2</sub>(1.5) and TiO<sub>2</sub>(1.8) samples matched the anatase phase (*101*, *004*, *200*, *205*, and *204* reflections), while the presence of rutile and brookite was hinted by the low intensity *110* and *211* reflections, respectively. One should note that most of the brookite diffraction lines are overlapped by those of anatase, and only the *211* reflection at  $2\theta = 30.8^\circ$  is left to emphasize the presence of the brookite phase. TiO<sub>2</sub>(1.5) consisted of rutile/anatase/brookite in a ratio of 14:67:19, while TiO<sub>2</sub>(1.8) had a composition of 12:64:24. The latter two samples primarily featured an anatase phase, with average

crystallite sizes of  $\sim 10$  nm and  $\sim 9$  nm, respectively. The crystalline phases mentioned above have been identified also by TEM-SAED coupled analyses (Fig. 1–middle).

The Raman spectra of the synthesized samples (Fig. 1–right-hand side), further supported the XRD findings. The peaks at  $237$ ,  $443$ , and  $610$   $\text{cm}^{-1}$  correspond to the rutile phase, those at  $145$ ,  $197$ ,  $395$ ,  $515$ , and  $638$   $\text{cm}^{-1}$  are assigned to the anatase phase, while the peaks at  $246$  and  $324$   $\text{cm}^{-1}$  belong to the brookite phase.

X-Band EPR spectra (9.88 GHz) was used to investigate the defect centres present in the  $\text{TiO}_2$  samples (Fig. 2). The weak signal with a  $g$ -value  $g_F = 2.0036$  can be attributed to a so-called F-centre, an electron trapped in an oxygen vacancy, which can be found in the EPR spectra of all samples. Samples (1.5) and (1.8), which have a majority anatase phase, exhibit an intense EPR signal with a large peak-to-peak line width ( $\approx 5.3$  mT), which probably originates from oxygen-related defects (hole centre). The large line width indicates a high concentration of defect centres in the anatase-based  $\text{TiO}_2$  samples, resulting in a strong exchange interaction between the paramagnetic centres.

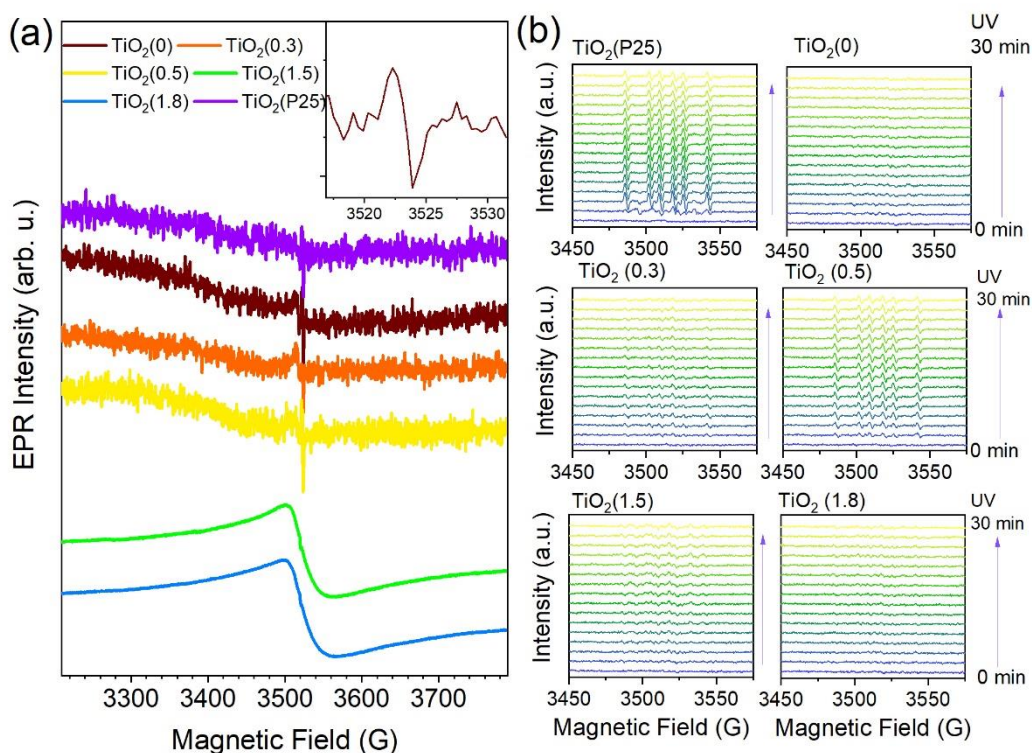


**Fig. 2** (a) EPR spectra of the  $\text{TiO}_2$ -based samples; (b) EPR spectra of the  $\text{TiO}_2$  samples in the presence of the spin trap under UV irradiation in an aqueous solution.

The efficiency of reactive oxygen species (ROS) photogeneration by  $\text{TiO}_2$ -based samples was assessed by EPR using the spin-trapping agent 5,5-dimethyl-1-pyrroline-N-oxide (DMPO). DMPO can trap oxygen radicals produced during the photoexcitation of  $\text{TiO}_2$ , collectively denoted by  $\bullet\text{R}$ , forming more stable adducts  $\text{DMPO} + \bullet\text{R} \rightarrow \bullet\text{DMPO-R}$ . The nature of the trapped radicals can be identified by analysing the hyperfine coupling constants in the experimental EPR spectra (Fig. 2), monitored during the exposure of  $\text{TiO}_2$  in mixed solvent water/DMSO (9:1 v/v). All samples excepting  $\text{TiO}_2(0.3)$  showed ROS generation, while  $\text{TiO}_2(1.5)$  has the highest EPR signal and, therefore, the highest concentration of photogenerated ROS.

To activate the photocatalysts by generating pairs of charge carriers (electron  $e^-$ -hole  $h^+$ ), ultraviolet light with a wavelength below 390 nm can induce electronic transitions in semiconductors. Based on this, the first experiment was performed with exposure to UV light with a 365 nm wavelength. At this wavelength, the dye remained stable and did not degrade independently. The second experiment was conducted under exposure to a sunlight simulator with an extensive spectral range of 250–2000 nm and 1 sun power, reproducing the sun's direct radiation spectrum on the ground at a 48.2 zenith angle.

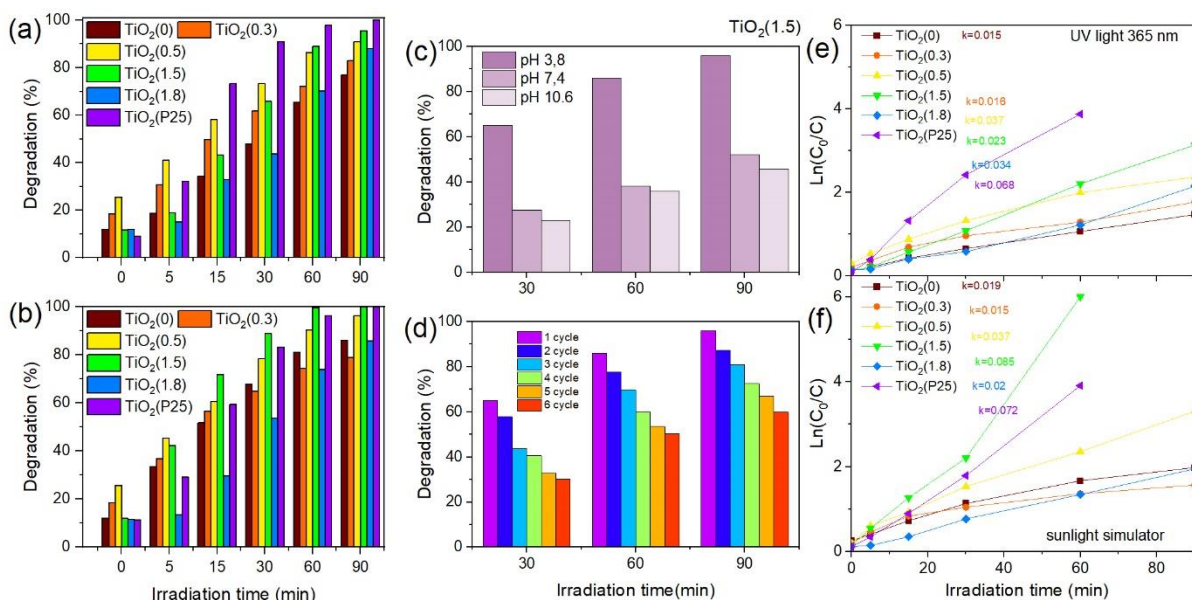


**Fig. 3** (a) Decolorization diagram for rhodamine B degradation with TiO<sub>2</sub> nanoparticles under UV (365 nm); (b) solar irradiation; (c) Effect of pH of the solution on photocatalysis for sample 1.5; (d) Degradation diagram for RhB degradation with a multiple-use of TiO<sub>2</sub>(1.5) photocatalyst without regeneration nanoparticles under UV (365 nm); (e) Kinetic plot for rhodamine B degradation with TiO<sub>2</sub> nanoparticles under UV (365 nm); (f) solar irradiation.

By comparing the degradation activity of the samples under UV light, it was showed that the commercial P25 sample had a rate constant (Fig. 3e) of  $0.07 \text{ min}^{-1}$ , and after 60 min of irradiation, RhB was degraded to 98% (Fig. 3a). However, when the solar simulator was used, the TiO<sub>2</sub>(1.5) sample, with 67% anatase, showed better results. The rate constant of the reaction was  $0.08 \text{ min}^{-1}$  compared to  $0.06 \text{ min}^{-1}$  for P25 (Fig. 3f). Even though the anatase phase is not the main factor affecting the photoactivity, it significantly improved the ability of the photocatalyst to degrade the dye. Nevertheless, the sample with a highest rutile content, TiO<sub>2</sub>(1.5), showed impressive results regardless of the irradiation source. The effect of the pH value on the photocatalysis process was investigated on a model solution of RhB with TiO<sub>2</sub>(1.5). Even though the initial solution of RhB had a pH value of 7.07, adding the TiO<sub>2</sub>(1.5) photocatalyst changed the pH to 3.8. Changing the pH value to 7 and 10 led to a decrease in photocatalytic efficiency (Fig. 3c).

The photostability of the photocatalyst was tested using the best-performing sample under UV irradiation, TiO<sub>2</sub>(1.5), while 6 RhB degradation cycles were performed. The photocatalytic activity of the TiO<sub>2</sub>(1.5) slowly reduced with each cycle without regeneration, but despite this, it remained high enough (Fig. 3d).

#### References

1. A. Stepanova, T. Tite, I. Ivanenko, *et al.*, "TiO<sub>2</sub> Phase Ratio's Contribution to the Photocatalytic Activity", *ACS Omega* 8, 41664–41673 (2023).

# Novel Cr/Fe Mixed Transition-Metal Phosphates: Structural and Electrical Properties

Z. Mighri <sup>a</sup>, K. Souiwa <sup>a</sup>, A.M. Rostas <sup>b,c</sup>, R.E. Patru <sup>c</sup>, A.E. Bocirnea <sup>c</sup>, N. Iacob <sup>c</sup>, V. Kuncser <sup>c</sup>, O. El Khouja <sup>c</sup>, L.N. Leonat <sup>c</sup>, M. Hidouri <sup>a</sup>, H. Nasri <sup>a</sup>, A.C. Galca <sup>c</sup>

<sup>a</sup>University of Monastir, Avenue de l'Environnement, 5019 Monastir, Tunisia

<sup>b</sup>National Institute of Isotopic and Molecular Technologies, 400293 Cluj-Napoca, Romania

<sup>c</sup>National Institute of Materials Physics, 077125 Magurele, Romania

The limitation of natural lithium resources and their high cost makes the Lithium-ion batteries (LIBs) technology infeasible to be embraced in future energy storage systems. Therefore, the developing of other abundant and low-cost alkali-metal-ion batteries, such as potassium-ion batteries (PIBs), is highly demanded. The PIBs have great potential because of the high voltage (4.5 V K<sup>+</sup>/K), and due to a redox potential (−2.93 V) close to the one of lithium (−3.04 V). K<sup>+</sup> ions possess a lower Lewis acidity than other alkali metals, this being an important factor for transfer of the ion in the electrolyte and at the electrode/electrolyte interface. K<sup>+</sup> ions are pivotal for developing and exploring suitable electrode materials considering their environmental safety and atomic and electrochemical properties, which are very similar to those of lithium.

Polyanion-type electrode materials, such as phosphates, are characterized by thermal stability and different structural frameworks in which the K<sup>+</sup> ions are arranged in a 3D structure and separated by large polyanions, effectively reducing the strength of the K<sup>+</sup>–K<sup>+</sup> repulsion. The weaker K<sup>+</sup>–K<sup>+</sup> interaction leads to a higher operating voltage, being one of the key properties of battery-suited materials. New combinations of chromium and iron phosphates might be a candidate, considering that the structure of these compounds consists of very flexible covalent networks. This flexibility is given by the diversity of the association modes of the MO<sub>x</sub> polyhedra (M = metal, alkaline, or P), either directly through vertices, edges, or even common faces, thus forming finite or infinite polymeric groups, or through the intermediary of PO<sub>4</sub> groups, which often generates complex anionic networks of excellent chemical, thermal, and mechanical stability. The new compounds should be in the form of two-dimensional (2D) layers or three-dimensional (3D) structures with hexagonal, rectangular, or triangular cavities or tunnels where the alkaline or alkaline-earth ions are placed.

Mixed transition-metal phosphates with KCoCr<sub>1-x</sub>Fe<sub>x</sub>(PO<sub>4</sub>)<sub>2</sub> (x = 0, 0.25, 0.5, and 0.75) were synthesized, while the microstructure and physical properties were investigated through a wide range of microscopic and spectroscopic methods, indicating that these compounds are promising as positive and/or negative electrode materials for PIBs [1]. All obtained compounds crystallize in the P2<sub>1</sub>/n (No. 14) space group (diffractograms in Fig. 1), the crystallographic data, structure refinement parameters, half-width parameters, and η values extracted from the Rietveld refinement being presented in Table T1 from [1]. K<sup>+</sup> cations occupy a single-type site at the crossing tunnels intersection. Its environment has a wide range of cation–oxygen distances being difficult to distinguish between the binding and nonbinding contacts. The KCoCr<sub>1-x</sub>Fe<sub>x</sub>(PO<sub>4</sub>)<sub>2</sub> structure presents 13 atomic positions that characterize the asymmetric pattern, including one for K, one for M(1) (shared between Cr and Fe), one for Co-symbolized M(2), two for P, and eight for O atoms. A projection of this structure along the [101] direction is represented in Fig. 1.

The EPR signals (Fig. 1) exhibited a single resonance signal at g<sub>eff</sub> ~ 1.98 characteristic of Cr<sup>3+</sup> ions. The EPR spectrum of powder samples containing Cr(III) species should have three lines, while in present study a single broad EPR signal is due to increased dipole–dipole interaction between the Cr<sup>3+</sup> ions and to the inhomogeneities in the internal field<sup>3</sup> due to a random distribution of the Cr<sup>3+</sup> ions. By partially Fe-substituting the Cr centres, the EPR signal of the Cr<sub>0.75</sub>Fe<sub>0.25</sub> increases compared to the one of Cr<sub>1</sub>Fe<sub>0</sub>. The intensity and line width of the EPR signal drop significantly when the Fe content is further increased. The spins of the Cr and Fe ions in KCoCr<sub>1-x</sub>Fe<sub>x</sub>(PO<sub>4</sub>)<sub>2</sub> are coupled by a strong exchange interaction that narrows the EPR signal and its intensity in the paramagnetic phase.

From the temperature dependence measurements performed between 140 and 360 K (selection presented in Fig. 1) no ferromagnetic component can be observed because the EPR line width does not increase, which would be the case for ferromagnetic behaviour.

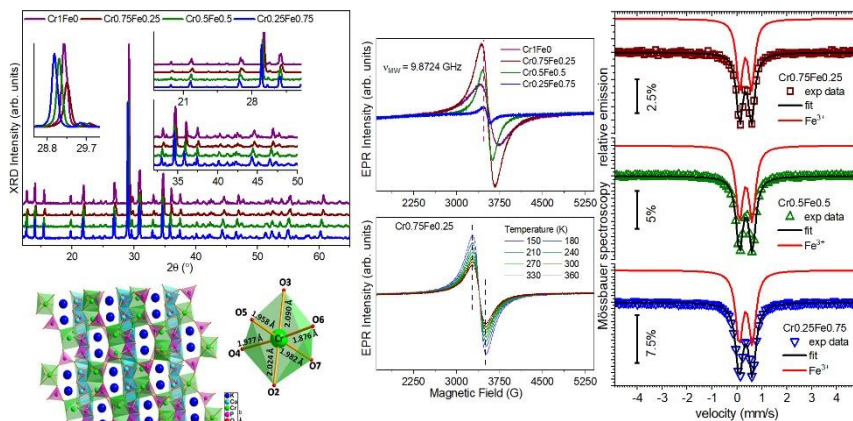


**Fig. 1** XRD patterns of the Cr/Fe phosphate compounds and the projection along the [101] direction. EPR spectra of the mixed Cr/Fe phosphate samples and temperature dependence of the Cr<sub>0.75</sub>Fe<sub>0.25</sub> EPR signal. <sup>57</sup>Fe Mössbauer spectra collected at RT on mixed Cr/Fe phosphates.

The unique Mössbauer spectral component (Fig. 1) is a doublet, specific to paramagnetic Fe(III) ions. The isomer shift values only slightly increased for higher concentration of Fe, from 0.448(2) mm s<sup>-1</sup> in Cr<sub>0.75</sub>Fe<sub>0.25</sub> to 0.454(2) mm s<sup>-1</sup> in Cr<sub>0.25</sub>Fe<sub>0.75</sub>, these values being in close agreement with Fe<sup>3+</sup> ions in the high-spin state ( $S = 5/2$ ) and occupying octahedral positions. On the other hand, the quadrupole splitting (QS) values increase more consistently, from 0.477(2) mm s<sup>-1</sup> in the mixed phosphate Cr<sub>0.75</sub>Fe<sub>0.25</sub> to 0.527(2) mm s<sup>-1</sup> in Cr<sub>0.25</sub>Fe<sub>0.75</sub>, indicating the distortion of the FeO<sub>6</sub> octahedral configurations. Finally, the spectral line widths also increase with x, from 0.303(3) mm s<sup>-1</sup> for Cr<sub>0.75</sub>Fe<sub>0.25</sub> to 0.342(2) mm s<sup>-1</sup> for Cr<sub>0.75</sub>Fe<sub>0.25</sub>, proving an increased disorder around the central Fe ions.

The dielectric permittivity suffered a slight decrease from ~4.3 (Cr<sub>1</sub>Fe<sub>0</sub>) to ~3.8 for Cr<sub>0.75</sub>Fe<sub>0.25</sub>. For higher Fe amounts, it increased to ~5.5 for Cr<sub>0.5</sub>Fe<sub>0.5</sub> and ~6.8 for Cr<sub>0.25</sub>Fe<sub>0.75</sub>, consistent with the increased vacancies and substitutional defects affecting the Cr<sup>3+</sup> structures.

At low temperatures near the cryogenic regime, all of the compounds exhibited almost linear frequency dependence and low losses ( $\epsilon''$  and  $\tan \delta$ ).  $\epsilon'$  measured for the Cr<sub>1</sub>Fe<sub>0</sub> compound remained unchanged when the frequency and temperature were varied. The contrast was given by the mixed Cr/Fe phosphate, for which  $\epsilon'$  and  $\epsilon''$  follow a decreasing trend with increasing frequency (Fig. 2). This behaviour is attributed to the extrinsic contributions (space charges, grains, and grain boundaries) on the dielectric polarization, best described by the Maxwell–Wagner model for the polarization mechanisms. When subjected to an external electric field, charge carriers accumulate at the highly insulating grain boundaries and readily migrate to the highly conductive grains. Such a conducting path created through charge transfer leads to a larger polarization and, consequently, to a higher dielectric permittivity at low frequencies. The highly conductive grains that dominate the high-frequency regions facilitate the charge transfer between cations.

A small direct-current (dc) characterize the conductivity spectra. The frequency-independent plateau is followed by two frequency-dependent regions, best described by the Jonscher power-law variation, the exponents showing the strength of interactions during the hopping process between ions and charge carriers.

The Arrhenius equation relates the temperature dependence of conductivity to the activation energy, *i.e.*, the minimum energy required for the conduction process to occur. A low activation energy means the material has good thermal stability and electrical conductivity over a wide range of temperatures. The activation energy inferred from the ac conductivity decreases when the amount of Fe in the KCoCrFe phosphate system increases because the presence of Fe augments the number of charge carriers available for conduction.

Incorporating Fe ions in the matrix lowers as well the activation energies calculated based on the Arrhenius-type equation of the dc conductivity (Fig. 2). The values of the activation energy, attributed to the long-range movement of free  $K^+$  ions, vary between 490 meV for pure  $Cr_1Fe_0$  and 181 meV for  $Cr_{0.25}Fe_{0.75}$ , suggesting that those phosphates are among the materials with good ionic conductivity. Lower energy barriers are calculated for the mixed Cr/Fe compounds when the Fe content increases. This trend is ascribed to the increased concentration of the Cr vacancies that cause lower resistivity with rapid charge transfer at the interfaces. Hence, the conductivity increases.

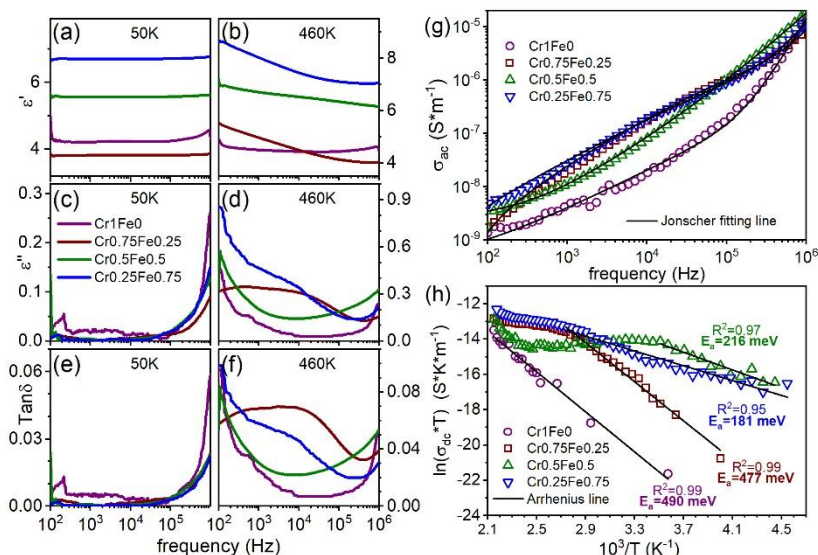


**Fig. 2** Dielectric properties of the mixed Cr/Fe transition-metal phosphates: real part of the dielectric permittivity (a and b), loss factor (c and d), and dissipation factor (e, f) shown for 50 and 460 K, respectively. Frequency dependence of the ac electrical conductivity at a fixed temperature of 450 K together with the Jonscher fit (a) and Arrhenius plot for the dc electrical conductivity (b) of the mixed Cr/Fe phosphate compounds with  $x = 0, 0.25, 0.5$  and  $0.75$ .

The electrical conductivity of all compounds increases with the frequency and temperature without a dependence on the Fe concentration. Incorporation of Fe in the matrix led to a decrease in the activation energy from 490 meV for  $Cr_1Fe_0$  to 181 meV for  $Cr_{0.25}Fe_{0.75}$ , generating a lower resistivity and leading to an increase in the conductivity. These compounds could be suitable for PIBs development.

#### References

1. Z. Mighri, K. Souiwa, A.M. Rostas, *et al.*, “Structural and Electrical Properties of Novel Cr/Fe Mixed Transition-Metal Phosphates”, *Inorganic Chemistry* 62, 8530–8542 (2023).

# Resistive-like Behaviour in Ferroelectric p-n Homojunction based on Epitaxial $\text{Pb}(\text{Zr}_{0.2}\text{Ti}_{0.8})\text{O}_3$ Thin Films

A.G. Boni, C. Chirila, L. Trupina, C. Radu, L.D. Filip, V. Moldoveanu, I. Pintilie, L. Pintilie

National Institute of Materials Physics, 077125 Magurele, Romania

Ferroelectric materials like lead zirconate titanate (PZT) with a perovskite structure have diverse applications due to properties such as controllable polarization. PZT, studied extensively for its high polarization and quality films *via* pulse laser deposition (PLD), has conductivity challenges. Traditional assumptions of p-type conduction face debates as recent studies suggest a probable n-type conductivity in PZT films. However, clear p- and n-type conduction remains elusive, hindering the creation of true p-n homojunctions.

The lack of a pure PZT reference complicates the understanding of dopant effects. Current PLD targets often contain impurities, affecting carrier concentrations. To address this, researchers propose preparing higher purity films and introducing controlled dopants like Fe and Nb. Recent studies showed promising results, indicating Schottky contact behaviour in both Fe and Nb doping, with Nb doping exhibiting lower leakage current. This success opens possibilities for creating epitaxial p-n junctions through successive deposition of Nb and Fe-doped PZT layers.

This study successfully created and analysed p-n and n-p homojunctions using Nb- and Fe-doped layers. Symmetric and asymmetric structures were explored, showing good epitaxial qualities. Despite challenges in determining individual layer thicknesses, all structures exhibited ferroelectric behaviour with varying properties. Notably, the current-voltage characteristics were quasi-linear across a wide temperature range. Resistance extracted from the characteristics demonstrated an exponential dependence on temperature. The findings suggest that, under specific conditions, the homojunction's total current is a combination of linear and exponential terms related to voltage and temperature, respectively.

Hysteresis measurements revealed distinct hysteresis loops for both bi-layers, PZT-Nb/PZT-Fe and PZT-Fe/PZT-Nb, with noticeable differences in loop shapes, magnitudes, remnant polarizations, and coercive voltages (Fig. 1a). Notably, when the first deposited layer is PZT-Fe, higher polarization and coercive voltage values are observed compared to the case where PZT-Nb is the first layer. This discrepancy is attributed to varying electrostatic conditions at the interface with the bottom SRO electrode. Specifically, the estimated potential barrier for the PZT-Nb/SRO interface is larger ( $\approx 0.3$  eV) than for the PZT-Fe/SRO case ( $\approx 0.1$  eV). This difference influences the compensation of the depolarization field during both the growth process and polarization switching. A larger potential barrier impedes the flow of charges involved in compensating the depolarization field, resulting in a lower polarization value.

Surprisingly, the obtained I–V characteristics, as depicted in Fig. 1b), exhibited an unexpected symmetric linear shape, despite the different potential barriers at the interfaces with the bottom and top SRO electrodes. The anticipated asymmetry and non-linear shapes, typical for structures with Schottky-like contacts at electrode interfaces, were contradicted by the observed linear I-V characteristics in the bi-layer structures. This unexpected behaviour is attributed to the coexistence of two types of carriers (electrons and holes) in the p-n homojunction, as well as the intricate charge compensation processes near the contacts and at the PZT-Nb/PZT-Fe interface.

The slope of the linear I–V characteristic represents electrical conductance or the reciprocal of resistance. Extracting resistance values from I–V measurements at different temperatures (Fig. 2) revealed a remarkable approximately four orders of magnitude decrease at 300 K, indicative of semiconductor behaviour. Arrhenius plots were employed to derive an activation energy for conduction in the two bi-layer structures [1], resulting in values within the range of 0.13 – 0.17 eV. These values fall between the estimated potential barriers at the SRO electrodes: approximately 0.1 eV at the PZT-Fe/SRO interface and 0.3 eV at the PZT-Nb/SRO interface for single-phase capacitor

structures. Additionally, the PZT-Fe/PZT-Nb/SRO/STO structure exhibited lower resistance than the PZT-Nb/PZT-Fe/SRO/STO structure.

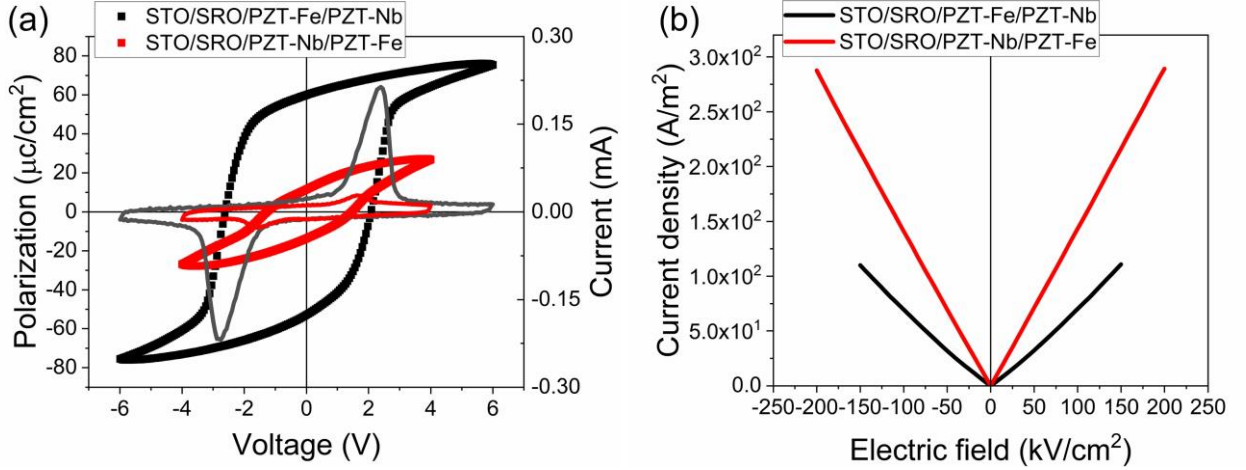


**Fig. 1** (a) Polarization and current hysteresis loops recorded for the bi-layers structures, recorded at RT. A triangular voltage signal with 1 kHz frequency was used for the hysteresis measurement. (b) I–V characteristics for the bi-layer structures. Reprinted with permission from Ref. [1]. ©Copyright 2023 American Chemical Society.

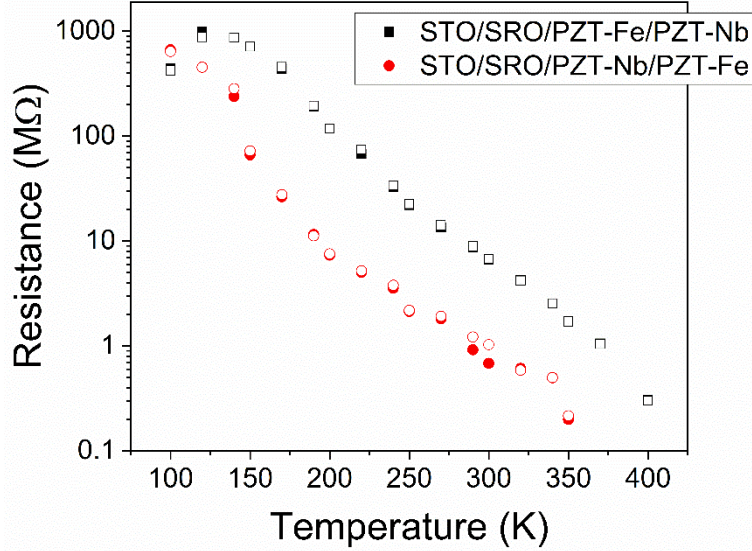


**Fig. 2** The temperature dependence of the resistance of the two bi-layer structures. Reprinted with permission from Ref. [1]. ©Copyright 2023 American Chemical Society.

To elucidate the temperature and voltage dependencies observed in the p-n structures, one must consider the ambipolar nature of transport and refer to the expression of the current density flowing through an epitaxial PZT layer with Schottky contacts. For instance, the electron current density ( $J_e$ ) is described by the following equation:

$$J_e = 2q \left( \frac{2\pi m_e^* k_B T}{h^2} \right)^{\frac{3}{2}} \mu_e E \exp \left\{ -\frac{q}{k_B T} \left[ \left( \Phi_B^0 - \sqrt{\frac{qP}{4\pi\epsilon_0^2\epsilon_{op}\epsilon_{st}}} \right) - \sqrt{\frac{q^2 N_{eff} V}{8\pi\epsilon_0\epsilon_{op}P}} \right] \right\}. \quad (1)$$

Where:  $m_e^*$  is the electron effective mass,  $k_B$  is the Boltzmann constant,  $T$  is the temperature,  $h$  is the Planck constant,  $\mu_e$  is the electron mobility,  $E$  is the applied electric field,  $q$  is the electron charge,  $\Phi_B^0$  is the potential barrier at 0 V,  $P$  is the ferroelectric polarization,  $\epsilon_0$  is the vacuum permittivity,  $\epsilon_{op}$  is the optical dielectric constant,  $\epsilon_{st}$  is the static dielectric constant.  $N_{eff}$  is the effective density of fixed charge in the depleted region,  $V$  is the applied voltage.

A similar formula holds for the hole density current  $J_h$ , with appropriate notations for the hole effective mass, hole mobility and effective density of fixed charge in the depleted region. Then the total current density  $J_{tot} = J_e + J_h$ . (2)

For a wide range of doping concentrations  $\frac{q}{k_B T} \sqrt{\frac{q^2 N_{eff} E d}{8 \pi \epsilon_0 \epsilon_{op} P}} \ll 1$  (this condition holds for concentrations up to  $10^{20} \text{ cm}^{-3}$ ). Then by expanding the corresponding exponential terms in  $J_e$  and  $J_h$  up to the first order term we identify linear (L) and non-linear (NL) contributions to the electron/hole density currents. For instance, the electron current density acquires the form:

$$J_e \approx \underbrace{2 q \left( \frac{2 \pi m_e^* k_B T}{h^2} \right)^{\frac{3}{2}} \mu_e E \exp \left\{ -\frac{q}{k_B T} \left[ \left( \Phi_B^0 - \sqrt{\frac{q P}{4 \pi \epsilon_0^2 \epsilon_{op} \epsilon_{st}}} \right) \right]}_{J_{e,L}} + \underbrace{2 q \left( \frac{2 \pi m_e^* k_B T}{h^2} \right)^{\frac{3}{2}} \mu_e E \sqrt{\frac{q^2 N_{eff} E d}{8 \pi \epsilon_0 \epsilon_{op} P}} \exp \left\{ -\frac{q}{k_B T} \left[ \left( \Phi_B^0 - \sqrt{\frac{q P}{4 \pi \epsilon_0^2 \epsilon_{op} \epsilon_{st}}} \right) \right]}_{J_{e,NL}}, \quad (3)$$

This equation shows that the main contribution to the two density currents has a linear dependence on the field, whereas the non-linear corrections depend on the doping concentrations. The temperature dependence is controlled by the exponential term in Eq. (3).

p-n and n-p PZT homojunctions were grown using pulsed laser deposition on single crystal STO substrates with top and bottom SRO contacts. The ferroelectric properties were found to be influenced by the order in which the n-type (Nb-doped PZT) and p-type (Fe-doped PZT) layers were deposited. Surprisingly, the I–V characteristic deviated from the rectifying behaviour seen in semiconductor p–n junctions, exhibiting linearity. This behaviour was explained by the unique nature of the p–n ferroelectric homojunction, where ionized acceptors and donors are spatially separated in the doped layers, while free carriers move freely to compensate polarization charges near the electrode interfaces. The resulting non-uniform distribution of space charges and Schottky contacts led to this distinct behaviour. A model was developed to explain the I–V characteristics and temperature dependence, based on the assumption that the total current is a combination of electron and hole currents. The study demonstrated that by optimizing the balance between n-type and p-type doping and adjusting layer thicknesses, rectifying behaviour could be achieved in ferroelectric p–n homojunctions.

#### References

1. G.A. Boni, C. Chirila, L. Trupina, *et al.*, “Resistive-like Behaviour in Ferroelectric p–n Homojunction based on Epitaxial  $\text{Pb}(\text{Zr}_{0.2}\text{Ti}_{0.8})\text{O}_3$  Thin Films”, *ACS Applied Electronic Materials* 5, 957–967 (2023).

# Grain Size-driven Effect on the Functional Properties in Ba<sub>0.6</sub>Sr<sub>0.4</sub>TiO<sub>3</sub> Ceramics Consolidated by Spark Plasma Sintering

R.E. Pătru <sup>a</sup>, C.A. Stanciu <sup>b,c</sup>, E.M. Soare <sup>b</sup>, V.A. Surdu <sup>b</sup>, R.D. Trușcă <sup>b</sup>, A.I. Nicoară <sup>b</sup>, B.Ș.Vasile <sup>b</sup>, A.G. Boni <sup>a</sup>, L. Amarande <sup>a</sup>, N. Horchidan <sup>d</sup>, L.P. Curecheriu <sup>d</sup>, L. Mitoseriu <sup>d</sup>, L. Pintilie <sup>a</sup>, I. Pintilie <sup>a</sup>, A.C. Ianculescu <sup>b</sup>

<sup>a</sup>National Institute for Materials Physics, 077125 Magurele, Romania

<sup>b</sup>Department Oxide Materials Science & Engineering, Faculty of Applied Chemistry & Materials Science, Politehnica University of Bucharest, 011061 Bucharest, Romania

<sup>c</sup>National Institute for Lasers, Plasma and Radiation Physics, 077125 Magurele, Romania

<sup>d</sup>Dielectrics, Ferroelectrics & Multiferroics Group, Faculty of Physics, “Alexandru Ioan Cuza” University of Iasi, 700506 Iasi, Romania

Ferroelectric materials are increasingly important for miniaturized electronic and photovoltaic devices due to their high permittivity and tenability [1]. Adjusting the Ba/Sr ratio in barium strontium titanate (BST) solid solutions can control properties like permittivity and Curie temperature, making them ideal for high-frequency applications [2]. However, challenges arise in reducing permittivity for specific applications, often leading to decreased tunability. While the effects of down-scaling on BaTiO<sub>3</sub> ceramics are well-understood [3], BST ceramics, especially with higher solute content, need more investigation. Smaller grain sizes in ferroelectrics impact the material's properties, as the increased surface and interface atoms affect overall ferroelectricity. Various methods like doping and creating composites have been explored to reduce BST's dielectric permittivity while addressing the challenges of grain growth in porous materials. In addition, conventional sintering does not control grain growth well, so innovative wet-chemical preparation and non-conventional sintering techniques are used for fine-grained ceramics. This study explored the role of microstructural features like grain size (GS) and morphology on the electrical properties of fine-grained Ba<sub>0.6</sub>Sr<sub>0.4</sub>TiO<sub>3</sub> ceramics, prepared by sol-gel and consolidated by Spark Plasma Sintering (SPS) (Fig. 1) [4].

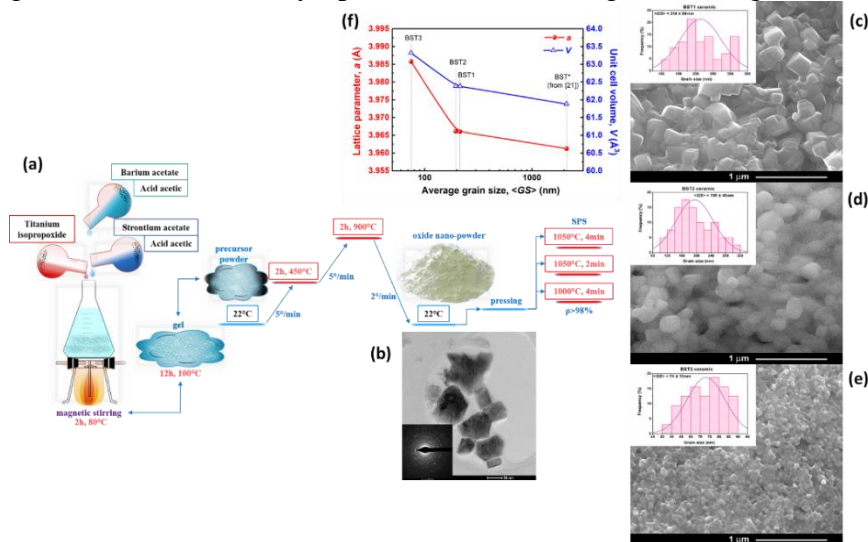


**Fig. 1** (a) Schematic representation of the preparation of sol-gel Ba<sub>0.6</sub>Sr<sub>0.4</sub>TiO<sub>3</sub> powders; (b) TEM image of the powder, related ceramics consolidated by SPS at 1050 °C/4 min (BST1), 1050 °C/2 min (BST2), and 1000 °C 4 min (BST3); (c–e) corresponding FE-SEM images with (f) the structural parameters (lattice parameter and unit cell volume) vs. average grain size.

Three types of dense (98%, 99%), single-phased with cubic structure, fine-grained Ba<sub>0.6</sub>Sr<sub>0.4</sub>TiO<sub>3</sub> (BST) ceramics were created using spark plasma sintering (SPS) under varying conditions: BST1 at 1050 °C/4 min, BST2 at 1050 °C/2 min, and BST3 at 1000 °C/4 min. All were sintered at a pressure of 35 MPa and a heating rate of 100 °C/min. Post-sintering re-oxidation treatment at 800 °C for 30 h was applied to each ceramic to reduce oxygen vacancies and carbon contamination. The powder consisted of polyhedral nanoparticles with an average size of around 68.55 nm as observed by SEM,

and slightly larger by TEM. Most particles were found to be polycrystalline, consisting of 2 – 3 crystallites. SEM investigations showed that BST1 (214 nm) and BST2 (195 nm) had grains in the submicron range, whereas BST3 (74 nm) had nanosized grains. Notably, the microstructure of BST1 exhibited larger, more faceted grains compared to the more rounded grains of BST2. BST3 showed a dense, homogeneous microstructure with nanocrystalline grains.

The GS variations influence the dielectric and ferroelectric properties across a broad frequency and temperature range (Figs. 2 & 3). A common trait among all synthesized ceramics is the diffuse nature of the ferroelectric-to-paraelectric phase transition, with a settled Curie point around 280 K. They exhibit low maximum dielectric permittivity, dielectric nonlinearity (tunability), and P(E) switching character with low-area tilted hysteresis loops and small remnant polarization. The maximum permittivity in fine-grained ceramics is significantly lower and decreases further as GS is reduced. High field measurements show changes in field-dependent permittivity and a decrease in electrical tunability with smaller GS. The GS decrease from submicron- toward nano-scale in BST ceramics does not determine a shift in the specific Raman peaks, but causes an obvious flattening of the overall Raman spectra in BST2 and, especially, in BST3. The hysteretic character decreases with smaller GS and higher temperatures. Energy storage densities are comparable or higher than previously reported BST ceramics [5,6], but energy loss at high fields is also significant.

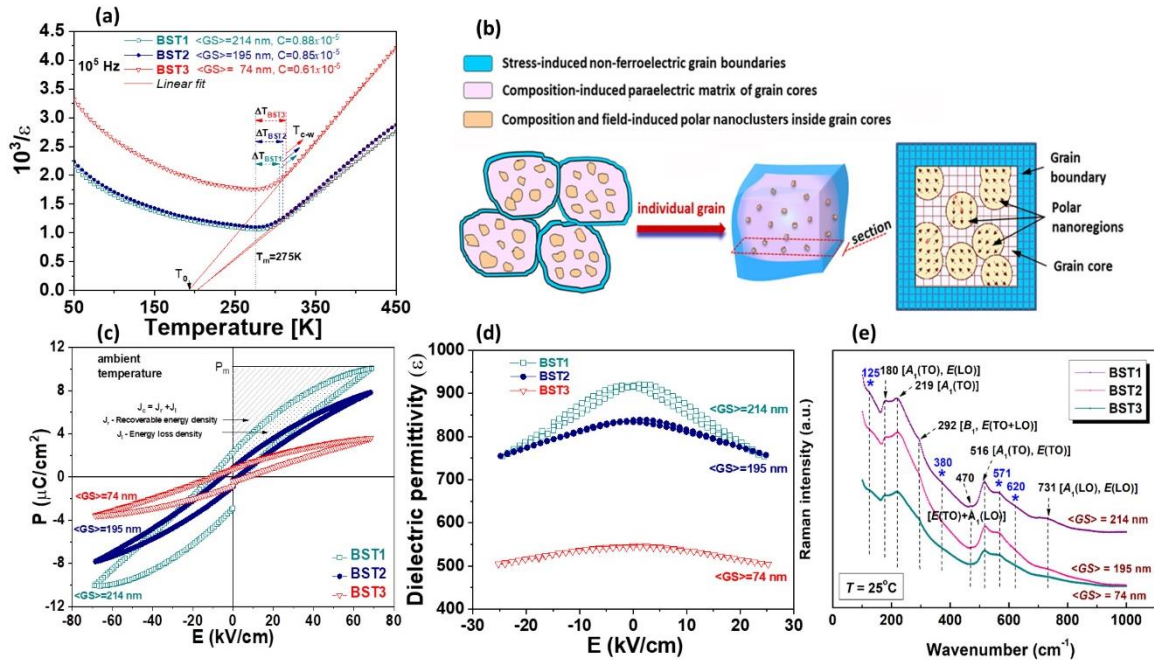


**Fig. 2** (a) Analysis performed according to the classical Curie-Weiss law; (b) schematic representation of the grain structure; (c) room-temperature P(E) loops measured under a triangular waveform with frequency of 1/3 Hz; (d) dielectric permittivity at the fixed frequency of  $10^4$  Hz and under electric fields of up to 25 kV/cm; and (e) Raman spectra at room-temperature for the fine-grained SP-sintered  $\text{Ba}_{0.6}\text{Sr}_{0.4}\text{TiO}_3$  ceramics.

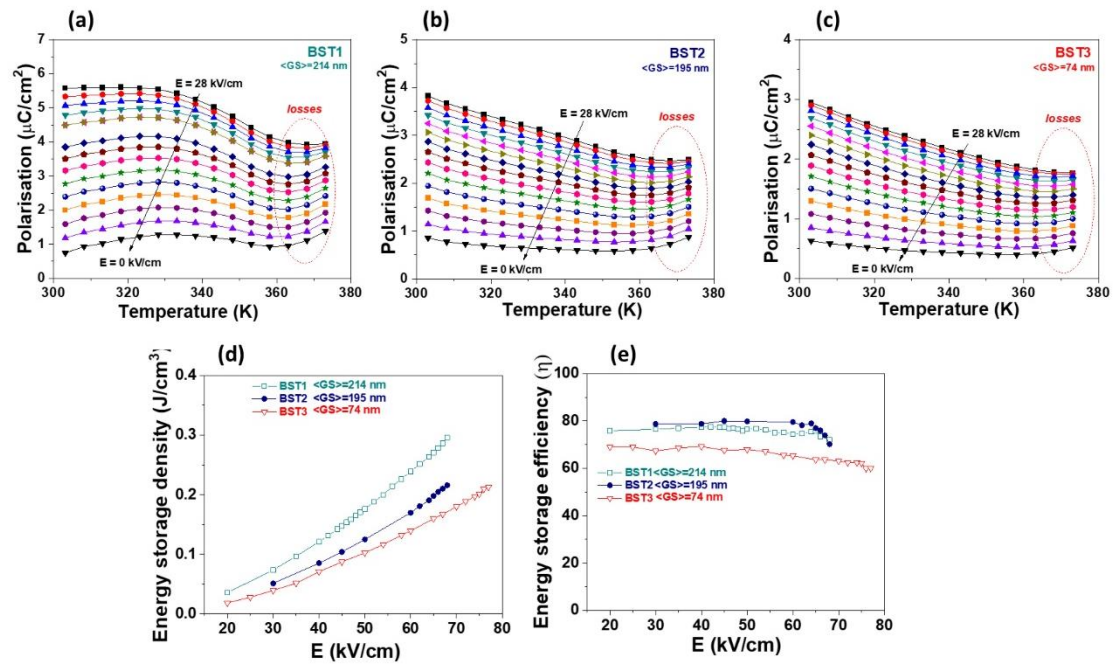


**Fig. 3** (a–c) Polarisation vs. temperature  $P(T)$  determined at various field amplitudes for the fine-grained structured ceramics: (a) BST1, (b) BST2, and (c) BST3; (d) energy storage density; and (e) energy storage efficiency at ambient temperature for the fine-grained  $\text{Ba}_{0.6}\text{Sr}_{0.4}\text{TiO}_3$  structured ceramics.

Key advantages of nanostructuring in dense BST ceramics include reduced permittivity while maintaining tunability, linear permittivity–field dependence, increased electrostatic energy storage capability, and thermally stable polar nanoclusters [7] above the Curie temperature. These findings suggest that nanostructured dense electroceramics have potential in microwave and tuneable devices, highlighting the benefits of controlling grain size at the nanoscale.

#### References

1. J.F. Scott, *Ferroelectric Memories*, Springer Series in Advanced Microelectronics, Springer Berlin, Heidelberg, Germany, 2000.
2. V. Buscaglia, M.T. Buscaglia, G. Canu, “ $\text{BaTiO}_3$ -based Ceramics: Fundamentals, Properties and Applications”, *Encyclopaedia of materials: Technical Ceramics and Glasses* 3, 311–344 (2021).
3. L. Mitoseriu, L.P. Curecheriu, Nanostructured barium titanate ceramics: Intrinsic versus extrinsic size effects, in: M. Alguero, J.M. Gregg, L. Mitoseriu (Eds.), *Nanoscale Ferroelectr. Multiferroics*, Ch. 15, John Wiley & Sons, Ltd, Chichester, UK, pp. 473–511, 2016.
4. R.E. Patru, C.A. Stanciu, E.M. Soare, *et al.*, “Grain Size-Driven Effect on the Functional Properties in  $\text{Ba}_{0.6}\text{Sr}_{0.4}\text{TiO}_3$  Ceramics Consolidated by Spark Plasma Sintering”, *Journal of the European Ceramic Society* 43, 3250–3265 (2023).
5. Q. Zhang, L. Wang, J. Luo, *et al.*, “Improved Energy Storage Density in Barium Strontium Titanate by Addition of  $\text{BaO-SiO}_2\text{-B}_2\text{O}_3$  Glass”, *Journal of the American Ceramic Society* 92, 1871–1873 (2009).
6. Y.H. Huang, Y.J. Wu, J. Li, *et al.*, “Enhanced Energy Storage Properties of Barium Strontium Titanate Ceramics Prepared by Sol-Gel Method and Spark Plasma Sintering”, *Journal of Alloys and Compounds* 701, 439–446 (2017).
7. H. Xue, Z. Xiong, H. Zhou, “The Structure and Dielectric Tunable Properties of Fine-Grained  $\text{Ba}_{0.6}\text{Sr}_{0.4}\text{TiO}_3$  Ceramics Prepared by Spark Plasma Sintering”, *Journal of the American Ceramic Society* 90, 2653–2656 (2007).

# Sequential Deposition and Annealing Process for the Synthesis of High-quality $\text{Cu}_2\text{ZnSnSe}_4$ Absorber Layers

M.Y. Zaki <sup>a</sup>, F. Sava <sup>a</sup>, I.D. Simandan <sup>a</sup>, A.T. Buruiană <sup>a,b</sup>, A.E. Bocîrnea <sup>a</sup>, I. Stavarache <sup>a</sup>, A. Velea <sup>a</sup>, A.C. Gâlcă <sup>a</sup>, L. Pintilie <sup>a</sup>

<sup>a</sup>National Institute of Materials Physics, 077125 Magurele, Romania

<sup>b</sup>Faculty of Physics, University of Bucharest, 077125 Magurele, Romania

As global energy demands rise and the need for sustainable alternatives to fossil fuels grows, attention turns to renewable sources like solar power. Traditional silicon-based photovoltaic cells dominate the market, but there is an increasing interest in thin-film alternatives like CZTSe ( $\text{Cu}_2\text{ZnSnSe}_4$ ). CZTSe offers advantages such as a tuneable band gap and an earth-abundant composition [1]. This study uniquely employs a two-step sputtering and annealing process. Initially, four different stacks are deposited, followed by an annealing step to form non-stoichiometric  $\text{Cu}_2\text{SnSe}_3$  (CTSe) films. Subsequently, a ZnSe layer is sputtered onto the films, and a second annealing process in Sn+Se atmosphere is conducted (Fig. 1a–b). This final step transforms the films into stoichiometric and single-phase CZTSe thin films. By meticulously optimizing the deposition and annealing parameters, this process offers a systematic and reproducible method for achieving high-quality CZTSe thin films, showcasing potential advancements in solar cell applications.

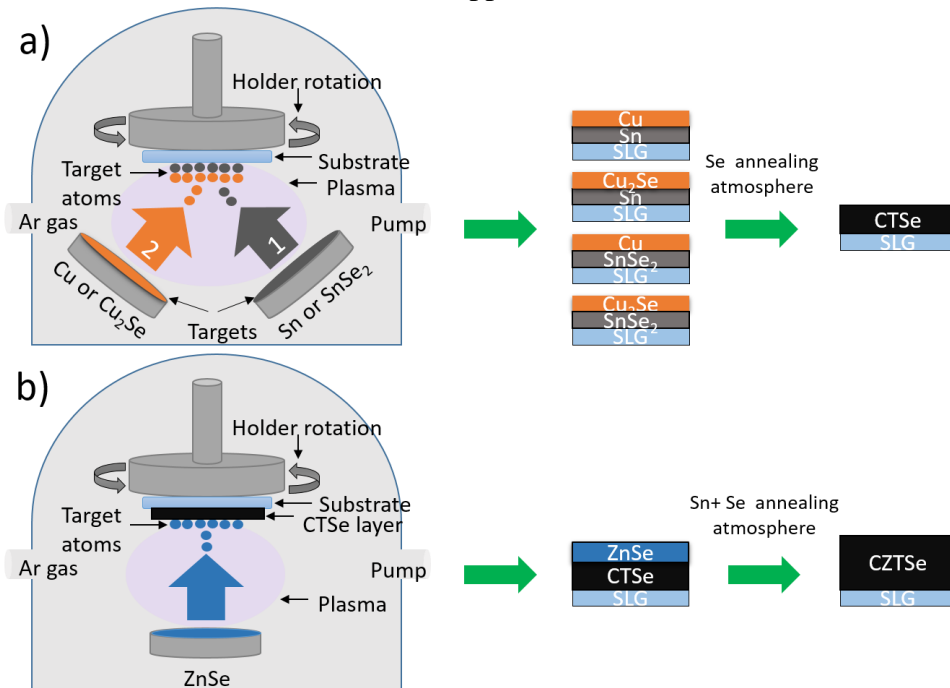


**Fig. 1** Magnetron sputtering deposition and annealing procedure for (a) the CTSe layer and (b) the final CZTSe films.

The GIXRD patterns of Cu-Sn-Se films, obtained by annealing of various stacks in a selenium atmosphere at 550 °C for 15 min, are depicted in Fig. 2. GIXRD fails to differentiate between monoclinic  $\text{Cu}_2\text{SnSe}_3$  and cubic  $\text{Cu}_{2-x}\text{Se}$  phases [2]. Additionally, the final thickness of selenized stacks with Cu as the top film is doubled compared to those with  $\text{Cu}_2\text{Se}$  capped layer, indicating the superiority of the former stacking configuration. Raman spectroscopy aids in differentiating between  $\text{Cu}_{2-x}\text{Se}$  and Cu-Sn-Se phases, revealing intense peaks at 260  $\text{cm}^{-1}$  corresponding to the Se-Se vibration in the  $\text{Cu}_2\text{Se}$  phase. Weak peaks at 190  $\text{cm}^{-1}$  suggest the presence of  $\text{Cu}_2\text{SnSe}_3$ . SEM images of the stacked CTSe samples display rough surfaces, with the SLG\Sn\Cu<sub>2</sub>Se stack exhibiting hexagonal flat grains. Evaporation of Sn and Se during annealing leads to void formation, contributing to the surface roughness. EDS analysis reveals off-stoichiometric compositions rich in copper and poor in selenium, with tin atoms likely localized near grain boundaries or interfaces within the films.

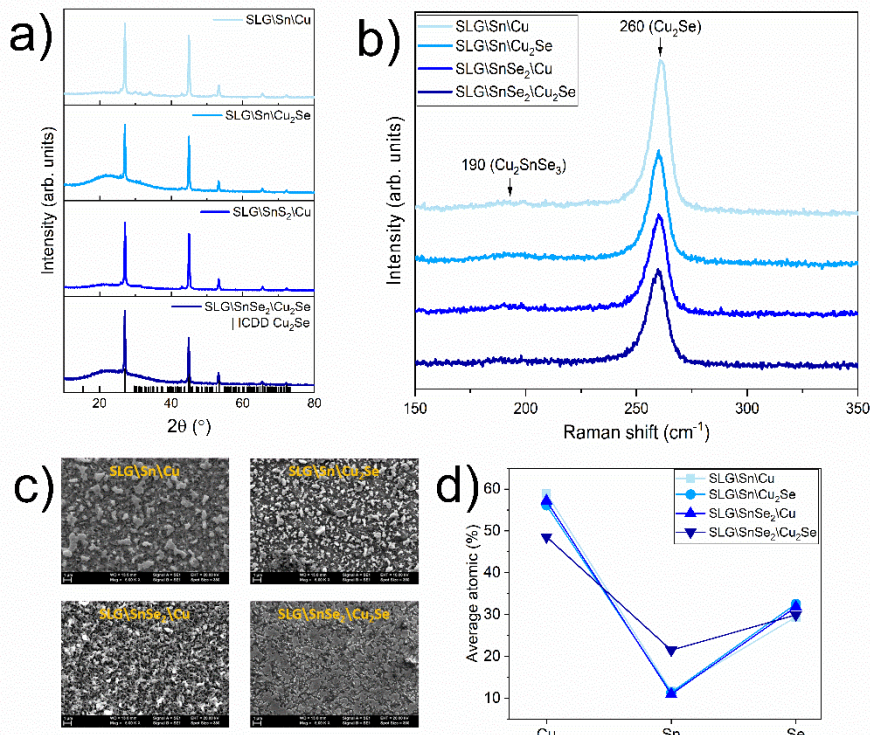


**Fig. 2** Structural, compositional and optical properties of the CTSe films with (a) GIXRD diagrams of the SLG/Sn/Cu, SLG/SnSe<sub>2</sub>/Cu, SLG/Sn/Cu<sub>2</sub>Se and SLG/SnSe<sub>2</sub>/Cu<sub>2</sub>Se stacks; (b) Raman spectra of the four CTSe films; (c) SEM images of the four stacks; and (d) EDS elemental composition of the CTSe films.

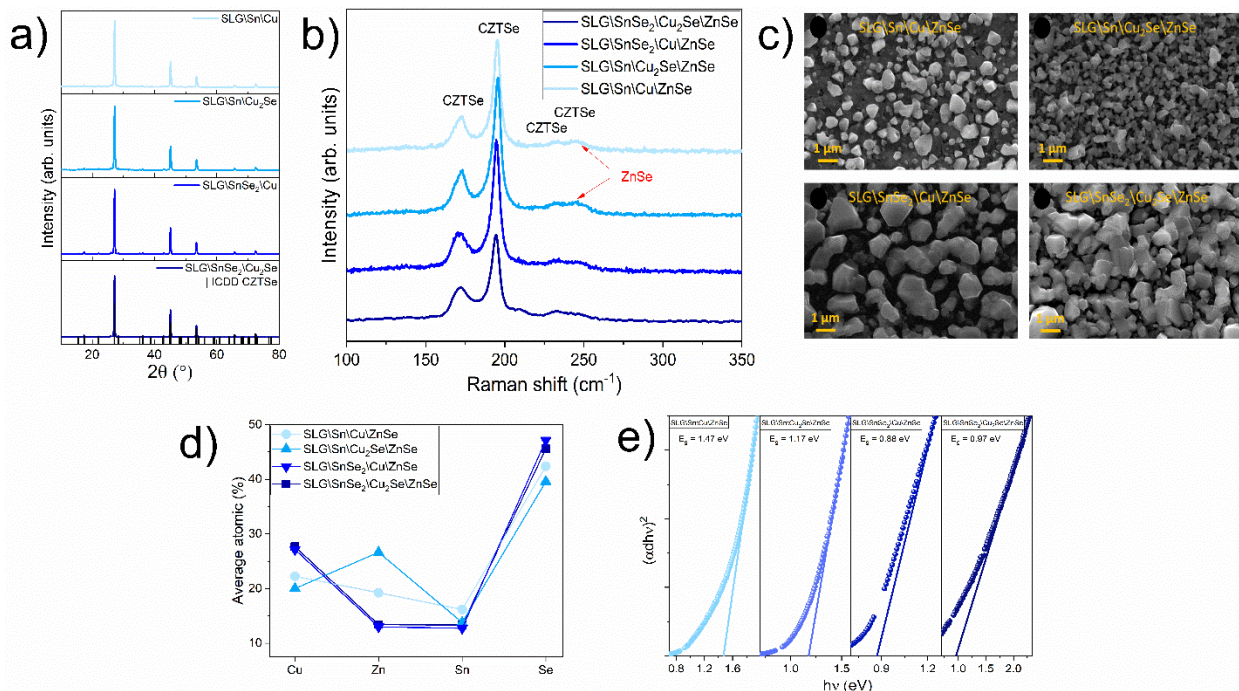


**Fig. 3** Structural, compositional and optical properties of the CZTSe films annealed in Sn+Se with (a) GIXRD diagrams of SLG/Sn/Cu/ZnSe, SLG/SnSe<sub>2</sub>/Cu/ZnSe, SLG/Sn/Cu<sub>2</sub>Se/ZnSe and SLG/SnSe<sub>2</sub>/Cu<sub>2</sub>Se/ZnSe stacks; (b) Raman spectra of the four films; (c) SEM images; (d) EDS elemental composition; and (e) Tauc plot of the CZTSe films.

Fig. 3 displays the GIXRD patterns of CZTSe films post-annealing under a Sn+Se atmosphere at 550 °C. The patterns reveal well-defined diffraction peaks characteristic of the CZTSe kesterite structure, affirming the presence of a tetragonal crystal structure. Despite the potential overlap with XRD patterns of CTSe and ZnSe, GIXRD analysis suggests the absence of secondary phases in the CZTSe films. Raman spectroscopy further supports these findings, detecting characteristic peaks of the CZTSe kesterite phase with a minimal presence of ZnSe in specific stacks. SEM images showcase

distinct surface morphologies among the CZTSe films, with varying grain sizes and void formations attributed to the annealing process. EDS measurements reveal compositional variations, with certain stacks exhibiting favourable stoichiometries for CZTSe. XPS spectra (not shown) illustrated similar surface chemistries across all samples, emphasizing the efficiency of Sn+Se annealing in CZTSe phase formation. Optical band gap analysis indicated that the SLG\SnSe<sub>2</sub>\Cu\ZnSe (0.88 eV) and SLG\SnSe<sub>2</sub>\Cu<sub>2</sub>Se\ZnSe (0.97 eV) stacks consisted of single-phase CZTSe, aligning with reported band gap values. This comprehensive characterization contributes to a better understanding of the structural, morphological, and compositional properties of CZTSe films, essential for optimizing their performance in thin-film solar cell applications.

Using a sequential magnetron sputtering technique, four film stacks underwent annealing in a Se atmosphere. The initial annealing resulted in off-stoichiometric CTSe films, mostly Cu<sub>2</sub>Se. Adding a ZnSe top layer and subsequent annealing in Sn+Se facilitated the formation of the desired CZTSe kesterite phase, confirmed by GIXRD and Raman spectroscopy. Surface morphology was compact and homogeneous, with SLG\SnSe<sub>2</sub>\Cu\ZnSe and SLG\SnSe<sub>2</sub>\Cu<sub>2</sub>Se\ZnSe samples showing larger grains. EDS revealed stoichiometric CZTSe composition in these samples. CZTSe film band gaps were within the optimal range for efficient light absorption. The SLG\SnSe<sub>2</sub>\Cu\ZnSe and SLG\SnSe<sub>2</sub>\Cu<sub>2</sub>Se\ZnSe stacks exhibited the most favourable properties as absorbers, showcasing the potential of these films for enhancing thin-film solar cell efficiency [3].

#### References

1. D.S. Catana, M.Y. Zaki, I.D. Simandan, et al., "Understanding the Effects of Post-Deposition Sequential Annealing on the Physical and Chemical Properties of Cu<sub>2</sub>ZnSnSe<sub>4</sub> Thin Films", *Surfaces* 6, 466–479, (2023).
2. M.Y. Zaki, F. Sava, I.D. Simandan, et al., "Cu<sub>2</sub>SnSe<sub>3</sub> Phase Formation from Different Metallic and Binary Chalcogenides Stacks using Magnetron Sputtering", *Materials Science in Semiconductor Processing* 153, 107195, (2023).
3. M.Y. Zaki, F. Sava, I.D. Simandan, et al., "From Non-stoichiometric CTSe to Single Phase and Stoichiometric CZTSe Films by Annealing under Sn+Se Atmosphere", *Ceramics International* 49, 33692–33702, (2023).

# Advanced Techniques for Local Investigations Down to Single Molecular Level and Beyond

**B. Borca**

National Institute of Materials Physics, 077125 Magurele, Romania

Scanning Probe Microscopy (SPM) and in particular Scanning Tunnelling Microscopy and Spectroscopy (STM/STS) are powerful techniques that allow the investigation at atomic and molecular scale of structural and electronic phenomena on a variety of different emerging materials. Therein, new research contributions on systems that contain organic molecules and biomolecules that reveal new properties are of great importance in material sciences and innovative technologies. Here, I briefly present two individual research studies realised in close international collaborations exploiting STM techniques and developing strategies beyond their standard functionalities for investigation of single molecules. One is focused on the unambiguous identification of specific amino acids within different peptides by molecular tip sensitisation and selective intermolecular interactions [1]. The other one explores chiral and catalytic effects of adsorption-induced molecular configurations by the selective molecular-moieties interaction with first and second surface atomic layers [2].

## I. Molecular sensitised probe for amino acid recognition within peptide sequences

X. Wu<sup>1,2,=</sup>, B. Borca<sup>3,4,=</sup>, S. Sen<sup>1</sup>, S. Koslowski<sup>1</sup>, S. Abb<sup>1</sup>, D.P. Rosenblatt<sup>1</sup>, A. Gallardo<sup>5,6</sup>, J.I. Mendieta-Moreno<sup>5</sup>, M. Nachtigall<sup>5</sup>, P. Jelinek<sup>5</sup>, St. Rauschenbach<sup>1,7</sup>, K. Kern<sup>1,8</sup>, U. Schlickum<sup>1,3</sup>

<sup>1</sup> Max Planck Institute for Solid State Research, Stuttgart, Germany

<sup>2</sup> School of Integrated Circuits and Electronics, Beijing Institute of Technology, Beijing 100081, China

<sup>3</sup> Institute of Applied Physics and Laboratory for Emerging Nanometrology, Technische Universität Braunschweig, 38104 Braunschweig, Germany

<sup>4</sup> National Institute of Materials Physics, 077125 Magurele, Romania

<sup>5</sup> Institute of Physics of the Czech Academy of Science, Prague, Czech Republic

<sup>6</sup> Department of Condensed Matter Physics, Faculty of Mathematics and Physics, Charles University, Prague, Czech Republic

<sup>7</sup> Department of Chemistry, University of Oxford, Oxford, United Kingdom

<sup>8</sup> Institut de Physique, École Polytechnique Fédérale de Lausanne, Lausanne, Switzerland

= These authors contributed equally: Xu Wu, Bogdana Borca

*Nature Communications* **14**, 8335 (2023). <https://doi.org/10.1038/s41467-023-43844-5>

The chemical detection and identification, *i.e.* the proteomics, of amino acids that are the building blocks of biopolymers, such as peptides and proteins, are essential in the emergent technologies of bioengineering and medical investigations, as these biomolecules are vital parts of living organisms. Lately, the development of methods and strategies to precisely identify and accurately quantify the amino acids sequences in single molecule peptides and proteins, that allows such precision and accuracy, is becoming a prominent and expanding field [3,4]. These amino acids identification processes often and widely rely on the presence of markers, antibodies, extensive simulations, combination of several techniques or are not possible at all.

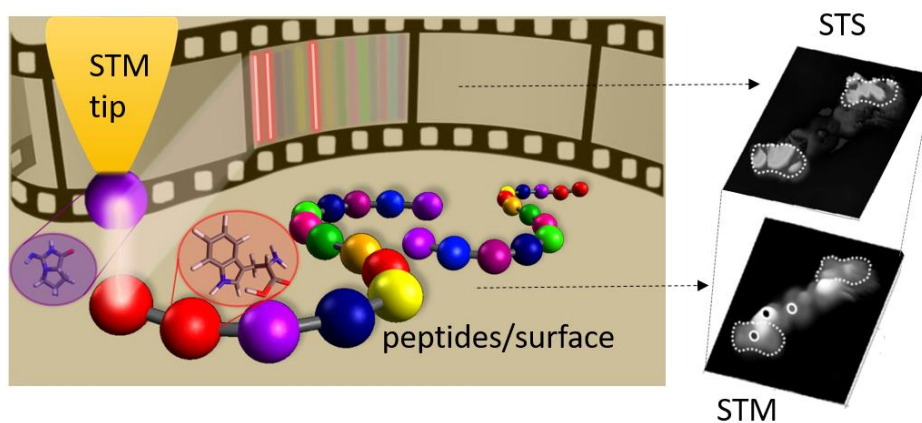


**Fig. 1 Left panels:** Schematic representation of the experimental procedure based on STM-tip sensitisation for amino acids identification within single molecular peptides deposited on surfaces. **Right panels:** STM topographic and STS spectroscopic images of a peptide dimmer, revealing the enhanced signal of specific amino acids by selective interaction with the sensitizer molecule at the tip apex.

In the article presented in Ref. [1], we develop a procedure to reliably spatially determine the exact location of a specific amino acid within different peptide sequences using a low temperature STM by tip sensitisation. The mechanism is based on a selective intermolecular interaction between a sensitizer molecule on the apex of the STM tip and the target amino-acid on the surface incorporated in the peptide (Fig. 1). The amino acid specific interaction induces an enhanced tunneling conductance of one spectral feature mapped in spectroscopic imaging STS and then associated to the location of one specific amino acid in the topography image STM (Fig. 1). Density functional theory calculations (DFT) suggest that the origin of the chemically specific interaction between the probe sensitizer and the amino acid within the peptide can be understood via a docking mechanism that modifies the geometry as well as the local charge distribution of the molecular probe. The proof-of-concept of this procedure is demonstrated for the amino acid tryptophan in several different peptide sequences, that are deposited intact on a clean surface in ultrahigh vacuum after mass selection by using an electrospray ion beam deposition technique. Thus, our study provides a new step towards single-molecule proteomics.

## II. Chiral and catalytic effects of site-specific molecular adsorption

*B. Borca*<sup>1,2\*</sup>, *T. Michnowicz*<sup>1</sup>, *F. Aguilar-Galindo*<sup>3</sup>, *R. Pétuya*<sup>3</sup>, *M. Pristl*<sup>1</sup>, *V. Schendel*<sup>1</sup>, *I. Pentegov*<sup>1</sup>, *U. Kraft*<sup>1,4</sup>, *H. Klauk*<sup>1</sup>, *P. Wahl*<sup>1,5</sup>, *A. Arnau*<sup>3,6</sup>, *U. Schlickum*<sup>1,7\*</sup>

<sup>1</sup> Max Planck Institute for Solid State Research, 70569 Stuttgart, Germany.

<sup>2</sup> National Institute of Materials Physics, 077125 Magurele, Romania.

<sup>3</sup> Donostia International Physics Center, E-20018 Donostia - San Sebastián, Spain.

<sup>4</sup> Max Planck Institute for Polymer Research, Mainz 55128, Germany

<sup>5</sup> SUPA, School of Physics and Astronomy, University of St Andrews, North Haugh, United Kingdom

<sup>6</sup> Departamento de Polímeros y Materiales Avanzados: Física, Química y Tecnología UPV/EHU and Material Physics Center (MPC), Centro Mixto CSIC-UPV/EHU, E-20018 Donostia - San Sebastián, Spain

<sup>7</sup> Institute of Applied Physics and Laboratory for Emerging Nanometrology, Technische Universität Braunschweig, 38104 Braunschweig, Germany.

\* corresponding author

*J. Phys. Chem. Lett.* **14**, 2072 (2023). <https://doi.org/10.1021/acs.jpcclett.2c03575>

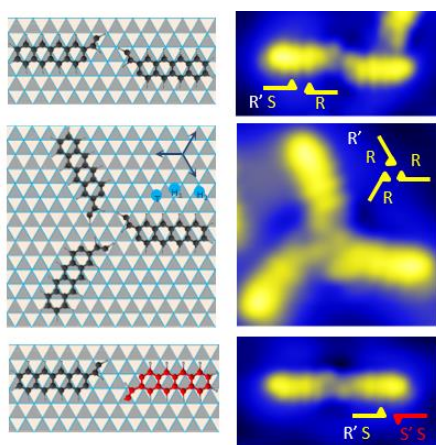


**Fig. 2 Left panels:** Schematic representation of the adsorption configurations of the TC-D. **Right panels:** STM topographic images of dimers and trimers marking different enantiomers [2].

Chirality represents an important property of molecular systems that may appear intrinsically in the molecular units or it can be the result of a particular adsorption geometry for molecules on surfaces. Nowadays, there exist a large variety of processes, such as recognition of enantiomerically pure substances or some chemical reactions, in which chirality plays an important role [5]. Moreover, scientific interest is also focused in the development of chiral materials or structures for the construction of devices. However, it is not easy to create such chiral systems using as building blocks molecules without chirality or starting as racemic mixtures. In this context, prochiral molecules and metal surfaces with catalytic properties arise as a promising alternative. In the article presented in Ref. [2], we have investigated the adsorption characteristics of pentacene thio-derivatives (TCT molecules) on the Cu(111) surface. We find strong evidence of a well characterized preferential adsorption along the 3-fold high symmetry axes of the Cu(111) surface with the thiophene unit atop a Cu atom and of the acene rings on the hollow-hcp sites. This particular adsorption geometry induces a

molecular chirality of right R and left S handed TCT enantiomers. Importantly, upon adsorption of the monomer, a direct desulfurization reaction of the thiophene moiety is activated even below room-temperature under the catalytic properties of the Cu(111) surface resulting the TC-D molecules. Furthermore, as the molecular coverage is increased, competing intramolecular interactions gives rise to a delicate balance in the hierarchy of interactions at play that permits the formation of different superstructures with both type of enantiomers, forming dimers with different orientation and composition, as well as trimers occasionally (Fig. 2). The topic has a high relevance nowadays and our results pave the way for the comprehension of the interactions between an important family of chemical compounds, such as the acenes, and metal surfaces. The article explores additional features of this category of molecules and systems that have great potential for molecular electronics and/or catalysis [6–9].

#### References

1. X. Wu, B. Borca, S. Sen, *et al.*, “Molecular Sensitised Probe for Amino Acid Recognition within Peptide Sequences”, *Nature Communications* 14, 8335 (2023).
2. B. Borca, T. Michnowicz, F. Aguilar-Galindo, *et al.*, “Chiral and Catalytic Effects of Site-Specific Molecular Adsorption”, *The Journal of Physical Chemistry Letters* 14, 2072 (2023).
3. C. Seydel, “Diving Deeper into the Proteome”, *Nature Methods* 19, 1036–1040 (2022).
4. V. Marx, “A Dream of Single-cell Proteomics”, *Nature Methods* 16, 809–812 (2019).
5. M. Liu, L. Zhang, T. Wang, “Supramolecular Chirality in Self-Assembled Systems”, *Chemical Reviews* 115, 7304–7397 (2015).
6. T. Michnowicz, B. Borca, R. Pétuya, *et al.*, “Controlling Single Molecule Conductance by A Locally Induced Chemical Reaction on Individual Thiophene Units”, *Angewandte Chemie International Edition* 59, 6207–6215 (2020).
7. B. Borca, T. Michnowicz, R. Pétuya, *et al.*, “Electric-Field-Driven Direct Desulfurization Reaction”, *ACS Nano* 11, 4703 (2017).
8. B. Borca, V. Schendel, R. Pétuya, *et al.*, “Bipolar Conductance Switching of Single Anthradithiophene Molecules”, *ACS Nano* 9, 12506–12512 (2015).
9. V. Schendel, B. Borca, I. Pentegov, *et al.*, Remotely Controlled Isomer Selective Molecular Switching, *Nano Letters* 16, 93–97 (2016).

# Assessment of Thermoelectric Performance through Synthesis and Doping Strategies in $Mg_2(Si,Sn)$ Solid Solutions

I. Assahsahi <sup>a</sup>, M. Enculescu <sup>a</sup>, M. Galatanu <sup>a</sup>, A. Galatanu <sup>a</sup>, B. Popescu <sup>a</sup>, R. El Bouayadi <sup>b</sup>, D. Zejli <sup>b</sup>, V. Cebotari <sup>c</sup>, F. Popa <sup>c</sup>, T.F. Marinca <sup>c</sup>, B.V. Neamtu <sup>c</sup>, N.A. Sechel <sup>c</sup>, I. Chicinaş <sup>c</sup>

<sup>a</sup>National Institute of Materials Physics, 077125 Magurele, Romania

<sup>b</sup>ISA Laboratory, ENSA, Ibn Tofail University, 14000 Kenitra, Morocco

<sup>c</sup>Technical University of Cluj-Napoca, 400641 Cluj-Napoca, Romania

$Mg_2Si_{1-x}Sn_x$  solid solutions are notable for their element's abundance in the Earth's crust, cost-effectiveness of the constituent elements, non-toxic nature, lightweight properties, and excellent thermoelectric performance. These characteristics make them attractive for various applications. The figure of merit,  $ZT$  [1] which results from low thermal conductivity and high power factor ( $PF=\sigma S^2$ ), can reach 1.7 for doped  $n$ -type  $Mg_2Si_{1-x}Sn_x$  ( $0.4 < x < 0.7$ ), whereas their  $p$ -type counterparts achieve only 0.7 within the temperature range of 500 K to 800 K. To achieve optimal device efficiency, both  $n$ -type and  $p$ -type materials with comparable thermoelectric and thermomechanical properties are necessary for applications. Therefore, it is crucial to explore methods to enhance material properties, such as doping, substitutions, and material synthesis.

(i)  $p$ -type  $Mg_2Si_{0.3}Sn_{0.7}$  doped with silver and gallium

Theoretical investigations suggest that achieving a  $ZT_{max}$  of around 0.8 at 700 K is feasible in  $p$ -type  $Mg_2(Si,Sn)$  solid solutions, but this requires a high level of charge carrier concentration. However, experimental efforts to optimize carrier concentration face challenges, as the synthesis of  $p$ -type samples often results in low carrier concentration, leading to subpar thermoelectric performance. The main obstacles associated with  $p$ -type  $Mg_2Si_{1-x}Sn_x$  primarily revolve around the low charge carrier concentration and high thermal conductivity. While a double doping strategy is commonly employed for  $n$ -type counterparts, it is uncommon for  $p$ -type materials. For instance, dual doping with Li and Ag significantly boosts the carrier concentration compared to single Li or Ag doping. Therefore, this study aims to substitute Ag and Ga at both Mg and Si/Sn sites to enhance the charge carrier concentration and simultaneously reduce thermal conductivity by introducing mass fluctuations through Ag doping, thereby improving the transport properties.

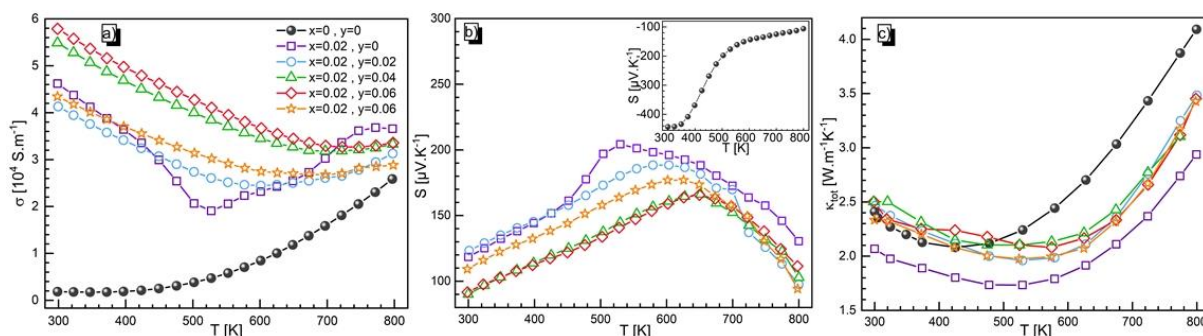


**Fig. 1** Temperature dependencies of (a) electrical conductivity, (b) Seebeck coefficient, and (c) thermal conductivity of  $Mg_{2-x}Ag_x(Si_{0.3}Sn_{0.7})_{1-y}Ga_y$  materials ( $x = \{0, 0.02\}$ ,  $y = \{0, 0.02, 0.04, 0.06\}$ ).

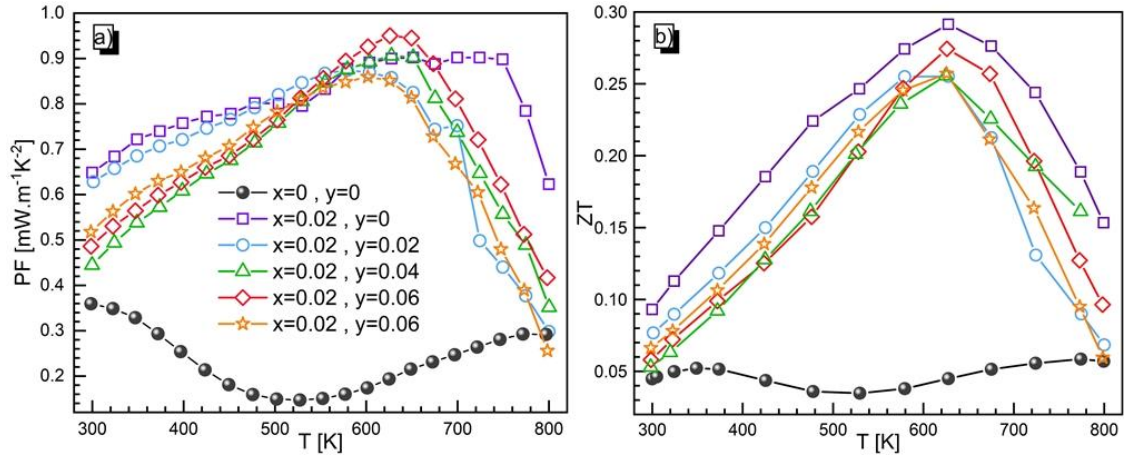


**Fig. 2** Thermoelectric performance of  $\text{Mg}_{2-x}\text{Ag}_x(\text{Si}_{0.3}\text{Sn}_{0.7})_{1-y}\text{Ga}_y$  materials ( $x = \{0, 0.02\}$ ,  $y = \{0, 0.02, 0.04, 0.06\}$ ).

The method of sample preparation is innovative, and consists of melting the precursors into a closed graphite crucible, with the interior walls covered with graphite foil, which is subsequently sealed under vacuum in quartz tubes. The melting takes place in a vertical tubular furnace at 1000 °C for 20 min to achieve compositional homogeneity, and is followed by quenching the sample in cold water. Then, powders of each composition are sintered (SPS) at 973 K and 50 MPa pressure for 20 min. The samples are biphasic with the main phase rich in Sn, compositionally close to the calculated stoichiometry, and the other with a composition similar to  $\text{Mg}_2\text{Si}$ .

The undoped specimen exhibits the typical behavior of an intrinsic semiconductor in terms of its electrical conductivity temperature dependence. In contrast, all doped samples show a decrease in conductivity ( $\sigma(T)$ ) from room-temperature (RT) to around 500 K, followed by an increase, which is characteristic of degenerate semiconductors (refer to Fig. 1a). The presence of Ag and the gradual introduction of Ga lead to a significant enhancement in conductivity values due to a substantial increase in hole concentration, reaching  $7.06 \times 10^{19} \text{ cm}^{-3}$  when  $x = y = 0.02$ . The negative Seebeck coefficient (refer to Fig. 1b) observed across the temperature range indicates the expected  $n$ -type behavior, with the coefficient increasing with temperature from  $-442 \mu\text{V K}^{-1}$  at RT due to intrinsic carrier excitation. All doped samples transition to  $p$ -type semiconductors with reduced positive Seebeck values and similar temperature dependencies, indicating the effective hole-doping effects of both Ag and Ga. The  $S(T)$  curves exhibit a downturn above 500 K, attributed to the transition into the intrinsic carrier transport regime, leading to an adverse impact on the Seebeck coefficient. This turnover in  $S(T)$  occurs at progressively higher temperatures with increasing Ga content in the sample. Furthermore, the absolute values of the Seebeck coefficient decrease as the Ga content increases. The decrease in total thermal conductivity ( $\kappa_T$ ), particularly at lower temperatures, can be attributed to the presence of Ag (refer to Fig. 1c). Ag serves to reduce lattice thermal conductivity by increasing phonon scattering, counteracting the rise in the electronic contribution to thermal conductivity resulting from the higher carrier concentration achieved through Ga doping.

Due to the influence of Ag and Ga substitutions on the physical properties of the  $\text{Mg}_{2-x}\text{Ag}_x(\text{Si}_{0.3}\text{Sn}_{0.7})_{1-y}\text{Ga}_y$  system, the power factor reaches its maximum values (as shown in Fig. 2a) for  $\text{Mg}_{1.98}\text{Ag}_{0.02}\text{Si}_{0.27}\text{Sn}_{0.67}\text{Ga}_{0.06}$  within a narrowed temperature range (575–675 K) around the peak value of  $9.10 \times 10^{-4} \text{ Wm}^{-1} \text{ K}^{-2}$  at 625 K. The elevated thermal conductivity values of the doubly doped compounds lead to ZT values below 0.29, with the highest value achieved at 627 K for the  $\text{Mg}_{1.98}\text{Ag}_{0.02}\text{Si}_{0.3}\text{Sn}_{0.7}$  sample (refer to Fig. 2b).

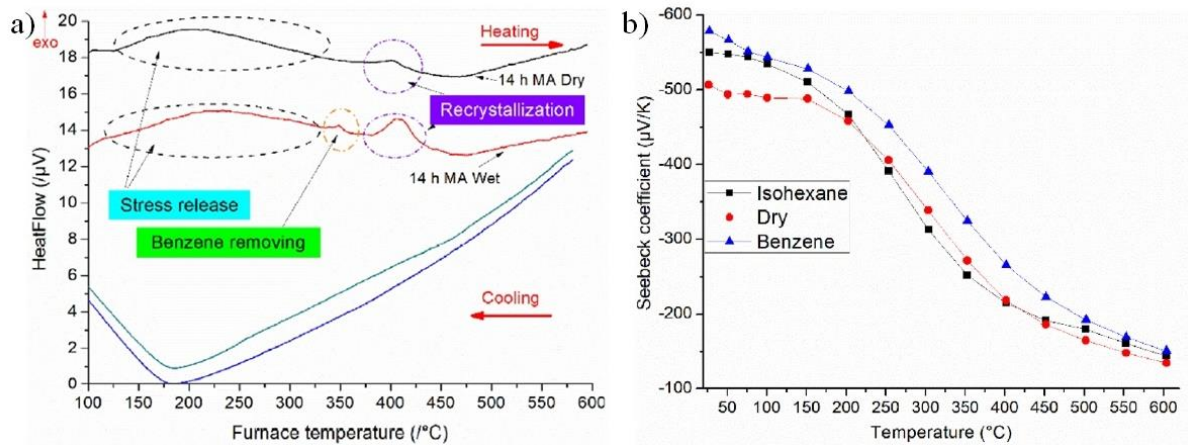


**Fig. 3** (a) DSC analysis of 14 h milled powders, red curve corresponds to wet milling and dark to dry milling; (b) Influence of the processing route on temperature dependence of Seebeck coefficient.

(ii) *Mg<sub>2</sub>Si synthesis via wet and dry mechanical alloying*

The study investigates the impact of milling type (dry or wet) and process control agent (PCA) type (benzene or isohexane) on the synthesis and evolution of properties of Mg<sub>2</sub>Si powders and spark plasma sintered compacts [2]. The aim is to scale up material production and comprehend the influence of each processing step. Mg<sub>2</sub>Si was synthesized under various mechanical alloying conditions, revealing that 14 hours of milling time are needed for complete reaction. The PCA accelerates the solid-state reaction of elements, with prolonged milling time reducing the reaction rate. Benzene adsorbed on the powder surface shields against oxidation during milling, but heat treatment reverses this effect, leading to increased oxide formation due to the large specific surface area allowing more oxygen adsorption. Differential scanning calorimetry (DSC) analysis indicates Mg<sub>2</sub>Si compound formation in two stages (refer to Fig. 3a).

The negative sign of the Seebeck coefficient (Fig. 3b) suggests Mg<sub>2</sub>Si is an *n*-type semiconductor, with a value of 580 μV/K at room-temperature. Compacts from wet mechanical alloyed powders exhibit a higher Seebeck coefficient at room-temperature compared to those from dry mechanical alloyed powders, possibly due to varying grain boundary lengths dependent on mean crystallite size acting as filters/barriers. The Seebeck coefficient decreases with temperature increase, likely due to rising charge carrier concentration through intrinsic conduction. Conversely, electrical conductivity is low at room-temperature but increases with temperature as charge carrier concentration rise. Samples with superior physical properties, potentially enhancing thermoelectric performance, are derived from powders processed with benzene.

*References*

1. I. Assahsahi, B. Popescu, R. El Bouayadi, et al., “Thermoelectric Properties of p-type Mg<sub>2</sub>Si<sub>0.3</sub>Sn<sub>0.7</sub> Doped with Silver and Gallium”, *Journal of Alloys and Compounds* 94, 169270 (2023).
2. V. Cebotari, F. Popa, T.F. Marinca, B.V. Neamțu, N.A. Sechel, M. Galatanu, A. Galatanu, I. Chicinaș, “Obtaining and Characterisation of Thermoelectric Mg<sub>2</sub>Si Compound via Wet and Dry Mechanical Alloying and Spark Plasma Sintering”, *Journal of Materials Research and Technology* 26, 8904 (2023).

# Composites with Boron-based Compounds for Extreme Conditions

A.C. Kuncser, M. Grigorescu, P. Badica

National Institute of Materials Physics, 077125 Magurele, Romania

in collaboration with National Institute for Materials Science, Tohoku University, and Otto von Guericke University Magdeburg [1,2].

Strategic domains such as energy, aerospace and defense industries depend on successful engineering of innovative advanced functional materials. Many of these materials have to work under extreme conditions being able to withstand very high or low temperatures and pressures, possess high hardness, toughness, and ideally a good thermal, electrical conductivity, and chemical stability. All the above-mentioned features should occur simultaneously. Moreover, production of these materials should be cheap, fast, and scalable. Only few families of materials meet the particular, narrow set of above-mentioned requirements. Among them are refractory metals (*e.g.*, W and Mo), oxides (ZrO<sub>2</sub> and MgO), borides (TiB<sub>2</sub> and TaB), carbides (TaC, ZrC, TiC and boron carbide denoted BC) or nitrides (TaN and HfN). In general, at room-temperature metals are ductile and undergo plastic deformation, while ceramics are brittle, hard, and deform elastically. It is noteworthy that in the last few years literature presents evidence for totally unexpected deformation behavior by unusual physical mechanisms. For example, some ceramics such as tantalum carbide (TaC), hafnium boride (HfB<sub>2</sub>) and boron carbide (BC) are able to accommodate at high temperatures plastic deformation similar to metals due to *e.g.* the dynamics of crystallographic defects. Under mechanical load, the interplay between the intrinsic properties of the material (crystal chemistry and defects) and microstructure at nano and micro scale (grain size, distribution, and shape and grain boundaries) can promote novel physical mechanisms of energy relaxation. These mechanisms result in the peculiar profiles of the stress *vs.* strain curves. It is also well known that one has to consider the load application conditions (*e.g.*, the load type, application rate and angle), sample size and shape.

In the last years there is a large interest in TiB<sub>2</sub> ceramic and composites reinforced with *e.g.* BC and SiC. These ceramics are investigated by bending tests usually at room-temperature. In general, depending on grain size, reinforcement, and microstructure of the composite considering also defects, the room-temperature bending strength attains values of 600–900 MPa. Macroscopic fracture mechanisms are related to cracks formation and development, these mechanisms being typical for brittle ceramics. Among them, literature indicates interfacial micro crack toughening due to thermal expansion coefficient differences of the composite components, cracks deflection, cleavage and enhancement of the intergranular fracture. A much lower number of studies on the mechanical properties of these materials at high temperatures have been reported. However, they indicate that bending strength values also do not exceed 1 GPa although a rising trend with an increasing temperature of the test is notable and deserves attention. It was recently reported that bending strength of TiB<sub>2</sub>-BC composite achieves ultrahigh values up to 8.4 GPa at 2000 °C. These values significantly exceed the limit of 1 GPa for bending strength at room-temperature.

Another practical ceramic is boron carbide (BC). Macroscopic fracture mechanisms at room-temperature share similarities with those of TiB<sub>2</sub>, although crystal structure and chemistry are very different. The room-temperature bending strength of BC-based ceramic composites also does not exceed 1 GPa. Bending strength curves versus temperature of BC-based composites show a complex behavior and there are situations when, at high temperatures, bending strength exceeds the values measured at room-temperature.

Presented information suggest that mechanical properties studies of TiB<sub>2</sub> and BC and of their composites at high temperatures is of much interest. Expectations are that novel deformation mechanisms are active at high temperatures and they do not necessarily follow the conventional trends and understanding established for mechanical tests at room-temperature. Few works reported ceramic composites of TiB<sub>2</sub>-BC, TiB<sub>2</sub>-TaC, or BC-TaB<sub>2</sub> with a plastic behavior during bending at high temperatures, while an increased bending strength was also recorded. The unexpected increase in strength at high temperatures when compared to values at room-temperature was linked with nano-twinning, or twins' rearrangement at high temperatures. Some mechanisms have been revealed in

detail, but they are valid for very particular systems/classes of systems, thus not allowing to comprehend the full picture of the observed mechanical properties.

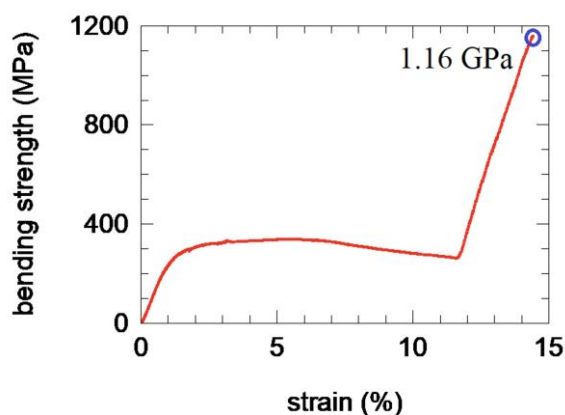


**Fig. 1** Typical bending strength curve at 1800 °C measured on the TiB<sub>2</sub>-BC sample obtained by SPS. Note three regions of deformation: (i) conventional elastic, typical for ceramics, (ii) plastic-like, and (iii) elastic-like strengthening at large strains.

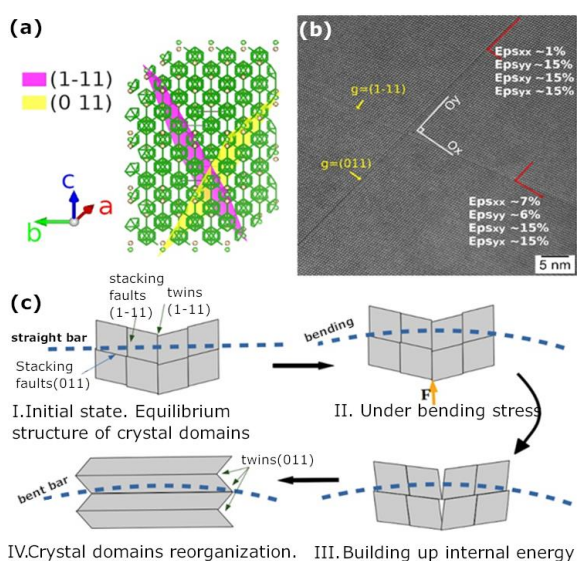


**Fig. 2** (a) Boron carbide crystal representation by VESTA software showing equivalent planes (1-11) and (011); (b) HRTEM image taken on sample in the fractured area showing strain components with Oy being parallel to (011) planes; (c) Schematics of the transition under bending load between a twinned and stacking faulted structure to a new nano-twinned one.

In our recent work [1] a high density (99.5 %) ceramic composite made of titanium boride and boron carbide (70/30 vol. %) was obtained by spark plasma sintering and was tested by 3-point bending test in Ar atmosphere at 1800 °C. Bending strength was high, around 1.1 GPa (Fig. 1). The strength-strain curve presents a peculiar shape composed of three regions (i-iii) where elastic and plastic deformations are active with a different weight. Based on transmission electron microscopy observations we propose a process of mechanical energy absorption driven by shear stress in the boron carbide crystals (Fig. 2): stacking faults with (1-11) and (011) stacking planes and twins with (1-11) twinning plane rearrange into nano-twins with (10-1) twinning planes, orthogonal but equivalent to the initial ones. This rearrangement mechanism provides in the first instance a plastic signature (Fig. 1(ii)), but further contributes strengthening (Fig. 1(iii)).

High-strength steels, Ni-based alloys and titanium-based materials are used as structural high-temperature materials, sometimes as metal-matrix composites (MMC). New alloys and composites based on refractory metals such as Mo, Nb, and Cr are the subject of ongoing research, much attention being made on Co-based super alloys, new intermetallic systems Ni-Al-Mo, Ru-Ni-Al, and Mo-based multiphase materials, as their properties partially go beyond those of reference alloys such as Ni-based super alloys.

Mo-based alloys show great potential for ultra-high-temperature applications, but it is necessary to overcome some of their deficiencies. The most promising Mo-based alloys are Mo-Si-B(-X) alloys, while X represents elements or compounds that improve specific key properties. Certain alloys of this class can be used up to 1370 °C in air due to their superior mechanical properties and good

oxidation resistance. Mo-Si-B alloys provide the best combination of properties with a three-phase microstructure consisting of a plastically deformable Mo solid solution phase (Moss) and two intermetallic phases Mo<sub>3</sub>Si (A15) and Mo<sub>5</sub>SiB<sub>2</sub> (T2). However, the properties are highly dependent on the type of microstructure and size of the microstructural constituents. For optimum oxidation resistance, a fine-grained structure and a high proportion of intermetallic phases (>50%) are desirable. The best fracture toughness is achieved in alloys with a Moss matrix containing large intermetallic grains. It is known that the oxidation resistance and mechanical properties strongly depend on the grain size of Mo-Si-B alloys. On the one hand, finer grains lead to higher strength, but small grains have low ability to accumulate dislocations so that the ductility and toughness of the alloy are usually low. Casting of these alloys cannot provide a controlled microstructure and often segregation occurs. Powder metallurgy routes are investigated as a possible solution.

Mo matrix composites (MMC) with Mo-9Si-8B inclusions were fabricated by pressure-less sintering (PLS) and spark plasma sintering (SPS) techniques at temperatures between 1200–1500 °C using 1 wt.% Ni sinter additive [2]. The positive impact of the addition Ni addition on the sinterability and formation of a continuous Mo-MMC with randomly distributed Mo<sub>3</sub>Si and Mo<sub>5</sub>SiB<sub>2</sub> inclusions was determined. The Ni addition increased the shrinkage of MMC during PLS by almost a third. The continuous Mo matrix of MMC and a relative density of more than 98 % was obtained after SPS at 1400–1500 °C. The composite with the maximum relative density of 98 % showed a Vickers hardness of 482 ± 9 (HV20). The potential of using Ni-activated PLS and SPS to produce high-density MMC was shown.

#### References

1. A. Kuncser, O. Vasylykiv, H. Borodianska, *et al.*, “High Bending Strength at 1800 °C Exceeding 1 GPa in TiB<sub>2</sub>-B<sub>4</sub>C Composite, *Scientific Reports* 13, 6915 (2023).
2. I. Solodkyi, V. Petrusha, M.A. Grigoroscuta, *et al.*, “Efficient Sintering of Mo Matrix Composites—A Study of Temperature Dependences and the Use of the Sinter Additive Ni”, *Metals* 13, 1715 (2023).

# Doped Zinc-Oxide Nanostructures – Optimization of Processing Conditions and Original Approaches in Explaining Different Functionalities

V. Mihalache, C. Negrila, M. Secu, I. Mercioniu, N. Iacob, A. Leca, C. Bartha, V. Kuncser

National Institute of Materials Physics, 077125 Magurele, Romania

in collaboration with National Institute of Laser, Plasma and Radiation Physics, Magurele, Romania [2].

Doped zinc-oxide systems with magnetic, electric and optical properties in conjunction with high adsorption and catalytic activity are of great interest in present nanotechnologies.

As a first example, transition metal (TM) doped ZnO dilute magnetic semiconductors, DMS, with Curie temperature exceeding room-temperature, have gained special attention due to potential applications in spintronic devices. The origin and mechanism of ferromagnetism in TM-doped ZnO are still challenging and contradictory results are frequently reported. Some theoretical calculations predicted that the ferromagnetic state could be the ground state for the  $3d$  TM-doped ZnO system, while other experimental and theoretical reports demonstrate that in the absence of defects, the paramagnetic, antiferromagnetic, or spin-glass states are more favorable to the ferromagnetic one and that the occurrence of ferromagnetism in TM-doped ZnO requires extra carriers. The extra carriers can be provided particularly by  $p$ -type or  $n$ -type intrinsic defects correlated with non-equilibrium conditions of ZnO processing. The properties (*e.g.*, ferromagnetism) of both doped and un-doped ZnO are generally recognized to depend strongly on the preparation conditions. We have investigated the structural, local chemical, optical and magnetic behaviour of zinc-oxide (nanostructures) with different types and amounts of dopants [1]. Concerning Fe-doped ZnO, our research aimed to provide some insights into the mechanism of ferromagnetism of  $Zn_{1-x}Fe_xO$  in case of nanoparticles with the iron concentration level in the *dilute* regime (0.1 – 1 at.%) prepared by thermal decomposition of Zn(II)-Fe(III)-carboxylates (derived from acetate precursors).

(i) *Structural and morphological characteristics (X-Ray diffraction, scanning electron microscopy, and transmission electron microscopy)*

$Zn_{1-x}Fe_xO$  nanoparticles with the iron concentrations level in the dilute regime ( $x=0.001 - 0.01$ ) were produced by a sol-gel route from acetate precursors along with an un-doped and 3 at.% Fe-doped reference. The X-ray diffraction of the un-doped and 0.1 – 1 at.% Fe-doped samples reveal the reflections for only the ZnO wurtzite structure. The increase of Fe concentration from 0.1 to 1 at.% enhances the  $a$ -axis lattice constant, the unit cell volume and the microstrain (Fig. 1a). Iron doping reduces the average crystallite/particle size (confirmed by *Scanning Electron Microscopy*), improving the surface-to-volume ratio related to the increase of the fraction of Fe ions in defective surface sites. The (ultra)fine  $ZnFe_2O_4$  particles were found on the surface of ZnO for  $Zn_{0.97}Fe_{0.03}O$  by HRTEM investigations (Fig. 1b and 1c).

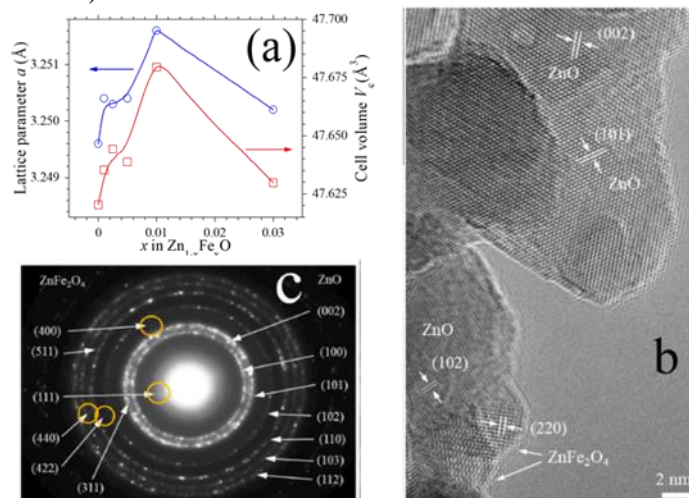


**Fig. 1.** (a) The iron concentration dependence of the  $a$ -axis lattice constant and unit cell volume,  $V_c$ , determined by Rietveld fitting of the XRD patterns. The (b) HRTEM and (c) SAED analysis of  $Zn_{0.97}Fe_{0.03}O$ .

(ii) *The evidence of distorted  $Fe^{3+}$  sites and intrinsic defects on the surface of ZnO particles.*

(X-ray photoelectron spectroscopy. Photoluminescence.  $^{57}\text{Fe}$  Mossbauer spectroscopy)  
 XPS identifies the iron in both  $\text{Fe}^{3+}$  and  $\text{Fe}^{2+}$  states.  $^{57}\text{Fe}$  Mossbauer spectroscopy (Fig. 2a–e) and XPS (Fig. 2f) indicate a wide distribution of energies for the  $\text{Fe}^{3+}$  valence state consistent with the presence of distorted  $\text{Fe}^{3+}$  sites on the surface of ZnO particles. The blue shift and broadening of the UV emission, and quenching of defect-related photoluminescence (Fig. 2g) in the Fe-doped samples verify the presence of iron in the ZnO lattice and surface intrinsic defects.

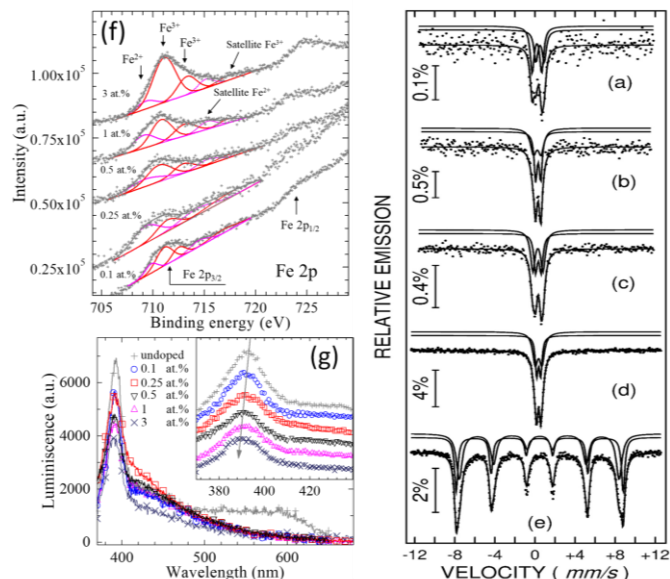


**Fig. 2 (a–e)**  $^{57}\text{Fe}$  Mossbauer spectroscopy recorded at 5.5 K and RT (295 K) of (a) 0.5 at.%, (b) 3 at.%, (c) 3 at.% (annealed at 405 °C) Fe-doped ZnO and (d,e)  $\text{ZnFe}_2\text{O}_4$  reference. (f) XPS.  $\text{Fe } 2p_{3/2}$  spectra are deconvoluted into three components, one for  $\text{Fe}^{2+}$  and two for  $\text{Fe}^{3+}$  states. The need for an extra component (712 – 713 eV) suggests a wide distribution of energies for this valence state and, thus, the presence of surface  $\text{Fe}^{3+}$  sites with distorted configuration. (g) RT luminescence spectra for undoped and Fe-doped ZnO. Inset: Magnified view.

### (iii) Magnetic studies

Fe-doped ZnO (0.1 – 1 at.%) shows weak room-temperature ferromagnetism, RTFM, (Fig. 3a) characteristic of dilute magnetic semiconductors, DMS. Room-temperature  $M_s$ ,  $H_c$  at 5 K and  $M_s$  at 5 K increase with the increase of Fe concentration level up to 1 at.%. The magnetization measurements with temperature (e.g., Fig. 3b) evidence a nearest-neighbor antiferromagnetic alignment and an increase of ferromagnetic-like contribution with Fe doping up to 1 at.%.  $\text{ZnFe}_2\text{O}_4$  found on the surface of ZnO for  $\text{Zn}_{0.97}\text{Fe}_{0.03}\text{O}$  (Fig. 1b) is SPM at room-temperature ( $H_c=0$ ) with a blocking temperature of 20 K. The inverse spinel  $\text{ZnFe}_2\text{O}_4$  (whose ferrimagnetism below  $T_B$  is generated by the antiferromagnetic interaction between the  $\text{Fe}^{3+}$  ions in tetrahedral and octahedral sites) is the only secondary phase found in the given conditions of processing for 3 at.% Fe doping level.

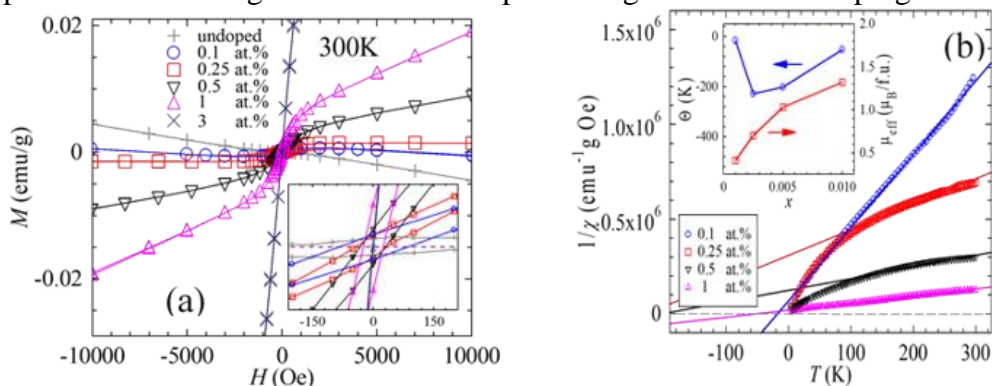


**Fig. 3 (a)**  $M$  vs  $H$  curves registered at 300 K for undoped and Fe-doped samples. (b) The inverse susceptibility vs. temperature curves for 0.1, 0.25, 0.5 and 1 at.% doped ZnO fitted with Curie-Weiss law; Inset: The Weiss temperature and the effective moment per formula unit determined from the Curie-Weiss fit.

(iv) A possible source for RTFM in  $(\text{Zn},\text{Fe})\text{O}$  with the iron concentration level in the dilute regime. Potential for optimisation and applications

The analysis of experimental (structural, local chemical, and magnetic) data of 0.1 – 1 at.% Fe-doped ZnO was done in terms of iron coupling with intrinsic defects (specifically  $V_{Zn}$  and  $O_i$ ), which can generate surface  $Fe^{3+}$  states with geometries similar to the  $Fe^{3+}$  in inverse spinel  $ZnFe_2O_4$ . The superexchange interaction (resembling that in the inverse spinel  $ZnFe_2O_4$ ) between the  $Fe^{3+}$  sites with distorted octahedral coordination and  $Fe^{3+}$  sites with distorted tetrahedral coordination resulting in ferrimagnetism was hypothesised as a possible mechanism of RTFM.

The results of our study can be used to optimize further the processing conditions for (Zn,Fe)O to serve as effective DMS for *e.g.* spintronic applications.  $Zn_{0.97}Fe_{0.03}O$  is an SPM ZnO/ $ZnFe_2O_4$  nanocomposite that can find applications as *e.g.* gas and magnetic (nano)sensors and antibacterial agents.

As a second example, the ZnO–graphene heterostructure nanohybrids integrate the physical properties of graphene and ZnO, providing a unique platform for the exploration of a wide variety of applications, ranging from photodetectors and gas sensors to stress/strain sensors and piezoelectric nanogenerators. In this respect, hybrid structures of ZnO thin films doped with  $P_2O_5$  and reduced graphene oxide (rGO) was produced by sol-gel synthesis and subsequent spin-coating method (from 1 to 20 successive layers) and investigated with respect to fluorescence and opto-electronic and conduction properties [2]. XRD patterns of the analyzed samples proved a hexagonal phase of ZnO, with the crystallite size decreasing with increasing  $P_2O_5/ZnO$  molar ratios from 10/90 (18 nm) to 20/80 (10 nm), respectively. The band gaps, as estimated from the UV-VIS-NIR investigations, decreased as a result of the rGO and phosphorous oxide contents with a minimum of 3.77 eV for the 20-layered 90ZnO10P2O5rGO film. The optical band gap ( $E_g$ ) was found to be dependent on the number of layers and  $P_2O_5$  content.

A doping with 1 wt. % rGO decreased the film's resistivity by about 15%, while a molar ratio of 10/90 of  $P_2O_5/ZnO$  decreased the resistivity almost seven-fold, as identified from the electrical measurements performed at room-temperature.

#### References

1. V. Mihalache, C. Negrila, M. Secu, *et al.*, “Defect Structures and (Ferro)magnetism in  $Zn_{1-x}Fe_xO$  Nanoparticles with the Iron Concentration Level in the Dilute Regime ( $x = 0.001 - 0.01$ ) Prepared from Acetate Precursors”, *Results in Physics* 51, 106644 (2023).
2. I.C. Vasiliu, A.V. Filip, C. Irinela, *et al.*, “Effect of  $P_2O_5$  Content on Luminescence of Reduced Graphene Oxide Doped ZnO- $P_2O_5$  Nanostructured Films Prepared Via the Sol-Gel Method”, *Materials* 16, 6156 (2023).

# Vortex Dynamics and Pinning in some representative Iron-based Superconductors

A. Crisan, A.M. Ionescu, I. Ivan, C.F. Miclea, D.N. Crisan

National Institute of Materials Physics, 077125 Magurele, Romania

The discovery of iron-based superconductors (IBS)  $\text{La}(\text{O}_{1-x}\text{Fe}_x)\text{FeAs}$ , ( $x = 0.05 - 0.12$ ) with a critical temperature  $T_c = 26$  K, with unique superconducting mechanism and potential of use in various applications led to a world-wide effort in the discovery and comprehensive studies of this new class of superconducting materials. Up to now there are literally thousands of possible chemical compositions and doping levels of various IBS, of different types of crystalline structure. Among those different types of IBSs reported in the literature, 1111-type  $\text{REFeAsO}_{1-x}$  ( $\text{RE}$  being a rare-earth element) has the highest critical temperature of 55 K. Another type, namely 11-type  $\text{Fe}(\text{Se}, \text{Te})$ , have relatively low  $T_c$  (10 – 20 K depending on composition), but is promising as thin film, having a high critical current density  $J_c$  in very high magnetic field (over  $10^4$  A/cm<sup>2</sup> in fields larger than 10 T). Lately, superconductors based on  $\text{AEFe}_2\text{As}_2$  ( $\text{AE}$  being alkali-earth metal Ca, Sr, Ba) parent compound, the so-called 122 system, became the most popular materials for both physical explorations and wire applications because of their  $T_c$  as high as 38 K [4], very high upper critical fields  $\mu_0 H_{c2}$  ( $> 70$  T) and low anisotropies  $\gamma$  ( $< 2$ ), attracting substantial attention in comparison with other IBSs that have been reported in the literature. This is mainly due to the fact that in the 122 system, relatively large single crystals were relatively easy to grow using the self-flux technique. Superconductivity in  $\text{AEFe}_2\text{As}_2$  is primarily induced by alkali metal ( $A = \text{Na}, \text{K}, \text{Rb}, \text{Cs}$ ) substitution at  $\text{AE}$  sites. However, this type of charge doping creates strong scattering potentials that affect superconducting properties such as the vortex pinning, the upper critical field, and even the superconducting gap symmetry. Another type of 122 materials are isovalently substituted compounds such as  $\text{Ba}(\text{Fe}_{1-x}\text{Ru}_x)_2\text{As}_2$  and  $\text{BaFe}_2(\text{As}_{1-x}\text{P}_x)_2$ , which are closer to the clean limit. More recently, a new type of IBSs has been reported, having a new structure, abbreviated as  $\text{AEA1144}$ , namely  $\text{CaAFe}_4\text{As}_4$  ( $A = \text{K}, \text{Rb}, \text{Cs}$ ) and  $\text{SrAFe}_4\text{As}_4$  ( $A = \text{Rb}, \text{Cs}$ ). In these cases, because  $A$  does not mix with  $\text{AE}$  due to the large difference in atomic radii,  $\text{AEA1144}$  crystallizes through alternate stacking of the  $\text{AE}$  and  $A$  layers across the  $\text{Fe}_2\text{As}_2$  layer, changing the space group from  $I4/mmm$  to  $P/4 mmm$ , the compounds being superconductors with  $T_c$  values between 31 and 36 K. From the point of view of potential applications in high magnetic fields, the behavior of the critical current density, and the overall vortex dynamics and pinning are of paramount importance. We have investigated such properties in three types of iron-based superconducting single crystals:  $\text{CaKFe}_4\text{As}_4$ ,  $\text{BaFe}_2(\text{As}_{0.68}\text{P}_{0.32})_2$  and  $\text{Fe}(\text{Se}_{0.5}\text{Te}_{0.5})$ .

(i) *Vortex melting lines in  $\text{CaKFe}_4\text{As}_4$  and  $\text{BaFe}_2(\text{As}_{0.68}\text{P}_{0.32})_2$*

By using multi-harmonic susceptibility studies, we have investigated the vortex glass—vortex liquid phase transitions in  $\text{CaKFe}_4\text{As}_4$  and  $\text{BaFe}_2(\text{As}_{0.68}\text{P}_{0.32})_2$  single crystals [1]. The principle of our method relates the on-set of the third-harmonic susceptibility response with the appearance of a vortex-glass phase in which the dissipation is non-linear. Similar to the high-critical temperature cuprate superconductors, we have shown that even in these iron-based superconductors with significant lower critical temperatures, such phase transition can be treated as a melting in the sense of Lindemann's approach, considering an anisotropic Ginzburg-Landau model. The experimental data are consistent with a temperature-dependent London penetration depth given by a 3D XY fluctuations model (see Fig. 1). The fitting parameters allowed us to extrapolate the vortex melting lines down to the temperature of liquid hydrogen, and such extrapolation showed that  $\text{CaKFe}_4\text{As}_4$  is a very promising superconducting material for high field applications in liquid hydrogen, with a melting field at 20 K of the order of 100 T.

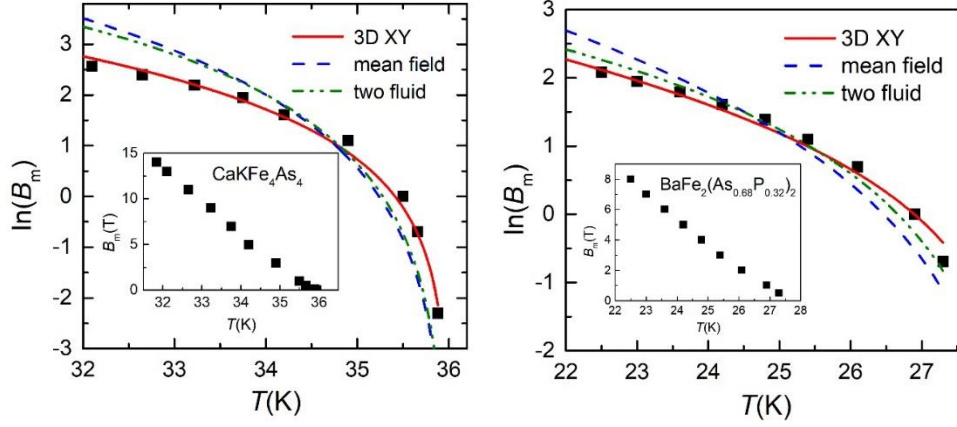


**Fig. 1** Temperature dependence of  $\ln(B_m)$  for the: (a)  $\text{CaKFe}_4\text{As}_4$  single crystal; and (b)  $\text{BaFe}_2(\text{As}_{0.68}\text{P}_{0.32})_2$  single crystal. Lines represent the fit with the two-fluid, mean field and 3D XY models of the temperature dependence of penetration depth. Inserts show the same experimental data presented as  $B_m(T)$ . Inserts show the experimental data in normal scale, melting field  $B_m$  as function of temperature  $T$ .

(ii) *Pinning potential and critical current density in  $\text{CaKFe}_4\text{As}_4$*

We have performed DC magnetization relaxation and frequency-dependent AC susceptibility measurements on high-quality single crystals of  $\text{CaKFe}_4\text{As}_4$  with the aim of determining the pinning potential  $U^*$  [2]. The magnetization relaxation curves  $m_{\text{irr}}(t) \propto J(t)$  lead to a normalized relaxation rate  $S = -\text{dln}(|m_{\text{irr}}|)/\text{dln}(t) = -\text{dln}(J)/\text{dln}(t)$  and a normalized pinning potential  $U^* = T/S$ , shown in Fig. 2 (left) while the dependence of  $\ln(U^*)$  on  $\ln(1/m_{\text{av}}) = \ln(1/J_{\text{av}})$  taken from the experimental data for each temperature, shown in Fig. 2 (right), allow the distinction between elastic creep and plastic creep, and the determination of the creep exponents.

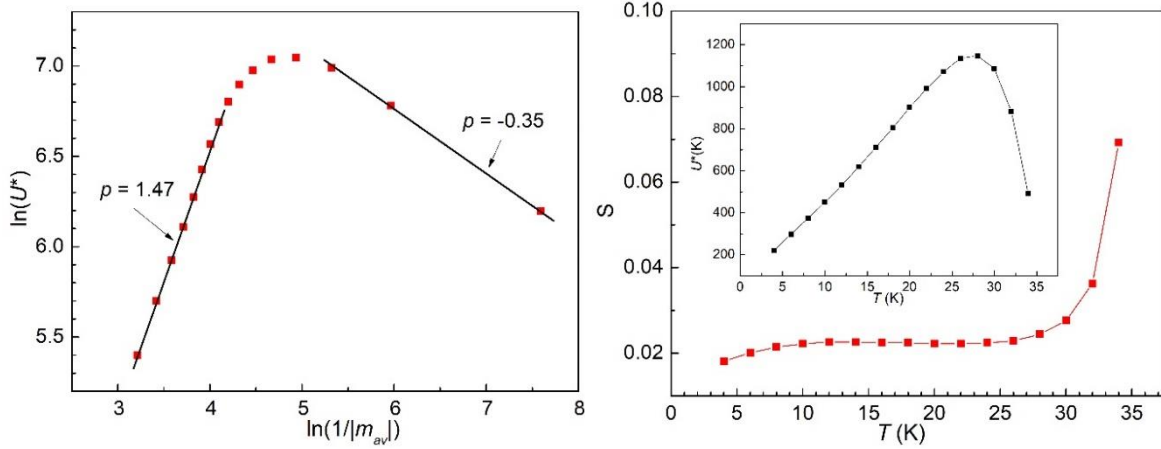


**Fig. 2 (left)** Dependence of the normalized relaxation rate  $S = -\text{dln}(|m|)/\text{dln}(t)$  on the temperature, for the 1 DC magnetic field of 1 T. Insert: Temperature dependence of the normalized pinning potential. **(right)** Double logarithmic plot of the normalized pinning potential  $U^*$  as a function of the inverse of irreversible magnetization, averaged logarithmically over the measurement time, for the DC field of 1 T.

The temperature dependence of  $U^*$  display a clear crossover between elastic creep and plastic creep. At temperatures around 27 – 28 K  $U^*$  has a very high value, up to 1200 K, resulting in a probability of thermally-activated flux jumps infinitesimally small. From the dependence of the normalized pinning potential on the irreversible magnetization we have determined the creep exponents in the two creep regimes which are in complete agreement with theoretical models. The estimation of the pinning potential from multi-frequency AC susceptibility measurements was possible only near the critical temperature due to equipment limitation, and the resulting value is very close to the one resulted from the magnetization relaxation data.

We have performed magnetization hysteresis measurements to determine the field dependence of the irreversible magnetization, at various temperatures [2]. From the irreversible magnetization  $\Delta m(H)$

data we can estimate the critical current density as function of temperature and field, using the modified Bean critical state model, with the resulted 3D plots of  $J_c(T,H)$  shown in Fig. 3.

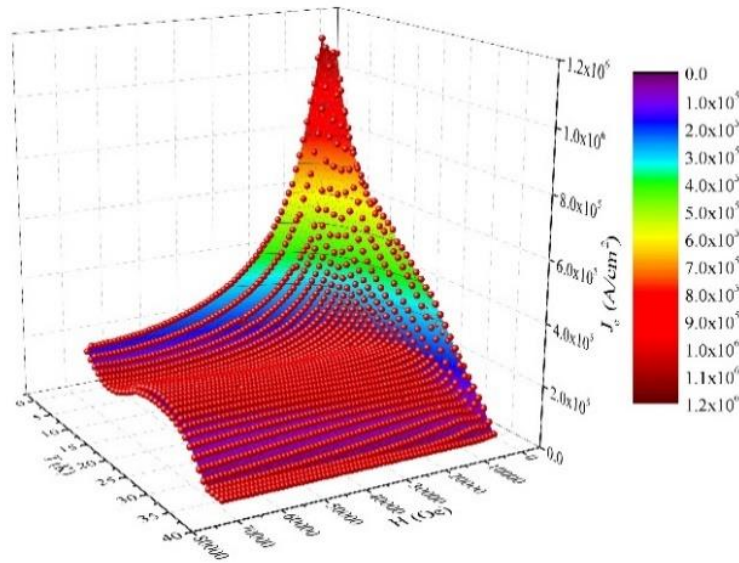


**Fig. 3** Three-dimensional plot of the field and temperature dependence of the critical current density.

(iii) *Demagnetization effects in Fe(Se<sub>0.5</sub>Te<sub>0.5</sub>) single crystal*

The effect of the demagnetizing factor, regarding the determination of the de-pairing current density  $J_{dep}$ , has been studied in the case of a Fe(Se,Te) crystal [3], using DC magnetic measurements as a function of a magnetic field ( $H$ ) at different temperatures ( $T$ ). First, the lower critical field  $H_{c1}$  (T) values were obtained, and the demagnetization effects acting on them were investigated after calculating the demagnetizing factor. The temperature behaviors of both the original  $H_{c1}$  values and the ones obtained after considering the demagnetization effects ( $H_{c1}^{demag}$ ) were analyzed, and the temperature dependence of the London penetration depth  $\lambda_L(T)$  was obtained in both cases, then fitted with a power law dependence, indicating the presence of low-energy quasiparticle excitations. Furthermore, by plotting  $\lambda_L^{-2}$  as a function of  $T$ , we found that our sample behaves as a multigap superconductor, which is similar to other Fe-11 family iron-based compounds. After that, the coherence length  $\xi$  values were extracted, starting with the  $H_{c2}(T)$  curve. The knowledge of  $\lambda_L$  and  $\xi$  allowed us to determine the  $J_{dep}$  values and to observe how they are influenced by the demagnetizing factor.

*References*

1. I. Ivan, A.M. Ionescu, D.N. Crisan, A. Crisan, "Vortex Glass-Vortex Liquid Transition in BaFe<sub>2</sub>(As<sub>1-x</sub>P<sub>x</sub>)<sub>2</sub> and CaKFe<sub>4</sub>As<sub>4</sub> Superconductors from Multi-Harmonic AC Magnetic Susceptibility Studies", *International Journal of Molecular Sciences* 24, 7896 (2023).
2. A.M. Ionescu, I. Ivan, C.F. Miclea, *et al.*, "Vortex Dynamics and Pinning in CaKFe<sub>4</sub>As<sub>4</sub> Single Crystals from DC Magnetization Relaxation and AC Susceptibility", *Condensed Matter* 8, 93 (2023).
3. A. Galluzzi, K. Buchkov, V. Tomov, *et al.*, "The Depairing Current Density of a Fe(Se,Te) Crystal Evaluated in Presence of Demagnetizing Factors", *Condensed Matter* 8, 91 (2023).

# Surface Energetic Landscape of Thin Ferroelectric Pb(Zr,Ti)O<sub>3</sub>(001) Single Crystals: The Case of a “Dirty” Surface in Ultra High Vacuum

L.E. Abramiuc <sup>a</sup>, L.C. Tanase <sup>a,b</sup>, M.J. Prieto <sup>b</sup>, L. de Souza Caldas <sup>b</sup>, A. Tiwari <sup>b</sup>, N.G. Apostol <sup>a</sup>, M.A. Husanu <sup>a</sup>, C.F. Chirila <sup>a</sup>, L. Trupina <sup>a</sup>, T. Schmidt <sup>b</sup>, L. Pintilie <sup>a</sup>, C.M. Teodorescu <sup>a</sup>

<sup>a</sup> National Institute of Materials Physics, 077125 Magurele, Romania

<sup>b</sup> Department of Interface Science, Fritz-Haber Institute of the Max Planck Society, 14195 Berlin, Germany.

Ferroelectrics (FE) are a class of materials which exhibit spontaneous bulk polarization in the absence of an external field [1]. The perpendicular component of the FE polarization can induce polarization-dependent charges on the surface, under the influence of the depolarization field, changing their surface chemistry [2]. The origin of the charge accumulated at the surface of a film could be typically the charge carriers produced by doping, ionized impurities, metal contacts or air contaminants [3]. Using low energy/minor electron microscopy (LEEM/MEM) combining with photoemission electron microscopy (PEEM) and high-resolution X-ray photoelectron spectroscopy (HRXPS) a significant extrinsic negative compensation charge was proven to accumulate on a surface of a thin ferroelectric lead zirconate titanate (PZT) exhibiting outward polarization [4] if we compare it with values measured on other systems in the same experimental setup [5–7], or to previous reports on FE surfaces [8–10].

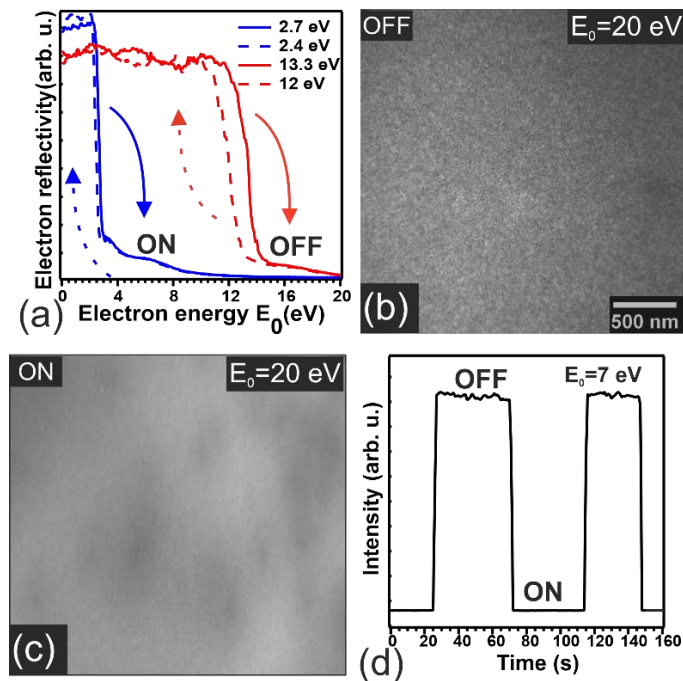


**Fig. 1** X-ray ( $h\nu = 215$  eV) induced screening in a fresh area of Pb(Zr,Ti)O<sub>3</sub> sample (with thickness of 100 nm prepared by pulsed laser deposition on (3–10 nm) SrRuO<sub>3</sub> – buffered SrTiO<sub>3</sub>(001) substrates). **(a)** LEEM I–V curves recorded by increasing and decreasing  $E_0$  (incident electron energy), in the absence (OFF, red) or presence (ON, blue) of X-rays.

The MEM–LEEM transition values are indicated as legends. **(b)** and **(c)** LEEM contrast intensity ( $E_0 = 20$  eV) as a function of X-ray irradiation. **(d)** LEEM/MEM intensity variation in the presence or absence of X-ray exposure ( $E_0 = 7$  eV). Time scale in **(d)** represents the exposure time with  $E_0 = 7$  eV. Adapted from Ref. [4].

Unusual high values of the reflectivity curve (MEM–LEEM transition) of 13.3 eV were detected on “fresh areas” correlated with a surface potential energy of about 10.3 eV which could be decreased by longer electron exposure or by soft X-rays through ejection of secondary electrons and generation of positive charge under the surface. In this study, we have demonstrated that the polar state extracted from piezoresponse force microscopy (PFM) measurements is directly linked not only to the observed band bending in XPS spectra but also to the accumulation of charge on the surface layer due to inherent contamination. Analysis of the PFM data reveals an outward polarization within the layer, indicating negative charge accumulation outside the surface, which in turn influences the trajectories

and energetics of incoming electrons. Furthermore, additional charge redistribution is evidenced by local fluctuations in LEEM images and the shift of the C 1s core level towards lower binding energies, indicating that carbon clusters on the surface can acquire negative charge upon X-ray exposure without affecting the position of the main surface core level peaks, and thus not altering the surface band bending, at least initially after X-ray irradiation.

#### References

1. D. Pravarthana, J. Wei, B. Wang, *et al.*, “Crystal Orientations Dependent Polarization Reversal in Ferroelectric  $\text{PbZr}_{0.2}\text{Ti}_{0.8}\text{O}_3$  Thin Films for Multilevel Data Storage Applications”, *Advanced Materials Interfaces* 8, 2100871 (2021).
2. L.E. Ștoflea, N.G. Apostol, L. Trupină, C.M. Teodorescu, “Selective Adsorption of Contaminants on  $\text{Pb}(\text{Zr,Ti})\text{O}_3$  Surfaces Shown by X-ray Photoelectron Spectroscopy”, *Journal of Materials Chemistry A* 2, 14386–14392 (2014).
3. L. Pintilie, C. Ghica, C.M. Teodorescu, *et al.*, “Polarization Induced Self-Doping in Epitaxial  $\text{Pb}(\text{Zr}_{0.20}\text{Ti}_{0.80})\text{O}_3$  Thin Films”, *Scientific Reports* 5, 14974 (2015).
4. L.E. Abramiuc, L.C. Tanase, M.J. Prieto, *et al.*, “Surface Charge Dynamics on Air-exposed Ferroelectric  $\text{Pb}(\text{Zr,Ti})\text{O}_3(001)$  Thin Films”, *Nanoscale* 15, 13062–13075 (2023).
5. S. Kunze, L.C. Tanase, M.J. Prieto, *et al.*, “Plasma-assisted Oxidation of  $\text{Cu}(100)$  and  $\text{Cu}(111)$ ”, *Chemical Science* 12, 14241–14253 (2021).
6. M.J. Prieto, H.W. Klemm, F. Xiong, *et al.*, “Water Formation under Silica Thin Films: Real-Time Observation of a Chemical Reaction in a Physically Confined Space”, *Angewandte Chemie International Edition* 57, 8749–8753 (2018).
7. H.W. Klemm, M.J. Prieto, G. Peschel, *et al.*, “Formation and Evolution of Ultrathin Silica Polymorphs on  $\text{Ru}(0001)$  Studied with Combined In Situ, Real-Time Methods”, *The Journal of Physical Chemistry C* 123, 8228–8243 (2018).
8. N. Barrett, J.E. Rault, J. L. Wang, *et al.*, “Full Field Electron Spectromicroscopy Applied to Ferroelectric Materials”, *Journal of Applied Physics* 113, 187217 (2013).
9. I. Krug, N. Barrett, A. Petraru, *et al.*, “Extrinsic Screening of Ferroelectric Domains in  $\text{Pb}(\text{Zr}_{0.48}\text{Ti}_{0.52})\text{O}_3$ ”, *Applied Physics Letters* 97, 222903 (2010).
10. M. Lachheb, Q. Zhu, S. Fusil, *et al.*, “Surface and Bulk Ferroelectric Phase Transition in Super-Tetragonal  $\text{BiFeO}_3$  Thin Films”, *Physical Review Materials* 5, 024410 (2021).

# Single-step Continuous Hydrothermal Flow Synthesis of Visible Light Active, Efficient [Nano-TiO<sub>2</sub>-NCQDs-rGO] Hybrid Photocatalysts

I.-A. Baragau <sup>a,b</sup>, J. Buckeridge <sup>a</sup>, K.G. Nguyen, <sup>a</sup> T. Heil <sup>c</sup>, M. Tariq Sajjad <sup>a</sup>, S.A.J. Thomson <sup>d</sup>, A. Rennie <sup>d</sup>, D.J. Morgan <sup>e</sup>, N.P. Power <sup>f</sup>, S.A. Nicolae <sup>b,g</sup>, M.M. Titirici <sup>h</sup>, S. Dunn, <sup>a</sup> S. Kellici<sup>a</sup>

<sup>a</sup>School of Engineering, London South Bank University, London, SE1 0AA, United Kingdom

<sup>b</sup>National Institute of Materials Physics, 077125 Magurele, Romania.

<sup>c</sup>Department of Colloid Chemistry, Max Planck Institute of Colloids and Interfaces, 14476 Potsdam, Germany.

<sup>d</sup>Edinburgh Instruments Ltd, Livingston, EH54 7DQ, UK.

<sup>e</sup>Cardiff Catalysis Institute, School of Chemistry, Cardiff University, Cardiff, CF10 3AT, United Kingdom

<sup>f</sup>School of Life Health & Chemical Sciences, The Open University, Milton Keynes, MK7 6AA, United Kingdom.

<sup>g</sup>School of Engineering and Materials Science, Queen Mary University of London, London E1 4NS, United Kingdom

<sup>h</sup>Department of Chemical Engineering, Imperial College, South Kensington, London, SW7 2AZ, United Kingdom

Titanium dioxide (TiO<sub>2</sub>) is one of the most extensively explored and engineered photocatalysts[1], having real-life applications and being commercially available worldwide in plenty of products[2] (inks, paints, construction materials, cosmetics, solar cells, *etc*). TiO<sub>2</sub> photocatalysts suffer from a large bandgap (~3.2 eV anatase and ~3 eV rutile) and fast charge recombination.[3] In this study[4], we reported the use of green, rapid, single-step continuous hydrothermal flow synthesis for the preparation of TiO<sub>2</sub> and TiO<sub>2</sub> nanocomposites with reduced graphene oxide (rGO) and/or nitrogen-doped carbon quantum dots (NCQDs) with a significant improvement in their photocatalytic activity. Continuous hydrothermal flow synthesis enabled the rapid and efficient production of homogeneous nano-TiO<sub>2</sub> hybrid composites with nitrogen-doped carbon quantum dots and/or reduced graphene oxide with outstanding photocatalytic activities (see Fig. 1a– e). TiO<sub>2</sub> particles exhibited a particle size of <5 nm, high crystallinity (anatase form) and large surface area (typically >232 m<sup>2</sup> g<sup>-1</sup>). NCQDs showed spherical morphology (mean particle size *ca.* 3.4 nm) with a graphitic core arrangement, and the graphene (rGO) sheets consisted of 5–8 layers.

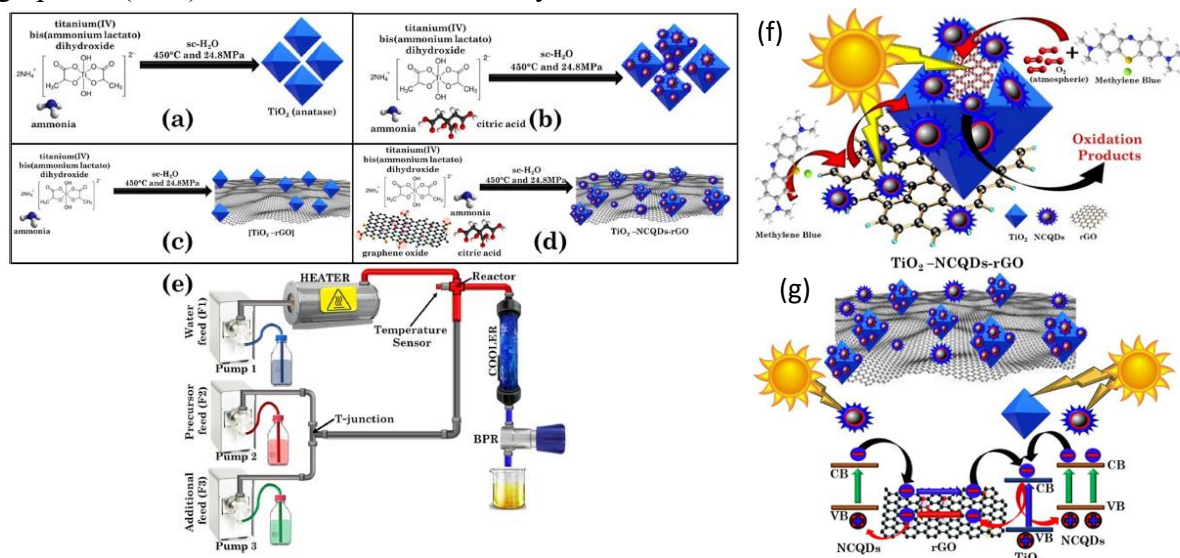


**Fig. 1** Continuous hydrothermal flow synthesis (CHFS) process detailing the synthetic protocols for (a–d) production of TiO<sub>2</sub> and its nanocomposites with reduced graphene oxide (rGO) and/or nitrogen-doped carbon quantum dots (NCQDs), (e) simplified representation of the CHFS reactor and (f) and (g) the mechanism of the photocatalytic process which takes place between methylene blue and TiO<sub>2</sub>-NCQDs-rGO hybrid nanocomposite.

By using a solar light generator under ambient conditions with no extra oxygen gas added, we observed the evolution reaction of the methylene blue photodegradation in real time. Tailoring of the light absorption to match that of the solar spectrum was achieved by a combination of materials of nano-TiO<sub>2</sub> hybrids of nitrogen-doped carbon quantum dots and graphene in its reduced form with a

photocatalytic rate constant of  $ca. 25 \times 10^{-5} \text{ s}^{-1}$ . The highlight of the  $\text{TiO}_2$  hybrid nanocomposites' remarkable photocatalytic activity was  $\text{TiO}_2\text{-NCQDs-rGO}$  providing 93% conversion of methylene blue with a 6-fold photocatalytic rate enhancement ( $25.24 \times 10^{-5} \text{ s}^{-1}$ ) over that of  $\text{TiO}_2$  alone under solar light simulation was facilitated by longer emission lifetimes (6.13 ns), faster charge transfer rates ( $2.6 \times 10^8 \text{ s}^{-1}$ ), and a narrowed band gap. Changes in the bandgap are supported by hybrid DFT calculations based on a model system that indicated a shift in band edges to a more favourable alignment between anatase and graphene, and recombination would be suppressed. The combination of these two effects accounts for the considerable improvement in photocatalytic performance identified for the  $\text{TiO}_2\text{-rGO}$  example (emission lifetime, 3.15 ns and charge transfer rate,  $1.0 \times 10^8 \text{ s}^{-1}$ ). The model proposed for  $\text{TiO}_2\text{-NCQDs-rGO}$  would also incorporate this, facilitated by NCQDs, further increasing the photosensitivity, the emission lifetimes and charge transfer rates via multilevel electron transfer, thus significantly enhancing photocatalytic activity (see Fig. 1f–g).

Using a diversity of state-of-the-art techniques, including high-resolution transmission electron microscopy, transient photoluminescence, X-ray photoelectron spectroscopy and high accuracy, sophisticated hybrid density functional theory calculations this study gained substantial insight into the charge transfer and modulation of the energy band edges of anatase due to the presence of graphene or carbon dots, parameters which play a crucial role in improving drastically the photocatalytic efficiencies when compared to pristine titania.

More importantly, the study proves that a combination of features and materials displays the best photocatalytic behaviour. This performance is delivered in a greener synthetic process that produces photocatalytic materials with optimised properties and tailored visible light absorption and efficiency and provides a path to industrialisation.

The Journal of Materials Chemistry A awarded the paper an internal cover (see Fig. 2) to acknowledge the relevance of research, synthetic methodology and environmental application perspectives.

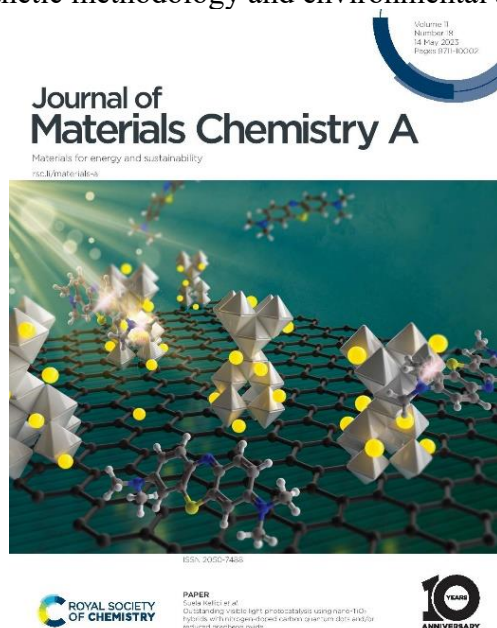


**Fig. 2** The Journal of Materials Chemistry A's internal cover awarded to this study.

### References

1. D. Chen, Y. Cheng, N. Zhou, *et al.*, "Photocatalytic Degradation of Organic Pollutants Using  $\text{TiO}_2$ -based Photocatalysts: A Review", *Journal of Cleaner Production* 268, 121725 (2020).
2. T. Ayorinde, C.M. Sayes, "An Updated Review of Industrially Relevant Titanium Dioxide and its Environmental Health Effects", *Journal of Hazardous Materials Letters* 4, 100085 (2023).
3. R. Qian, H. Zong, J. Schneider, *et al.*, "Charge Carrier Trapping, Recombination and Transfer During  $\text{TiO}_2$  photocatalysis: An Overview", *Catalysis Today* 335, 78–90 (2019).
4. I.-A. Baragau, J. Buckridge, K.G. Nguyen, *et al.*, "Outstanding Visible Light Photocatalysis Using Nano- $\text{TiO}_2$  hybrids with Nitrogen-Doped Carbon Quantum Dots and/or Reduced Graphene Oxide", *Journal of Materials Chemistry A* 11, 9791–9806 (2023).

# Topological Phase Transitions in Graphene Induced by Circularly Polarized Light and Magnetic Field

A. Pena

National Institute of Materials Physics, 077125 Magurele, Romania,

Topological insulators (TIs) [1,2] are special materials which behave as common insulators in their bulk, while at the surfaces (edges), they host conduction states. The *dimensionality* and *symmetries* of these materials play a fundamental role in the underlying physics of the topological phase transitions. In the realm of 2D systems, the Chern insulators represent a very important class. These TIs present time reversal symmetry (TRS) and by breaking it, a topological phase is induced. Otherwise, the system remains in the trivial (non-topological) phase. Moreover, TIs which undergo a phase transition as a result of TRS breaking caused by a time periodic process are called Floquet topological insulators (FTIs), given that their physics is modeled within the Floquet framework. The iconic (literally) 2D TI is graphene [3,4]. In 1988, Haldane elaborated a model for TRS breaking in graphene based on imaginary hopping parameters [5]. In recent years, it was observed that circularly polarized light triggers in graphene exactly the Haldane's mechanism [6]. Thus, the interaction of a Chern insulator with circularly polarized light induces a topological phase transition.

Besides light, it is well-known that a magnetic field breaks the TRS, giving rise to Quantum Hall effect. Since both interactions induce topological phases, it is worth studying the behavior of a Chern insulator in the presence of their combination. Schematically, the system is depicted in Fig. 1.

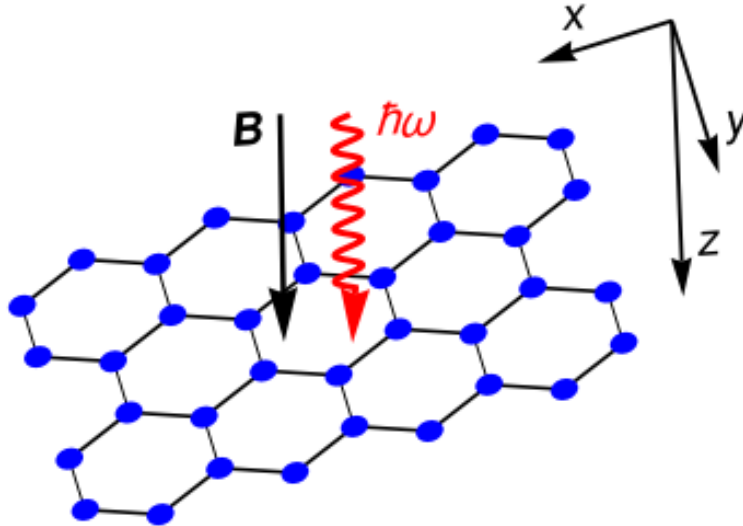


**Fig 1** The sketch of the studied system. The graphene sheet is placed on the horizontal  $xy$ -plane, while the magnetic field ( $\mathbf{B}$ ) and the light ( $\hbar\omega$ ) are applied on the vertical  $z$ -direction. Reproduced from Ref. [7].

A topological phase signature is revealed in the energy dispersion. When the light irradiation is present and the FTI lies in its topological phase, in a ribbon, there arises a band gap which hosts so-called *chiral edge states*, namely electronic quantum states localized at the edges of the ribbon, having opposed momentum orientations. In this way, at the edges, two conduction channels will arise, transporting charge in opposite directions, activating the Hall conduction. In Fig. 2 (left panel), such a specific dispersion is depicted. As one may see, inside the quasienergy gap, there are present two crossed bands, being actually the chiral edge states. Graphene structure may be seen as formed by two sublattices, each of them containing one atom type, as depicted in the inset (blue or A and red or B). In a topological phase, the chiral bands are sublattice polarized. In our case, inside the gap, the A states have a positive momentum direction, while B states, a negative one. In the present example, the light helicity is  $\Lambda = 1$ . Thus, in this topological phase, one may measure a non-zero Hall resistance ( $R_H$ ). In the right panel, such a simulation is presented, showing  $R_H$  vs.  $A_0$  which represents a measure of light intensity. Thus, the formation of the specific resistance plateaus is clearly visible. Moreover,

when the light helicity is reversed ( $\Lambda = -1$ ), the particles chirality is also reversed, changing the  $R_H$  sign. As well, it was observed that each topological phase transition ( $R_H$  value switching from non-zero to zero) is encountered in a zero of the first order Bessel functions  $J_0(A_0)$  and  $J_1(A_0)$ .

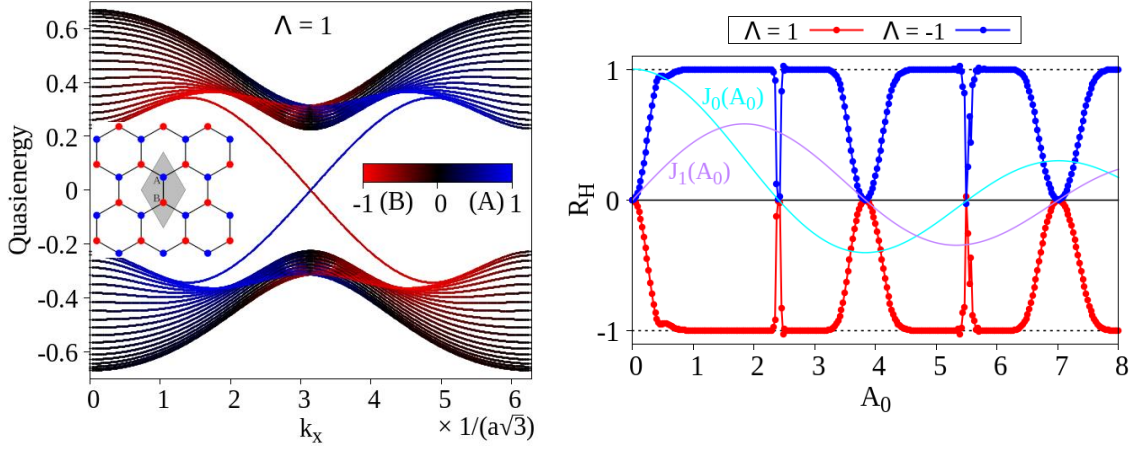


**Fig. 2** Topological signatures of circularly polarized light irradiated graphene. **Left:** quasienergy dispersion in the case of a topological phase. **Right:** Hall transport simulation showing  $R_H$  vs.  $A_0$ . Reproduced from Ref. [7].

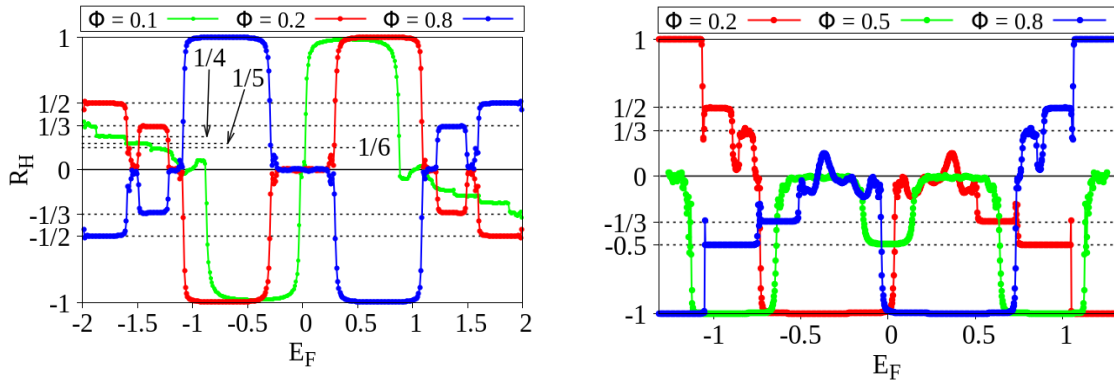


**Fig 3** Hall transport for different values of the magnetic field flux  $\Phi$ . **Left:**  $R_H$  vs.  $E_F$  in the absence of light irradiation. **Right:**  $R_H$  vs.  $E_F$  in the presence of light irradiation. Reproduced from Ref. [7].

Going further, when applying a combination of magnetic field and circularly polarized light, the topological properties of the system become more intricate and this will reflect in the Hall transport. A simulation is presented in Fig. 3 which illustrates the  $R_H$  values vs. Fermi level  $E_F$ , for three magnetic flux values  $\phi$ , as indicated on each plot. The left panel shows  $R_H$  in the absence of light irradiation, while the right one, when the light is switched on. The first observed effect is that the Hall effect is activated also for  $\phi = 0.5$ , which in the absence of light, it is absent. Second, comparing the blue curves ( $\phi = 0.8$ ), we observe that the light irradiation moves the position of the specific  $R_H$  plateaus and introduces or removes some of them. Third, the light irradiation breaks the symmetry of  $R_H$  curve with respect to  $E_F = 0$ , which in the absence of light is present, as may be observed in the left panel.

All the results presented above are obtained for the case of a non-resonant regime, namely when the processes of absorption and/or emission of photons by the charged particles are suppressed. This condition is achieved whenever the photon energy  $\hbar\omega$  is higher than the band width of the quasienergy spectrum. However, when the interaction becomes resonant, inside the quasienergy band gap arise more pairs of chiral bands.

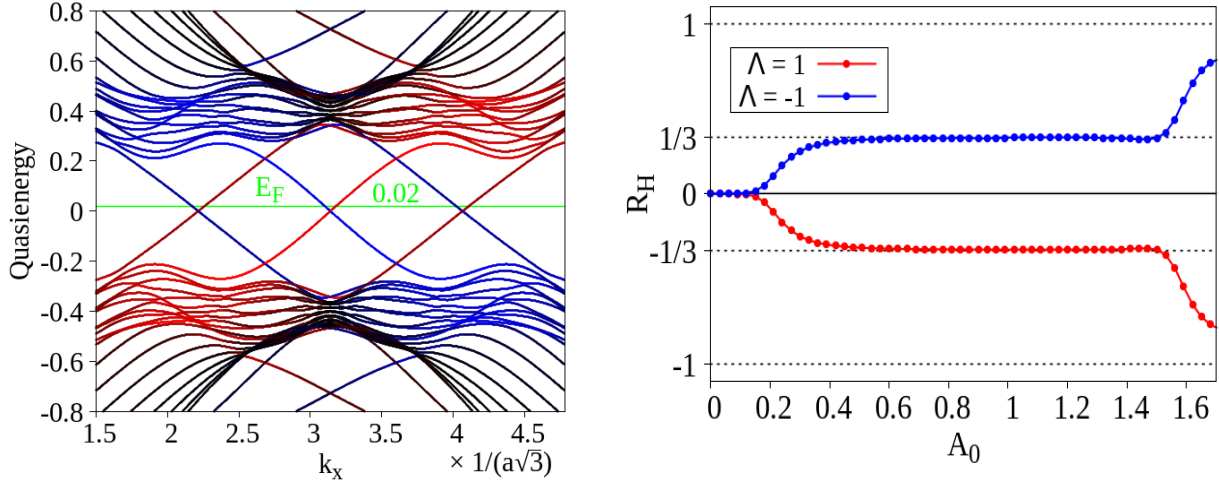


**Fig. 4** The case of a resonant interaction regime. **Left:** quasi energy dispersion. **Right:**  $R_H$  vs.  $A_0$ . Reproduced from Ref. [7].

In Fig. 4 (left panel), we show the quasienergy dispersion for the case of a resonant regime. In this case, inside the topological gap, three pairs of chiral bands arise. Consequently, in a Hall transport experiment, one must measure a Hall resistance value of  $R_H = \pm 1/3$ , as shown in the right panel.

#### References

1. J. Moore, “The Birth of Topological Insulators”, *Nature* 464, 194–198 (2010).
2. F. Duncan, M. Haldane, “Nobel Lecture: Topological Quantum Matter”, *Reviews of Modern Physics* 89, 040502 (2017).
3. A.H. Castro Neto, F. Guinea, N.M.R. Peres, et al., “The Electronic Properties of Graphene”, *Reviews of Modern Physics* 81, 109 (2009).
4. K.S. Novoselov, “Nobel Lecture: Graphene: Materials in the Flatland”, *Reviews of Modern Physics* 83, 837 (2011).
5. F.D.M. Haldane, “Model for a Quantum Hall Effect without Landau Levels: Condensed-Matter Realization of the “Parity Anomaly”, *Physical Review Letters* 61, 2015 (1988).
6. T. Mikami, S. Kitamura, K. Yasuda, et al., “Brillouin-Wigner Theory for High-Frequency Expansion in Periodically Driven Systems: Application to Floquet Topological Insulators”, *Physical Review B* 93, 144307 (2016).
7. A. Pena, “Control of Spectral, Topological and Charge Transport Properties of Graphene via Circularly Polarized Light and Magnetic Field”, *Results in Physics* 46, 106257 (2023).

# One- and Two-Dimensional Ferromagnetic Domains, Including Effects on Magnetic Hysteresis Curves

**C.M. Teodorescu**

National Institute of Materials Physics, 077125 Magurele, Romania

Magnetic domain dynamics are the most reasonable origin of the shape and characteristic quantities of magnetic hysteresis, in particular it is a reasonable explanation for the low coercive field in soft metals along the easy magnetization axis. The venerable Kittel's theory of ferromagnetic domains developed by the end of 1940s [1,2] is still a cornerstone of micromagnetism and it is remarkable by its simplicity. The model considers ferromagnetic domains as infinitely parallel stripes of width  $l$ , the film thickness being  $d$ , with the magnetization oriented perpendicular to the film. Then one estimates the energy per unit area on a plane perpendicular to the magnetization, separated into two terms. The first one is called the 'bulk' term and it scales with  $l$  times a volume density of energy. The second is a term due to the energy of the domain walls and (per unit area) it scales with the ratio  $d/l$ . Minimizing the sum of these two terms one obtains the well-known proportionality  $l \propto d^{1/2}$ . Kittel's theory is valid for the case of thick samples, *i.e.* for  $l \ll d$ ; however, nowadays many experiments and applications involve thin magnetic films with uniaxial anisotropy, and the extension of the domain theory to such samples was still lacking. Also, although domain wall migration is supposed to be intrinsically connected with the shapes of magnetic hysteresis curves, to date very few works dealt with this aspect [3].

Kittel's theory is revised in Ref. [4], with a more detailed demonstration and emphasizing the main assumptions utilized. The wall energy density is written in terms of the physical parameters of the sample (the uniaxial magnetic anisotropy energy density  $K_v$  and the exchange integral  $J$ ). The validity limits of the Kittel's scaling law is derived, with the possibility of evolution towards large domains for ultralow thicknesses. The equation governing the domain size is:

$$\frac{d_0}{d} = \left(\frac{l}{d}\right)^2 \sum_{m=0}^{\infty} \frac{1 - \exp\{-(2m+1)\pi d/l\}}{(2m+1)^3} - \pi \left(\frac{l}{d}\right) \sum_{m=0}^{\infty} \frac{\exp\{-(2m+1)\pi d/l\}}{(2m+1)^2} \equiv \eta_0 \left(\frac{d}{l}\right)$$

(1)

where  $d_0$  is a 'scaling size' which captures all involved material parameters:

$$d_0 = \frac{w_{\text{wall}}}{w_0} = \frac{\pi^3 w_{\text{wall}}}{4\mu_0 M_0^2} = \frac{\pi^4 S}{4\mu_0 M_0^2} \left(\frac{2JK_v}{a}\right)^{1/2} = \frac{\pi^4 (2JK_v a^{11})^{1/2}}{16S\mu_0 \mu_B^2}$$

(2)

where  $w_{\text{wall}}$  is the Bloch wall's surface energy density,  $w_0 = 4\mu_0 M_0^2 / \pi^3$ ,  $M_0$  is the saturation magnetization,  $\mu_0$  the vacuum permeability,  $M_0 = 2S\mu_B a^{-3}$  with  $S$  the atomic spin,  $\mu_B$  the Bohr magneton and  $a$  the lattice constant (for simplicity, the structure was supposed simple cubic). For  $a \approx 0.25$  nm,  $J \approx 10$  meV,  $K_v \approx 4 \times 10^5$  erg cm<sup>-3</sup>  $\approx 2$   $\mu$ eV/atom,  $S \approx 1$  one obtains  $d_0 \approx 10$  nm. From eq. (1) it follows that  $d/l = \eta_0^{-1}(d_0/d)$  and these solutions are represented in Fig. 1, insert (i<sub>1</sub>). From here, one may derive numerically the dependence  $l/d_0$  vs.  $d/d_0$ , which is represented in Fig. 1, the main panel. It is also easy to derive that for large sample thickness one retrieves the Kittel's scaling law, since one obtains from eq. (1)  $d_0/d = S_3(l/d)^2$  with  $S_3 = \sum_{m \geq 0} (2m+1)^{-3} \approx 1.0518$ .

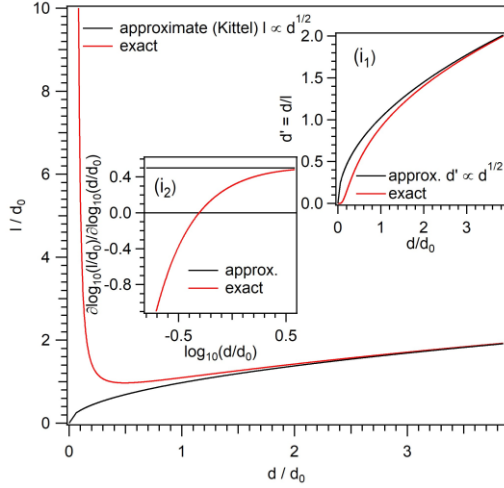


**Fig. 1** Dependence of the domain size of the sample thickness, in the model considering the finite sample thickness. Red curve: exact solutions of eq. (1). Black curve: Kittel's approximate scaling law. Insert (i<sub>1</sub>): solutions of the equation (1), compared with solutions for  $d/l \gg 1$ . Insert (i<sub>2</sub>): derivation of the exponent  $\gamma$  (locally  $l \propto d^\gamma$ ) from the derivation of the logarithmic dependence  $\log(l/d_0)$  vs.  $\log(d/d_0)$ .

For  $d/d_0 \lesssim 1$ , there are deviations from Kittel's „1/2” scaling law, up to the reversing of the sign of the exponent (Fig. 1(i<sub>2</sub>)). For low sample thickness, the domain width becomes very large.

Further, Kittel's model is extended to the case where the sample has a non-vanishing net magnetization and it is shown how magnetization curves at zero temperature can be obtained. This is discussed by supposing constant width of a pair of neighboring domains with opposed magnetization, or by allowing this width to vary as function on the net magnetization of the sample. Though this latter assumption seems to be more reasonable from the point of view of the evolution towards a single domain state at saturation, it seems that the model able to yield most accurate (i. e. smaller) values of the coercive field is the domain with fixed width of the pair of domains, which justifies the assumption of „domain wall pinning”. The introduction of the demagnetization factor  $D$  associated with the finite size of the film yields a maximum thickness up to which the films present hysteresis curves. Also, the demagnetization field precludes the occurrence of hysteresis for thick samples. The validity of this theory for ferroelectric domains is also briefly discussed.

In Ref. [5], the above study is extended to samples featuring two-dimensional domain landscapes, for materials with strong magnetic anisotropy, typically characterized by a superunitary ratio between the anisotropy energy and the stray field energy densities. For two-dimensional films with perpendicular magnetic anisotropy, the most stable structure for null average magnetization is found to be that with domains infinitely elongated along one in-plane direction, i. e. the one-dimensional case treated in Ref. [4]. The equivalent of eq. (1) for the two-dimensional case is:

$$\frac{d_0}{d} = \frac{4}{\pi^2} \left(\frac{l}{d}\right)^2 \sum_{n,m=0}^{\infty} \frac{1 - \exp\left\{-\pi[(2m+1)^2 + (2n+1)^2]^{1/2} d/l\right\}}{(2m+1)^2(2n+1)^2\{(2m+1)^2 + (2n+1)^2\}^{1/2}} - \frac{4}{\pi} \left(\frac{l}{d}\right) \sum_{n,m=0}^{\infty} \frac{\exp\left\{-\pi[(2m+1)^2 + (2n+1)^2]^{1/2} d/l\right\}}{(2m+1)^2(2n+1)^2}$$

(3)

For thin stripes with in-plane magnetization, the domain size  $l$  is approximately linear with the stripe lateral size  $d$  for low film thickness, while for large film thicknesses it follows a Kittel-like law, but as function of the stripe size  $l \sim d^{1/2}$ . For in-plane magnetized thin films of infinite lateral extent, the most stable structure is the single domain.

As for hysteresis curves, the two-dimensional case with perpendicular magnetic anisotropy is shown to evolve from a 2D landscape derived from the checkerboard structure, but with unbalanced domains for magnetization near saturation, towards one-dimensional domain structures for lower magnetization, as shown in Fig. 2. In some cases, and depending also on the demagnetization factor, the one-dimensional case is not reached, and the film exhibit 2D structures on the whole range of the magnetization curve. The hysteresis obtained for thin magnetic stripes with in-plane magnetization also can exhibit a rich structure, with minor cycles on the wings of the magnetization curves evolving

towards „normal” hysteresis (again, depending on the film thickness, stripe lateral size and demagnetization factor), see Fig. 3. An infinite thin film with in-plane anisotropy features a steplike magnetization dependence on the applied field.

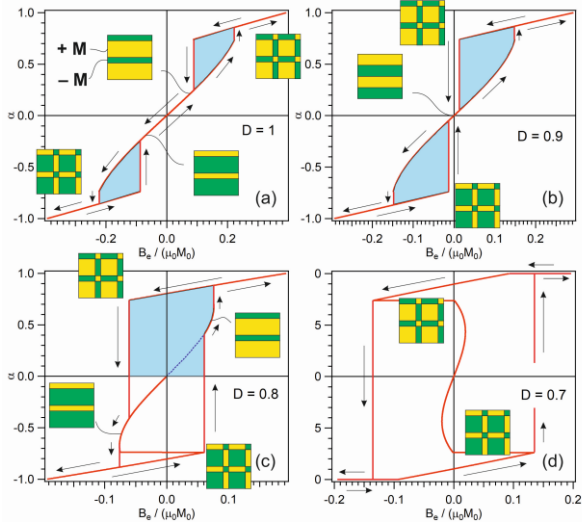


**Fig. 2** Magnetization curves obtained by derivation of the energy density for  $d/d_0 = 1$ , for different values of the demagnetization factor  $D$ . The arrows describe the sense of description of the hysteresis curves. The squares represent schemes of the domain topography corresponding to each branch of the hysteresis curve.

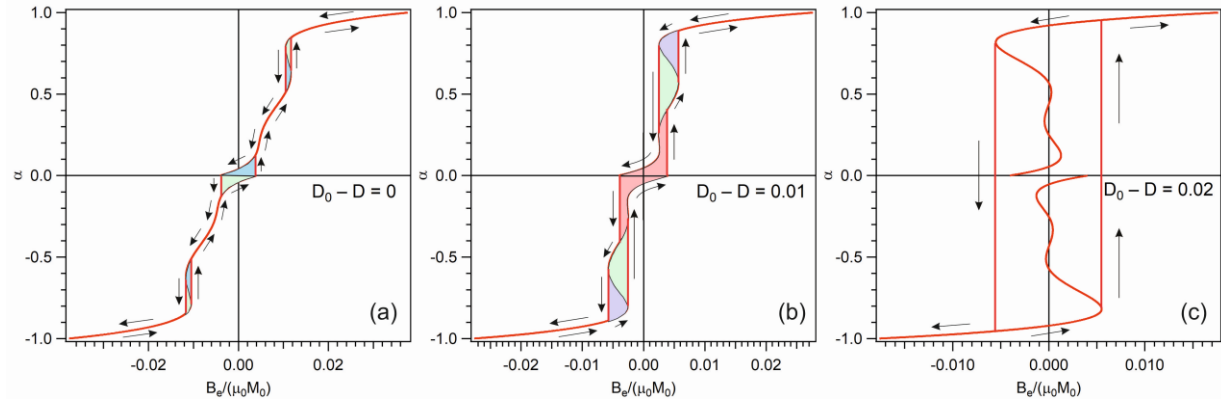


**Fig. 3** Examples of complete magnetization curves (for positive and negative branches) together with the derivation of the hysteretic behavior for in-plane magnetized films of thickness  $\Delta y = d_0$  and lateral size  $d = 10d_0$ , by introducing demagnetization factors slightly different from unity.

### References

1. C. Kittel, “Theory of The Structure of Ferromagnetic Domains in Films and Small Particles”, *Physical Review* 70, 965–971 (1946).
2. C. Kittel, “Physical Theory of Ferromagnetic Domains”, *Reviews of Modern Physics* 21, 541–583 (1949).
3. C. Kooy, U. Enz, “Experimental and Theoretical Study of the Domain Configuration in Thin Layers of  $\text{BaFe}_{12}\text{O}_{19}$ ”, *Philips Research Reports* 15, 7–29 (1960).
4. C.M. Teodorescu, “Kittel’s Model for Ferromagnetic Domains, Revised and Completed, Including the Derivation of the Magnetic Hysteresis”, *Results in Physics* 46, 106287 (2023).
5. C.M. Teodorescu, “Two Dimensional Landscape of Ferromagnetic Domains and the Resulting Magnetization Curves”, *Results in Physics* 54, 107109 (2023).

# Exploring Many-Body Topology with Multiparticle Quantum Walks in Strongly Interacting Systems

**B. Ostahie**<sup>a</sup>, **D. Sticlet**<sup>b</sup>, **C. Pascu Moca**<sup>c,d</sup>, **B. Dóra**<sup>c,e</sup>, **M.A. Werner**<sup>c,f</sup>, **J.K. Asbóth**<sup>c,g</sup>, **G. Zaránd**<sup>c,g</sup>

<sup>a</sup> National Institute of Materials Physics, 077125 Magurele, Romania

<sup>b</sup> National Institute for R&D of Isotopic and Molecular Technologies, 400293 Cluj-Napoca, Romania

<sup>c</sup> Department of Theoretical Physics, Institute of Physics, Budapest University of Technology and Economics, H-1111 Budapest, Hungary

<sup>d</sup> Department of Physics, University of Oradea, 410087 Oradea, Romania

<sup>e</sup> MTA-BME Lendület Topology and Correlation Research Group, H-1111 Budapest, Hungary

<sup>f</sup> MTA-BME Quantum Dynamics and Correlations Research Group, H-1111 Budapest, Hungary

<sup>g</sup> Institute for Solid State Physics and Optics, Wigner Research Centre for Physics, H-1525 Budapest, Hungary

The conventional understanding of phase transitions, typically associated with symmetry breaking and the emergence of a local order parameter, has expanded with the discovery of topological insulators. Unlike conventional materials, topological insulators lack a local order parameter and are characterized by various topological phases identified by topological invariants [1]. These invariants describe the topological nature of single-particle wave functions and are accompanied by robust low-energy features at the boundaries of the system. This understanding not only sheds light on the fundamental properties of matter but also holds promise for applications in quantum computation, quantum technologies, and spintronics.

While significant progress has been made in understanding noninteracting topological systems, research into analogous, strongly correlated systems has been slower. It remains unclear whether topology persists in the presence of strong interactions. Electron-electron interactions can lead to topological phase transitions, destabilizing single quadratic band crossings and inducing transitions from trivial to nontrivial phases. However, understanding the topology of these phases and distinguishing them from single-particle topological states remains challenging.

Establishing methods for characterizing interacting topological insulators is crucial. One promising approach is the quantized many-body Berry phase, which extends the underlying noninteracting Berry phase. However, experimental verification of these hypotheses in bulk systems is challenging.

The quench dynamics of quantum particles in single-particle quantum walks provide a simple and experimentally accessible means to probe topology. Recent experiments have revealed bound states at the interface of systems with different topological phases, allowing for the detection of topological invariants in cold atoms or nanophotonic topological lattices through mean chiral displacement (MCD) measurements [2]. While these measurements have been successful in noninteracting setups, experimental verification in interacting systems remains an area of active research. Hence, it is intriguing to investigate whether the MCD remains an effective measure for capturing topology even in the presence of strong interactions.

In this study, we investigate the impact of interactions on the topology of bulk states in a multiparticle quantum walk configuration. We compare results obtained from Berry phase calculations in excited states with reduced particle numbers, as well as single-particle and many-body mean chiral displacements (MCDs). For the noninteracting SU(N) Su-Schrieffer-Heeger (SSH) model, distinctions arise between cases of odd and even N, where the Berry phase exhibits a  $\pi N$  jump at the topological transition, making it ineffective for even N. In the interacting version of the model, the many-body Berry phase only displays a  $\pi$  jump for odd N, providing a useful indicator of the topological transition. We primarily focus on the simplest case of N = 3, where the Berry phase also serves as a reliable indicator. The prototypical SU(N) SSH model with an onsite Hubbard interaction is described by Eq. (1), encompassing dimerized hopping terms and Hubbard interactions between fermions with different flavors.

$$H = \sum_{x=-L/2}^{L/2} \left\{ -J \sum_{\alpha=1}^N [1 + (-1)^x \delta] (c_{x,\alpha}^\dagger c_{x+1,\alpha} + h.c.) + U \sum_{1 \leq \alpha \leq \beta \leq N} c_{x,\alpha}^\dagger c_{x,\alpha} c_{x,\beta}^\dagger c_{x,\beta} \right\} \quad (1)$$

The initial term in Equation (1) represents dimerized hopping, featuring amplitudes  $J_{1,2} = J(1 \pm \delta)$  between adjacent sites (refer to Fig. 1). Here,  $c_{x,\alpha}^{(\dagger)}$  denotes the creation (annihilation) operator of a fermion with flavor  $\alpha$  at site  $x$ . The second, the Hubbard term, describes the on-site interaction between fermions with different flavors.

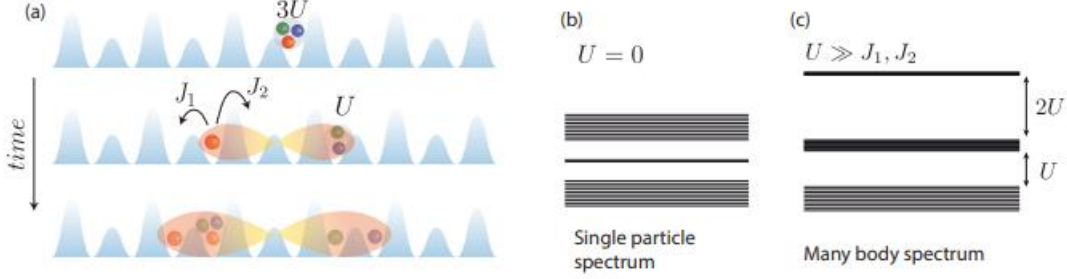


**Fig. 1** (a) A multiparticle quantum walk unfolds on an SU (3) SSH lattice, with  $U$  denoting the strength of on-site interaction. At  $t=0$ , three particles are injected. Subsequent measurements of single- or multiparticle MCDs yield insights into the topology of bulk states. Here,  $J_{1,2}$  represent the hoppings of the dimerized lattice. (b) Illustrated is the typical single-particle spectrum within the topological realm of the noninteracting spinless SSH model. Mid-gap lines denote the presence of topological edge states. (c) The three-particle many-body spectrum of the SU (3) model under the condition  $U \gg J$ . The spectrum comprises three bands separated by energy gaps of the order of  $\approx U$  [4].

The band structure of the spinless Su-Schrieffer-Heeger (SSH) model in the topological regime, with a focus on zero-energy modes, is illustrated in Fig. 1b. The interacting Hamiltonian maintains chiral symmetry but includes a chemical potential term that is negligible for the system dynamics. In the interacting model, despite the absence of zero-energy edge excitations, two distinct topological phases persist due to inversion symmetry. This parallels noninteracting systems where inversion symmetry enforces Zak phase quantization. Experimental validation of this quantization was achieved in a photonic lattice [3].

To probe excitation topology, three particles are introduced at the lattice midpoint, and interactions effects on quench dynamics are analysed using a multiparticle quantum walk setup, evolving unitarily as  $|\Psi(t)\rangle = e^{-iHt}|\Psi(t=0)\rangle$  [Fig. 1a].

The mean chiral displacement (MCD) serves as a dynamic measure capable to distinguish between trivial and topological regimes [2]. It is defined as:

$$P_1(t) = \sum_x \langle \Psi(t) | (x - x_0) \Gamma n(x) | \Psi(t) \rangle \quad (2)$$

Here,  $p(x) = (x - x_0)n(x)$  represents the regular polarization operator with respect to the reference point  $x_0$ , and using the chiral-symmetry operator  $\Gamma$  distinguishing between different sublattices, the "chiral polarization" operator or MCD is  $|(x - x_0)\Gamma n(x)|\Psi(t)\rangle$ .  $|\Psi(t)\rangle$  is the wave function evolved from an appropriate initial state, localized on site  $x_0$ , now set as the middle of the chain.

To extend the definition of the non-interacting MCD to many-body systems, we introduce the many-body MCDs as:

$$P_3(t) = \frac{1}{\langle n_3(t) \rangle} \langle \Psi(t) | \left[ \sum_x (-1)^x x \Phi_x^{(3)\dagger} \Phi_x^{(3)} \right] | \Psi(t) \rangle \quad (3)$$

The prefactor  $\langle n_3(t) \rangle \leq 1$  measures the probability of three-particle occupation,  $\langle n_3(t) \rangle = \sum_x \langle \Psi(t) | \Phi_3^\dagger \Phi_3 | \Psi(t) \rangle$ .

The MCDs  $P_{1,3}(t)$  are illustrated in Fig. 2. The two insets within Fig. 2a depict the time evolution of  $P_3(t)$  across the two regimes. The eventual convergence of  $P_3(t_\infty)$  depends on the value of  $\delta$ , reaching 0 (0.5) in the trivial (topological) regime. The main panel illustrates the  $\delta$  dependency of the eventual values. The minor fluctuations in these values stem from finite-size effects and the

limited duration of the simulations, diminishing as the system size increases. As evident from Fig. 2, both the many-body and single-particle MCDs prove effective in discerning between topologically distinct areas. Additionally, we show that both MCDs maintain a reasonable degree of quantization even beyond the strongly correlated region.

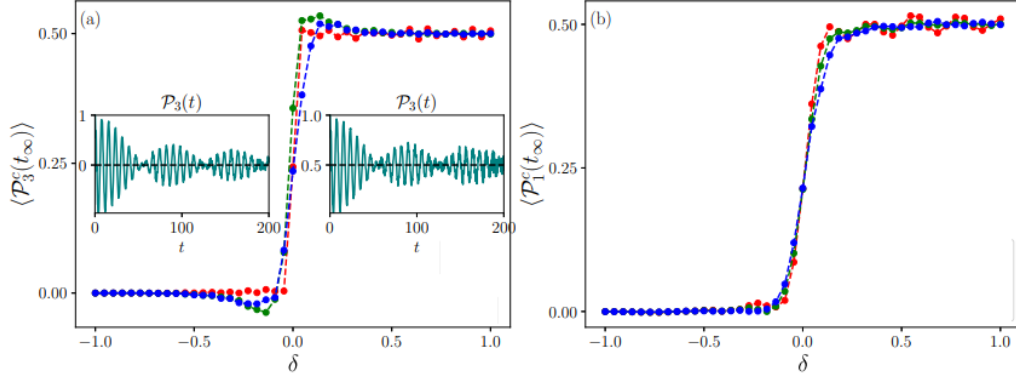


**Fig. 2** Mean chiral displacement in the interacting SU (3) SSH model. **(a)** MCD  $P_3$  as a function of dimerization parameter  $\delta$ , for lattice size  $L = 30$ , and  $t_\infty = 40/J$ . Insets: Typical evolution of the MCD  $P_3(t)$  at (right)  $\delta = 0.5$  and (left)  $\delta = -0.5$ . **(b)** MCD  $P_1$  as a function of dimerization parameter  $\delta$ , for  $L = 40$ , and  $t_\infty = 20/J$ . In both panels  $U = 3J$ . [4]

#### References

1. M.Z. Hasan, C.L. Kane, “Colloquium: Topological Insulators”, *Reviews of Modern Physics* 82, 3045 (2010).
2. F. Cardano, A. D’Errico, A. Dauphin, *et al.*, “Detection of Zak Phases and Topological Invariants in a Chiral Quantum Walk of Twisted Photons”, *Nature Communications* 8, 15516 (2017).
3. Z.-Q. Jiao, S. Longhi, X.-W. Wang, *et al.*, “Experimentally Detecting Quantized Zak Phases without Chiral Symmetry in Photonic Lattices”, *Physical Review Letters* 127, 147401 (2021).
4. B. Ostahie, D. Sticlet, C. Pascu Moca, *et al.*, “Multiparticle Quantum Walk: A Dynamical Probe of Topological Many-Body Excitations”, *Physical Review B* 108, 035126 (2023).

# Switching the Spin-Vibron Coupling in Molecular Magnets

V. Moldoveanu, R. Dragomir

National institute of Materials Physics, 077125 Magurele, Romania

We present a theoretical study of the interaction between the localized spin  $S$  of a molecular magnet (MM) connected to spin-polarized source and drain electrodes and its *quantized* vibrational modes (vibrons). The molecular spin and the electronic spins tunnelling on the lowest unoccupied molecular orbital (LUMO) are also coupled by the exchange interaction of strength  $J$ . The electron-vibron (EV) and spin-vibron (SV) interactions are introduced as follows:

$$H_{el-vb} = \lambda \hat{N}(a + a^\dagger), \quad H_{sp-vib} = -i\alpha E(S_+^2 - S_-^2)(a + a^\dagger). \quad (1)$$

Here  $\lambda$  and  $\alpha$  are coupling constants,  $\hat{N}$  is the charge operator associated to the hybrid system,  $\hat{S}_\pm$  are the jump molecular spin operators and  $a, a^\dagger$  are the operators of the vibronic mode. We recall that molecular magnets possess axial magnetic anisotropy  $DS_z^2$  as well as a transverse anisotropy component  $E(\hat{S}_x^2 - \hat{S}_y^2)$ . In this work we considered a MM of spin  $S = 2$ ; larger values of the molecular spin could be also taken into account albeit with higher computational costs. The relevant parameters of the numerical simulations are as follows:  $D = 0.056$  meV,  $E/D = 1/15$ , the isotropic exchange interaction  $J = 0.25$  meV,  $\lambda = 0.5$  meV and  $\alpha = 0.15$ . The energy of the spin-degenerate LUMO  $\varepsilon_\uparrow = \varepsilon_\downarrow = 1$  meV and the temperature  $T = 50$  mK. The spin polarization of the lead  $\beta$  is defined as  $P_\beta^\sigma = (N_\beta^\sigma - N_\beta^{\bar{\sigma}})/(N_\beta^\sigma + N_\beta^{\bar{\sigma}})$ ,  $N_\beta^\sigma$  and  $N_\beta^{\bar{\sigma}}$  being the density of states for the majority ( $\sigma$ ) and minority ( $\bar{\sigma}$ ) spin in the lead  $\beta$ . The bias  $eV = \mu_L - \mu_R$ , where  $\mu_{L,R}$  are the chemical potentials of the source (L)/drain (D) reservoirs. The hybrid quantum system is investigated by solving the generalized Master equation for the reduced density operator. We calculated the transient and stationary currents, the statistical average of the molecular spin and of the vibron number. Full details are given in Ref. [1].

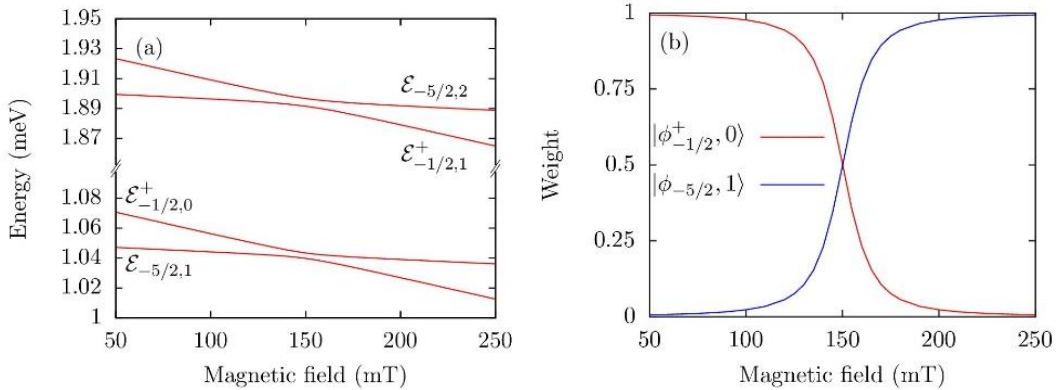


**Fig. 1** (a) The magnetic field dependence of the  $N = 0$  and  $N = 1$  energy doublets associated to pairs of dressed states made  $|\varphi_{-5/2; N+1}\rangle$  and  $|\varphi_{-1/2; N}\rangle$  “free” states. (b) The weights of the “free” states in the lowest-energy dressed state.

The first signature of the spin-vibron coupling consists in the removal of the Coulomb blockade. To see how this mechanism works we consider a quasi-antiparallel configuration of the electrodes, namely the left electrode provides only spin-down carriers (*i.e.*,  $P_L^\downarrow = 1$ ), while the drain electrode carries mostly spin-up electrons, *i.e.*,  $N_R^\uparrow > N_R^\downarrow$ . The vibrational quanta is set to  $\hbar\omega_0 = 0.85$  meV, which for the magnetic field  $B = 150$  mT corresponds to the resonant condition  $E_{-5/2, N+1} = E_{-1/2, N}$ . Here  $E_{S_z, N}$  are the  $N$ -vibron energy levels of the hybrid system in the absence of the spin-vibron coupling and  $S_z$  is the dominant spin number of the corresponding eigenstate  $|\varphi_{S_z; N}\rangle$  (see Ref. [1] for more details). Around this resonance the system will be described by vibron-dressed states. In Fig. 1a we plot the magnetic field dependence of the energies corresponding to four such dressed

states containing up to  $N = 2$  vibrons. In full analogy with the Jaynes-Cummings (JC) model of quantum optics one notices avoided crossing points for each pair of energies at resonant magnetic field. Moreover, the spectral branches for  $N = 0$  and  $N = 1$  are roughly separated by the single-vibron energy  $\hbar\omega_0$  and the energy gap at the resonance point increases with  $N$ . Fig. 1b also shows the weights of the “free” states  $|\varphi_{-5/2; N+1}\rangle$  and  $|\varphi_{-1/2; N}\rangle$  in the lowest-energy dressed state. Again, as in the JC model, these weights vary smoothly between 0 and 1, being nearly equal at resonance. Far away from the avoided crossing point one recovers the “free” states and their corresponding eigenvalues  $E_{-5/2, N+1}$  and  $E_{-1/2, N}$  (indicated in Fig. 1a).

In Fig. 2a we present the steady-state current as a function of the magnetic field and for several polarizations  $P_R^\uparrow$  of the drain electrode. As one enters the resonant regime, symmetric peaks develop for all values of  $P_R^\uparrow$ . Their height decreases if the polarization is reduced, whereas the background off-resonant current increases. This amplification of the stationary current in the resonant regime could be observed in typical transport measurements and witnesses the activation of the SV coupling and the corresponding transitions. Let us note that the difference between the off-resonant and resonant stationary currents is sizeable. The dependence of the stationary average molecular spin  $\langle S_z \rangle$  on the magnetic field is shown in Fig. 2b. One notices that  $\langle S_z \rangle$  also displays a series of peaks as a function of  $P_R^\uparrow$  while in the off-resonant regime spin  $\langle S_z \rangle = -2$ . The correspondence between the peaks in Figs. 2a and 2b also allows the reading of changes in the molecular spin from the enhancement of the current in the resonant or nearly resonant regime.

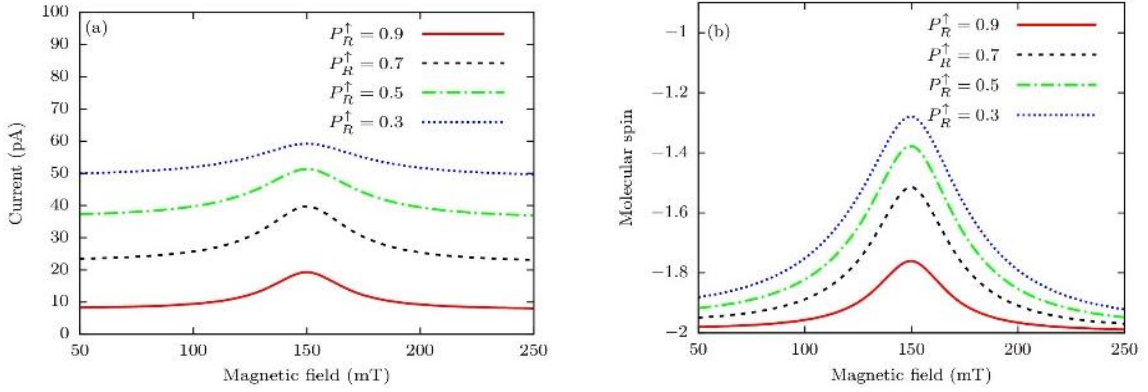


**Fig. 2** (a) The stationary current as a function of the magnetic field. (b) The average molecular spin. The removal of the spin blockade around the  $B = 150$  mT coincides with the enhancement of charge transport. The amplitude of the correlated peaks depends on the spin polarization  $P_R^\uparrow$ . Other parameters:  $V_L = 25 \mu\text{eV}$ ,  $V_R = 10 \mu\text{eV}$ .

The second effect of the spin-vibron coupling is identified by placing the system in the current-induced magnetic switching regime (CIMS) [2,3]. This is achieved by selecting a fully polarized source electrode ( $P_L^\uparrow = 1$ ) and a right electrode which carries mostly spin-down electrons. Then the occupation of the fully spin-polarized state  $|\varphi_{-5/2; N}\rangle$  is forbidden and the incident spin-up electrons feed only the intermediate states  $|\varphi_{S_z; N}\rangle$  with  $|S_z| \leq 3/2$ . On the other hand, the dominant depletion of the spin-down electrons to the right electrode allow transitions the empty molecular states with increasing spin. As shown in Ref. [4], in this case the stationary state corresponds to a full magnetic switching  $-S \rightarrow S$ , being described only by the fully polarized states  $|\varphi_{5/2; N}\rangle$  and  $|\varphi_{2; N}\rangle$ . To check the effect of the spin-vibron interaction in this configuration we select a frequency of the vibrational mode which activates transitions on the right side of the anisotropy barrier, namely between the fully-polarized states  $|\varphi_{5/2; N}\rangle$  and the excited molecular states  $|\varphi_{1/2; N-1}\rangle$ . For  $B = 150$  mT we find that  $\hbar\omega_0 = 0.78$  meV. Fig. 3 shows the stationary current and the spin occupations as functions of the polarization of the right electrode. Fig. 3a allows a comparison of the resonant and off-resonant steady-state currents. A small difference (around 6.5 pA) between the two currents is noticed even

for non-magnetic drain electrode (*i.e.*, for  $P_R^\downarrow = 0$ ). As  $P_R^\downarrow$  increases, both currents decrease but at different slopes and eventually vanish in the fully antiparallel configuration  $P_R^\downarrow = 1$ , while the spin-up occupation  $N_\uparrow = 1$  both in the resonant and off-resonant regimes (see Fig. 3b).

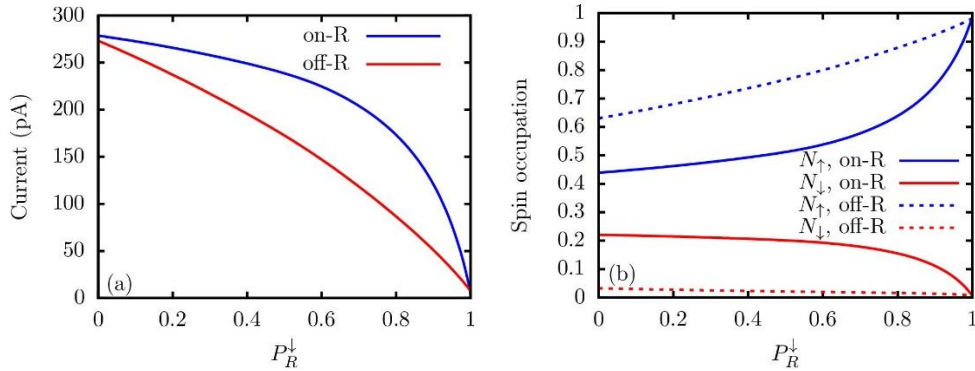


**Fig. 3** Steady-state quantities as functions of  $P_R^\downarrow$  in the resonant and off-resonant regimes. **(a)** The current; **(b)** The spin-dependent electronic occupations  $N_\sigma$ .

In summary, we implemented the Lindblad approach to the single-molecule magnets with spin-vibron interaction and predicted specific and sizeable effects of the spin-vibron coupling on the transport properties.

#### References

1. V. Moldoveanu, R. Dragomir, “Climbing the Anisotropy Barrier of Single-Molecule Magnets with Spin-Vibron Interaction”, *Physical Review B* 108, 024416 (2023).
2. M. Misiorny, J. Barnas, “Spin Polarized Transport through a Single-Molecule Magnet: Current-induced Magnetic Switching”, *Physical Review B* 76, 054448 (2007).
3. M. Misiorny, J. Barnas, “Effects of Transverse Magnetic Anisotropy on Current-Induced Spin Switching”, *Physical Review Letters* 111, 046603 (2013).
4. V. Moldoveanu, I.V. Dinu, B. Tanatar, C.P. Moca, “Quantum Turnstile Operation of Single-Molecule Magnets”, *New Journal of Physics* 17, 083020 (2015).

# Multi-Analytical Characterization of the White Inlaid Decoration on the Prehistoric Pottery from Southern Romania

M. Secu<sup>a</sup>, E. Matei<sup>a</sup>, C.E. Secu<sup>a</sup>, T.A. Buruiana, A.M. Rostas<sup>a</sup>, A.D. Popescu<sup>b</sup>, A. Boroneanț<sup>b</sup>, R. Băjenaru<sup>b</sup>

<sup>a</sup>National Institute of Materials Physics, 077125 Magurele, Romania

<sup>b</sup>Vasile Pârvan” Institute of Archaeology of the Romanian Academy, 010667 Bucharest, Romania

Pottery artefacts are the most abundant archaeological findings and reflect the socio-economic framework of past cultures. Their deep and complex examination by using a multi-analytical characterization approach imply the correlation of complementary data such as color, shape, morphology, mineralogical and elemental composition, age, *etc.* All the gathered data are used as indicators of the ancient technologies of manufacture and technical skills, provenance, trade routes, interactions between settlements and offers an image of the ancient society.

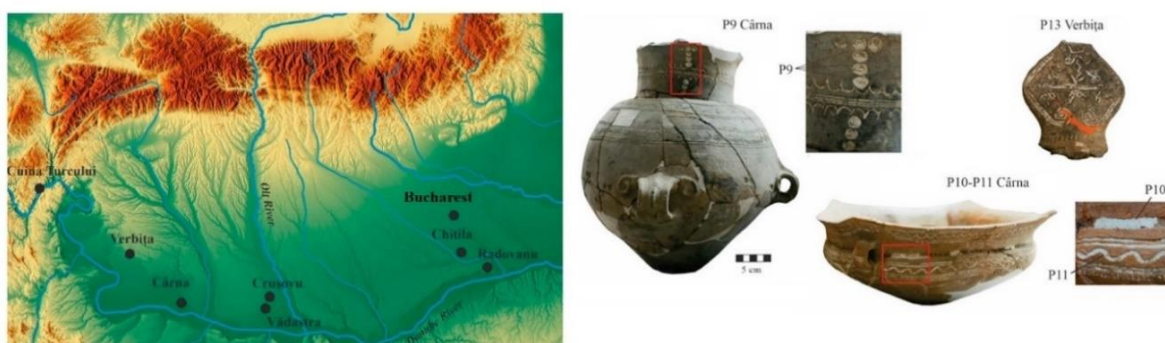


**Fig. 1** The location of sampled areas and some examples of artefacts investigated.

The infill with white paste of the incised/excised decoration on pottery is a frequent practice in the Middle and Lower Danube area, from the Chalcolithic onwards throughout the Bronze Age [1,2]. The aim of the study is to extend the previous studies of white decoration on prehistoric pottery in southern Romania [2-4], by using a multi-analytical characterization approach and novel techniques such as EPR and thermoluminescence. A number of artefacts decorated with white pigment and lying from the Early Chalcolithic to the Early Bronze Age, Middle Bronze age up to the Late Bronze Age and spread along the Danube River were analyzed by using physical-chemical studies methods (Table 1). For the understanding of the pigment’s composition and manufacture technology a complex analysis was performed on a small amount of powder collected.

**Table 1** Archaeological data about the selected samples for investigation and the results of the mineralogy investigation from the XRD analysis and of the morphological imaging by SEM.

Sample	Pigment/time period/Artefact			XRD crystalline phase			Morphology
	Cultural assignment	Period	Artefact type	Calcite (CaCO <sub>3</sub> )	Hydroxyapatite (HA)	Quartz (SiO <sub>2</sub> )	
P1(Vădastra)	Vădastra	Early Chalcolithic	Unidentified pot shape	Dominant	Not detected	Not detected	Microsized grains
P2(Vădastra)	Vădastra	Early Chalcolithic	Unidentified pot shape	Dominant	Not detected	Detected (≅ 5%)	with plate-like morphology
P3(Vădastra)	Vădastra	Early Chalcolithic	Unidentified pot shape	Dominant	Not detected	Detected (≅ 10%)	
P3(Radovanu)	Boian (Spanțov)	Early Chalcolithic	Pedestalled bowl	Dominant	Not detected	Not detected	Uniform, ball-shaped grains
P4(Crușovu)	Vădastra	Early Chalcolithic	Bowl	Dominant	Not detected	Weak	Coarsed, ball-shaped grains
P5(Crușovu)	Vădastra	Early Chalcolithic	Unidentified pot shape	Dominant	Not detected	Weak	Coarsed, ball-shaped grains
P6(Crușovu)	Vădastra	Early Chalcolithic	Unidentified pot shape	Dominant	Not detected	Weak	Coarsed, ball-shaped grains
P7(Crușovu)	Vădastra	Early Chalcolithic	Unidentified pot shape	Dominant	Very weak	Weak	
P8(Cuina Turcului)	Kostolac	Early Bronze Age	Bowl	Detected	Not detected	Detected (≅ 23%)	Compact, porous aspect
P2(Chitila)	Tei, III-IV phases	Middle/Late Bronze Age	Cup handle	Weak	Dominant	Not detected	Distribution ball-shaped grains
P9(Cârna)	Gârla Mare	Late Bronze Age	Amphora	Detected (≅ 51%)	Detected (≅ 48%)	Weak (≅ 1%)	Ball-shaped grains
P10-11(Cârna)	Gârla Mare	Late Bronze Age	Bowl	Weak	Dominant	Weak	Distribution ball-shaped grains
P13(Verbița)	Gârla Mare	Late Bronze Age	Human figurine	Weak	Dominant	Weak	Distribution ball-shaped grains

A detailed and complex analysis of the X-ray diffraction patterns (XRD) and FTIR spectra (Fig. 2 and Table 1) indicated the presence of two main crystalline phases in the pottery pigments: a calcite (CaCO<sub>3</sub>)-based group and a hydroxyapatite (HA)-based group. The calcite (CaCO<sub>3</sub> mineral) is the

main constituent of the white inlaid decoration on the Chalcolithic pottery, frequently in combination with variable quantities of quartz. The recipe changed through the Middle Bronze Age, where HA has become the predominant ingredient in the composition (Table 1).

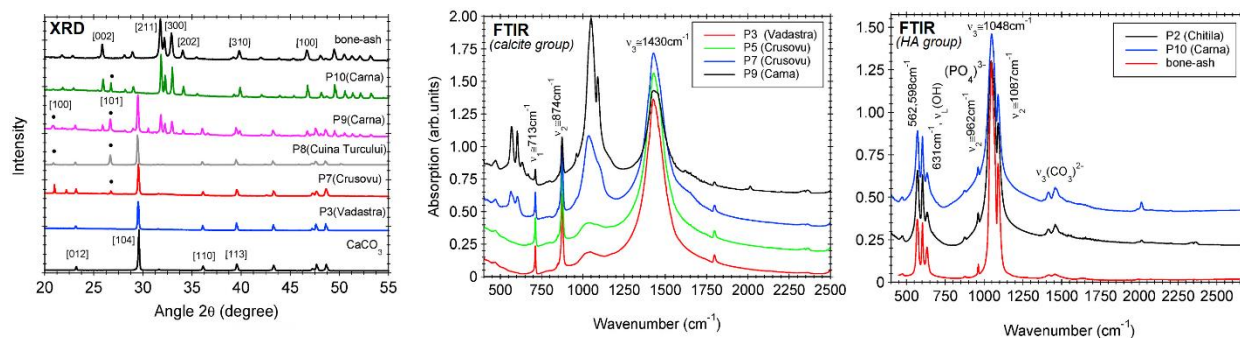


**Fig. 2** The structural analysis by using XRD patterns and FTIR spectra of the pigment samples (selection).

The FTIR spectra analysis agree with the XRD analysis and confirmed the presence of two main crystalline phases in the pottery pigments, calcite and HA, along with small amount of quartz (Fig. 3). The *calcite-based group* showed dominantly the absorption peaks the  $(\text{CO}_3)^{2-}$  group, specific to calcite compound (Fig. 3). Moreover, the analysis of the crystallinity index (CI) from the FTIR spectra indicated a calcination temperature of the pigments between 600 and 800 °C [5], that correlates very well with the expected temperatures of firing (600 to 825 °C) of the ancient furnaces. Therefore, we might suppose that the white decoration was performed on the air-dried ceramics which were fired, for the better adherence and stabilize of the decoration on the pottery.

The scanning electron microscopy (SEM) images analysis of the *HA-based group* pigments has indicated a relatively uniform distribution of small particles (hundreds on nm sized) and microsized particles for the *calcite-based group* and their diverse morphology is possibly triggered by the local recipes for the preparation of the ingredients: the pigment aspect features (*i.e.*, plate or balls grains, porous) are linked to the variations in the sample composition. The elemental analysis for *HA-based group* the Ca/P molar ratio was higher than expected for stoichiometric HA. This, together with various trace elements (*i.e.*, Mg, Na, Si, Cu, Cl, S) characteristic of mammal bone mineral and FTIR spectra details, suggest a biogenic nature of these pigments.

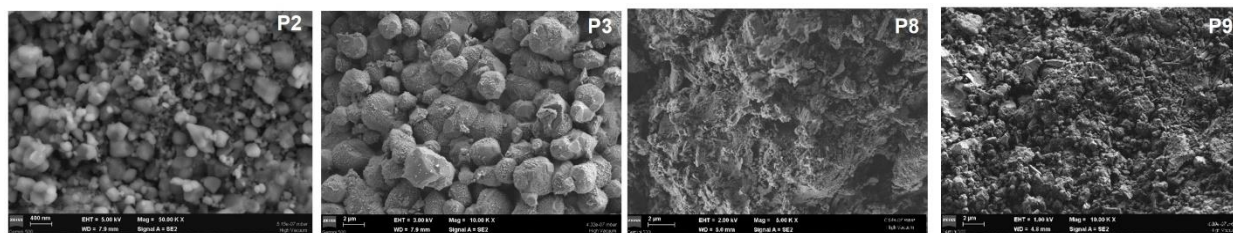


**Fig. 3** SEM images of the investigated pigment samples (selection).

New information was revealed by the electron paramagnetic resonance (EPR) spectroscopy technique through the comparison made between the spectra recorded on pigments,  $\text{Mn}^{2+}$ -doped  $\text{CaCO}_3$  and bone ashes resulted from the bone calcination of different animals (Fig. 4). The (EPR) spectra recorded on *calcite-based group* and  $\text{Mn}^{2+}$ -doped  $\text{CaCO}_3$  powder shows typical  $\text{Mn}^{2+}$  six main lines with a well-defined complex hyperfine (HF) structure that indicate calcite as material used for the pigment manufacture. The *HA-based group* showed only broad signals related to the carbonate-derived anionic radicals (*e.g.*,  $\text{CO}_2^-$ ,  $\text{CO}_3^-$ ,  $\text{CO}_3^{3-}$  [6]). A clear assignment to a specific mammal bones is hardly, analysis on a higher diversity of animal bones being necessary.

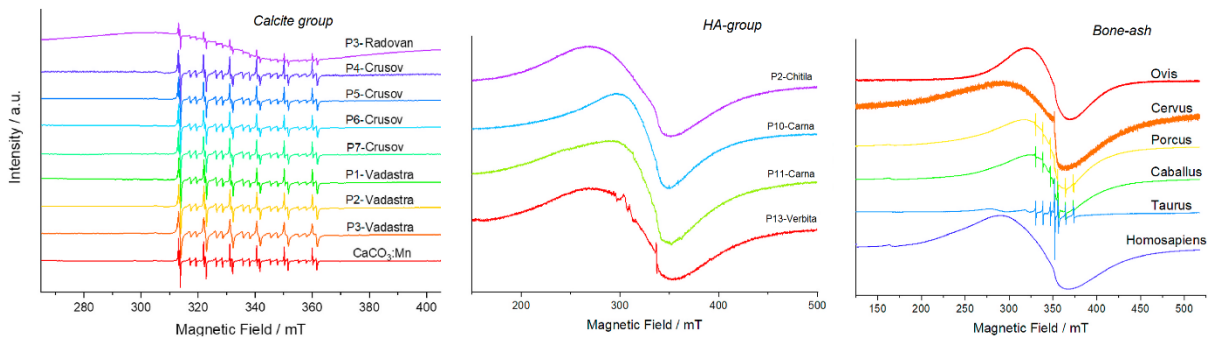


**Fig. 4** EPR spectra of the investigated pigment samples (selection).

Thermoluminescence curves on naturally irradiated pigment samples (induced by naturally occurring radioactivity and from cosmic radiation) were recorded on *calcite-based* pigments. Even if is very weak the high radio-sensitivity of thermoluminescence techniques may provide valuable qualitative information regarding the calcite source mineral used during the pigment manufacture and their age, the time elapsed since the pottery was fired. However, further detailed investigations are needed to develop a methodology using this approach.

The study indicated that geographical proximity was not a decisive factor in using the same compounds for the manufacture of the white pigment decorating the vessels in the Lower Danube area. In other words, there is no universal recipe used by local communities in the same region from the Chalcolithic to the Bronze Age. The mineralogical composition of the white pigment showed a chronological differentiation. The nature of the ingredients used, their aspect and proportions suggest certain preferences, possibly local recipes even for vessels with the same cultural background and within the same site there were different choices of used ingredients.

An accurate identification of the standard recipe and its variants of the pigment at a specific site or cultural area requires physical-chemical studies on a higher larger number of samples.

#### References

1. W.A. Parkinson, E. Peacock, R.A. Palmer, *et al.*, “Elemental Analysis of Ceramic Incrustation Indicates Long-Term Cultural Continuity in the Prehistoric Carpathian Basin”, *Archaeology, Ethnology and Anthropology of Eurasia* 38, 64–70 (2010).
2. J. Sofaer, S. Roberts, “Technical Innovation and Practice in Eneolithic and Bronze Age Encrusted Ceramics in the Carpathian Basin, Middle and Lower Danube”, *Archäologisches Korrespondenzblatt* 46, 479–496 (2016).
3. M. Secu, E. Matei, C. Secu, *et al.*, “Multi-Analytical Characterization of the White Inlaid Decoration on the Prehistoric Pottery from Southern Romania”, *Solid State Sciences* 140, 107193 (2023).
4. V. Opreș, A. Velea, M. Secu, *et al.*, “‘Put Variety in White’: Multi-Analytical Investigation of the White Pigments Inlaid on Early Chalcolithic Pottery from Southern Romania”, *Journal of Archaeological Science: Reports* 42, 103402 (2022).
5. T.A. Surovell, M.C. Stiner, “Standardizing Infra-Red Measures of Bone Mineral Crystallinity: An Experimental Approach”, *Journal of Archaeological Science* 28, 633–642 (2001).
6. F. Callens, G. Vanhaelewyn, P. Matthys, E. Boesman, “EPR of Carbonate Derived Radicals: Applications in Dosimetry, Dating and Detection of Irradiated Food”, *Applied Magnetic Resonance* 14, 235–254 (1998).

# Functionalization of the Graphene Oxide Sheets with Organic Compounds

**A.G. Mihis<sup>a</sup>, L.C. Cotet<sup>a,b</sup>, C. Cadar<sup>a</sup>, L.C. Pop<sup>b</sup>, M. Todea<sup>c</sup>, M.M. Rusu<sup>c</sup>, A. Vulpoi<sup>c</sup>, I. Szekely<sup>a,c</sup>, C.A. Salagean<sup>a,d</sup>, K. Magyari<sup>a,c</sup>, M. Muresan-Pop<sup>c</sup>, O. Cadar<sup>e</sup>, M. Baia<sup>a,d</sup>, I.E. Sofrani<sup>f</sup>, G Lisa<sup>g</sup>, I Anghel<sup>f</sup>, V Danciu<sup>a</sup>, L Baia<sup>a,d</sup>, M. Baibarac<sup>h</sup>**

<sup>a</sup> Institute of Research-Development-Innovation in Applied Natural Sciences, “Babes-Bolyai” University, 400327 Cluj-Napoca, Romania

<sup>b</sup> Faculty of Chemistry and Chemical Engineering, “Babes-Bolyai” University, 400028 Cluj-Napoca, Romania

<sup>c</sup> Nanostructured Materials and Bio-Nano-Interfaces Center, Institute of Interdisciplinary Research in Bio-Nano-Sciences, “Babes-Bolyai” University, Cluj-Napoca, Romania

<sup>d</sup> Faculty of Physics, “Babes-Bolyai” University, Cluj-Napoca, Romania

<sup>e</sup> INCDO-INOE 2000, Research Institute for Analytical Instrumentation, 400293 Cluj-Napoca, Romania

<sup>f</sup> Fire Officers Faculty, “Alexandru Ioan Cuza” Police Academy, 014031 Bucharest, Romania

<sup>g</sup> Faculty of Chemical Engineering and Environmental Protection “Cristofor Simionescu”, “Gheorghe Asachi” Technical University of Iasi, 700050 Iasi, Romania

<sup>h</sup> National Institute of Materials Physics, 077125 Magurele, Romania

Functionalization of graphene oxide (GO) sheets with organic compounds has attracted particular attention with a view to obtaining new precursors for obtaining polymer/graphene oxide composites [e.g., 1,2] or as flame-retardants for various materials [e.g., 3,4]. The functionalization of GO with various compounds involves the generation of new covalent bonds. Such processes cause the “bulk properties” of GO to be diminished in favor of surface-induced properties, these materials being reported as “Sutter” materials [5]. A drawback of GO as flame-retardant agent consists in its tendency of agglomeration when van der Waals forces are established between GO sheets [6]. In order to overpass this disadvantage, the functionalization of GO sheets with organic compounds containing P, Si and N is necessary. To exemplify such a GO functionalization processes, the synthesis of the composite based on GO functionalized with polyhedral oligomeric silsesquioxane (labeled as HAK) and 9, 10-dihydro-9-oxa-10-phospha-phenantrene-10-oxide (DOPO), labeled in the following as GO-DOPO-HAK, will be presented below [4]. The synthesis of the GO-DOPO-HAK composite involve: (i) synthesis of HAK; (ii) the functionalization of the GO sheets with DOPO; and (iii) the interaction of GO-DOPO with HAK. Briefly, the synthesis of HAK is shown in Fig. 1 [4]. According to Fig. 1, the synthesis of HAK involves: (i) the condensation reaction of 2-hydroxyethylacrylate (HEA) with 3-amino-propyl-triethoxy-silane (APTES) [7] and (ii) the interaction of HEA-APTES with 3-(methacryloyloxy) propyl-trimethoxy silane. Fig. 2 shows the functionalization of the GO sheets with DOPO and HAK [4]. The functionalization of GO takes place via the reaction between P-H bonds existing in DOPO with the epoxy groups present in GO sheets, highlighted by FTIR spectroscopy, when the temperature is 70 °C in the presence of tetrahydrofuran (THF) and N<sub>2</sub> [8]. The successively functionalization of GO-DOPO with HAK was achieved by the adding of N, N-dicyclo-hexylcarbodiimide in THF to GO-DOPO and then of HAK in THF. The functionalization reaction of GO-DOPO with HAK took place at 70 °C for 48 h, the reaction product being washed with THF and methanol, later dispersed in ethanol and finally dried at 60 °C for 12 hours [4].

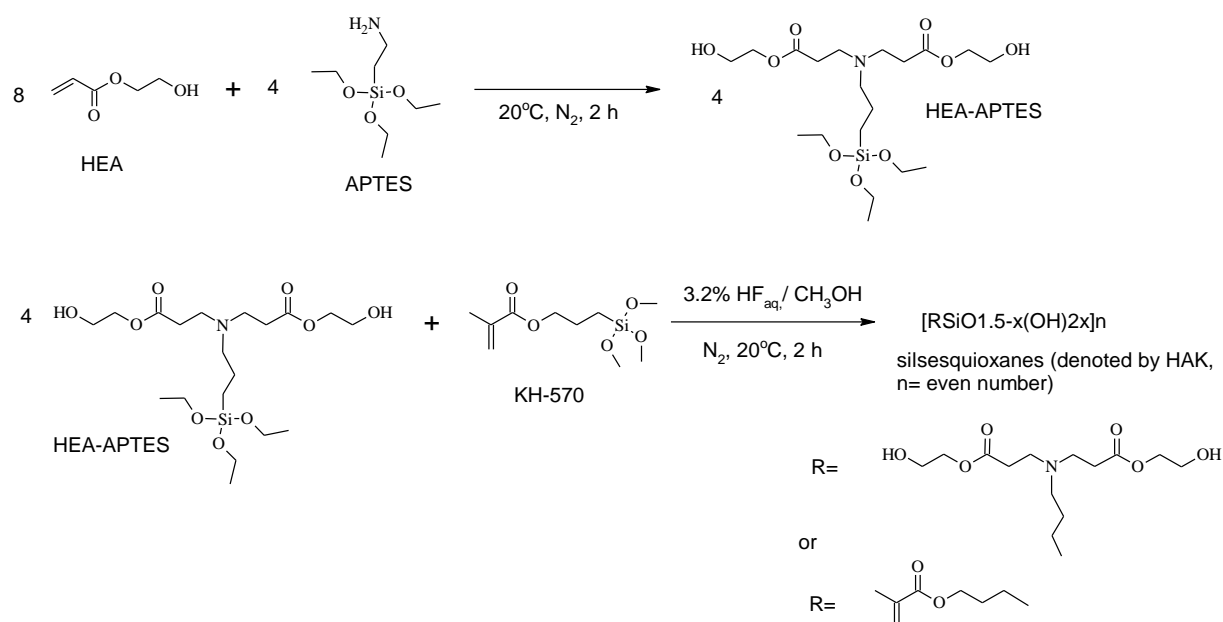


**Fig. 1** The chemical mechanism of the synthesis of HAK [4].

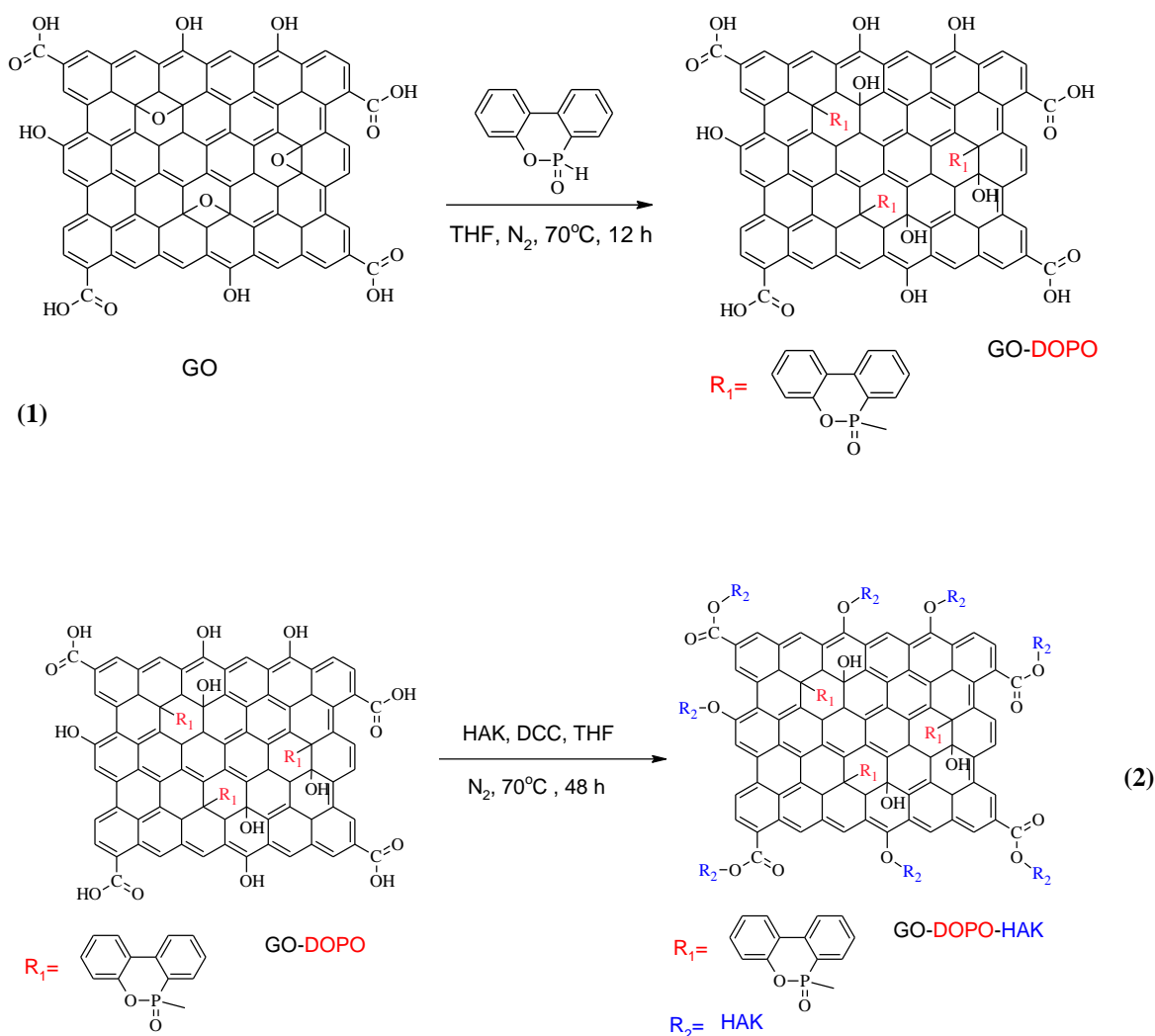


**Fig. 2** Chemical functionalization of GO sheets with (reaction 1) DOPO and successively with HAK (reaction 2) [4].

The reactions shown in Fig. 2 were confirmed by: (a) FITR spectroscopy, when changes in the absorbance of the IR bands assigned to the vibrational modes of the C=O, C=C, C–O–C and Si–O–

Si bonds and the appearance of a new P–O–C bond peaked at  $1080\text{ cm}^{-1}$  were reported [4]; (b) X-ray photoelectron spectroscopy, when a decrease in the C=O, C–O and C–OH bond weight simultaneous with the increase of the C–P, C–S and C–N bonds weight was highlighted [4]; (c) Raman scattering, when a variation of the ratio between the intensities of the D and G bands of GO from 0.94 to 1.16 was evidenced after the functionalization of the GO sheets with DOPO-HAK [4]. Using thermogravimetry analysis (TGA), in the case of the GO-DOPO-HAK composite a heat resistance index equal to  $123\text{ }^{\circ}\text{C}$  was reported, the value which is superior to those of GO-DOPO ( $87\text{ }^{\circ}\text{C}$ ) and GO ( $66\text{ }^{\circ}\text{C}$ ) [4]. Studies by the microscale combustion calorimetry (MCC) have demonstrated a significant decrease of the heat release capacity (HRC), when GO is functionalized with DOPO-HAK, from  $343.13\text{ J}/(\text{g K})$  up to  $28.30\text{ J}/(\text{g K})$  and an increase in char yield from  $41.82\%$  up to  $51.58\%$ . Summarizing these results, we conclude that knowledge of the vibrational, structural, morphological and thermal properties of the GO-DOPO-HAK composite opens new opportunities in the use of this material as flame-retardant agent in building materials such as polystyrene and poly(vinyl chloride) [4].

#### References

1. M. Baibarac, M. Daescu, S.N. Fejer, “Adsorption of 1, 4-Phenylene Diisothiocyanate onto the Graphene Oxide Sheets Functionalized with Polydiphenylamine in Doped State”, *Scientific Reports* 9, 11968 (2019).
2. M. Vaduva, M. Baibarac, O. Cramariuc, “Functionalization of Graphene Derivatives with Conducting Polymers and their Applications in Uric Acid Detection”, *Molecules* 28, 135 (2023).
3. I. Anghel, G. Lisa, I.E. Sofran, *et al.*, “Pyrolysis and Combustion of Polystyrene Composites based on Graphene Oxide Functionalized with 3-(Metha-Cryloyloxy)-Propyltrimethoxysilane”, *Journal of Polymer Engineering* 41, 615–626 (2021).
4. A.G. Mihis, L.C. Cotet, C. Cadar, *et al.*, “Structural and Flame Retardancy Properties of GO-DOPO-HAK Composite”, *Journal of Materials Science* 58, 7025–7047 (2023).
5. M. Chipara, M. Baibarac, G. Compagnini, J. Gao, “From Interface to Interphase”, *Surfaces and Interfaces* 42, 103425 (2021).
6. G. Yuan, B. Yang, Y. Chen, Y. Jia, “Preparation of Novel Phosphorus-Nitrogen-Silicone Grafted Graphene Oxide and its Synergistic Effect in Intumescent Flame-Retardant Polypropylene Composites”, *RSC Advances* 8, 36286–36297 (2018).
7. G. Wang, G. Ma, C. Hou, *et al.*, “Preparation and Properties of Waterborne Polyurethane /Nanosilica Composites: A Diol as Extender with Triethoxysilane Group”, *Journal of Applied Polymer Science* 131, 40526 (2014).
8. G. Yuang, B. Yang, Y. Chen, Y. Lia, “Synthesis of a Novel Multi-Structure Synergistic POSS-GO-DOPO Ternary Graft Flame Retardant and its Applications in Polypropylene”, *Composites Part A: Applied Science and Manufacturing* 117, 345–356 (2019).

# Atomic Scale Insight into the Decomposition of Nanocrystalline Zinc Hydroxynitrate Toward ZnO using Mn<sup>2+</sup> Paramagnetic Probes

I.D. Vlaicu <sup>a</sup>, M. Stefan <sup>a</sup>, C. Radu <sup>a,b</sup>, D.C. Culita <sup>c</sup>, D. Radu <sup>a</sup>, D. Ghica <sup>a</sup>

<sup>a</sup>National Institute of Materials Physics, 077125 Magurele, Romania

<sup>b</sup>University of Bucharest, Faculty of Physics, 077125 Magurele, Romania

<sup>c</sup>“Ilie Murgulescu” Institute of Physical Chemistry, Romanian Academy, 060021 Bucharest, Romania

Layered hydroxide salts (LHS) exhibit interesting properties such as anion-exchange and intercalation capacity, which enable their use as catalysts and in functional nanocomposites. Other applications in nanomedicine, agriculture and cosmetics are due to their biocompatibility, *e.g.* slow releasing drug delivery agents, biomolecule reservoirs, fertilizers, herbicides, sunscreens. A typical representative of LHS is zinc hydroxynitrate – Zn<sub>5</sub>(OH)<sub>8</sub>(NO<sub>3</sub>)<sub>2</sub>·2H<sub>2</sub>O (ZHN). One of the problems limiting the large-scale use of this compound for most applications is its thermal stability. As the morpho-structural properties affect material's stability and efficiency for specific applications, it is important to establish performant and reproducible synthesis algorithms, resulting in ZHN with defined morpho-structural characteristics. Only few reports provide information on the ZHN morphology, but its influence on the material thermal stability and the structural phase transformation path are not considered. Electron paramagnetic resonance (EPR) spectroscopy of lightly doped (nano)-crystals has been successfully used to investigate structural phase transformations at atomic scale using paramagnetic probing ions, resulting in a richer information and higher accuracy than in the case of thermal analysis methods [1]. Mn<sup>2+</sup> is a good paramagnetic probe in Zn-based compounds, due to the similar charge state and close ionic radii with the host Zn<sup>2+</sup> ions. In low concentrations (< 1%) the Mn<sup>2+</sup> ions do not affect the host lattice and allow the determination with high sensitivity and accuracy of the on-set of the phase transformations [1–3].

In this work [4] we have synthesized nanostructured ZHN by two cost-effective methods and investigated the morpho-structural properties and thermal stability of the resulting Mn-doped nano-ZHN powders, within an original approach. The localization of the low concentration Mn<sup>2+</sup> ions and the doping efficiency in the two nano-ZHN systems, of particular interest for applications, were evaluated by EPR. The structural phase transformation was monitored at atomic scale by EPR with the Mn<sup>2+</sup> probing ions, showing with high accuracy the on-set of the structural transformation toward ZnO and the differences in the two nano-systems. Nano-ZHN doped with a small amount of Mn<sup>2+</sup> ions (0.1 % nominal concentration) was prepared by two synthesis routes, coprecipitation and solid state reaction, using the same environment-friendly reactants. The resulting samples (ZHN<sub>COPP</sub> and ZHN<sub>SSR</sub>, respectively) have distinct morpho-structural and textural properties, clearly influenced by the synthesis method. While in both cases the structure and crystallite size are similar (Fig. 1), the sample obtained by coprecipitation exhibits much larger platelets (Fig. 2) with specific surface area and total pore volume more than two times larger than in the case of the sample obtained by solid state reaction. From the EPR analysis we determined that the Mn<sup>2+</sup> dopant ions are localized substitutionally in the Zn<sup>2+</sup> sites of the host lattice in both samples and the Mn<sup>2+</sup> concentration is three times higher in the coprecipitation sample, showing that this synthesis route ensures an enhanced doping efficiency (Figs. 3a,b). The on-set of the ZHN structural phase transformation toward ZnO was observed by EPR at 110 °C and 130 °C for the samples synthesized by coprecipitation and solid-state reaction, respectively (Fig. 4). A comparison of the EPR results with the structural and compositional XRD results showed that the Mn<sup>2+</sup> dopant ions promote the local transformation of ZHN into ZnO at lower temperatures.

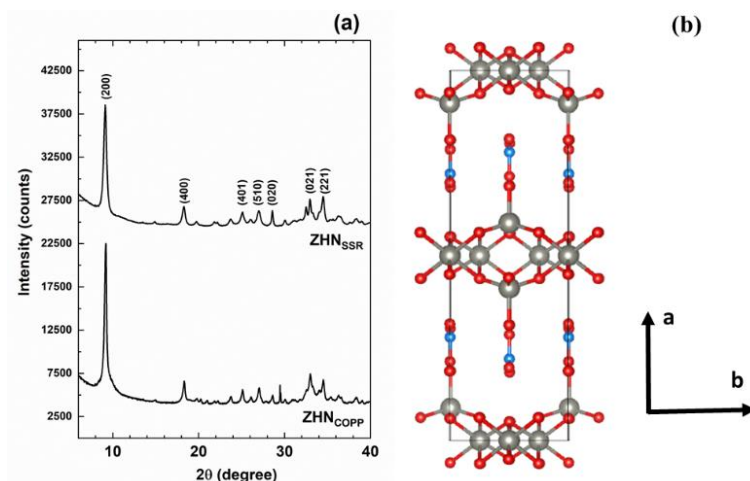


**Fig. 1** (a) XRD patterns of the ZHN samples. The most intense peaks of the  $\text{Zn}_5(\text{OH})_8(\text{NO}_3)_2(\text{H}_2\text{O})_2$  structure are marked. (b) Structural model along the *c*-axis with the color codes for atoms: grey - Zn, red - O, light blue - N.

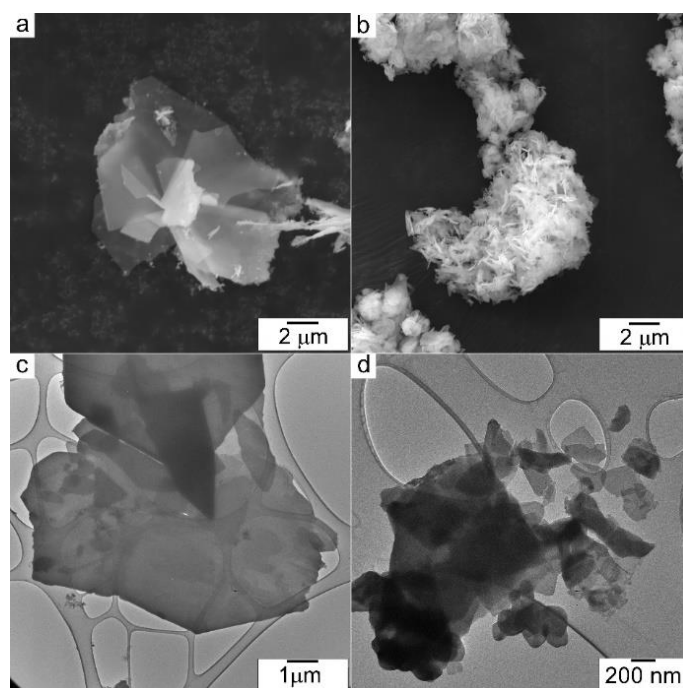


**Fig. 2** SEM images of the (a)  $\text{ZHN}_{\text{COPP}}$  and (b)  $\text{ZHN}_{\text{SSR}}$  samples. TEM images of (c)  $\text{ZHN}_{\text{COPP}}$  and (d)  $\text{ZHN}_{\text{SSR}}$ .

We have shown [4] that thermal decomposition at low temperatures of  $\text{Mn}^{2+}$  doped ZHN is a good method to obtain uniformly doped nano-ZnO. Moreover, while the coprecipitation method provides an enhanced Mn-doping efficiency in ZHN, the solid-state reaction method has the advantage of a cleaner and simpler process, with less reactants, and a higher thermal stability of the resulted ZHN. Our results provide a basis for the selection of the appropriate synthesis method for nano ZHN suitable for the envisaged application in nanotechnology, healthcare or agriculture and for the development of new, cost-effective synthesis routes of  $\text{Mn}^{2+}$  doped nano-ZnO.

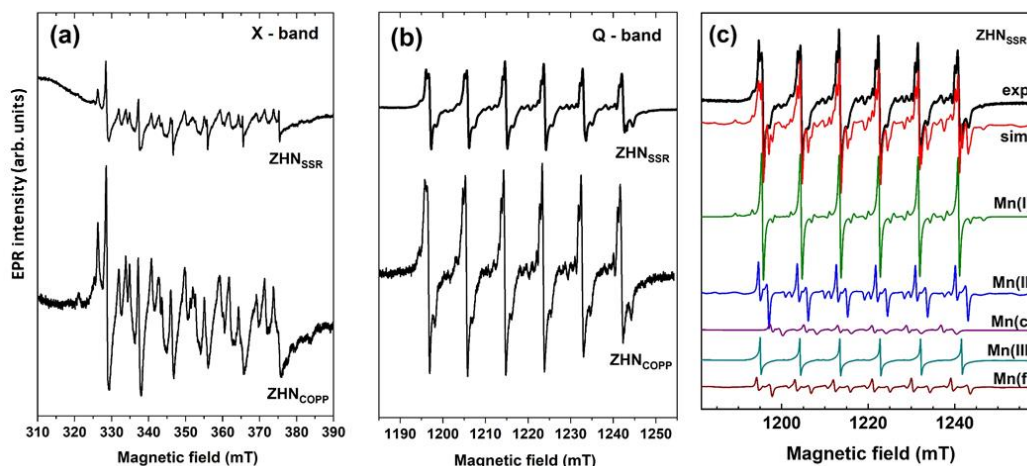


**Fig. 3** EPR spectra of the as-prepared samples measured at room-temperature in (a) X-band (9.86 GHz), and (b) Q-band (34.12 GHz). (c) Experimental (exp.) and simulated (sim.) EPR spectrum in Q-band of the  $ZHN_{SSR}$  sample. The component spectra of the indicated centers, calculated with the SH parameters from Ref. [5], are presented below.

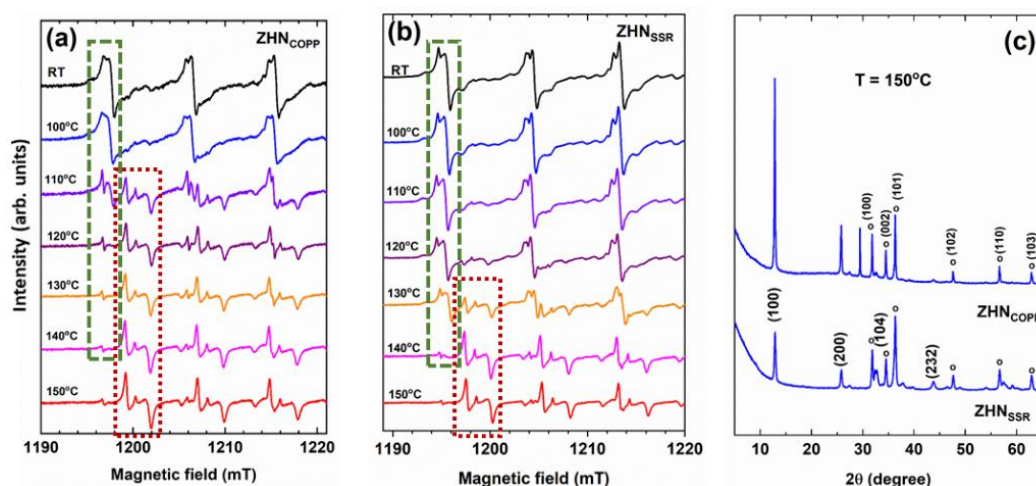


**Fig. 4** EPR spectra of  $Mn^{2+}$  ions in (a)  $ZHN_{COPP}$ , and (b)  $ZHN_{SSR}$ , as-prepared (RT) and annealed (10 min at each temperature). The first three hyperfine transitions at low-field are displayed for simplicity. Transformation of the  $Mn^{2+}$  centers in the zinc hydroxynitrate phases into  $Mn^{2+}$  centers in  $ZnO$  is shown with green and dark red dotted lines, respectively, for the first hyperfine transition. (c) XRD patterns of both samples after annealing up to 150 °C.  $ZnO$  (open circles) is indexed in the upper pattern, while  $Zn_3(OH)_4(NO_3)_2$  is indexed in the lower pattern.

**Acknowledgments:** Core Program project PC1- PN23080101, project 35PFE/2021.

#### References

1. S.V. Nistor, M. Stefan, D. Ghica, “Pulse Annealing Electron Paramagnetic Resonance with Probing Transition Ions: Application to Thermal Formation and Growth of NanoZnO”, *Journal of Thermal Analysis and Calorimetry* 118, 1021–1031 (2014).
2. D. Ghica, S.V. Nistor, L.C. Nistor, *et al.*, “Structural Phase Transformations in Annealed Cubic ZnS Nanocrystals”, *Journal of Nanoparticle Research* 13, 4325–4335 (2011).
3. D. Ghica, I.D. Vlaicu, M. Stefan, *et al.*, “Tailoring the Dopant Distribution in ZnO:Mn Nanocrystals”, *Scientific Reports* 9, 6894 (2019).
4. I.D. Vlaicu, M. Stefan, C. Radu, *et al.*, “Atomic Scale Insight into the Decomposition of Nanocrystalline Zinc Hydroxynitrate Toward ZnO using  $Mn^{2+}$  Paramagnetic Probes,” *Frontiers in Chemistry* 11, 1154219 (2023).

# Strain Induced Multiferroicity in ZrO<sub>2</sub> Thin Films: Nanoscale Studies by HRTEM

M.C. Istrate<sup>a,b</sup>, C. Ghica<sup>a</sup>, V.S. Teodorescu<sup>a</sup>, J.P.B. Silva<sup>c</sup>

<sup>a</sup>National Institute of Materials Physics, 077125 Magurele, Romania

<sup>b</sup>Faculty of Physics, University of Bucharest, 077125 Magurele, Romania

<sup>c</sup>Centre of Physics of Minho and Porto Universities (CF-UM-UP), 4710-057 Braga, Portugal

The discovery of ferroelectricity in silicon-doped hafnium oxide (Si:HfO<sub>2</sub>) thin films in 2011 offered strong promise for the integration and scalability of ferroelectric films into a range of electronic devices. Since then, a sustained effort has been made to understand the ferroelectric behavior. This has included exploring other dopants to induce ferroelectricity in HfO<sub>2</sub>, the most investigated dopant being Zr, giving (Hf<sub>x</sub>Zr<sub>1-x</sub>)O<sub>2</sub> (HZO).

Extensive research work has been done to integrate HZO materials into ferroelectric memory, ferroelectric field-effect transistors (Fe-FETs), energy storage capacitors, energy harvesters and pyroelectric sensors. HZO is appealing because of its a simple pseudo-binary phase, it has a wide bandgap ( $\approx 5.3\text{--}5.7\text{ eV}$ ), and it is compatible with complementary metal oxide semiconductor (CMOS) technologies as it can be processed at  $\sim 400\text{ }^\circ\text{C}$  on Si.

ZrO<sub>2</sub> thin film was deposited on a Nb:SrTiO<sub>3</sub> substrate with three different orientations [1,2], namely (001), (011) and (111) in order to stabilize the ferroelectric orthorhombic phase of ZrO<sub>2</sub>, because the orientation of the substrate plays a key role in this process. For the (111) orientation a novel polar rhombohedral phase is obtained with unprecedented ferroelectric characteristics. The influence of the oxygen vacancies on the ferroelectric properties will be studied for the latter orientation. Besides the orientation of the substrate, the method used for the crystallization process of ZrO<sub>2</sub> also has an important effect on the crystalline phase of the ZrO<sub>2</sub> thin film. In this context, the use of W electrodes to promote the formation of the *o*-phase with improved ferroelectric performance is investigated. We first grew W/ZrO<sub>2</sub>/W structures onto Si/SiO<sub>x</sub> substrates by ion beam sputtering at a maximum temperature of 330 °C and then we performed the crystallization of the ZrO<sub>2</sub> layer by nanosecond laser annealing [3].

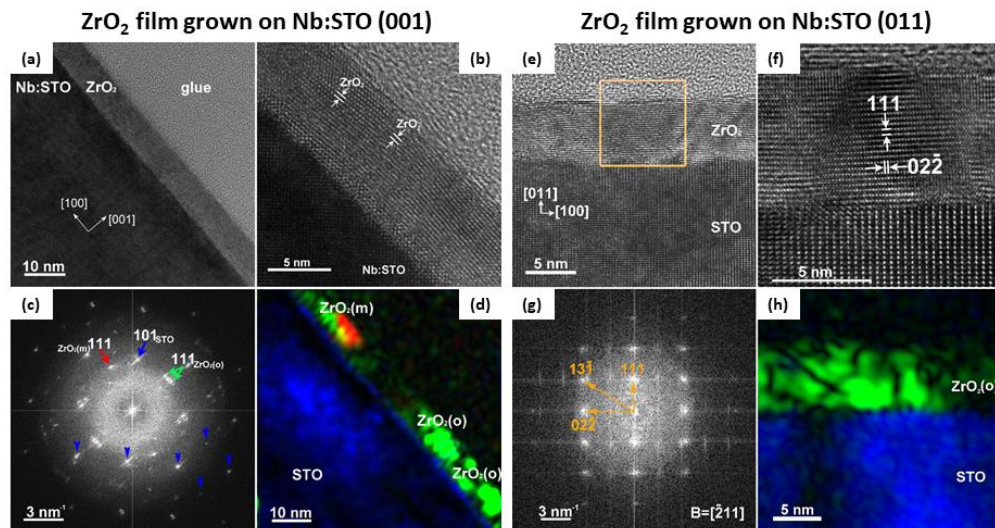


**Fig. 1** (a) HRTEM image of ZrO<sub>2</sub> film grown on (001)Nb:STO; (b) magnified view showing the atomic structure of the ZrO<sub>2</sub>/Nb:STO(001) film; {111}<sub>ZrO<sub>2</sub></sub> planes are labelled; (c) FFT pattern of the HRTEM image in (a); the peak labelled by a red arrow corresponds to *m*-ZrO<sub>2</sub>, the green arrows corresponds to *o*-ZrO<sub>2</sub>, and the blue arrow to the Nb:STO substrate; (d) structural map obtained by FFT<sup>-1</sup> of the pattern in (b), showing the spatial distribution of the *o*- and *m*-phases; (e) HRTEM image of the ZrO<sub>2</sub>/(011)Nb:STO structure; (f) magnified view of an oriented ZrO<sub>2</sub> crystallite; (g) FFT pattern corresponding to the area delimited by the orange square in the HRTEM image (e); (h) Bragg Filtered Image obtained using the (111) spot from the FFT diagram.

Transmission electron microscopy combined with microstructural simulations were used to characterize the crystalline structure of the  $\text{ZrO}_2$  thin film. It will be demonstrated that the orthorhombic phase will be much more stable for the (011) orientation of the Nb:SrTiO<sub>3</sub> substrate and the using of the nanosecond laser in the crystallization process is a good alternative for the stabilization of the o-phase of  $\text{ZrO}_2$ .

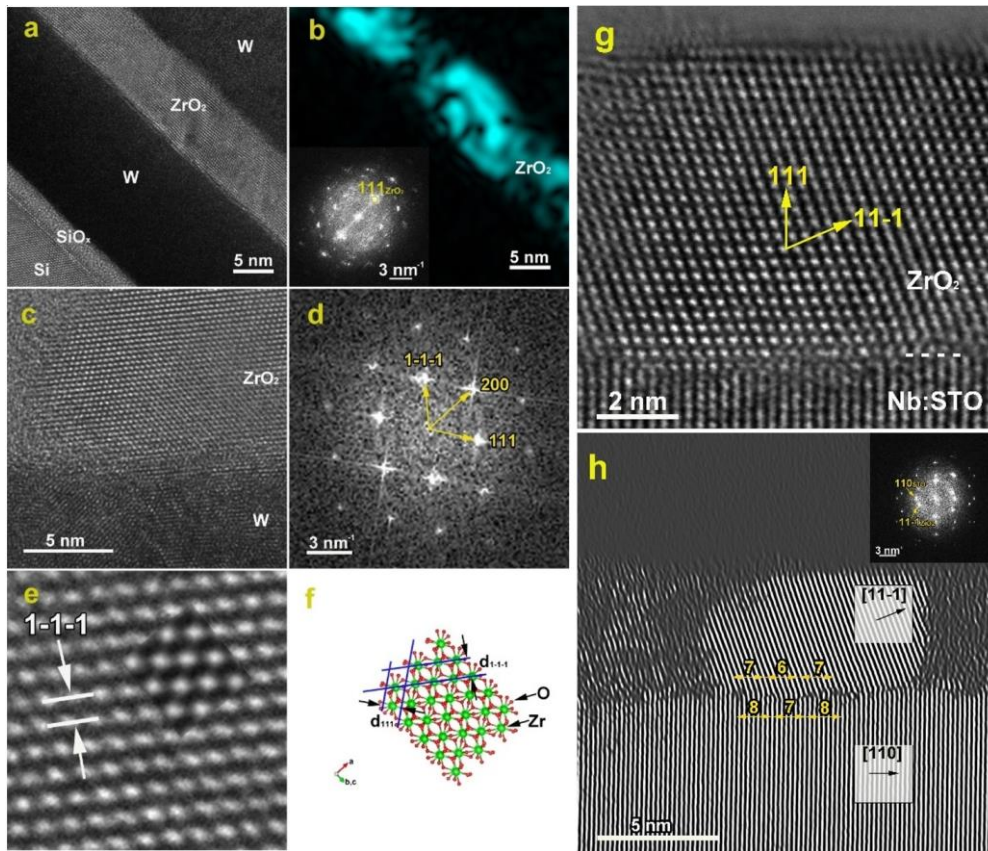


**Fig. 2** (a) Large-area HRTEM image of the Si/SiO<sub>x</sub>/W/ZrO<sub>2</sub>/W structure; (b) Spatial distribution of the  $111_{\text{ZrO}_2}$  lattice fringes obtained by filtering the power spectrum (inserted) of the HRTEM micrograph in (a); (c) HRTEM image of a zone axis oriented ZrO<sub>2</sub> grain at the W/ZrO<sub>2</sub> interface. (d) FFT pattern from an area containing the ZrO<sub>2</sub> crystallite in (c); (e) enlarged HRTEM image of the ZrO<sub>2</sub> crystallite in (c) and the embedded simulated HRTEM pattern of the orthorhombic ZrO<sub>2</sub> (defocus -10 nm, thickness 40 nm); (f) Atomic structural model of ZrO<sub>2</sub> in the [01-1] orientation in perfect agreement with structural data provided by the experimental images, (g) HRTEM image of the ZrO<sub>2</sub>/(111)Nb:STO structure, (h) Inverse FFT pattern of an area which contains both ZrO<sub>2</sub> thin film and STO substrate obtained by filtering the two peaks indicated by yellow arrows from the FFT pattern overlapped in the right top corner of the IFFT image

The cross-section HRTEM micrographs recorded on the ZrO<sub>2</sub>/Nb:STO(001) sample oriented along the [010]<sub>STO</sub> direction did not allow us to conclude on the in-plane crystallographic orientation of the ZrO<sub>2</sub> thin film with respect to the substrate. Although, occasionally, ZrO<sub>2</sub> nanograins may be noticed showing two families of lattice fringes (*e.g.* the outer ZrO<sub>2</sub> nanograin in Fig. 1b, only the (111)<sub>o</sub> lattice fringes of the orthorhombic ZrO<sub>2</sub> phase can be constantly observed running parallel to the interface. A periodic loss of contrast of the (111) lattice fringes along the interface delimits ZrO<sub>2</sub> nanograins/domains with a lateral size of the order of 2–3 nm, depicted also by the structural map in Fig. 1d (the green ZrO<sub>2</sub> nanodomains). The cross-section HRTEM images of the ZrO<sub>2</sub>/(011)Nb:STO film are presented in Fig. 1e and enlarged in Fig. 1f. Both images show an 8-nm thick ZrO<sub>2</sub> layer with a sharp substrate-film interface. The FFT pattern shown in Fig. 1g corresponds to an area delimited by the orange square inside the ZrO<sub>2</sub> layer in Fig. 1e. It contains a well-defined pattern of spots, proving a high crystalline quality of the ZrO<sub>2</sub> film in terms of grain size and preferential crystallographic orientation. The main FFT peaks were measured, indexed and assigned to the (13 $\bar{1}$ ), (111) and (02 $\bar{2}$ ) planes of the *o*-structure of ZrO<sub>2</sub> in the  $[\bar{2}11]$  zone axis orientation. From this structural analysis we can conclude that the orthorhombic phase is much more stable for the (011)

orientation of the STO substrate, whereas for the other orientation fractions of monoclinic ZrO<sub>2</sub> grains was observed.

For the W/ZrO<sub>2</sub>/W/Si sample in which the crystallization process was performed by a nanosecond laser, the fully crystallized state and texturing of the ZrO<sub>2</sub> layer can be observed on the large-area HRTEM image, Fig. 2a, showing 111<sub>ZrO<sub>2</sub></sub> lattice fringes with a preferential orientation parallel to the substrate. The film texturing is better illustrated by the Fourier-filtered image in Fig. 2b. The 111<sub>ZrO<sub>2</sub></sub> texturing of the ZrO<sub>2</sub> thin film is demonstrated on one side by the power spectrum (inserted in Fig. 2b), showing the strong 111<sub>ZrO<sub>2</sub></sub> spots oriented along a direction perpendicular to the substrate. In our case, from the measurements performed both on the HRTEM micrograph and on the FFT picture performed on an area which contains an oriented ZrO<sub>2</sub> crystallite (Fig. 1b), we obtained the following interplanar distances: 0.296 nm ± 0.004 nm, which can be assigned to {111} planes of the o-phase with space group Pca<sub>21</sub>, but this measured distance can be assigned also to the {101} family of planes of the tetragonal phase with space group P4<sub>2</sub>/nmc. The (101) planes of the tetragonal phase are spaced at a 0.3006 nm distance, which is in the error limits of our measurements. Since the FFT pattern, shown in Fig. 2d, contains a well-defined pattern of spots, thus proving a high crystallization degree in terms of grain size and preferential crystallographic orientation, we measured and assigned three peaks to the (1-1-1), (111) and (200) planes of the o-structure of ZrO<sub>2</sub> the crystallite being viewed along the [01-1] zone axis. The structure parameters for this spatial group are: a=0.52336 nm, b=0.52684 nm and c=0.54184 nm. In order to distinguish between tetragonal and orthorhombic phases we use microstructural simulations. The best fit between the experimental and simulated image was obtained for the o-structure as it is indicated in Fig. 1e in which we overlapped the simulated image over the experimental image. We can conclude that nanosecond laser can be used for the crystallization process of the ZrO<sub>2</sub> thin film and the stabilization of the o-phase. For the ZrO<sub>2</sub>/(111)Nb:STO sample we used high resolution transmission electron microscopy to describe the thin film-substrate orientation relationship. In the FFT pattern embedded in Fig. 2h, a well-defined set of peaks emerged from the zone axis of the oriented ZrO<sub>2</sub> grains and from the (111) Nb:STO substrate. The (110)<sub>STO</sub> and (11-1)<sub>ZrO<sub>2</sub></sub> peaks were identified and assigned as indicated by the yellow arrows. The interplanar distances of the planes ( $d_{11-1} = 0.294$  nm) and the (110)<sub>STO</sub> planes ( $d_{110} = 0.275$  nm) give a lattice mismatch of around -6.9%, which rules out conventional epitaxy. The epitaxial relationship can be explained via a near coincidence lattice model or domain matching epitaxy (DME), with the formation of dislocations as the stress relief mechanism. The image in Fig. 2h, obtained with the (11-1)<sub>ZrO<sub>2</sub></sub> and (110)<sub>STO</sub> peaks from the FFT diagram, is a Fourier filtered image and shows the formation of the misfit dislocations at the ZrO<sub>2</sub>-STO interface with epitaxy domains of variable lateral size. Therefore, r-phase ZrO<sub>2</sub> films can be grown on (111) Nb:STO substrates through DME. We note that we examined several regions of the film using HRTEM and found the same features throughout the film. Thus, HRTEM provides representative information about the growth mechanism of the ZrO<sub>2</sub> thin film deposited on the (111)Nb:STO substrate.

#### References

1. J.P.B. Silva, M.C. Istrate, M. Hellenbrand, *et al.*, “Negative Piezoelectric Coefficient in Ferroelectric Orthorhombic Phase Pure ZrO<sub>2</sub> Thin Films”, *Applied Materials Today* 30, 101708 (2023).
2. A.P.S. Crema, M.C. Istrate, A. Silva, *et al.*, “Ferroelectric Orthorhombic ZrO<sub>2</sub> Thin Films Achieved Through Nanosecond Laser Annealing”, *Advanced Science* 10, 2207390 (2023).
3. V. Lenzi, J.P.B. Silva, B. Šmíd, *et al.*, “Ferroelectricity Induced by Oxygen Vacancies in Rhombohedral ZrO<sub>2</sub> Thin Films”, *Energy & Environmental Materials* 7, e12500 (2022).

# Microstructural and EPR Investigation of n-type Co<sub>3</sub>O<sub>4</sub> Nanowire for Hydrogen Gas Sensing

C.G. Mihalcea <sup>a</sup>, V.A. Maraloiu <sup>a</sup>, M. Stefan <sup>a</sup>, G.W.C. Kumarage <sup>b</sup>, D. Zappa <sup>b</sup>, E. Comini <sup>b</sup>

<sup>a</sup>National Institute of Materials Physics, 077125 Magurele, Romania

<sup>b</sup>SENSOR Lab, Department of Information Engineering, University of Brescia, 25133 Brescia, Italy

Gaseous hydrogen is a nonpoisonous, colorless, odorless, highly volatile and flammable compound that has recently become a popular field of research as a potential replacement for petroleum fuel, which is expected to run out within the next 5–6 decades [1,2]. The appeal of hydrogen lies in its green, clean, and renewable qualities, producing minimal environmental impact during combustion [3]. However, if not handled properly, hydrogen can be extremely dangerous as the lower flammability level is just 4%. A proper leakage detection should be always considered in hydrogen storage, to avoid an explosion danger. Moreover, in medicine, detecting hydrogen in breath can assist in diagnosing gastrointestinal illnesses, abnormal digestion of dietary sugars and the speed of food movement through the small intestine.

Semiconducting n-type MOXs have always been considered the primary choice for the fabrication of chemoresistive sensors. Even though p-type MOX sensors have lower gas-sensing capabilities compared to n-type MOX sensors, they are still an interesting subject of study due to their lower dependency on humidity, superior catalytic properties and high chemical stability [4]. In this context, Co<sub>3</sub>O<sub>4</sub> is considered one of the most stable and promising p-type materials for gas sensing [5,6].

We have investigated by analytical transmission electron microscopy (TEM) the structure and morphology of Co<sub>3</sub>O<sub>4</sub> nanowires synthesized through thermal oxidation at 300 °C of a 50 nm metallic cobalt layer deposited on alumina (Al<sub>2</sub>O<sub>3</sub>) substrates by DC magnetron sputtering techniques [7].

The TEM image in Fig. 1a confirms the creation of nanowires with diameters between 6 and 50 nm and lengths of 1–5 μm. The electron diffraction pattern in Fig. 1b indicates the presence of four main reflection planes of Co<sub>3</sub>O<sub>4</sub>, (111), (220), (311) and (400) (CIF no. 9005896). High-resolution transmission electron microscopy (HRTEM) images in Fig. 1c,d indicate that the (311) plane is the most prominent, suggesting that the material is primarily grown in the (311) direction of the spinal Co<sub>3</sub>O<sub>4</sub>. The TEM characterization of various sections of the Co<sub>3</sub>O<sub>4</sub> nanowires is presented in Fig. 2a and the corresponding electron diffraction patterns confirm that the Co<sub>3</sub>O<sub>4</sub> nanowires are grown along the (311) direction throughout the entire wire (Fig. 2b–d). Energy-dispersive X-ray (EDS) analysis of the grown Co<sub>3</sub>O<sub>4</sub> nanowires on TEM grid reveals that the nanowires are composed of only Co and O.

We have also investigated by electron paramagnetic resonance (EPR) the possible presence of paramagnetic defects and/or minority phases in the Co<sub>3</sub>O<sub>4</sub> nanowires, which could affect the sensing process.

Fig. 3a,b shows the X- and Q-band EPR spectra of samples of Co<sub>3</sub>O<sub>4</sub> nanowires deposited on alumina substrates, measured before and after a thermal aging treatment at 400 °C in air for 8 h. Reference spectra of the alumina substrates are also displayed in both figures. The X-band spectrum of the Co<sub>3</sub>O<sub>4</sub> sample before thermal aging exhibits a very broad line at low magnetic fields, which further broadens as the temperature is decreased to 100 K (Fig. 3c). After the thermal aging of the Co<sub>3</sub>O<sub>4</sub> sample, this line disappears and the X-band spectrum shows no difference from the spectrum of the alumina substrate (Fig. 3a).

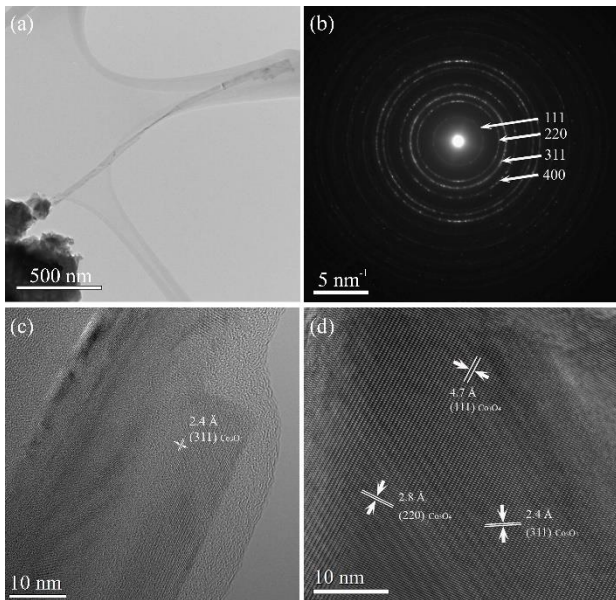


**Fig. 1** (a) Conventional TEM image of a grown  $\text{Co}_3\text{O}_4$  nanowire; (b) electron diffraction pattern, and (c,d) HRTEM image of the TEM image shown in (a).

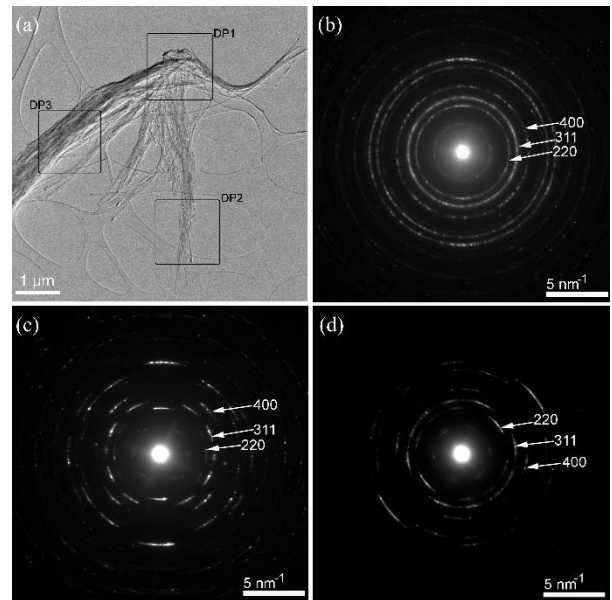


**Fig. 2** (a) An agglomeration of  $\text{Co}_3\text{O}_4$  nanowires and the electron diffraction patterns obtained from different regions of the area showed in image a: (b) area “DP1”, (c) area “DP2”, (d) area “DP3”.

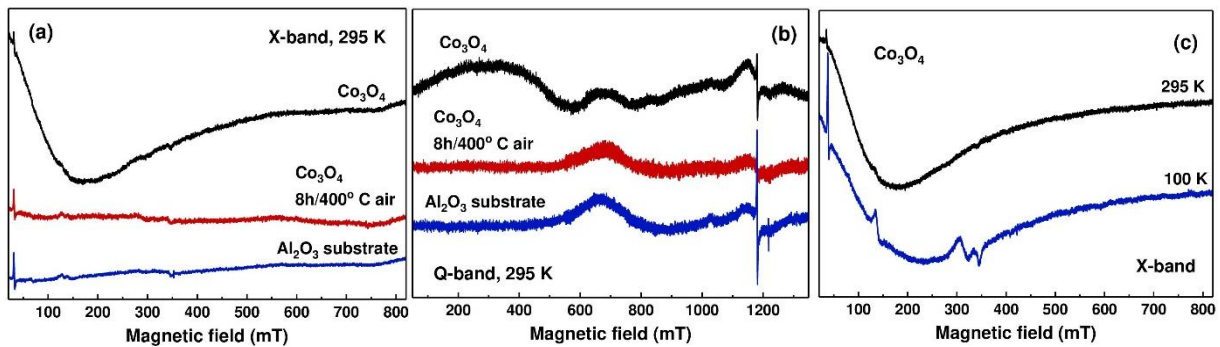


**Fig. 3** EPR spectra of the  $\text{Co}_3\text{O}_4$  nanowires grown on alumina substrates, before and after annealing at  $400^\circ\text{C}$  for 8 h, measured in the (a) X- and (b) Q-band at room-temperature. The spectra of the alumina substrates are also given for reference. (c) X-band EPR spectra of the untreated  $\text{Co}_3\text{O}_4$  sample measured at room-temperature and at 100 K. The narrow lines marked with \* are from paramagnetic centers in the alumina substrate.

The Q-band spectrum of the untreated  $\text{Co}_3\text{O}_4$  sample also consists of a broad line at low magnetic field (up to 550 mT), which disappears after thermal aging (Fig. 3b). This broad line is associated with the presence of a minority ferromagnetic phase, consisting probably of Co and/or CoO clusters [8] due to the incomplete oxidation of the cobalt layer. The disappearance of the line after the  $400^\circ\text{C}$  annealing could be due to the dissolution of the ferromagnetic clusters or oxidation processes that affected the ferromagnetic coupling. A comparison of the X- and Q-band spectra of the  $\text{Co}_3\text{O}_4$  sample with the reference spectra of the alumina substrate shows that all the narrower features superposed on the broad line are due to paramagnetic centers in the substrate. The absence of EPR signals from other paramagnetic centers in  $\text{Co}_3\text{O}_4$  [9] can be explained by the very small amount of  $\text{Co}_3\text{O}_4$  present in the measured sample. Given that the  $\text{Co}_3\text{O}_4$  volume in the EPR samples is of the order of  $10^{-3}\text{ mm}^3$ , such centers could be below the detection limit.

The gas-sensing tests indicated that a higher nanowire density leads to a more pronounced hydrogen-sensing response. Notably, the sensors demonstrate an unusual reversal of the sensor signal from p-type to n-type behavior when operated at temperatures exceeding  $300^\circ\text{C}$ . This behavior is attributed to the participation of lattice oxygen in the gas-sensing mechanism, which is activated by the elevated operating temperature. Remarkably, the sensors maintain a stable baseline conductance even under severe RH conditions (90%) over a testing period of 25 d. This stability is attributed to the catalytic activity of  $\text{Co}_3\text{O}_4$  and the high operating temperature. In comparison to acetone, ethanol, carbon

monoxide, methane, and nitrogen dioxide, the sensors exhibit exceptional selectivity toward hydrogen. The reported response is remarkable, reaching the value of 2.32 in the presence of 100 ppm of hydrogen, with an estimated detection limit of  $\approx 360$  ppb.

Acknowledgments: CERIC-ERIC Consortium proposal no. 20217049, Contract POC 332/390008/29.12.2020-SMIS 109522.

#### References

1. N.A. Utama, A.M. Fathoni, M.A. Kristianto, B.C. McLellan, "The End of Fossil Fuel Era: Supply-Demand Measures through Energy Efficiency", *Procedia Environmental Sciences* 20, 40 (2014).
2. O. Joy, J. Al-Zaili, "On Effectiveness of Current Energy Policy Instruments to Make H<sub>2</sub> Production Projects Financially Viable for Developers: Case of the UK", *International Journal of Hydrogen Energy* 46, 32735–32749 (2021).
3. H. Nam, H. Nam, D. Lee, "Potential of Hydrogen Replacement in Natural-Gas-Powered Fuel Cells in Busan, South Korea based on the 2050 Clean Energy Master Plan of Busan Metropolitan City", *Energy* 221, 119783 (2021).
4. A. Moumen, G.C. Kumarage, E. Comini, "p-Type Metal Oxide Semiconductor Thin Films: Synthesis and Chemical Sensor Applications", *Sensors* 22, 1359 (2022).
5. J. M. Xu, J. P. Cheng, "The Advances of Co<sub>3</sub>O<sub>4</sub> as Gas Sensing Materials: A Review", *Journal of Alloys and Compounds* 686, 753–768 (2016).
6. G.W.C. Kumarage, E. Comini, "Low-Dimensional Nanostructures Based on Cobalt Oxide (Co<sub>3</sub>O<sub>4</sub>) in Chemical-Gas Sensing", *Chemosensors* 9, 197 (2021).
7. G.W.C. Kumarage, D. Zappa, C.G. Mihalcea, *et al.*, "Revolutionizing n-type Co<sub>3</sub>O<sub>4</sub> Nanowire for Hydrogen Gas Sensing", *Advanced Energy and Sustainability Research* 4, 2300067 (2023).
8. R.V. Santos, G.A. Cabrera-Pasca, C.S. Costa, *et al.*, "Crystalline and Magnetic Properties of CoO Nanoparticles Locally Investigated by using Radioactive Indium Tracer", *Scientific Reports* 11, 21028 (2021).
9. Z. Seidov, M. Açıkgöz, S. Kazan, F. Mikailzade, "Magnetic Properties of Co<sub>3</sub>O<sub>4</sub> Polycrystal Powder", *Ceramics International* 42, 12928 (2016).

# **Towards applications**

# Dextran-Coated Iron Oxide Nanoparticles Loaded with 5-Fluorouracil for Drug-Delivery Applications

D. Predoi <sup>a</sup>, M. Balas <sup>b</sup>, M.A. Badea <sup>b,c</sup>, S.C. Ciobanu <sup>a</sup>, N. Buton <sup>d</sup>, A. Dinischiotu <sup>b</sup>

<sup>a</sup> National Institute of Materials Physics, 077125 Magurele, Romania

<sup>b</sup> Department of Biochemistry and Molecular Biology, Faculty of Biology, University of Bucharest, 050095 Bucharest, Romania;

<sup>c</sup> Research Institute of the University of Bucharest (ICUB), University of Bucharest, 050663 Bucharest, Romania

<sup>d</sup> HORIBA Jobin Yvon S.A.S., CEDEX, 91165 Longjumeau, France

Colorectal cancer (CRC) is the third most prevalent malignant tumor and the second most prevalent cause of cancer death in the world. Generally, CRC occurs in people older than 50 [1], more in men than in women [2], and in those who have a family history of CRC [3] as well as inflammatory bowel disease [4]. Surgical resection is the standard treatment for patients with CRC, followed by adjuvant chemotherapy [5]. Current chemotherapy frequently involves 5-Fluorouracil (5-FU), an inhibitor of thymidylate synthase, which impairs DNA replication, exerting an antitumor effect. In this context, new formulations of 5-FU to diminish the side effects and increase the therapeutic efficacy are needed. The aim of our study was to design and test different formulations composed of dextran-coated IONPs loaded with 5-FU with varying nanoparticle:drug ratios on colorectal cancer cells [6]. Our focus was to find a relationship between the formulation ratio of nanoparticles and drug and the cellular response resulting after exposure as a strategy to increase the efficacy of the drug-delivery system [6]. This study demonstrates also, for the first time, the decrease in MCM-2 expression in Caco-2 cells exposed to dextran-coated IONPs loaded with 5-FU. The stable suspension of IONPs was synthesized by the adapted co-precipitation method. The stable suspension of IONPs was mixed with a solution of dextran and 5-FU solubilized in a saline solution. The final suspensions with optimized ratios of IONP:5-FU in the final suspension were 0.5:1, 1:1, and 1.5:1. The information on the morphology and size distribution of the IONPs suspension and IONP loads with 5-FU was obtained using SEM and the results are revealed in Fig. 1. The average particle size was  $6.88 \pm 2$  nm. Thus, the 5-FU presented a morphology in the form of flakes that are arranged circularly.

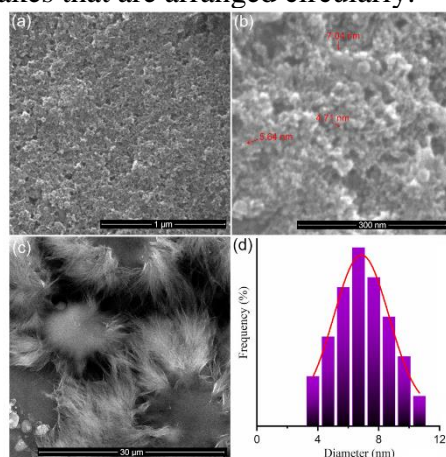


**Fig. 1** SEM images of the (a, b) iron oxide nanoparticles at magnifications of (a) 50,000 $\times$  and (b) 400,000 $\times$  and (c) 5-FU at a magnification of 50,000 $\times$ . (d) Size distributions of the IONPs.

The ratio between IONPs and 5-FU has a slight influence on the morphology of the particles (Fig. 2). Fig. 2a shows the SEM image of IONP:5-FU 0.5:1. Spherical particles with a nanometric size

were observed. The traces of 5-FU that were not completely involved in the particle-coating process were observed (Fig. 2a–lower left). Fig. 2b shows the SEM image of IONP:5-FU 1:1. In this case, particles with a nanometric size and spherical shape that tend to form larger spheres were observed. Fig. 2c shows the SEM image of IONP:5-FU 1.5:1. It can be seen that the size of the particles is nanometric, and the spheres formed by the nanometric particles are well-defined. High-resolution SEM micrographs of IONP:5-FU 0.5:1, IONP:5-FU 1:1, and IONP:5-FU 1.5:1 are presented in Fig. 2d–f. The size distributions for the three samples are also presented in Fig. 2g–i. The average particle size for sample IONP:5-FU 0.5:1 was  $17.23 \pm 2$  nm. The average particle size was  $28.98 \pm 2$  nm for IONP:5-FU 1:1 and  $30.19 \pm 2$  nm for IONP:5-FU 1.5:1.

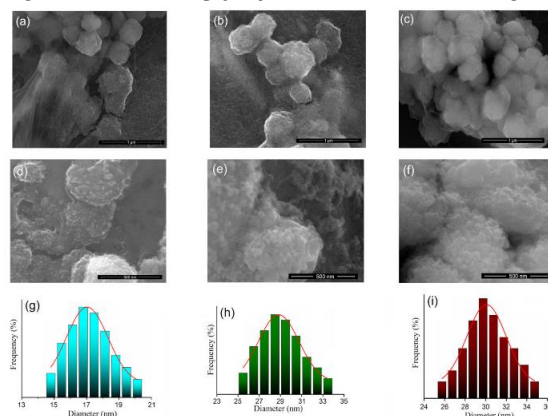


**Fig. 2** SEM image of (a) IONP:5-FU 0.5:1, (b) IONP:5-FU 1:1, and (c) IONP:5-FU 1.5:1 at 50,000 $\times$  magnification. SEM micrographs of (d) IONP:5-FU 0.5:1, (e) IONP:5-FU 1:1, and (f) IONP:5-FU 1.5:1 at 500,000 $\times$  magnification. Size distributions of the (g) IONP:5-FU 0.5:1, (h) IONP:5-FU 1:1, and (i) IONP:5-FU 1.5:1.

The toxicity of IONP:5-FU suspensions on human colorectal cancer cells was assessed using an MTT cell viability assay. The cytotoxic effects were determined after 24 and 48 h exposure and the results were depicted in Fig. 3. The results revealed that the IONPs did not induce any reduction in cell viability across the tested doses.

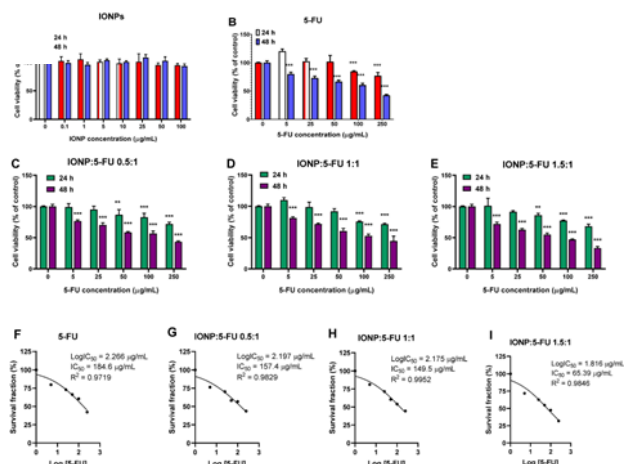


**Fig. 3** Cytotoxicity of nanoformulations in Caco-2 cells. The graphs illustrate the percentages of cell viability after 24 and 48 h exposure to (a) IONPs alone; (b) free 5-FU; (c) IONP:5-FU 0.5:1; (d) IONP:5-FU 1:1; (e) IONP:5-FU 1.5:1. (f–i) IC<sub>50</sub> values for each condition are represented at points. Untreated cells (0  $\mu$ g/mL) were used as a control. Results (control vs. sample) were significant at  $p < 0.01$  (\*\*), and  $p < 0.001$  (\*\*\*)

The administration of 5-FU depicted a time and dose-dependent cytotoxic effects (Fig. 3B). The IONP:5-FU 1.5:1 sample exhibited the most cytotoxic effects, leading to a significant 68%

decrease in cell viability after 48 hours of exposure to a 250  $\mu\text{g}/\text{mL}$  dose of 5-FU. In comparison to the free 5-FU, all the samples exhibited increased cytotoxicity. Moreover, to elucidate the mechanisms underlying the toxic effects of the samples, the morphology of Caco-2 cells, membrane integrity, and oxidative potential were investigated (Fig. 4). The results of the microscopic analysis of Caco-2 cells exposed to the samples, revealed a diminished cell density and the emergence of atypical morphological features characterized by cell shrinkage, membrane extension/retraction, and cell detachment (Fig. 4A). Also, there was no detectable LDH release occurred under any conditions, signifying that the membrane integrity remained unaltered.

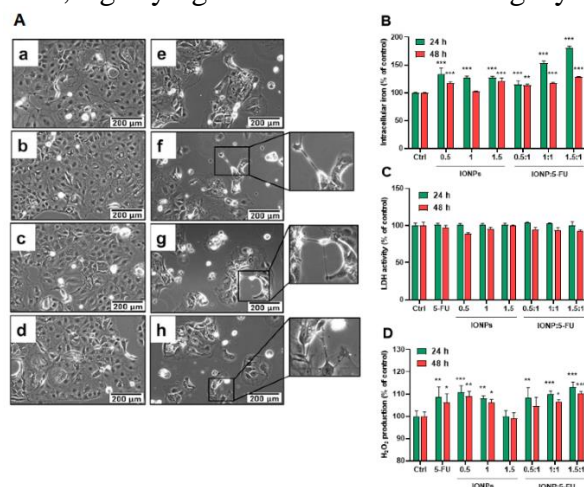


**Fig. 4** Cellular internalization of IONPs and anti-tumoral effects on Caco-2 cells. Cells were exposed for 24 and 48 h to the tested suspensions containing 5-FU in a concentration of 200  $\mu\text{g}/\text{mL}$  and IONP 0.5, 1, and 1.5 with the corresponding concentrations of 6, 12, and 18  $\mu\text{g}/\text{mL}$ , respectively. The figure shows (A) alterations of cell morphology after exposure of Caco-2 cells after 48 h to (a) 0  $\mu\text{g}/\text{mL}$  (control), (b) 6  $\mu\text{g}/\text{mL}$  of IONP, (c) 12  $\mu\text{g}/\text{mL}$  of IONP, (d) 18  $\mu\text{g}/\text{mL}$  of IONP, (e) 200  $\mu\text{g}/\text{mL}$  of 5-FU, (f) 6:200  $\mu\text{g}/\text{mL}$  of IONP:5-FU, (g) 12:200  $\mu\text{g}/\text{mL}$  of IONP:5-FU, and (h) 18:200  $\mu\text{g}/\text{mL}$  of IONP:5-FU. The zoomed images present suggestive cell morphological modifications, (B) intracellular iron content, (C) LDH leakage, and (D) H<sub>2</sub>O<sub>2</sub> production. Results (control vs. sample) were significant at  $p < 0.05$  (\*),  $p < 0.01$  (\*\*), and  $p < 0.001$  (\*\*\*) . Error bars reflect the standard deviation.

The levels of H<sub>2</sub>O<sub>2</sub> in the cells exposed to the samples did not exceed the ones found in the cells exposed to individual components (Fig. 4D). The results obtained in this study highlighted that iron ions could contribute to the augmentation of the antitumoral activity of 5-FU, paving the way for a novel strategy to enhance the effectiveness of 5-FU-based treatments for colorectal cancer.

#### References

1. R.L. Siegel, N.S. Wagle, A. Cercek, *et al.*, “Colorectal Cancer Statistics”, *CA: A Cancer Journal for Clinicians* 73, 17–48 (2023).
2. A. White, L. Ironmonger, R.J.C. Steele, *et al.*, “A Review of Sex Related Differences in Colorectal Cancer Incidence, Screening Uptake, Routes to Diagnosis, Cancer Stage and Survival in the UK”, *BMC Cancer* 18, 906 (2018).
3. K.W. Jasperson, T.M. Tuohy, D.W. Neklason, R.W. Burt, “Hereditary and Familial Colon Cancer”, *Gastroenterology* 138, 2044–2058 (2010).
4. K. Ishimaru, T. Tominaga, T. Nonaka, *et al.*, “Colorectal Cancer in Crohn’s Disease – A Series of 6 Cases”, *Surgical Case Reports* 7, 152 (2021).
5. D. Kotani, E. Oki, Y. Nakamura, *et al.*, “Molecular Residual Disease and Efficacy of Adjuvant Chemotherapy in Patients with Colorectal Cancer”, *Nature Medicine* 29, 127–134 (2023).
6. D. Predoi, M. Balas, M.A. Badea, *et al.*; “Dextran-Coated Iron Oxide Nanoparticles Loaded with 5-Fluorouracil for Drug-Delivery Applications”, *Nanomaterials* 13(12), 1811 (2023).

# Novel Cells Integrated Biosensor based on Superoxide Dismutase on Electrospun Fiber Scaffolds for the Electrochemical Screening of Cellular Stress

C.G. Sanz <sup>a</sup>, A. Aldea <sup>a</sup>, D. Oprea <sup>a,b</sup>, M. Onea <sup>a</sup>, A.T. Enache <sup>a</sup>, M.M. Barsan <sup>a</sup>

<sup>a</sup> National Institute of Materials Physics, 077125 Magurele, Romania

<sup>b</sup> Faculty of Physics, University of Bucharest, 077125 Magurele, Romania

A novel electrochemical biosensor was developed to monitor fibroblast cells stress levels for the first time *in situ* under external stimuli, based on the recognition of superoxide anion released upon cell damage. The biosensor comprised metallized polycaprolactone (PCL) electrospun fibers covered with zinc oxide for improved cell adhesion and signal transduction, whilst stable bioconjugates of mercaptobenzoic acid-functionalized gold nanoparticles/ superoxide dismutase (SOD) were employed as recognition bioelements. Biosensors were first tested and optimized for *in situ* generated superoxide detection by fixed potential amperometry at +0.3 V *vs.* Ag/AgCl, with minimal interferences from electroactive species in cell culture media. L929 fibroblast cells were implanted on the optimized biosensor surface and the scanning electron microscopy (SEM) and fluorescence microscopy investigation revealed a network-type pattern of fibroblasts adjacent to the fiber scaffold. The external cell stress induced by zymosan was monitored at the cells integrated biosensor using fixed potential amperometry (CA) with a sensitivity of 26 nA cm<sup>-2</sup> μg mL<sup>-1</sup> zymosan and electrochemical impedance spectroscopy (EIS), with similar sensitivity of the biosensor considering the *R*<sub>s</sub> and *Z'* parameters of around 0.13 Ω cm<sup>2</sup> μg<sup>-1</sup> mL and high correlation factors *R*<sup>2</sup> of 0.9994. The obtained results underline the applicability of the here developed biosensor for the electrochemical screening of the fibroblast cells stress. The concept in using low-cost biocompatible polymeric fibers as versatile scaffolds for both enzyme immobilization and cell adhesion, opens a new path in developing biosensors for the *in-situ* investigation of a variety of cellular events [1]. The working principle of the proposed biosensor to monitor fibroblast stress levels was based on the enzymatic dismutation of superoxide by SOD, released from living cells under zymosan induced damage. The monitored electrochemical signal was based on the regeneration of the enzymatic centre following the enzymatic dismutation of superoxide. The operational potential was +0.3 V *vs.* Ag/AgCl, chosen to hinder the interference from oxygen and other biological species in cell culture media, previously optimized [2,3].

PCL were first metallized with Au, modified with ZnO nanostructured films prior the SOD immobilization and cell implantation. To establish the role of each component in the biosensor performance, biosensors in different configurations were tested, PCL/Au/SOD, PCL/Au/AuNP<sub>MBA</sub>-SOD, PCL/Au/ZnO/SOD and PCL/Au/ZnO/AuNP<sub>MBA</sub>-SOD. The performance of PCL/Au/ZnO/AuNP<sub>MBA</sub>-SOD biosensors was initially investigated by CA at +0.3 V in 0.1 M PB pH 7.4. Superoxide was generated *in situ* using the xanthine/xanthine oxidase (XO) enzymatic reaction in solution, to better mimic the conditions of superoxide release by the cells, the parameters being optimized in terms of xanthine concentration (2, 5 and 10 μM xanthine) and XO concentration (2, 4, 6 and 8 μL mL XO), respectively. Addition of 10 μM xanthine in the electrolyte solution containing 4 μL mL<sup>-1</sup> XO was chosen for further investigations, equivalent to 2 μM superoxide [4].

For the morphological characterization of the biosensor ensemble, fibroblast adhesion was achieved using a fixation and dehydration protocol, without the introduction of a conductive layer commonly required for visualizing organic substrates. For comparison, a SEM image obtained at cells grown in biocompatible glass is given in Fig. 1A, revealing that fibroblasts grow in a single-cell and in a network-type pattern, adjacent to the surface, similarly to what is observed when grown on the biosensor surface (Fig. 1C). When grown on PCL (Fig. 1B), fibroblast cells have lower degree of

distribution and a circular shape, contrarily to their flattened and well spread morphology observed at the PCL/Au/ZnO/AuNP<sub>MBA</sub>-SOD biosensor, the latter attributed to the ZnO hydrophilicity and increased biocompatibility. Results indicate optimal adhesion of cells on and inside the PCL/Au/ZnO/AuNP<sub>MBA</sub>-SOD 3D fiber network, which means high active area and consequently a high biosensor signal. At higher magnifications, Fig. 1D, the cell surface was easily observed at high resolution, with minimum damage with other two main features: (i) the SOD enzymatic layer covering the fibers with a morphology and structure comparable to that observed in a previous study [1] and (ii) the proximity between fibroblasts and the SOD layer, both very important for the device operability.

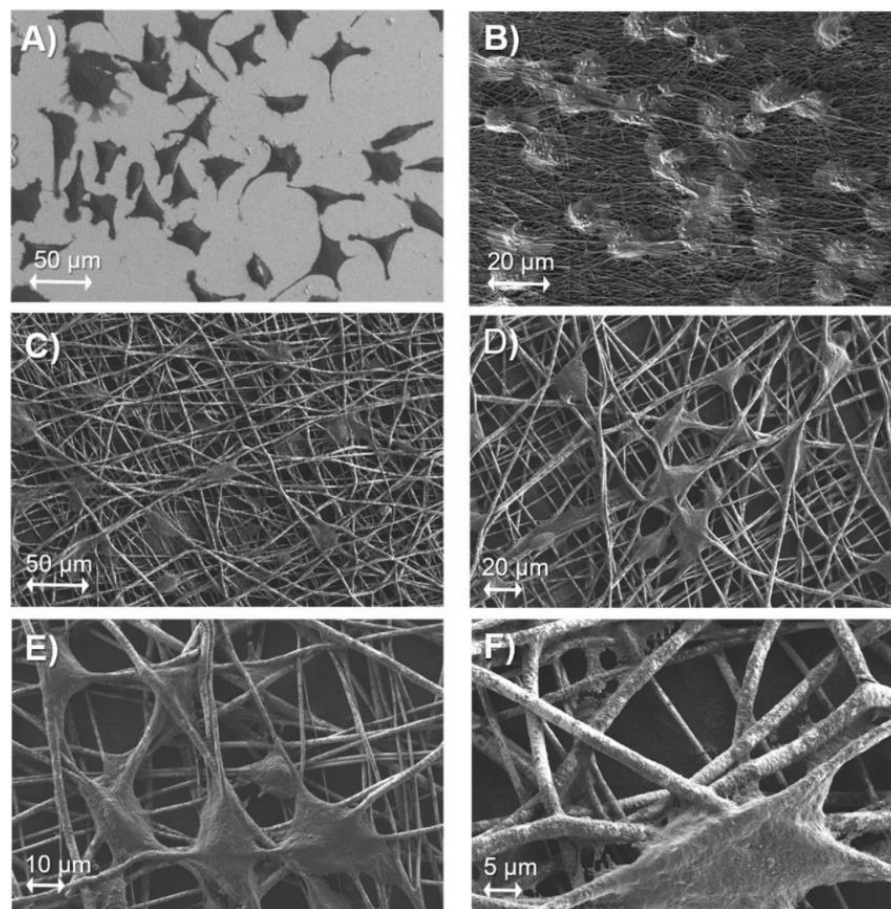


**Fig. 1** SEM images at (A) biocompatible glass flasks/L929, (B) PCL/L929, and (C–F) at PCL/Au/ZnO/AuNP<sub>MBA</sub>-SOD/L929 at different magnifications: (C) 300 $\times$ , (D) 500 $\times$ , (E) 1000 $\times$ , and (F) 2000 $\times$ . Reproduced from Ref. [1].

The quantitative analysis of zymosan-induced stress at the PCL/Au/ZnO/AuNP<sub>MBA</sub>-SOD/L929 biosensor was performed by recording EIS spectra in the frequency range from 65 to 1 kHz, Fig. 2A. The impedance spectra were fitted with an equivalent circuit consisting of only a  $R_s$  in series with an  $R_1$ - $CPE_1$  and another  $CPE_2$  for the final frequency region of the spectra (Fig. 2C). Impedance spectra were recorded before and after the successive addition of zymosan, in the following concentrations: 0–24, 24–152 and 152–248  $\mu\text{g mL}^{-1}$ . Two parameters had a linear dependency with the stressing agent concentration,  $R_s$  (obtained from fitting the spectra with the equivalent circuit) and the  $Z'$  value at 10 kHz. A typical calibration plot is depicted in Fig. 2A2, which shows similar sensitivity of the sensor considering the  $R_s$  and  $Z'$  parameters of around  $0.13 \Omega \text{ cm}^2 \mu\text{g}^{-1} \text{ mL}$ . The close to 1 value of the linear correlation factors denotes the high accuracy of the method here employed.

Control experiments were performed at the PCL/Au/ZnO/AuNP<sub>MBA</sub>-SOD biosensor for increasing concentrations of xanthine from 0 to 400  $\mu\text{M}$ , which corresponds to 0–80  $\mu\text{M}$  superoxide. Spectra recorded are displayed in Fig. 2B1, which shows the same profile as the ones recorded at the

PCL/Au/ZnO/AuNP<sub>MBA</sub>-SOD/L929 biosensor, with the same equivalent circuit being employed to fit the spectra. Similarly, an increase in the real part of the impedance values with increasing concentration of superoxide was observed, with a linearity of  $R_s$  and  $Z'$  within the concentration range of 0–20  $\mu\text{M}$  superoxide and saturation of the biosensor signal for higher superoxide concentrations (Fig. 2B2).

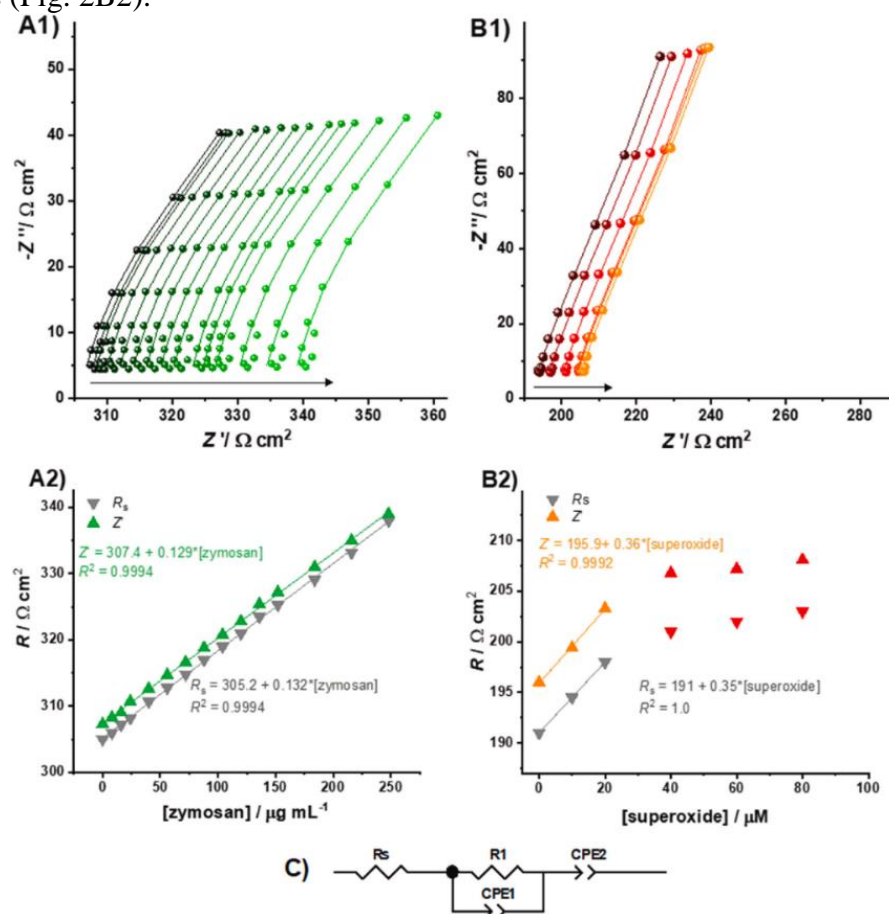


**Fig. 2** (1) Complex plane impedance plots recorded at OCP in cellular media with (A) PCL/Au/ZnO/AuNP<sub>MBA</sub>-SOD/L929 for increasing concentration of zymosan from 0 to 248  $\mu\text{g mL}^{-1}$  and (B) PCL/Au/ZnO/AuNP<sub>MBA</sub>-SOD for increasing superoxide concentration from 0 to 80  $\mu\text{M}$ ; (2) Corresponding calibration plots with the linear dependences of  $R_s$  and  $Z'$  (at 10 Hz) with zymosan in (A) and superoxide in (B); (C) the equivalent circuit used to fit the spectra. Reproduced from Ref. [1].

### References

1. C.G. Sanz, A. Aldea, D. Oprea, *et al.*, “Novel Cells Integrated Biosensor based on Superoxide Dismutase on Electrospun Fiber Scaffolds for the Electrochemical Screening of Cellular Stress”, *Biosensors & Bioelectronics* 220, 114858 (2023).
2. C.G. Sanz, D.N. Crisan, R.J.B. Leote, *et al.*, “Bioconjugates of Mercaptocarboxylic Acids Functionalized AuNP and Superoxide Dismutase for Superoxide Electrochemical Monitoring”, *Microchimica Acta* 189, 245 (2022).
3. C.G. Sanz, M. Onea, A. Aldea, M.M. Barsan, “Disposable Superoxide Dismutase Biosensors based on Gold Covered Polycaprolactone Fibers for the Detection of Superoxide in Cell Culture Media”, *Talanta* 241, 123255 (2022).
4. L. Wang, W. Wen, H. Xiong, *et al.*, “A Novel Amperometric Biosensor for Superoxide Anion based on Superoxide Dismutase Immobilized on Gold Nanoparticle-Chitosan-Ionic Liquid Biocomposite Film”, *Analytica Chimica Acta* 758, 66–71 (2013).

# Pulsed Laser Deposited $V_2O_3$ Thin-Films on Graphene/Aluminium Foil for Micro-battery Applications

T. Tite <sup>a</sup>, C. Ungureanu <sup>b,c</sup>, M. Buga <sup>b</sup>, I. Stavarache <sup>a</sup>, E. Matei<sup>a</sup>, C.C. Negrila <sup>a</sup>, L. Trupina <sup>a</sup>, A. Spinu-Zaulet <sup>b</sup>, A.C. Galca <sup>a</sup>

<sup>a</sup> National Institute of Materials Physics, 077125 Magurele, Romania

<sup>b</sup> National Research and Development Institute for Cryogenics and Isotopic Technologies – ICSI, 240050 Râmnicu Vâlcea, Romania

<sup>c</sup> Faculty of Power Engineering, Politehnica University of Bucharest, 060042 Bucharest, Romania

Currently, there is a frantic search for innovative technological solutions for the improvement of lithium-ions battery (LiBs), notably concerning their performance and the use of non-sustainable materials (*e.g.*, Cobalt). Over the past years, vanadium oxides ( $VO_x$ ) have been explored as promising electrodes for batteries owing to their sustainability, and their promising electrochemical properties such as their high theoretical capacity. Recently, vanadium sesquioxide, alias  $V_2O_3$ , has caught the interests of scientific community due to its outstanding theoretical capacity as anode. However, it is worth mentioning that the cathode constitutes the most crucial component of LIBs determining its energy density and capacity. Surprisingly, little attention has been paid to date to the application of  $V_2O_3$  as cathode. As cathode,  $V_2O_3$  can exhibit a theoretical specific capacity as high as  $\sim 356 \text{ mAhg}^{-1}$  which is far larger than most of commercial lithium ion cathodes. Various synthesis methods have been used to synthesize  $V_2O_3$ . Nowadays, the development of thin film by using physical vapor deposition (PVD) methods has become a critical basis for advanced binder-free high-performance cathode. In this work, we report on the feasibility to synthesize  $V_2O_3$  thin films directly on graphene (G)/Al current collector by ablating an inexpensive  $V_2O_5$  target and applying a rapid thermal annealing (RTA) at low temperature ( $430 \text{ }^\circ\text{C}$ ) (Fig. 1). The physico-chemical properties of the films were multi-parametrically ascertained, qualitatively and quantitatively, by various analytical techniques such as scanning electron microscopy (SEM), atomic force microscopy (AFM), energy-dispersive X-ray spectroscopy (EDXS), X-ray diffraction (XRD), Raman spectroscopy, X-ray photoelectron spectroscopy (XPS), and electrochemistry.

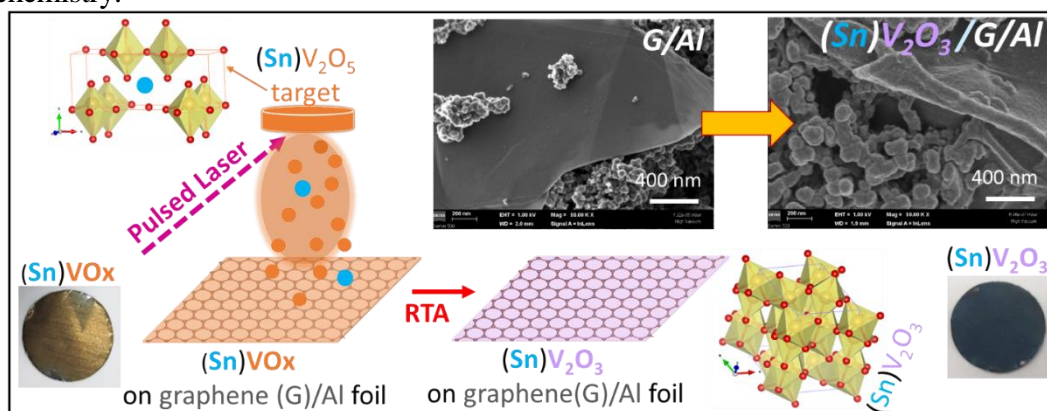


**Fig. 1** Overview of the synthesis of undoped or Sn doped  $V_2O_3$  thin films on G/Al by pulsed laser deposition. SEM top-view images of G/Al before and after coating.

SEM images have indicated good uniformity of the coatings (Fig. 1). The XRD patterns have shown that  $VO_x$  films after RTA have a rhombohedral  $V_2O_3$  structure (ICDD-PDF4: 04-008-7632,

space group  $R\bar{3}C$ ) (Fig. 2a). No supplemental phases other than  $V_2O_3$  and G/Al substrate were detected. The diffraction maxima of the Sn-doped  $V_2O_3$  samples were slightly shifted in comparison to the undoped sample and were situated at around  $24.24^\circ$ ,  $32.97^\circ$ ,  $36.19^\circ$ ,  $41.20^\circ$ ,  $49.78^\circ$ ,  $53.97^\circ$  ( $2\theta$ ). This could indicate an expanded  $V_2O_3$  lattice owing to the larger radius of  $Sn^{4+}$  ( $0.83 \text{ \AA}$ ) relative to  $V^{3+}$  ( $0.78 \text{ \AA}$ ). The average crystallite size estimated by the Scherrer equation for the 104 line of  $V_2O_3$  was found to be around 50 nm for both the undoped and Sn-doped  $V_2O_3$  films. The Raman spectra of both the undoped and Sn-doped vanadium oxides taken at different spots showed sharp peaks positioned at around 141, 211 ( $E_g$ ), 240 ( $A_{1g}$ ), 264 ( $A_{1g}$ ), 300 ( $E_g$ ), 355 ( $E_g$ ), 504 ( $A_{1g}$ ) and  $1005 \text{ cm}^{-1}$ , which have been attributed to the  $V_2O_3$  phase and further confirmed the stoichiometry of the films obtained after RTA (Fig. 2b). XPS measurements were performed to assess the composition and oxidation state of the hybrid materials. The proportion of  $V^{5+}$  valence which was around 70% for the as-deposited (AD) samples has been found to decrease after RTA for both undoped and Sn-doped  $V_2O_3$  samples in benefit of the presence of lower vanadium valences states (*e.g.*,  $V^{4+}$ ,  $V^{3+}$ ,  $V^{2+}$ ); thereby demonstrating the possibility to reduce the AD samples under neutral atmosphere. The V  $2p_{3/2}$  and V  $2p_{1/2}$  core levels of  $V_2O_3$  and Sn- $V_2O_3$  could be resolved with  $V^{3+}/V^{4+}/V^{5+}$  proportion of 28.8/41.6/18.2% and 27.2/34.7/38%, respectively (Fig. 2c). The high resolution XPS spectra also indicated the presence of Sn 3d photoelectron line (Sn  $3d_{5/2}$  and Sn  $3d_{3/2}$  doublet) for Sn- $V_2O_3$  confirming along with EDXS analysis its status as doped samples [1].

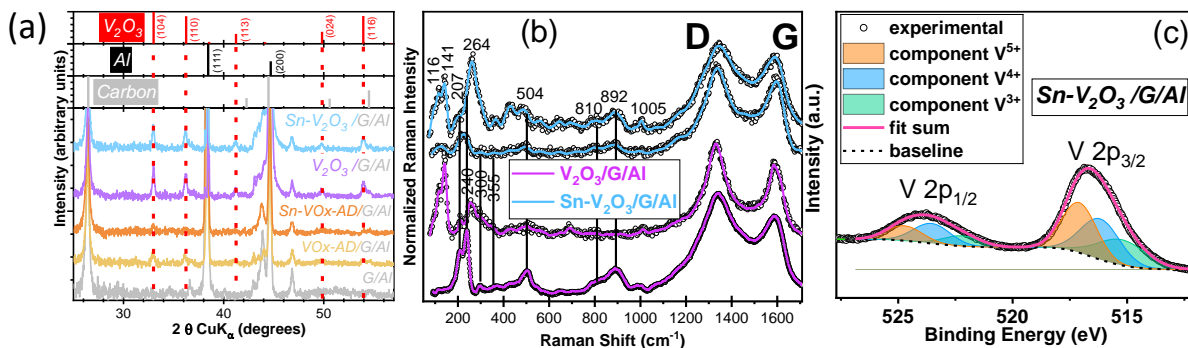


**Fig. 2** (a) XRD patterns of G/Al, AD and annealed undoped or Sn- $V_2O_3$  samples; (b) Raman spectra of annealed undoped or Sn- $V_2O_3$ ; (c) High resolution XPS spectra of V 2p core level of Sn- $V_2O_3$ .

The electrode has been proposed to be tested without the need of additional steps of preparation, as CR 2032 button cell cathode for LiBs. The electrochemical properties have been investigated by cyclic voltammetry (CV), galvanostatic charge-discharge (GCD) and electrochemical impedance spectroscopy (EIS).

The C–V curves of  $V_2O_3$  and Sn- $V_2O_3$  have shown some cathodic (*e.g.*, at around 2.5, 2.7, 3, 3.4 V) and reduction peaks (*e.g.*, at around 2.7, 3.2 and 3.5 V) indicating multi-step insertion of  $Li^+$  ions (Fig. 3a). The gravimetric specific capacity calculated based on the area under the CV curves were higher for  $V_2O_3$  ( $253 \text{ mAh g}^{-1}$ ) and Sn- $V_2O_3$  ( $271 \text{ mAh g}^{-1}$ ) than graphene ( $26 \text{ mAh g}^{-1}$ ), indicating their ability to store more charge. EIS analysis based on equivalent circuit element (Fig. 3b) has shown that Sn- $V_2O_3$  exhibited both the lowest ohmic resistance (*i.e.*, less extended electrolyte decomposition) and the lowest charge transfer resistance (*i.e.*, an easier lithium intercalation and less resistive migration of  $Li^+$  through the double layer).

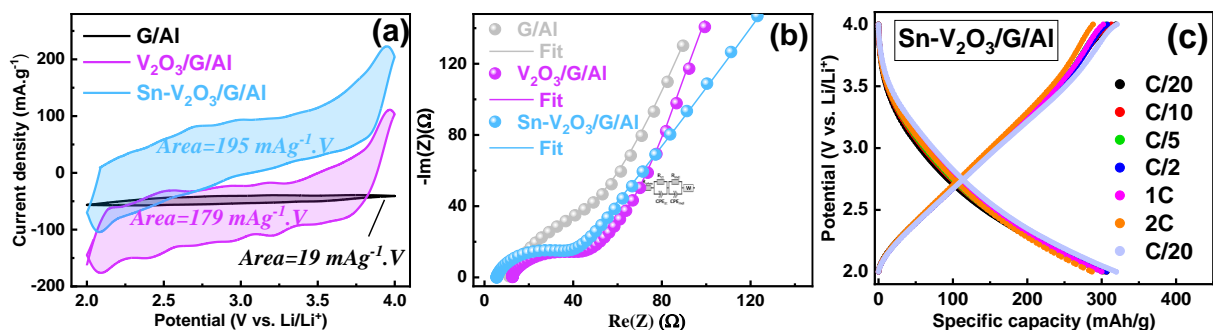


**Fig. 3** (a) CV curves of G/Al, V<sub>2</sub>O<sub>3</sub>/G/Al, and Sn-V<sub>2</sub>O<sub>3</sub>/G/Al; (b) EIS showing the Nyquist plots of the samples after cycling; (c) GCD profile of Sn-V<sub>2</sub>O<sub>3</sub>/G/Al at different C-rates (C/20, C/10, C/5, C/2, 1C, 2C and C/20).

GCD measurements were carried out to study the rate capability of the electrodes at different C-rates and cycling robustness of the electrodes. GCD has indicated that Sn-V<sub>2</sub>O<sub>3</sub> is a very stable electrode having a profile quite stable capacity over C-rate, in comparison to other electrodes. Cycling performance has been carried out at short (Fig. 4a) and long cycles (Fig. 4b). The initial discharge capacity for Sn-V<sub>2</sub>O<sub>3</sub>, V<sub>2</sub>O<sub>3</sub> and G was ~310.4, 299.6 and 10 mAh g<sup>-1</sup>, with a capacity loss estimated after 30 cycles of ~0.252, 0.455 and 2.07%/cycles respectively (Fig. 4a). After 200 cycles the capacity loss of Sn-V<sub>2</sub>O<sub>3</sub> was ~25% (~0.128%/cycle), which was 2.5 times lower than the value obtained for V<sub>2</sub>O<sub>3</sub> (Fig. 4b), indicating Sn-doped V<sub>2</sub>O<sub>3</sub> sample provides the best electrochemical performance in terms of higher specific capacity and higher retention capability.

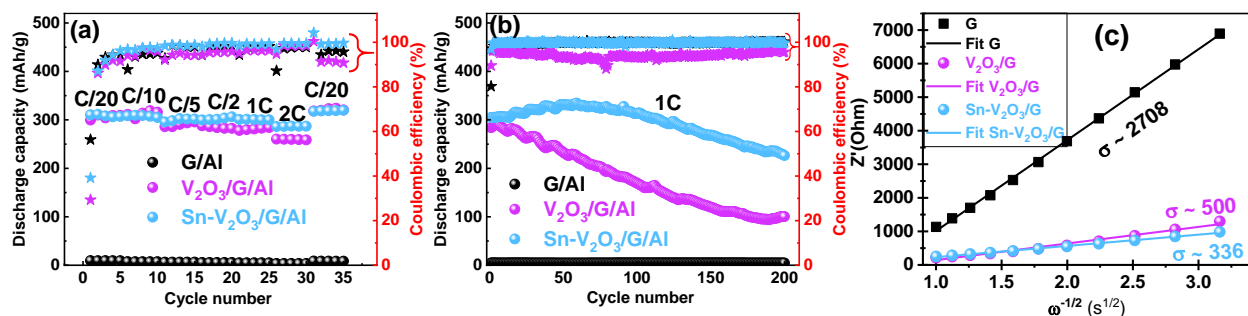


**Fig. 4** Cycling performance of (G/Al), V<sub>2</sub>O<sub>3</sub>/G/Al and Sn-V<sub>2</sub>O<sub>3</sub>/G/Al samples at (a) different C-rates and (b) at 1C for 200 cycles. (c) Linear fitting of Z' vs.  $\omega^{-1/2}$ .

It has been suggested that Sn-doping has the ability to enhance the intercalation/extraction reactions of Li (*i.e.*, Li<sup>+</sup> diffusion) and suppress the structural change of the host material during the electrochemical reactions. The Li<sup>+</sup> diffusion coefficients for Sn-doped V<sub>2</sub>O<sub>3</sub> calculated based on the Warburg region of EIS (Fig. 4c) was found 67 times higher compared to bare G/Al, and by 2.5 times increased with respect to the undoped V<sub>2</sub>O<sub>3</sub>. All the samples showed a Coulombic efficiency of approximately 100%, indicating a good efficiency of electron transfer between the electrode and lithium metal and negligible irreversible reactions within the cells.

Our work suggested the engineering of V<sub>2</sub>O<sub>3</sub> by Sn-doping could be a path towards improved electrochemical performance for LiBs and could be useful benchmark for future development of vanadium oxides-based cathode.

#### References

1. T. Tite, C. Ungureanu, M. Buga, *et al.*, "Pulsed Laser Deposited V<sub>2</sub>O<sub>3</sub> Thin-Films on Graphene/Aluminum Foil for Micro-Battery Applications", *Journal of Electroanalytical Chemistry* 933, 117290, (2023).

# Advances in Processing and Characterization of Materials for the DEMO Fusion Thermo-nuclear Reactor

**M. Galatanu <sup>a</sup>, M. Enculescu <sup>a</sup>, M. Grigorescu <sup>a</sup>, A. Galatanu <sup>a</sup>; D. Ticos *et al.* <sup>b</sup>; W. Pantleon *et al.* <sup>c</sup>; M. Dias *et al.* <sup>d</sup>; K. Poleschuk, D. Terentyev *et al.* <sup>e</sup>**

<sup>a</sup> National Institute of Materials Physics, 077125 Magurele, Romania

<sup>b</sup> National Institute for Laser, Plasma and Radiation Physics, 077125 Magurele, Romania

<sup>c</sup> Technical University of Denmark, Dept Civil & Mech Engr, Sect Mat & Surface Engr, DK-2800 Lyngby, Denmark

<sup>d</sup> Instituto de Plasmas e Fusão Nuclear, Instituto Superior Técnico, Universidade de Lisboa, 1049-001 Lisboa, Portugal

<sup>e</sup> Institute for Nuclear Materials Science, SCK CEN, 2400 Mol, Belgium

Obtaining energy using thermo-nuclear fusion reactors might be seen as the most promising long-term sustainable solution for the increasing world energy demand. Thus, an ambitious program, EUROfusion, is running at European level in order to achieve such a goal as soon as possible. According to the fusion [roadmap](#) the DEMO reactor should be the first reactor able to deliver electricity to the grid and therefore its operation will most likely require materials with better properties as those already decided for ITER, the reactor being now built in France. Tungsten (W) was selected as the main divertor armor material for ITER and is the „base-line” option for DEMO, but higher temperatures and irradiation doses are demanding a more advanced material. Some of the main concerns are related its high brittle to ductile transition temperature (BDTT), its low thermal expansion coefficient (CTE) - which generates problems in joining W to the structural materials and finally its evolution under intense neutron irradiation. Our group is involved in several tasks tackling these problems and some interesting results have been obtained in 2023 concerning a more ductile W material, producing better interfaces to the heatsink part and different joining routes.

Different to other bcc materials, W microstructure plays a major role in setting its mechanical behavior, in particular its intergranular fracture behavior, which is responsible for the high BDTT of W. In the frame of Prospective Research and Development package of the project, a fast forward screening of some ceramic and metallic candidate dispersions to be used in the W matrix have been performed to evaluate the effects on the thermo-physical and thermo-mechanical properties of W.

The dispersions considered were carbides like SiC or ZrC and diamond (the last one most likely producing W-C), metals which can interact with W during the processing steps, like Cr or metals which are melting during processing but do not react strongly with W, like Fe. The samples have been consolidated by SPS using for W a mixture of 75% 40 μm and 25 % 800 nm powders and various dispersions with dimensions below 60 nm. Based on micro-structural, thermo-physical and material evolution under 6 MeV electrons irradiation, ZrC and Cr containing materials have been selected for further investigations, while the other dispersions have been down selected.

The 3-point bending test results [1], obtained on W-ZrC 0.5% wt. are summarized in Fig. 1, for different temperatures: 20, 156, 206, 290, 395, 484 and 625 °C. Surprisingly, even the sample tested at 156 °C shows some ductility in these tests, as do all the other samples tested at higher temperatures. with stress-strain curves similar to those obtained in literature on hot rolled W-ZrC (see *e.g.*, Sci.Rep. 5, 2015, 16014). Even more surprisingly most of the samples maintained a macroscopic integrity in spite of severe cracking occurring during tests, as illustrated in the top left panel of Fig. 2 for specimens tested at 206 and 395 °C. It should be noted that an almost linear shape might be ascribed to a bulk elasticity of the specimen while

a bended shape points to ductile behavior. Post-mortem SEM analyses have been performed in order to clarify this peculiar behavior.

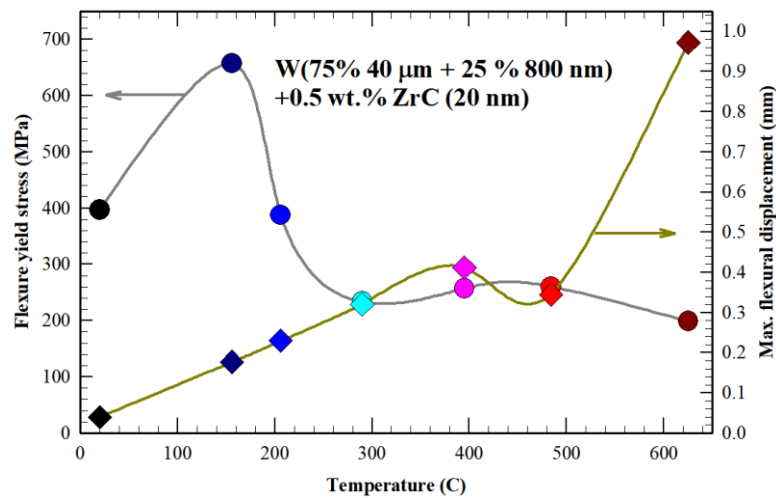


**Fig. 1** Temperature dependencies of the flexural yield stress and the maximal flexural displacement of the sample before complete cracking.

In Fig. 2 top right panel the tensile stressed part of the sample bended at 206 °C is shown. In this part an intergranular fracture is observed, while in the compression stressed part of the same sample, grains with intragranular fracture can be observed (Fig. 2–bottom right panel). In fact, intra-granular fracture is observed at all temperatures in the compressed parts, pointing to the fact that the dispersed ZrC powders have played a role in the reduction of intergranular fracture. However, as the test temperature increases, at the tensile stressed part signs of ductile fracture appear, as illustrated in the bottom left panel of Fig. 2 for the specimen tested at 395 °C.

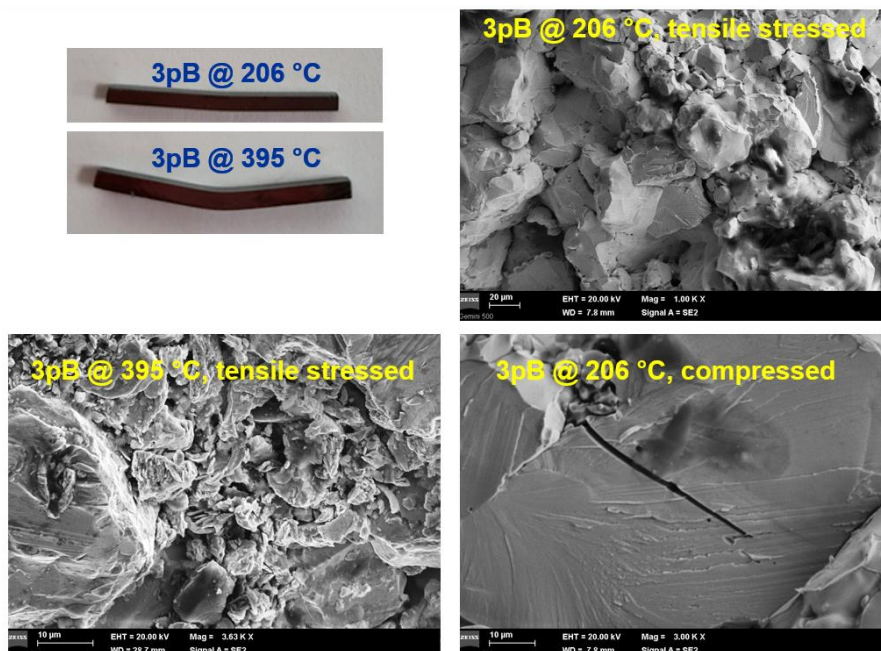


**Fig. 2** Specimens appearance after 3-point bending tests performed at 206 °C and 395 °C (top left); Fracture surface image of the tensile stressed part of the specimens tested at 206 °C (top right) and of at 395 °C (bottom left); Fracture surface image of the compression stressed part of the specimen tested at 206 °C (bottom right).

To characterize the thermal stability of the material, specimens have been analyzed by our partner from Technical University of Denmark using microstructural and recrystallization

investigations after long time exposure (12 weeks) at temperatures of 1350 and 1450 °C. The results show only minor changes even after 12 weeks at 1450 °C, without coarsening and a constant hardness. These promising results are being pursued and currently samples produced by a further elaborated route have shown a full ductile behavior above 300 °C.

In order to improve the connection between W and heat sink materials Cu-Y<sub>2</sub>O<sub>3</sub> and CuCrZr-Y<sub>2</sub>O<sub>3</sub> composites have been studied in collaboration with our partner from IST in Portugal [2]. Specimens produced in NIMP have been irradiated in Portugal with 300 keV Ar<sup>+</sup> beam to a fluence of 1×10<sup>19</sup> ions/cm<sup>2</sup> aiming to cause a damage level amounting to ~100 dpa. Although the irradiation of the samples did not show surface modification, nano-indentation testing resulted in a reduction of hardness due to foam-like behavior arising from nucleation of voids at vacancy clusters.

In spite of consistent research efforts invested in the development of the ITER divertor, some important aspects like degradation of the mechanical properties of the W/Cu/CuCrZr interface under the ITER operational conditions remain to be assessed. Therefore, in a collaborative work with SCK-CEN in Belgium we have produced in NIMP using our FAST technology different types of W-Cu and W-CuCrZr joints using ITER-grade materials which were further processed by our partners in Belgium in order to develop a sub-miniaturized testing methodology for W/Cu joints extracted from the ITER-specification monoblock [3].

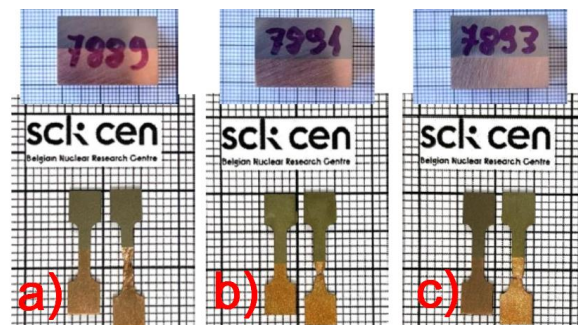


**Fig. 3** Joined W-Cu blocks processed by FAST in NIMP (top), standard specimens processed for tensile test (on the left) and the same specimens after tensile tests performed at (a) room-temperature and (b and c).350 °C.

Fig. 3 shows some results of tensile tests performed by the Belgian partner on standard specimens, both at RT and 350 °C. As it can be easily seen, the load affected part of the specimens is found only in the Cu part, illustrating the excellent quality of the joints produced by FAST.

#### References:

1. M. Galatanu, M. Enculescu, A. Galatanu, *et al.*, “Micro Engineering Design for Advanced W-Based Bulk Materials with Improved Properties”, *Nanomaterials* 13, 1012 (2023).
2. R. Martins, F. Antão, J.B. Correia, *et al.*, “Behavior of Cu-Y<sub>2</sub>O<sub>3</sub> and CuCrZr-Y<sub>2</sub>O<sub>3</sub> Composites Before and After Irradiation”, *Nuclear Instruments and Methods in Physics Research B* 539, 73–78 (2023).
3. K. Poleshchuk, D. Terentyev, C. Chang, *et al.*, “Development of Sub-miniaturised Testing Methodology for W/Cu Joints Extracted from the ITER-specification Monoblock”, *Fusion Engineering and Design* 194, 113925 (2023).

# Enhanced Magnetic performances in Novel RE-free Nanocomposite Magnets

O. Crisan, A.D. Crisan

National Institute of Materials Physics, 077125 Magurele, Romania

There is nowadays a strong interest for multipurpose materials, specifically designed for various applications. For instance, researching for novel RE-free nanocomposite magnets has yielded the discovery of several classes of magnets that are derived from systems bearing formation of  $L1_0$  phases. The tetragonal  $L1_0$  phase is the high ordered crystal structure which in the case of FePt-based alloys gives its hard magnetic features. Fe-Pt binary system and their derived FePt-based alloys usually crystallizes in a disordered face-centered-cubic fcc A1 structure. The fcc structure transforms after appropriate annealing into an ordered face-centered-tetragonal fct allotrope phase which is of interest since it exhibits high coercivity and large magnetocrystalline anisotropy.  $L1_0$ -phase magnets present equally good magnetic performance in terms of energy product, being also possible to perform at higher temperatures than classical RE magnets, and have good corrosion resistance properties. The nanocomposite magnets derived from FePt system is widely considered as potential candidates for applications requiring high temperatures of operation with potentially good resistance to corrosive media. The binary FePt nanoparticles have also strong catalytic response, being also a material with significant biocompatibility. With respect to catalytic properties, some other ternary systems such as Fe-Mo-B have shown good perspectives therefore a mixed stoichiometry compound deriving from FePt systems with Mo and B addition can presumably also yield good magnetic and catalytic properties. Motivated by the possibility to obtain a new class of RE-free magnet, derived from the FePt system, and at the same time by the possibility to obtain good catalytic properties, we had the idea to synthesize a quaternary Fe-Pt-Mo-B alloy, by taking advantage on both our previous expertise in developing FePt-based magnets, as well as on previous results obtained in Fe-Mo-B systems. Here [1] we reported on the synthesis for the first time of a quaternary alloy Fe-Pt-Mo-B, by using a rapid solidification from the melt method, studied on their structural and magnetic features and proved the formation of hard magnetic  $L1_0$  phase in our alloy, upon appropriate annealing of the as-obtained melt spun ribbons. The peak analysis, using a Rietveld-type refinement technique has allowed us to prove that the observed Bragg peaks belong to the FePt face-centered-cubic (fcc) lattice (A1 phase,  $Fm\bar{3}m$  space group, lattice parameter:  $a = 0.38$  nm), an average size of 4 nm, a symmetry that is commonly observed in the case of colloidal near-equiatomic FePt nanoparticles.

In the diffractogram obtained for the sample annealed at 600 °C for 1 hour, there are notable differences from the as-cast sample. Several additional Bragg lines are observed, much narrower, witnessing for the fact that the sample is in a fully crystallized state, thus confirming our assumptions regarding the origin of the exothermic effect observed at 550 °C. Most of the additional Bragg peaks were indexed as belonging to the face-centered-tetragonal (fct)  $L1_0$  FePt phase ( $P4/mmm$  space group), with the exception of two peaks of very low intensity, marked on the graph with #, which are attributed to the orthorhombic  $Fe_2B$  phase. There is some overlapping of the main Bragg peaks of A1 and  $L1_0$  FePt phases, for instance fcc (111) and fct (111), however upon formation of the  $L1_0$  phase, the fcc (200) undergoes a tetragonal splitting with the formation of (200) and (002) Bragg peaks of the fct phase. More important, we have noticed the two Bragg peaks occurring at around 24° and 33° in  $2\theta$ , which constitute the well-known signature of the tetragonal phase, *i.e.*, the so-called “superlattice” Bragg peaks (001) and (110). These peaks were

unambiguously observed and indexed in the spectrum and indicate without doubt the occurrence of the tetragonal  $L1_0$  FePt phase in the annealed sample. The Mössbauer spectrum of the sample annealed at 600 °C for 1 hour shows quite different features. The spectrum presents itself as a magnetic distributed sextet, but with much narrower lines. Here, lines 1 and 6 of the sextet are more intense and much better defined than in the case of the as-cast sample. The asymmetrical line profiles suggest that the sample is multi-phased, since there are contributions from various sublattices, convoluted, visible in the spectrum. The large, irregular shape of the transmission pattern, recorded between  $-2$  mm/s and  $+3$  mm/s suggests a contribution with low hyperfine field, probably due to the existence of a disordered residual matrix, with low Fe content, situated perhaps in the intergranular regions.

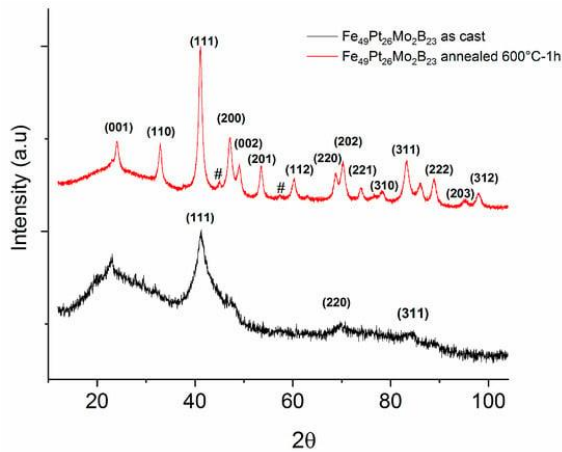


**Fig. 1** X-ray diffractograms of as-cast and annealed Fe-Pt-Mo-B sample.

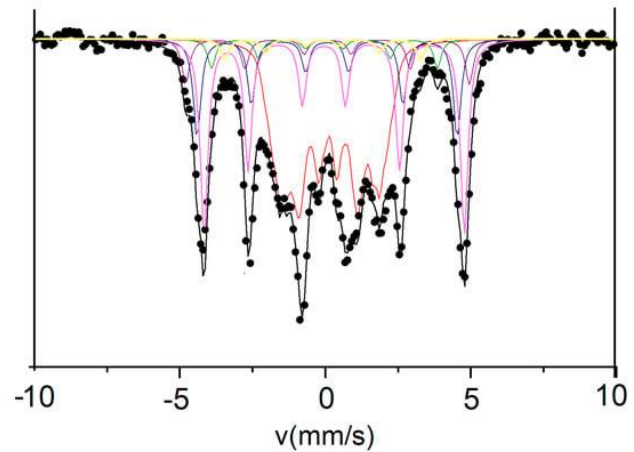


**Fig. 2** 300 K Mössbauer spectrum of the annealed Fe-Pt-Mo-B sample.

Considering that heavy noble metals such as Pt exhibit a quite large X-ray absorption, also taking into account the Pt abundance in the sample stoichiometry, it was surprising to reach such a clearly resolved spectrum with strong enough line intensities. We have successfully fitted the Mössbauer spectrum with 6 different magnetic sublattices, in good agreement with the microstructural findings. In all, we have determined the occurrence of  $L1_0$  phase also in the quaternary systems. At a larger scale, chemical synthesis and deposition techniques in controlled atmosphere or in high vacuum do not allow for a large yield of the material, as required for several applications; therefore, in this case, out-of-equilibrium synthesis pathways are the method of choice for such RE-free magnets. One of these methods is the rapid solidification from the melt, or melt-spinning. It has been shown that the direct formation of the  $L1_0$  phase can be promoted in FePt alloys by such out-of-equilibrium metallurgical methods, without the need for post-synthesis thermal annealing, as is needed currently in the case of nanoparticles or thin films. This is due to the ultrafast solidification from the melt, which can stabilize phases that are only possible in the liquid alloy, phases that are now accessible and attainable in the solid state. The method is particularly interesting in the case of MnGa system alloys [2]. As another system, which can promote the formation of the  $L1_0$  phase, the MnGa binary system has quite complicated phase structure in the Mn-rich part of the phase diagram. Therefore, a method that can stabilize the  $L1_0$  phase to the detriment of other possible structures, such as the mentioned melt-spinning phase, seems more than appropriate for producing stabilized  $L1_0$  MnGa alloys. We have reported the formation of the  $L1_0$  and  $D0_{22}$  tetragonal phases in the MnGa, Mn-rich alloys synthesized by an out-of-equilibrium method, suitable for industrial

applications. Moreover, we bring evidence for high magnetic performances for MnGa samples under various annealing conditions. We show that among other L1<sub>0</sub>-based magnetic materials, MnGa has promising prospects for applications in various industrial fields. Both being tetragonal, the D0<sub>22</sub> phase crystallizes in *I4/mmm* space group and it is encountered for Mn content between 63 and 81%, and L1<sub>0</sub> phase crystallizes in the *P4/mmm* and is encountered for Mn content between 50 and 70%. According to the MnGa phase diagram there could be a range of Mn content where these two tetragonal phases could co-exist. Their distinctive signature in XRD patterns is the occurrence of the so-called superlattice peaks. It is to be noted that while the *c* parameter of the D0<sub>22</sub> is basically the double of the *c* parameter of the L1<sub>0</sub> phase, the *a* parameter does not vary significantly. We indexed on the patterns recorded for the samples annealed at 400 °C and 500 °C the superlattice peaks (001), (011), (101) and (110), belonging to the tetragonal MnGa phase.

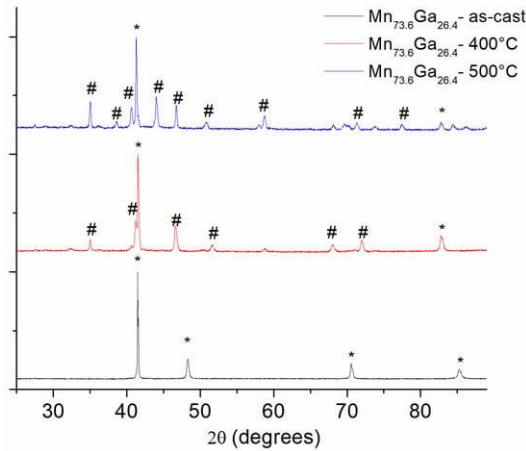


**Fig. 3** The XRD patterns of the as-cast as well as annealed at 400 °C and 500 °C samples. The corresponding symbols are: \*—D0<sub>19</sub>, #—tetragonal (L1<sub>0</sub>/D0<sub>22</sub>).

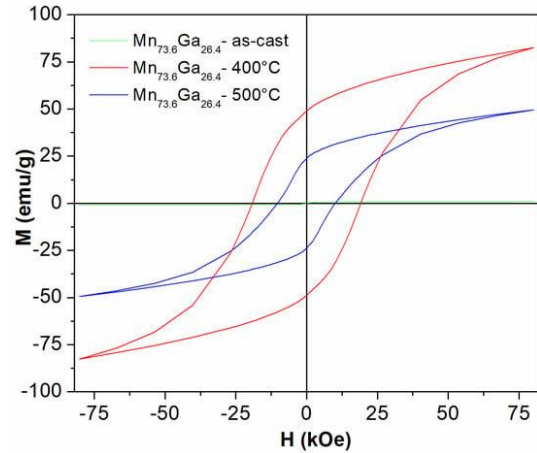


**Fig. 4** 300 K hysteresis loops for the as-cast MnGa sample and annealed at 400 °C and 500 °C.

Upon increasing the annealing temperature, at 500 °C annealing, the patterns show even more pronounced superlattice peaks with heightened intensity. Since the sole XRD pattern cannot give distinct proof of either of the two tetragonal phases, we infer that these additional peaks, marked with # on the graph belong to either of the two D0<sub>22</sub> and L1<sub>0</sub> tetragonal MnGa phases. The only indication at this point for tipping the scale in favor of one or the other is represented by the Mn content, which is, in fact, close to the border between L1<sub>0</sub> and D0<sub>22</sub>. The hysteresis loops of the annealed samples show a strong increase in both net magnetization and coercivity. The sample annealed at 400 °C exhibits a maximum specific magnetization of about 81 emu/g, while the sample annealed at 500 °C shows a smaller value of the maximum specific magnetization of about 49 emu/g. Considering the density of the sample (6.69 g/cm<sup>3</sup>), we calculated the maximum magnetization to be around 0.54 M A/m and 0.32 M A/m for the samples annealed at 400 °C and 500 °C, respectively. These findings are promising for further applications.

#### References:

1. A.D. Crisan, O. Crisan, “Novel Rare Earth (RE)-Free Nanocomposite Magnets Derived from L1<sub>0</sub>-Phase Systems”, *Nanomaterials* 13, 912 (2023).
2. O. Crisan, A.D. Crisan, “Remarkable Magnetic Properties in a Mn<sub>73.6</sub>Ga<sub>26.4</sub> Alloy Produced via Out-of-Equilibrium Method”, *Nanomaterials* 13, 3014 (2023).

# Metasurfaces for Metalens and Thermal Emitters Applications

**O. Rasoga<sup>a</sup>, C.A. Dirdal<sup>b</sup>, D. Dragoman<sup>c</sup>, A. Dinescu<sup>d</sup>, I. Zgura<sup>a</sup>, A. Summanwar<sup>b</sup>, K. Milenko<sup>b</sup>, F.T. Dullo<sup>b</sup>, P.C.V. Thrane<sup>b</sup>, F. Nastase<sup>d</sup>, A.M. Baracu<sup>d</sup>, A.M. Avram<sup>d</sup>, S. Iftimie<sup>c</sup>, A.C. Galca<sup>a</sup>**

<sup>a</sup> National Institute of Materials Physics, 077125 Magurele, Romania

<sup>b</sup> SINTEF Microsystems and Nanotechnology, 0737 Oslo, Norway

<sup>c</sup> University of Bucharest, Faculty of Physics, 077125 Magurele, Romania

<sup>d</sup> National Institute for Research and Development in Microtechnologies, 077190 Voluntari, Romania

The last decade has been characterized by an exponential growth of optical devices such as: lenses, waveplates, spectral filters, polarizers or thermal emitters based on metasurfaces that show the ability to modulate the light–matter interaction on the subwavelength scale [1,2] Metasurfaces are seen as two-dimensional planar surfaces composed of ultrathin periodic, quasi or aperiodic arrays of meta-atoms with specific sizes, shapes, orientations and subwavelength spatial resolution [3,4]. Compared to conventional optical elements consisting of curved surfaces or diffractive gratings, metasurfaces offer control over all degrees of freedom of the propagating field (amplitude, phase, polarization, propagation direction and dispersion) [5]. Therefore, working as metalenses, they are often called meta optical elements (MOEs) due to the fact that can provide completely new methods of field control, generating tremendous interest in the photonics community. This interest is heightened by the fact that these metalenses can “combine multiple optical functions into a single element” as reported by Metalenz on their website. Moreover, by studying the scientific literature and commercial research trends, it can be seen that the theory and fabrication techniques for mass production and commercialization of metalenses have gain special attention. One of the reasons is caused by the miniaturization trends of components in current commercial devices, thus implying the need to manufacture small, lightweight and cheap optical elements while maintaining optical quality [6]. However, metalens fabrication requires techniques that can provide a high aspect ratio for the fabricated patterns. These techniques are generally expensive, which is therefore a challenge for their scalable fabrication. The present study highlights both that metasurfaces can be used for various applications (metalens and as IR thermal emitters) and that there are different ways to fabricate them

For the metasurfaces working as metalenses, we demonstrate that by using UV-Nanoimprint lithography (UV-NIL) and Deep Reactive Ion Etching (DRIE) one can fabricate diffraction-limited dielectric metasurface lenses operating in the Near Infrared Domain (NIR) range  $\lambda \in (1.3 \mu\text{m}, 1.7 \mu\text{m})$  using cost-effective fabrication techniques that retain the high pattern fidelity [4]. The metalens design, obtained by using the geometric phase principle, consist of rectangular silicon pillars, with height ( $h$ ) = 1200 nm, width ( $w$ ) = 230 nm, length ( $l$ ) = 354 nm and periodicity ( $p$ ) = 835 nm, etched into silicon substrate. Process optimization compared to previously published work [6–8] started from the UV-NIL master. So, in order to minimize the various processes deviations (scallop sizes resulting from the Bosch DRIE process, tilting of the sidewalls, rounding of the rectangular pillars due to the thickness of the sacrificial layer after the isotropic RIE process) from the theoretical target dimensions, special attention was paid to the lateral dimensions of the silicon pillars populating the master.

Three types of metalenses were designed, each with different dimensions for the rectangular silicon pillars: (i)  $w = 351$  nm and  $l = 475$  nm; (ii)  $w = 292$  nm and  $l = 416$  nm; (iii)  $w = 237$  nm and  $l = 361$  nm. Metalenses obtained by using the UV-NIL followed by the optimized DRIE Bosch or Cryogenic showed a high degree of geometrical fidelity, as shown in Fig. 1. The measured

efficiencies of the fabricated metalenses are in the range of 50 – 52% close to the theoretical one at around 69 %. We expect that by replacing the silicon substrate with quartz, the metalenses efficiency can reach 90 % or higher.

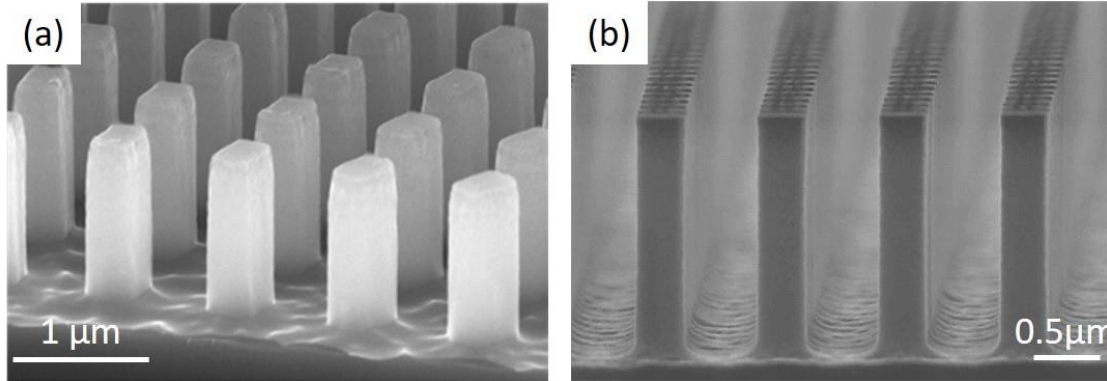


**Fig. 1** Cross-sectional SEM images of metalenses after cryogenic DRIE process (a) and Bosch DRIE process (b) taken from the results reported on the joint paper [4].

Another functionality of metasurfaces is to act as thermal emitters. In general, most of the metasurfaces designed to function as IR sources are fabricated for the mid-infrared or visible spectral ranges. We are currently focusing our interest on NIR sources that can be used for plastic detection applications. Therefore, we proposed two metasurface designs with a suitable (not very narrow) emissivity in the NIR range, consisting of periodic dielectric layers of  $\text{HfO}_2$  and  $\text{Al}_2\text{O}_3$  placed on a lower gold layer and with rectangular gold meta-atoms on top of them, so as illustrated in Fig. 2.

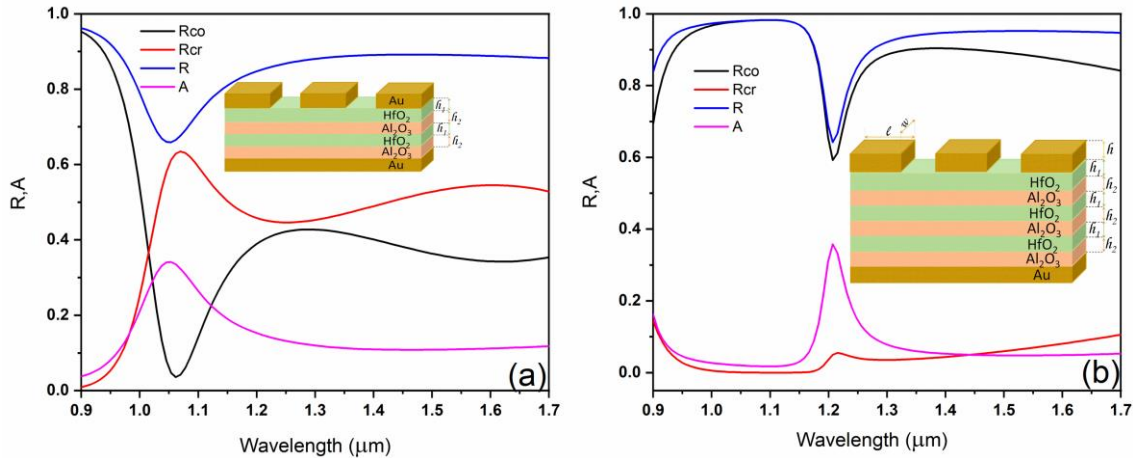


**Fig. 2**  $R_{cr}$ ,  $R_{co}$ , the total reflectance  $R$  and the absorbance  $A$  simulation curves of metasurfaces consisting of 2 and 3  $\text{HfO}_2/\text{Al}_2\text{O}_3$  periods for a circular polarized incident electromagnetic radiation [3]

For the chosen metasurface, the thicknesses of the  $\text{HfO}_2$  and  $\text{Al}_2\text{O}_3$  layers were  $h_1 = 50$  nm and  $h_2 = 40$  nm respectively, and the dimensions for the gold meta-atoms were:  $w = 100$  nm,  $l = 250$  nm, and  $h = 30$  nm. COMSOL was used to calculate  $R_{cr}$ ,  $R_{co}$ , the total reflectance  $R$  and the absorbance  $A$ . It can be seen, from Fig. 2, that the resonant wavelength as well as the resonance spectral width are dependent on the number of dielectric periods. Fabrication of the thermal emitters was accomplished using atomic layer deposition (ALD) and electron beam lithography (EBL). Optical

measurements to confirm the numerical simulation were performed by both Fourier Transform Infrared spectroscopy (FTIR) and by ellipsometry.

Our results showed that not only the resonance can be tuned by changing the number of periodic layers, but also that the value of reflectance at resonance depends on the orientation of the meta-atoms with respect to the direction of the incident electromagnetic wave (Fig. 3).

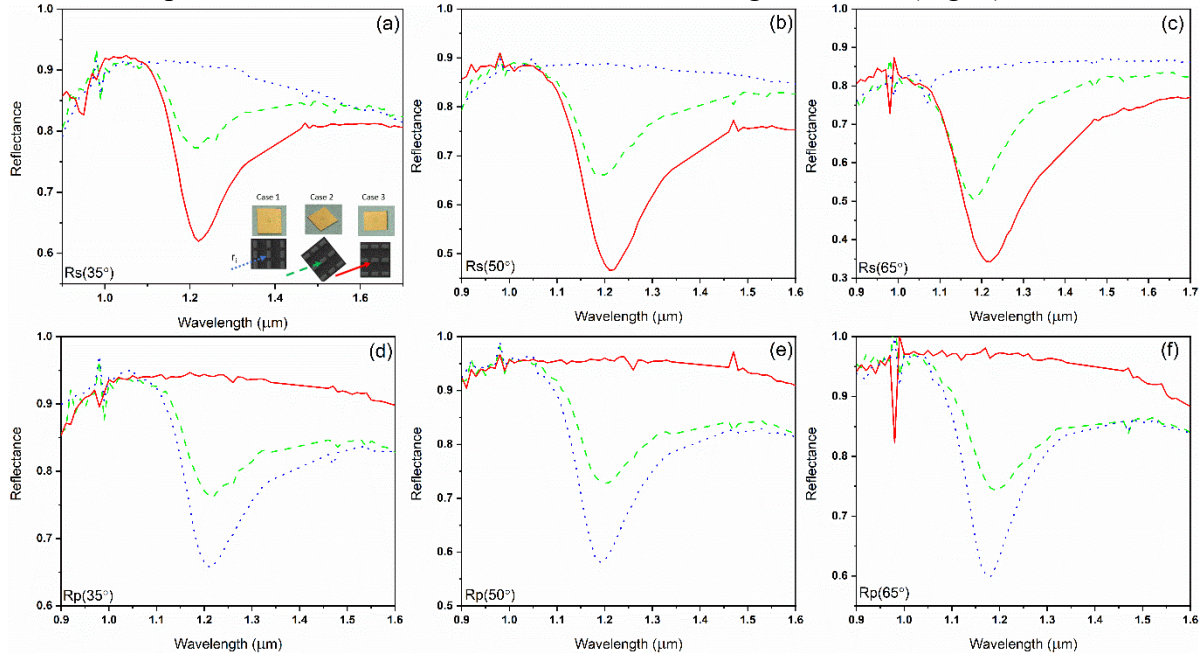


**Fig. 3** Reflectance measurements for light polarization perpendicular (a), (b), (c) and (d), (e), (f) parallel to the incidence plan in function of the meta-atoms position

## References

1. W. Ji, J. Chang, H.X. Xu, *et al.*, “Recent Advances in Metasurface Design and Quantum Optics Applications with Machine Learning, Physics-Informed Neural Networks, and Topology Optimization Methods”, *Light: Science & Applications* 12, 169 (2023).
2. S.A. Khan, N.Z. Khan, Y. Xie, *et al.*, “Optical Sensing by Metamaterials and Metasurfaces: From Physics to Biomolecule Detection”, *Advanced Optical Materials* 10, 2200500 (2022).
3. O. Rasoga, D. Dragoman, A. Dinescu, *et al.*, “Tuning the Infrared Resonance of Thermal Emission from Metasurfaces Working in Near-Infrared”, *Scientific Reports* 13, 7499 (2023).
4. C.A. Dirdal, K. Milenko, A. Summanwar, *et al.*, “UV-Nanoimprint and Deep Reactive Ion Etching of High Efficiency Silicon Metalenses: High Throughput at Low Cost with Excellent Resolution and Repeatability”, *Nanomaterials* 13, 436 (2023).
5. S. Kanwal, J. Wen, B. Yu, *et al.*, “Polarization Insensitive, Broadband, near Diffraction-Limited Metalens in Ultraviolet Region”, *Nanomaterials* 10, 1439 (2020).
6. C.A. Dirdal, G.U. Jensen, H. Angelskär, *et al.*, “Towards High-Throughput Large-Area Metalens Fabrication Using UV-Nanoimprint Lithography and Bosch Deep Reactive Ion Etching”, *Optics Express* 28, 15542 (2020).
7. A.M. Baracu, C.A. Dirdal, A.M. Avram, *et al.*, “Metasurface Fabrication by Cryogenic and Bosch Deep Reactive Ion Etching”, *Micromachines* 21, 501 (2021).
8. A.M. Baracu, M.A. Avram, C. Breazu, *et al.*, “Silicon Metalens Fabrication from Electron Beam to UV-Nanoimprint Lithography”, *Nanomaterials* 11, 2329 (2021).

# DRIFT Investigations of CO and H<sub>2</sub> Sensing with NiO based Gas Sensor

C.E. Simion <sup>a</sup>, A. Stănoiu <sup>a</sup>, B. Junker <sup>b</sup>, U. Weimar <sup>b</sup>, N. Bârsan <sup>b</sup>

<sup>a</sup> National Institute of Materials Physics, 077125 Magurele, Romania

<sup>b</sup> Institute of Physical and Theoretical Chemistry and Center for Light-Matter Interaction, Sensors & Analytics (LISA+), University of Tübingen, 72076 Tübingen, Germany

Nickel oxide (NiO) exhibits a *p*-type semiconductor behaviour due to its Ni<sup>2+</sup> vacancies and O<sub>2</sub> defects, showing moderate attention in the field of gas sensing based on semiconducting metal oxides [1]. It was demonstrated that NiO has a special relationship with the relative humidity (RH) by its inert electrical behaviour to the RH changes [2]. Although this aspect has a great impact on further developments, the deep understanding of the RH-NiO sensitive surface interaction is still a matter of debate. Aiming to explore fundamental insights about gas sensing performances with NiO based gas sensors, simultaneous electrical resistance and DRFIT (Diffuse Reflectance Infrared Fourier Transform) were involved [3], exploiting the fact that molecules absorb specific frequencies that are characteristic of their structure. The operating temperature was set to 250 °C, where the maximum in the sensor signal takes place. The resistance changes when going from dry air to 10% RH is very low (Signal=1.04) thus, the moisture does not have a significant impact on the sensor resistance like in the case of many other sensitive materials [4]. In order to understand this process, an electronically neutral reaction must be taken into account. Both H<sub>2</sub> and CO showed relatively good responses under dry air conditions. It deserves to be noted that, in humid conditions the sensor signals are higher than in dry air and in nitrogen atmosphere (in the absence of oxygen).

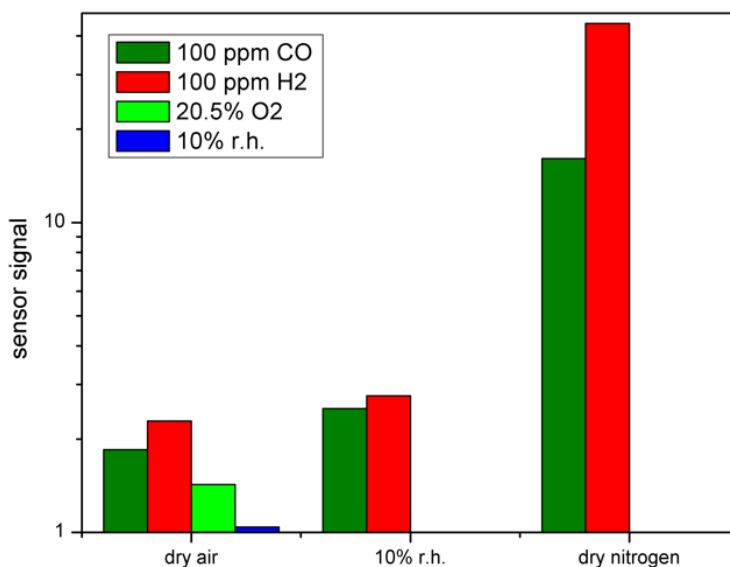


**Fig. 1** Sensor signals for CO and H<sub>2</sub> under different surrounding atmospheres (dry air, air with 10% RH and dry N<sub>2</sub>).

### Oxygen and water interactions with NiO sensitive material

From the spectra presented in Fig. 2, one can attribute the surface Ni–O vibrations to the following process:

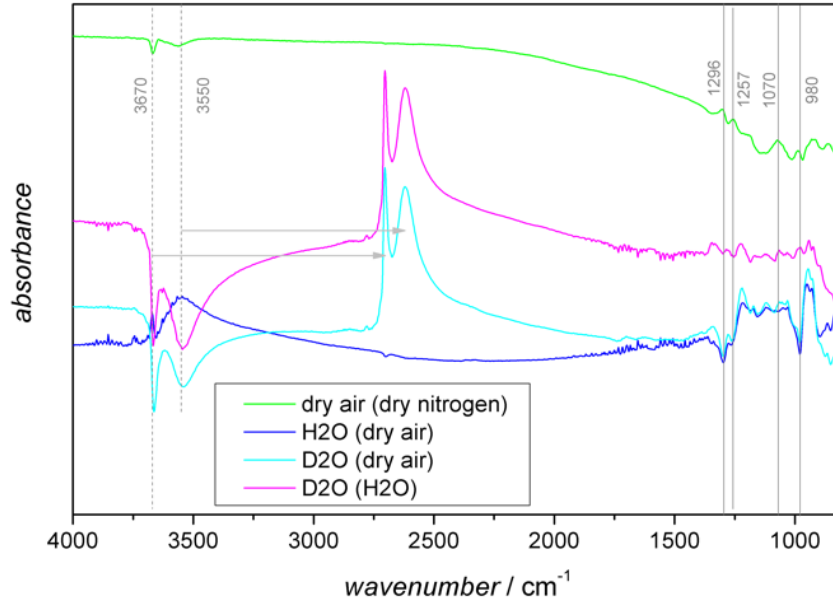
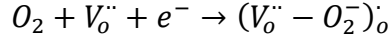


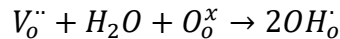
**Fig. 2** DRIFT absorbance spectra of NiO operated at 250 °C during exposure to air (20.5% O<sub>2</sub> in N<sub>2</sub>) and water (in form of H<sub>2</sub>O and D<sub>2</sub>O vapors, both as 10% RH@25 °C).

According to the Fig. 3a, the subsequent reaction is valid involving the filling of oxygen vacancies with oxygen molecules:

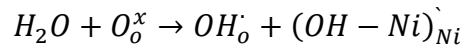


Regarding the relative humidity interaction with the NiO surface, two-fold scenarios must be taken into account:

The first refers to the formation of two rooted hydroxyl groups:



The second leads to the appearance of a rooted and isolated OH group with respect to the following equation:



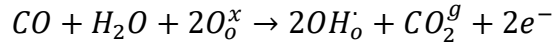
As one can see such reactions are electrically neutral, fact observed also from the experimental point of view.

### Carbon monoxide and Hydrogen interactions with NiO sensitive material

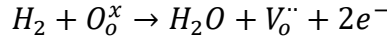
The possible reaction between the CO as target gas and NiO surface consists in the oxidation to CO<sub>2</sub> involving the lattice oxygen of the said material:



With respect to the Fig. 3b, the reaction of CO with the NiO in the presence of RH creates new reaction sites for humidity instead of a possible competition with these:



In the case of H<sub>2</sub> it is possible to reduce the NiO material according to the following reaction:



The sensor signals for H<sub>2</sub> are higher in the presence of humidity and this is due to the fact that H<sub>2</sub> and H<sub>2</sub>O are not competing for the same sites as in the case of SnO<sub>2</sub>.

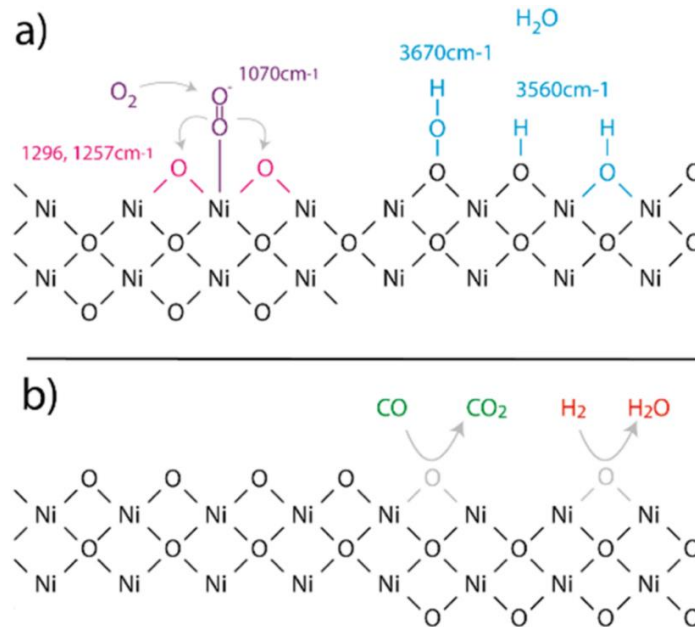


**Fig. 3** Cartoon of Ni (111) surface reactions: (a) adsorption and dissociation of O<sub>2</sub> (left) and possible reaction of H<sub>2</sub>O (right). (b) Oxidation of the NiO surface by CO and H<sub>2</sub>.

NiO have shown good response to CO and H<sub>2</sub> in O<sub>2</sub> and in the presence of humidity. DRIFT findings presented that O<sub>2</sub>, H<sub>2</sub> and CO exhibit quite similar surface reactivity. H<sub>2</sub>O has no reducing effect on NiO and is not competing for the same reaction sites like CO and H<sub>2</sub>.

#### References

1. T.P. Mokoena, H.C. Swart, D.E. Motaung, "A Review on Recent Progress of p-Type Nickel Oxide based Gas Sensors: Future Perspectives", *Journal of Alloys and Compounds* 805, 267–294, (2019).
2. R.L. Wilson, C.E. Simion, A. Stanoiu, *et al.*, "Humidity-Tolerant Ultrathin NiO Gas-Sensing Films", *ACS Sens.* 5, 1389–1397, (2020).
3. C.E. Simion, B. Junker, U. Weimar, A. Stanoiu, N. Barsan, "Sensing Mechanisms of CO and H<sub>2</sub> with NiO Material – DRIFTS Investigations", *Sensors and Actuators B: Chemical* 390, 134028 (2023).
4. B. Saruhari, R.L. Fomekong, S. Nahirmiak, "Review: Influences of Semiconductor Metal Oxide Properties on Gas Sensing Characteristics", *Frontiers in Sensors* 2, 657931, (2021).

# Design of Electrocatalysts for Energy Production

M.M. Trandafir, A. Kuncser, F. Neațu, Ș. Neațu, M. Florea

National Institute of Materials Physics, 077125 Magurele, Romania

Nowadays, covering the energy demands of humanity without generating toxic or harmful substances is a particularly important challenge. The need to solve this problem triggered an increased interest in the development of fuel cells as promising eco-friendly energy conversion devices. In the last decade, a range of oxide-containing electrocatalyst materials [1] were proposed for both the hydrogen oxidation reaction (HOR) and the oxygen reduction reaction (ORR). Even if in electrochemical experiments many oxide-containing electrocatalysts showed excellent properties, their utilization in fuel cells remains extremely rare. During this study, we performed experiments in two directions:

(i) On one hand, the interest in binary oxides with multiple valence states like nickel-tungsten mixed oxides ( $\text{NiWO}_4$ ) is related to the advantages they offer, such as inexpensiveness, non-toxicity, and electrical conductivity, depending on the calcination temperature. However,  $\text{NiWO}_4$  has relatively low electrical conductivity and low specific surface area, which is disadvantageous when it is applied in electrocatalysts for fuel cells. These disadvantages can be overcome by combining  $\text{NiWO}_4$  with a suitable carbonaceous material [2]. Thus, we aimed to prepare mesoporous  $\text{NiWO}_4$  through a facile co-precipitation synthesis route, by using poly(ethylene glycol) (PEG) as a template and using it, as support for the preparation of catalysts with a relatively low (8 wt.%) Pt content. To increase both the conductivity and the surface area of our catalysts, the mesoporous  $\text{NiWO}_4$  was combined with carbonaceous materials, *i.e.*, GNP and Black Pearls 2000 (BP, Cabot Corporation) carbon. The structural and morphological characterizations are presented in Fig. 1.

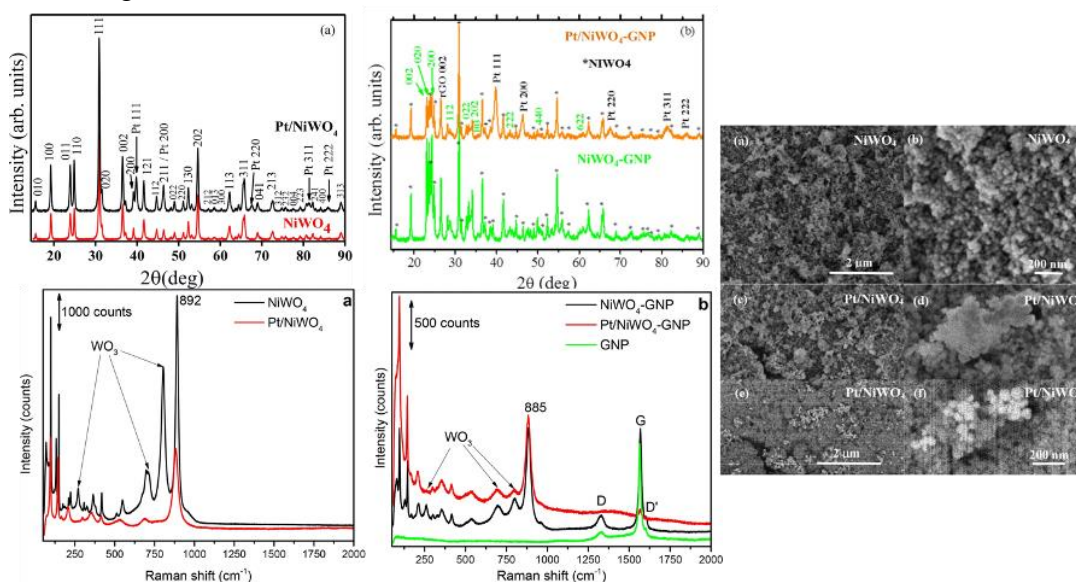


**Fig. 1** XRD patterns, Raman spectra, and SEM micrographs for  $\text{NiWO}_4$ ,  $\text{Pt/NiWO}_4$ ,  $\text{NiWO}_4\text{-GNP}$ ,  $\text{Pt/NiWO}_4\text{-GNP}$ .

To clarify the possibility of using these novel materials as cathode and/or anode in fuel cells, their electro-chemical characteristics were investigated. The corresponding cyclic voltammograms are presented in Fig. 2.

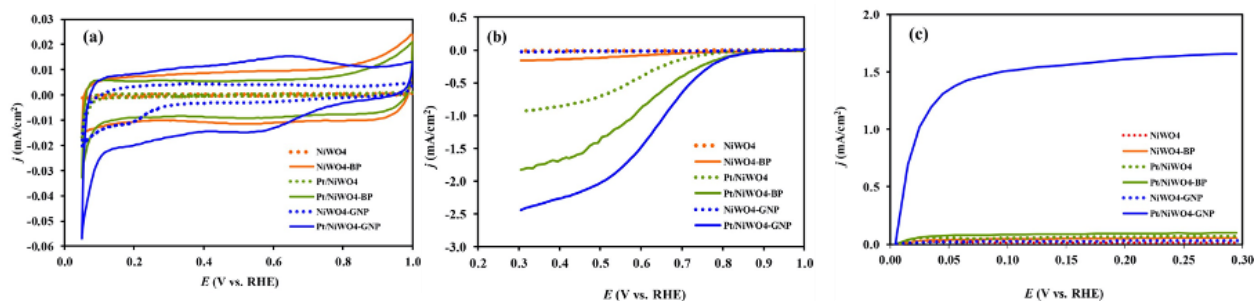


**Fig. 2** Electrochemical characterization of the NiWO<sub>4</sub>- based electrocatalysts: (a) Cyclic voltammograms obtained with and without addition of 20 wt.% BP carbon; (b) ORR curves obtained in O<sub>2</sub>-saturated 0.5 M H<sub>2</sub>SO<sub>4</sub> on a rotating disc electrode (RDE) at 1600 revolutions/min (rpm); (c) HOR curves obtained in a H<sub>2</sub>-saturated 0.5 M H<sub>2</sub>SO<sub>4</sub> on a RDE at 1600 rpm.

Since the NiWO<sub>x</sub> solid solution with mixed valence oxides can exhibit electrical conductivity or semiconductivity, initially the samples were tested without mixing with carbon. The addition of carbon resulted in slightly distorted rectangular curves with significantly wider hysteresis, indicating an increase in capacity compared to samples without carbon as a result of better electrolyte access to the electrode surface. The presence of 8 wt.% of Pt in the samples reflected in some increase of the peak associated with adsorption of under potentially deposited hydrogen on Pt surface. The mesoporous composite NiWO<sub>4</sub>-GNP bifunctional catalyst showed better electrochemical performance, as a result of the beneficial role played by GNP introduced by direct synthesis. The synergic phenomena between the NiWO<sub>4</sub> and GNP were induced by the direct synthesis route leading to a growth of NiWO<sub>4</sub> faceted crystallites with different W valence states. The addition of Pt to NiWO<sub>4</sub>-GNP induces an improvement in HOR, and also generates a final composite that is more efficient than the commercially available 20Pt/C material if we take into account the Pt loading of the electrodes. This behavior is a result of the synergy of the bifunctional NiWO<sub>4</sub>-GNP material and the reduced Pt content.

(ii) On another hand, we investigated the possibility of using Ni<sup>2+</sup>/Ni<sup>3+</sup> decorated mesoporous SnO<sub>2</sub> as anode material for bioethanol electrochemical oxidation [3]. There are reasons to believe that, due to its good electric conductivity and high stability [4,5], tin oxide is a suitable substrate material and the use of a high surface area mesoporous SnO<sub>2</sub> structure as support for Ni species would provide a large number of active sites in a small volume. Indeed, BET measurements have shown that the nickel deposition in a reducing environment does not alter the mesoporous structure of the SnO<sub>2</sub>, although it leads to a significant increase of its specific surface area. This increase is even more important in the presence of a slight amount of BP, in which case a small contribution of larger pores also appears. In addition, the surface chemistry assessment by XPS analysis confirms the presence of the Ni<sup>2+</sup>/Ni<sup>3+</sup> oxidation states in chemical species such as NiO, Ni(OH)<sub>2</sub> and Ni<sub>2</sub>O<sub>3</sub> on the outermost surface layer (<10 nm), with beneficial effects on the activity and stability of the electrocatalyst. Morphological characterization of the investigated electrocatalysts and the carbonaceous material was also carried out by Conventional TEM (CTEM) and High Resolution TEM (HRTEM) and Fig. 3 illustrates the results. It appears that Ni/SnO<sub>2</sub> samples (Figs.

3a and 3d), with a mesoporous aspect, consist of SnO<sub>2</sub> nanocrystalline grains with a size in the range of 20÷30nm. Conversely, BP system (Figs. 3b,e) shows amorphous C spheres (with particle diameters within the same range), whereas, as Figs. 3c,f indicate, in the Ni/SnO<sub>2</sub>-BP mixture the original morphology of both Ni/SnO<sub>2</sub> and BP components can be still observed. TEM and SEM results have put in evidence the homogeneity of the electrocatalysts, their particular spherical morphology and the lack of agglomerates formation. Linear sweep voltammetric experiments demonstrated that, both in the absence and in the presence of BP, bioethanol anodic oxidation begins almost simultaneously with NiOOH formation, in line with the well-known electrocatalytic activity for alcohol oxidation of these species. For this process, a Tafel slope of 80 mV decade<sup>-1</sup> was estimated at Ni/SnO<sub>2</sub> that favorably compares to those reported in the literature.

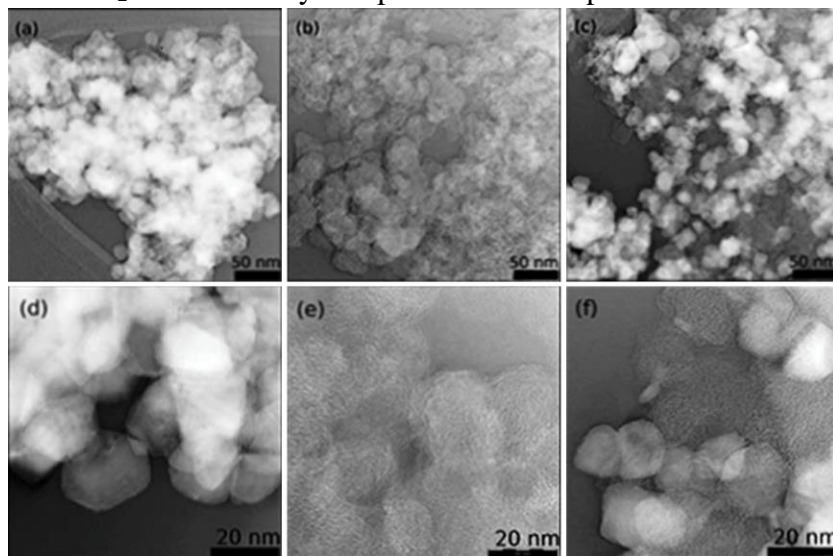


**Fig. 3** (a)–(c) C-TEM and (d)–(f) HRTEM images of (a,d) Ni/SnO<sub>2</sub>, (b,e) BP, and (c,f) Ni/SnO<sub>2</sub>-BP.

We conclude that the electrocatalytic performance is mainly derived from the Ni<sup>2+</sup>/Ni<sup>3+</sup> chemical states associated with Ni(OH)<sub>2</sub>, NiO and Ni<sub>2</sub>O<sub>3</sub>, which can oxidize the bioethanol and regenerate the nickel hydroxide as well as improve the CO<sub>x</sub> tolerance. Furthermore, it was found that BP incorporation leads to a decrease of the Tafel slope to 70 mV decade<sup>-1</sup>, without deleteriously affecting the stability of the electrocatalyst during long-term polarization, probably due to the intrinsic robustness of the SnO<sub>2</sub> support.

#### References

1. Z. Zhang, J. Liu, J. Gu, *et al.*, “An Overview of Metal Oxide Materials as Electrocatalysts and Supports for Polymer Electrolyte Fuel Cells”, *Energy and Environmental Science* 7, 2535–2558 (2014).
2. S. Somacescu, P. Osiceanu, J.M. Calderon Moreno, *et al.*, “Design of Electrocatalysts with Reduced Pt Content Supported on Mesoporous NiWO<sub>4</sub> and NiWO<sub>4</sub>-Graphene Nanoplatelets Composite for Oxygen Reduction and Hydrogen Oxidation in Acidic Medium”, *International Journal of Hydrogen Energy* 48, 6317–6335 (2023).
3. T. Spătaru, S. Somacescu, P. Osiceanu, *et al.*, “Nickel Species-Modified Mesoporous SnO<sub>2</sub> as a Non-Platinum Electrocatalyst for Bioethanol Anodic Oxidation”, *Journal of the Electrochemical Society* 170, 124518 (2023).
4. M.A. Mihai, T. Spataru, S. Somacescu, *et al.*, “Nitrite Anodic Oxidation at Ni(ii)/Ni(iii)-Decorated Mesoporous SnO<sub>2</sub> and its Analytical Applications”, *Analyst* 148, 6028–6035 (2023).
5. Ș. Neațu, F. Neațu, V.C. Diculescu, *et al.*, “Undoped SnO<sub>2</sub> as a Support for Ni Species to Boost Oxygen Generation through Alkaline Water Electrolysis”, *ACS Applied Materials & Interfaces* 12, 18407–18420 (2020).

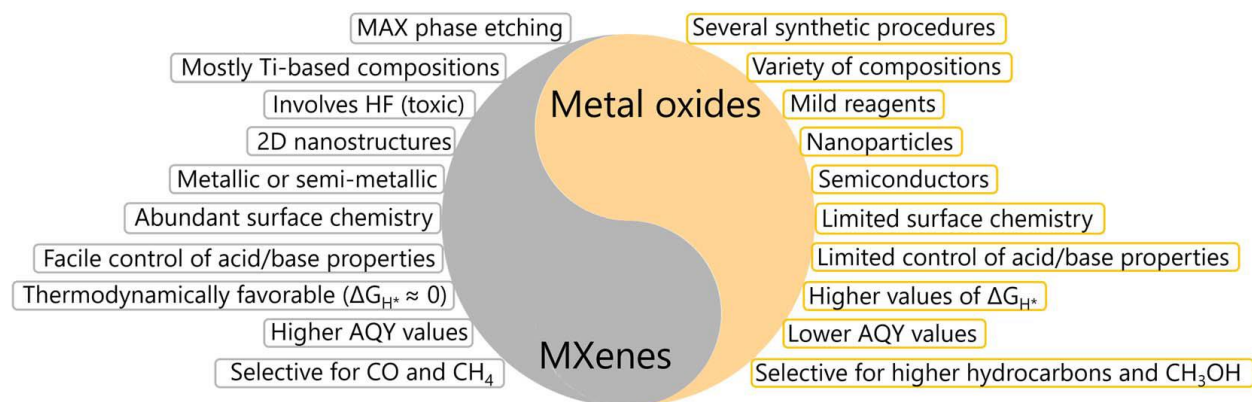
# Hydrogen Production through Photocatalysis

M.M. Nair, A.C. Iacoban, A. Kuncser, A.M. Rostas, F. Neațu, M. Florea, Ștefan Neațu

National Institute of Materials Physics, 077125 Magurele, Romania

The utilization of photocatalytic conversion of H<sub>2</sub>O, CO<sub>2</sub>, and N<sub>2</sub> is a highly promising method for capturing and storing solar energy [1–3]. To achieve this, it is crucial to have semiconductors that can efficiently respond to visible light. Frequently, the photocatalyst's effectiveness can be significantly improved by the addition of a little quantity of an extra component known as a "cocatalyst" [4]. In the past, significant endeavors were undertaken to discover cost-effective materials that may serve as cocatalysts. Among the conventional options, metal oxides (MOs) were considered. The recently found MXenes are a type of material that has a unique 2D layered structure, adjustable composition, many surface functions, and excellent electronic conductivity. These characteristics make MXenes highly promising in various applications. MOs and MXenes possess a range of unique and similar attributes that can be customized to varying degrees.

In a recent review, Nair *et al.* [5] aimed to highlight advances in two families of materials as cocatalysts for photoconversion of H<sub>2</sub>O, CO<sub>2</sub>, and N<sub>2</sub>. After providing a broad introduction, the authors briefly discuss the fundamental principles and role of cocatalysts in photocatalytic reactions. The employment of MOs and MXenes as cocatalysts for converting H<sub>2</sub>O, CO<sub>2</sub>, and N<sub>2</sub> was discussed in separate sections, while by critical evaluation of structure, morphology, surface properties, and stability the authors identified limits to advancement and suggested future research directions for H<sub>2</sub>O, CO<sub>2</sub>, and N<sub>2</sub> transformation.



**Scheme 1** A scheme that summarize the pros and cons of using MXenes and metal oxides as photocatalysts.

This review emphasizes the significance of optimizing the amount and kind of cocatalyst, and its careful consideration and control (Scheme 1). Additionally, parameters like as electrical characteristics, composition, loading, and morphology significantly impact hybrid materials' photocatalytic activity. This review found that using MXenes and MOs as cocatalysts can significantly enhance photocatalyst activity. The photocatalytic technologies outlined in this review are promising, the authors emphasizing that issues including activity, stability, and high cost must be addressed. Moreover, considering that the photocatalytic process occurs on photocatalyst surfaces, it is important to screen the surface and electrical properties of

photocatalytic composites more thoroughly. For instance, in MXenes, the surface termination of functional groups varies based on etching process and reaction conditions, impacting photocatalytic behavior of composites. In this view, a single characterization approach, typically done before photocatalytic reactions, is insufficient to fully comprehend MXene surface properties. Therefore, a combination of complementary techniques is necessary. More study is needed to address stability difficulties in photocatalytic systems, particularly the impact of reaction environments on composite surfaces.

In photocatalytic processes, MXenes have been less widely studied than MOs as cocatalysts. MXenes are unstable in watery settings and when exposed to O<sub>2</sub> and UV irradiation, as they convert into their corresponding oxides. However, this can yield materials with characteristics of both carbides and oxides, enabling new photocatalysis materials. Additionally, investigations confirm the importance of carbon in separating charge carriers and using MXenes as photocatalyst precursors. To conclude, in this review, the authors emphasized that the stability of MXenes and MOs as cocatalysts requires molecular-level investigation, such as *in situ/operando* spectroscopies, to understand reaction mechanisms on composite surfaces under specific chemical and photocatalytic conditions. However, further theoretical and practical research is needed to advance MXene- and MO-based composites for photocatalysis applications. Due to the high production cost of MXene chemical compositions, most photocatalytic studies focus on Ti-based MXenes, with limited research on other materials. Utilizing alternative MXene-based composites requires additional theoretical and experimental research. To sum up, MXene and MO cocatalysts offer a viable alternative to costly noble-metal cocatalysts for photocatalytic applications, although further research is necessary. Based on this, there is room for improvement in MXene-based composite design and synthesis.

With this in mind and based on recent discovery that powders of various Ti-containing precursors, including TiC, Ti<sub>3</sub>SiC<sub>2</sub>, TiB<sub>2</sub>, and TiN, transform into 1D lepidocrocite-based nanofilaments (NFs) when immersed in TMAH aqueous solution at 50–80 °C for a few days [6,7], Badr *et al.* [8] demonstrate that these NFs exhibit significant photocatalytic activity in H<sub>2</sub>O/MeOH mixtures, with an outstanding AQY value of 11.7%. Remarkably, the NFs remained effective for over 4,300 hours in aqueous solutions consisting of 20% methanol, with 300 hours of exposure to both UV-Vis light and continuous magnetic stirring. NFs exhibit resistance to stirring, and, in certain instances, the AQYs shown a rise over time.

Based on the characterization data, water serves as the source of H<sub>2</sub> gas, and it does not produce either O<sub>2</sub> or CO<sub>2</sub>. It is important to note that the lack of both gases significantly restricts the range of potential reaction routes. Thus, the significance of NFs' thermodynamic stability and photochemical activity in H<sub>2</sub>O/MeOH mixtures for long periods of time cannot be overstated.

The findings of Badr *et al.* indicate potential avenues for the development of cost-effective and durable materials that can efficiently generate H<sub>2</sub> gas from water using photocatalysis over extended durations. Regarding scalability, the authors emphasize that NFs can be produced in a range of 100 grams per batch in a laboratory environment. Furthermore, due to the absence of CO<sub>2</sub> emissions in this photocatalytic process, its environmental sustainability and potential for substantial expansion are significantly improved. Moreover, the results presented in this study are from the first stage of development, and significant advancements are anticipated as the comprehension of the photochemical processes improves.

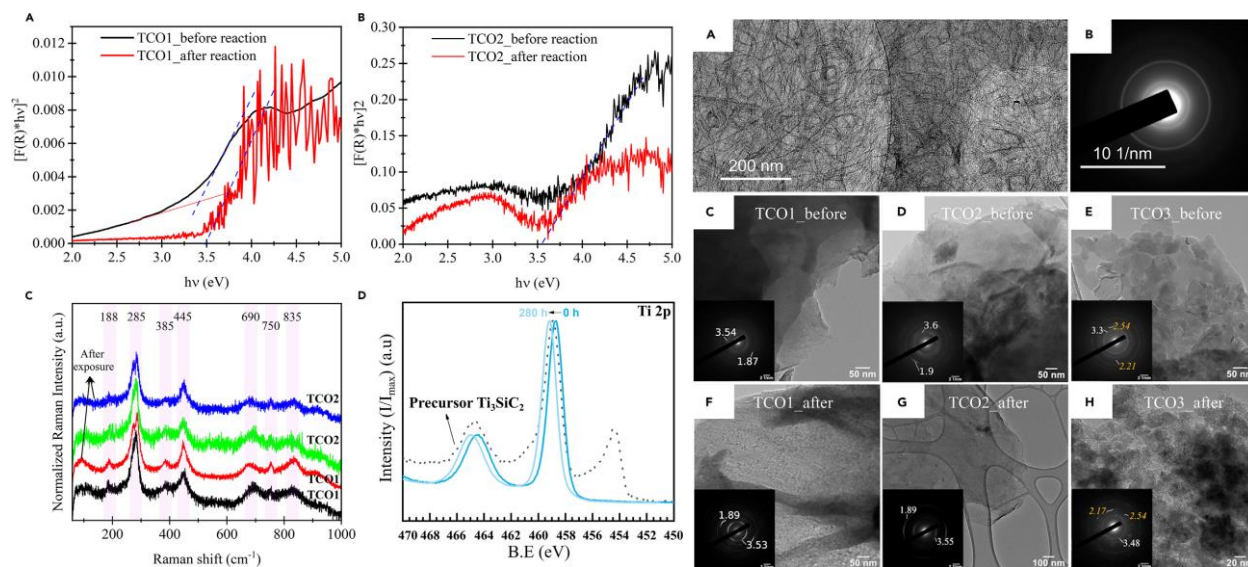


**Fig. 1** UV-Vis, Raman, XPS and TEM characterization of the most active NFs materials.

To conclude, these novel materials fulfill the criteria of an effective photocatalyst, including efficient charge separation, rapid charge transfer, and, notably, long-lasting stability under aqueous conditions. The current findings provide new opportunities for investigating energy generation systems utilizing one-dimensional nanofibers created from inexpensive, non-hazardous, and widely available starting materials by a straightforward, cost-effective, single-step, and scalable synthesis technique.

### References

1. N.S. Lewis, "Research Opportunities to Advance Solar Energy Utilization", *Science* 351, 1920 (2016).
2. R. Schäppi, D. Rutz, F. Dähler, *et al.*, "Drop-in Fuels from Sunlight and Air", *Nature* 601, 63–68 (2022).
3. Q. Wang, C. Pornrunroj, S. Linley, E. Reisner, "Strategies to Improve Light Utilization In Solar Fuel Synthesis", *Nature Energy* 7, 13–24 (2022).
4. D.G. Nocera, "The Artificial Leaf", *Accounts of Chemical Research*. 45, 767–776 (2012).
5. M.M. Nair, A.C. Iacoban, F. Neațu, M. Florea, S. Neațu, "A Comparative Overview of MXenes and Metal Oxides as Cocatalysts in Clean Energy Production through Photocatalysis", *Journal of Materials Chemistry A* 11, 12559–12592 (2023).
6. H.O. Badr, T. El-Melegy, M. Carey, *et al.*, "Bottom-up, Scalable Synthesis of Anatase Nanofilament-Based Two-Dimensional Titanium Carbo-Oxide Flakes", *Materials Today* 54, 8–17 (2022).
7. H.O. Badr, F. Lagunas, D.E. Autrey, *et al.*, "On the Structure of One-dimensional TiO<sub>2</sub> Lepidocrocite", *Matter* 6, 128–141 (2023).
8. H.O. Badr, V. Natu, S. Neațu, *et al.*, "Photo-stable, 1D-Nanofilaments TiO<sub>2</sub> Lepidocrocite for Photocatalytic Hydrogen Production in Water-Methanol Mixtures", *Matter* 6, 2853–2869 (2023).